FERMILAB-THESIS-2026-17

First Sterile Neutrino Search at NOvA Experiment Using both Neutrino and Anti-Neutrino Data

A dissertation submitted in partial fulfillment of the requirements for the degree of

Doctor of Philosophy

by

SHIVAM

Department of Physics,
Indian Institute of Technology Guwahati
Guwahati - 781039, Assam, India.

July 3, 2026

Declaration

Shivam
Roll No. 206121029
Department of Physics
Indian Institute of Technology Guwahati
Guwahati, India
email: shivam_1997@iitg.ac.in

I hereby declare that works presented in the thesis entitled **"First Sterile Neutrino Search at NOvA Experiment Using both Neutrino and Anti-Neutrino Data"** have been carried out by me under the supervision of **Prof. Bipul Bhuyan** at the Department of Physics, Indian Institute of Technology Guwahati, India. The thesis has not been submitted anywhere else for any degree. Works presented in the thesis are all my own unless referenced to the contrary in the thesis.

Signature

Certificate

Prof. Bipul Bhuyan
Department of Physics
Indian Institute of Technology Guwahati
Guwahati, India
email: bhuyan@iitg.ac.in

This is certified that the work contained in the thesis entitled **"First Sterile Neutrino Search at NOvA Experiment Using both Neutrino and Anti-Neutrino Data"** by Mr. Shivam (Roll No 206121029), a Ph.D. student in the Department of Physics, Indian Institute of Technology Guwahati, is carried out under my guidance. The results demonstrated in this thesis have not been submitted to any other Institute or University for the award of any other degree or diploma.

Signature

Acknowledgement

Science is not pursued in isolation; it is a collective endeavour and requires sustained efforts and collaboration, and this work is no exception. I would like to begin by expressing my sincere gratitude to all those who have supported me throughout this journey. If I unintentionally forgot to mention anyone, I offer my heartfelt apologies, as every contribution direct or indirect has been deeply valued.

First and foremost, I would like to express my sincere gratitude to my supervisor, Prof. Bipul Bhuyan, for providing me with the opportunity to work with him in the ever-evolving and fascinating field of neutrino physics. Under his mentorship, I have been granted complete academic freedom to explore and choose a research direction of my own interest, which has helped me grow as an independent and confident researcher. His continuous support and timely guidance have made my path through this entire journey easier.

I want to express my sincere gratitude to Dr Anne Norrick, who served as my supervisor during my two-year visit to Fermilab. Her continued efforts, guidance, constant availability, and encouragement have helped me grow as an individual and instilled a sense of scientific curiosity in me. I truly appreciate the insightful discussions that take place during the weekly meetings. I am also thankful to Dr Adam Lister, who was not only a collaborator but also someone I could always rely on whenever I encountered conceptual or technical challenges. His support, together with that of Dr Anne Norrick, extended well beyond formal collaboration and was sincerely appreciated.

I would also like to acknowledge the current and former conveners of the 'NuX' group, Prof. Adam Aurisano, Dr Adam Lister, Prof. Mario Acero Ortega and Prof. Brian Rebel (former group convener), for their continuous support and constructive feedback during the weekly meetings, which subsequently enhanced the quality of my research work. Although Prof. Aurisano was not formally my supervisor, his support, guidance and mentorship were no less significant and played a crucial role in shaping my ideas and understanding throughout the analysis. I am also grateful to Dr Alex Himmel for his willingness to help me understand several aspects of this work.

I am grateful to the India-Fermilab Neutrino Collaboration for giving me the opportunity to spend my time at Fermilab and work with the experts that gave me an exposure to the scientific community. This has helped me gain the experience of working in large scale neutrino experiments.

I sincerely thank my doctoral committee members, Dr Udit Raha, Dr Subhaditya Bhattacharya, and Dr Sovan Chakraborty, for their valuable feedback and encouragement during the annual review meetings.

I am thankful to Dr V. Hewes and Dr Alexander Booth for their continued support during my work on reconstruction and detector systematics. I want to give special mention to V, whose consistent assistance with debugging and guidance within the NOvA analysis framework, particularly ART and PISCES, made my coding journey considerably smoother.

It has been a pleasure sharing the laboratory environment with my colleagues, Dr Devender, Dr Shubhangi, Dr Jyotirmoi, Dr Dibyajoti, Shailesh, Arkodip, Rajesh, Anirban, and Dr Abinash. I cherish the countless memories we shared, from celebrating successes to overcoming challenges together. I also extend my gratitude to my friends Rakshanda, Dr Monu, and Amit for their constant support during my time at IIT Guwahati.

During my stay at Fermilab, I was fortunate to be surrounded by friends and colleagues who ensured that I never felt alone. My stay at Fermilab would have been impossible without the support of my friends, Ishwar, Itzelli, Ruchi, Felipe, Amay, Gabrieli, Luiz, Dhaval, Dominik, Francesco, Enrico, Fernanda, Sayeed, Prameet, Bhumika, Lipsa, Amit, Barnali, Vaniya, Renzo, Shiva, Everardo, Prachi, Abhishek, Sridhar, and Antonio, who made Fermilab my second home. I am also grateful to my colleagues, Stella, Maria, Teresa, Josh, and Barbara, for their valuable discussions and support.

No acknowledgement would be complete without expressing my deepest gratitude to my parents. Without their constant encouragement, sacrifices, and unwavering belief in me, completing this work would not have been possible. I am equally grateful to my brother, Satyam, who played a significant role in helping me complete my thesis. It was your support that strengthened my focus on work at Fermilab while you were at home taking care of our parents. This thesis is as much theirs as it is mine, and I dedicate it to them with all my heart.

Finally, I would like to thank my partner, Karishma, for her unwavering support and encouragement throughout this journey. It was her constant belief and unconditional support that kept me motivated even during my challenging times, which helped me focus on my work even when I was away from home. This work is as yours as mine.

Shivam

List of Publications

Primary Author

- Paper draft for “First Sterile Neutrino Search at NOvA Experiment Using both Neutrino and Anti-Neutrino Data” is in progress.

- **Shivam**, Bhuyan B., and Norrick A., Constraining Systematics for Future Sterile Neutrino Analysis at NOvA Experiment. Springer Proc. in Phys. **322**, 411-415 (2025). Proceedings of the 17th International Conference on Interconnections Between Particle Physics and Cosmology held at IIT Hyderbad India. PPC 2024.

- **Shivam** and Bhuyan B., Search for Sterile Neutrinos at NOvA, Springer Proc. Phys. **304**, 133-137 (2024). Proceedings for the XXV DAE BRNS High Energy Conference held at IISER Mohali.

- **Shivam** and Bhuyan B., NOvA Detector Validation Studies, Springer Proc. Phys. **304**, 710-712 (2024). Proceedings for the XXV DAE BRNS High Energy Conference held at IISER Mohali.

Following is the list of technical notes submitted to the collaboration.

- Sterile2025 Sidebands and Validation Technote, **Shivam**, Stella Haejun Oh, v Hewes, Adam Lister and Adam Aurisano, NOvA Internal Document. NOVA-doc- 66966.

- Sterile2025 Fitting Technote, **Shivam**, Jessica Burns, Adam Lister, and Stella Haejun Oh, NOvA Internal Document. NOVA-doc- 66963.

- Neutral Current (NC) Selection Technote for Joint FHC (ν)-RHC ($\bar{\nu}$) Analysis, **Shivam**, B. Bhuyan, and A. Norrick, NOvA Internal Document. NOVA-doc- 64862.

- Neutral Current (NC) Energy Estimator for the Joint FHC (ν)-RHC ($\bar{\nu}$) Analysis, **Shivam**, A. Lister, B. Bhuyan, and A. Norrick, NOvA Internal Document. NOVA-doc- 64475.

- MEC Systematics for the Joint FHC (ν)-RHC ($\bar{\nu}$) Analysis, **Shivam**, B. Bhuyan, and A. Norrick, NOvA Internal Document. NOVA-doc- 64481.

- Constraining the cross-section systematics for Sterile Analysis: Splitting of ND NC Sample, **Shivam**, B. Bhuyan, and A. Norrick, NOvA Internal Document. NOVA-doc- 64515.

- Detector Aging and Validation, **Shivam**, and v. Hewes, NOvA Internal Document. NOVA-doc- 53480.

Secondary Author

- Abubakar, S., Acero, M. A., Acharya, B., Adamson, P., Anfimov, N., Antoshkin, A., Arrieta-Diaz, E., Asquith, L., Aurisano, A., Azevedo, D., Back, A., Balashov, N., Baldi, P., Bambah, B. A., Bannister, E. F., Barros, A., Bat, A., Bays, K., Bernstein, R., Bezerra, T. J. C., Bhatnagar, V., Bhuyan, B., Bian, J., Booth, A. C., Bowles, R., Brahma, B., Bromberg, C., Buchanan, N., Butkevich, A., Calvez, S., Carceller, J. M., Carroll, T. J., Catano-Mur, E., Cesar, J. P., Chirco, R., Choudhary, B. C., Christensen, A., Cicala, M. F., Coan, T. E., Contreras, T., Cooleybeck, A., Coveyou, D., Cremonesi, L., Davies, G. S., Derwent, P. F., Ding, P., Djurcic, Z., Dobbs, K., Dolce, M., Dueñas Tonguino, D., Dukes, E. C., Dye, A., Ehrlich, R., Ewart, E., Filip, P., Frank, M. J., Gallagher, H. R., Giri, A., Gomes, R. A., Goodman, M. C., Group, R., Habig, A., Hakl, F., Hartnell, J., Hatcher, R., Hays, J. M., He, M., Heller, K., Hewes, V., Himmel, A., Horoho, T., Ivanova, A., Jargowsky, B., Kakorin, I., Kalitkina, A., Kaplan, D. M., Khanam, A., Kirezli, B., Kleykamp, J., Klimov, O., Koerner, L. W., Kolupaeva, L., Kralik, R., Kumar, A., Kuruppu, C. D., Kus, V., Lackey, T., Lang, K., Lasorak, P., Lesmeister, J., Lister, A., Liu, J., Lock, J. A., MacMahon, M., Magill, S., Mann, W. A., Manoharan, M. T., Manrique Plata, M., Marshak, M. L., Martinez-Casales, M., Matveev, V., Mehta, B., Messier, M. D., Meyer, H., Miao, T., Miller, W. H., Mishra, S. R., Mohanta, R., Moren, A., Morozova, A., Mu, W., Mualem, L., Muether, M., Mulder, K., Myers, D., Naples, D., Nelleri, S., Nelson, J. K., Nichol, R., Niner, E., Norman, A., Norrick, A., Oh, H., Olshevskiy, A., Olson, T., Ozkaynak, M., Pal, A., Paley, J., Panda, L., Patterson, R. B., Pawloski, G., Petti, R., Plunkett, R. K., Porter, J. C. C., Prais, L. R., Rafique, A., Raj, V., Rajaoalisoa, M., Ramson, B., Rebel, B., Robles, E., Roy, P., Samoylov, O., Sanchez, M. C., Sánchez Falero, S., Shanahan, P., Sharma, P., Sheshukov, A., **Shivam**, Shmakov, A., Shorrock, W., Shukla, S., Singh, I., Singh, P., Singh, V., Singh Chhibra, S., Singha, D. K., Smith, A., Smolik, J., Snopok, P., Solomey, N., Sousa, A., Soustruznik, K., Strait, M., Suter, L., Sutton, A., Swain, S., Sweeney, C., Sztuc, A., Talukdar, N., Tas, P., Thakore, T., Thomas, J., Tiras, E., Titus, M., Torun, Y., Tran, D., Trokan-Tenorio, J., Urheim, J., Vahle, P., Vallari, Z., Vockerodt, K. J., Waldron, A. V., Wallbank, M., Warburton, T. K., Weber, C., Wetstein, M., Whittington, D., Wickremasinghe, D. A., Wolcott, J., Wu, S., Wu, W., Wu, W., Xiao, Y., Yaeggy, B., Yahaya, A., Yankelevich, A., Yonehara, K., Zadorozhnyy, S., Zalesak, J., Zwaska, R., Abe, K., Abe, S., Adhkary, H., Akutsu, R., Alarakia-Charles, H., Alj Hakim, Y. I., Alonso Monsalve, S., Anthony, L., Aoki, S., Apte, K. A., Arai, T., Arihara, T., Arimoto, S., Ashida, Y., Atkin, E. T., Babu, N., Baranov, V., Barker, G. J., Barr, G., Barrow, D., Bates, P., Bathe-Peters, L., Batkiewicz-Kwasniak, M., Baudis, N., Berardi, V., Berns, L., Bhattacharjee, S., Blanchet, A., Blondel, A., Boistier, P. M. M., Bolognesi, S., Bordoni, S., Boyd, S. B., Bronner, C., Bubak, A., Buizza Avanzini, M., Caballero, J. A., Cadoux, F., Calabria, N. F., Cao, S., Cap, S., Carabadjac, D., Cartwright, S. L., Casado, M. P., Catanesi, M. G., Chakrani, J., Chalumeau, A., Cherdack, D., Chvirova, A., Coleman, J., Collazuol, G., Cormier, F., Craplet, A. A. L., Cudd, A., D'ago, D., Dalmazzone, C., Daret, T., Dasgupta, P., Davis, C., Davydov, Yu. I., de Perio, P., De Rosa, G., Dealtry, T., Densham, C., Dergacheva, A., Dharmapal Banerjee, R., Di Lodovico, F., Diaz Lopez, G., Dolan, S., Douqa, D., Doyle, T. A., Drapier, O., Duffy, K. E., Dumarchez, J., Dunne, P., Dygnarowicz, K., Eguchi, A., Elias, J., Emery-Schrenk, S., Erofeev, G., Ershova, A., Eurin, G., Fedorova, D., Fedotov, S., Feltre, M., Feng, L., Ferlewicz, D., Finch, A. J., Fitton, M. D., Forza, C., Friend, M., Fujii, Y., Fukuda, Y., Furui, Y., García-Marcos, J., Germer, A. C., Giannessi, L., The NOvA Collaboration and The T2K Collaboration, *Joint neutrino oscillation analysis from the T2K and NOvA experiments* Nature **646**, 818–824 (2025).

- S. Abubakar, M. A. Acero, B. Acharya, P. Adamson, N. Anfimov, A. Antoshkin, E. Arrieta-Diaz, L. Asquith, A. Aurisano, D. Azevedo, A. Back, N. Balashov, P. Baldi, B. A. Bambah, E. F. Bannister, A. Barros, A. Bat, R. Bernstein, T. J. C. Bezerra, V. Bhatnagar, B. Bhuyan, J. Bian, A. C. Booth, R. Bowles, B. Brahma, C. Bromberg, N. Buchanan, A. Butkevich, S. Calvez, T. J. Carroll, E. Catano-Mur, J. P. Cesar, **S. Chaudhary**, R. Chirco, S. Choate, B. C. Choudhary, O. T. K. Chow, A. Christensen, M. F. Cicala, T. E. Coan, T. Contreras, A. Cooleybeck, D. Coveyou, L. Cremonesi, G. S. Davies, P. F. Derwent, P. Ding, Z. Djurcic, K. Dobbs, M. Dolce, D. Dueñas Tonguino, E.

C. Dukes, A. Dye, R. Ehrlich, E. Ewart, G. J. Feldman, P. Filip, M. J. Frank, H. R. Gallagher, F. Gao, A. Giri, R. A. Gomes, M. C. Goodman, R. Group, A. Habig, F. Hakl, J. Hartnell, R. Hatcher, J. M. Hays, M. He, K. Heller, V. Hewes, A. Himmel, T. Horoho, X. Huang, A. Ivanova, B. Jargowsky, I. Kakorin, A. Kalitkina, D. M. Kaplan, A. Khanam, B. Kirezli, J. Kleykamp, O. Klimov, L. W. Koerner, L. Kolupaeva, R. Kralik, A. Kumar, C. D. Kuruppu, V. Kus, T. Lackey, K. Lang, J. Lesmeister, A. Lister, J. Liu, J. A. Lock, M. MacMahon, S. Magill, W. A. Mann, M. T. Manoharan, M. Manrique Plata, M. L. Marshak, M. Martinez-Casales, V. Matveev, A. Medhi, B. Mehta, M. D. Messier, H. Meyer, T. Miao, V. Mikola, W. H. Miller, S. R. Mishra, A. Mislivec, R. Mohanta, A. Moren, A. Morozova, W. Mu, L. Mualem, M. Muether, K. Mulder, C. Murthy, D. Myers, J. Nachtman, D. Naples, S. Nelleri, J. K. Nelson, O. Neogi, R. Nichol, E. Niner, A. Norman, A. Norrick, H. Oh, A. Olshevskiy, T. Olson, M. Ozkaynak, A. Pal, J. Paley, L. Panda, R. B. Patterson, G. Pawloski, R. Petti, R. K. Plunkett, L. R. Prais, A. Rafique, V. Raj, M. Rajaoalisoa, B. Ramson, B. Rebel, C. Reynolds, E. Robles, P. Roy, O. Samoylov, M. C. Sanchez, S. Sánchez Falero, P. Shanahan, P. Sharma, A. Sheshukov, A. Shmakov, W. Shorrock, S. Shukla, I. Singh, P. Singh, V. Singh, S. Singh Chhibra, D. K. Singha, E. Smith, J. Smolik, P. Snopok, N. Solomey, A. Sousa, K. Soustruznik, M. Strait, C. Sullivan, L. Suter, A. Sutton, K. Sutton, S. K. Swain, A. Sztuc, N. Talukdar, P. Tas, T. Thakore, J. Thomas, E. Tiras, M. Titus, Y. Torun, D. Tran, J. Trokan-Tenorio, J. Urheim, B. Utt, P. Vahle, Z. Vallari, K. J. Vockerodt, A. V. Waldron, M. Wallbank, T. K. Warburton, C. Weber, M. Wetstein, D. Whittington, D. A. Wickremasinghe, J. Wolcott, S. Wu, W. Wu, W. Wu, Y. Xiao, B. Yaeggy, A. Yahaya, A. Yankelevich, K. Yonehara, S. Zadorozhnyy, J. Zalesak, R. Zwaska (NOvA Collaboration), *Precision Measurement of Neutrino Oscillation Parameters with 10 Years of Data from the NOvA Experiment*, Phys. Rev. Lett. **136**, 011802 (2026) .

- S. Abubakar, M. A. Acero, B. Acharya, P. Adamson, N. Anfimov, A. Antoshkin, E. Arrieta-Diaz, L. Asquith, A. Aurisano, A. Back, N. Balashov, P. Baldi, B. A. Bambah, E. F. Bannister, A. Barros, J. Barrow, A. Bat, T. J. C. Bezerra, V. Bhatnagar, B. Bhuyan, J. Bian, A. C. Booth, R. Bowles, B. Brahma, C. Bromberg, N. Buchanan, A. Butkevich, T. J. Carroll, E. Catano-Mur, J. P. Cesar, **S. Chaudhary**, R. Chirco, S. Choate, B. C. Choudhary, O. T. K. Chow, A. Christensen, M. F. Cicala, T. E. Coan, T. Contreras,

A. Cooleybeck, D. Coveyou, L. Cremonesi, G. S. Davies, P. F. Derwent, Z. Djurcic, K. Dobbs, D. Dueñas Tonguino, E. C. Dukes, A. Dye, R. Ehrlich, E. Ewart, P. Filip, M. J. Frank, H. R. Gallagher, A. Giri, R. A. Gomes, M. C. Goodman, R. Group, E. Guan, A. Habig, F. Hakl, J. Hartnell, R. Hatcher, J. M. Hays, M. He, K. Heller, V. Hewes, A. Himmel, T. Horoho, X. Huang, A. Ivanova, I. Kakorin, A. Kalitkina, D. M. Kaplan, A. Khanam, B. Kirezli, J. Kleykamp, O. Klimov, L. W. Koerner, L. Kolupaeva, R. Kralik, A. Kumar, C. D. Kuruppu, V. Kus, T. Lackey, K. Lang, J. Lesmeister, A. Lister, J. Lock, S. Magill, W. A. Mann, M. T. Manoharan, M. Manrique Plata, M. L. Marshak, M. Martinez-Casales, V. Matveev, A. Medhi, B. Mehta, M. D. Messier, H. Meyer, T. Miao, V. Mikola, S. R. Mishra, R. Mohanta, A. Moren, A. Morozova, W. Mu, L. Mualem, M. Muether, C. Murthy, D. Myers, J. Nachtman, D. Naples, J. K. Nelson, O. Neogi, R. Nichol, E. Niner, A. Norman, A. Norrick, H. Oh, A. Olshevskiy, T. Olson, A. Pal, J. Paley, L. Panda, R. B. Patterson, G. Pawloski, R. Petti, L. R. Prais, A. Rafique, V. Raj, M. Rajaoalisoa, B. Ramson, B. Rebel, C. Reynolds, E. Robles, P. Roy, O. Samoylov, M. C. Sanchez, S. Sánchez Falero, P. Shanahan, P. Sharma, A. Sheshukov, A. Shmakov, W. Shorrock, S. Shukla, I. Singh, P. Singh, V. Singh, S. Singh Chhibra, A. Smith, J. Smolik, P. Snopok, N. Solomey, A. Sousa, K. Soustruznik, M. Strait, C. Sullivan, L. Suter, A. Sutton, K. Sutton, S. K. Swain, A. Sztuc, N. Talukdar, P. Tas, T. Thakore, J. Thomas, E. Tiras, M. Titus, Y. Torun, D. Tran, J. Trokan-Tenorio, J. Urheim, B. Utt, P. Vahle, Z. Vallari, K. J. Vockerodt, A. V. Waldron, M. Wallbank, B. Wang, C. Weber, M. Wetstein, D. Whittington, D. A. Wickremasinghe, J. Wolcott, S. Wu, W. Wu, Y. Xiao, B. Yaeggy, A. Yahaya, A. Yankelevich, K. Yonehara, S. Zadorozhnyy, J. Zalesak, R. Zwaska (NOvA Collaboration), *Explanation of the seasonal variation of cosmic multiple muon events observed with the NOvA Near Detector*, Phys. Rev. D **113**, 012001 (2026).

- M. A. Acero, B. Acharya, P. Adamson, L. Aliaga, N. Anfimov, A. Antoshkin, E. Arrieta-Diaz, L. Asquith, A. Aurisano, A. Back, N. Balashov, P. Baldi, B. A. Bambah, E. Bannister, A. Barros, S. Bashar, A. Bat, K. Bays, R. Bernstein, T. J. C. Bezerra, V. Bhatnagar, D. Bhattarai, B. Bhuyan, J. Bian, A. C. Booth, R. Bowles, B. Brahma, C. Bromberg, N. Buchanan, A. Butkevich, S. Calvez, T. J. Carroll, E. Catano-Mur, J. P. Cesar, A. Chatla, R. Chirco, B. C. Choudhary, A. Christensen, M. F. Cicala, T. E. Coan, A. Cooleybeck, C.

Cortes-Parra, D. Coveyou, L. Cremonesi, G. S. Davies, P. F. Derwent, P. Ding, Z. Djurcic, K. Dobbs, M. Dolce, D. Doyle, D. Dueñas Tonguino, E. C. Dukes, A. Dye, R. Ehrlich, E. Ewart, P. Filip, M. J. Frank, H. R. Gallagher, F. Gao, A. Giri, R. A. Gomes, M. C. Goodman, M. Groh, R. Group, A. Habig, F. Hakl, J. Hartnell, R. Hatcher, M. He, K. Heller, V. Hewes, A. Himmel, T. Horoho, Y. Ivaneev, A. Ivanova, B. Jargowsky, J. Jarosz, C. Johnson, M. Judah, I. Kakorin, D. M. Kaplan, A. Kalitkina, B. Kirezli-Ozdemir, J. Kleykamp, O. Klimov, L. W. Koerner, L. Kolupaeva, R. Kralik, A. Kumar, C. D. Kuruppu, V. Kus, T. Lackey, K. Lang, J. Lesmeister, A. Lister, J. Liu, J. A. Lock, M. Lokajicek, M. MacMahon, S. Magill, W. A. Mann, M. T. Manoharan, M. Manrique Plata, M. L. Marshak, M. Martinez-Casales, V. Matveev, B. Mehta, M. D. Messier, H. Meyer, T. Miao, W. H. Miller, S. Mishra, S. R. Mishra, R. Mohanta, A. Moren, A. Morozova, W. Mu, L. Mualem, M. Muether, K. Mulder, D. Myers, D. Naples, A. Nath, S. Nelleri, J. K. Nelson, R. Nichol, E. Niner, A. Norman, A. Norrick, T. Nosek, H. Oh, A. Olshevskiy, T. Olson, M. Ozkaynak, A. Pal, J. Paley, L. Panda, R. B. Patterson, G. Pawloski, R. Petti, R. K. Plunkett, L. R. Prais, M. Rabelhofer, A. Rafique, V. Raj, M. Rajaoalisoa, B. Ramson, B. Rebel, P. Roy, O. Samoylov, M. C. Sanchez, S. Sánchez Falero, P. Shanahan, P. Sharma, A. Sheshukov, **Shivam**, A. Shmakov, W. Shorrock, S. Shukla, D. K. Singha, I. Singh, P. Singh, V. Singh, E. Smith, J. Smolik, P. Snopok, N. Solomey, A. Sousa, K. Soustruznik, M. Strait, L. Suter, A. Sutton, K. Sutton, S. Swain, C. Sweeney, A. Sztuc, N. Talukdar, B. Tapia Oregui, P. Tas, T. Thakore, J. Thomas, E. Tiras, M. Titus, Y. Torun, D. Tran, J. Trokan-Tenorio, J. Urheim, P. Vahle, Z. Vallari, J. D. Villamil, K. J. Vockerodt, M. Wallbank, C. Weber, M. Wetstein, D. Whittington, D. A. Wickremasinghe, T. Wieber, J. Wolcott, M. Wrobel, S. Wu, W. Wu, W. Wu, Y. Xiao, B. Yaeggy, A. Yahaya, A. Yankelevich, K. Yonehara, Y. Yu, S. Zadorozhnyy, J. Zalesak, R. Zwaska (NOvA Collaboration), *Measurement of $d^2\sigma/d|\vec{q}|\,dE_{avail}$ in charged-current ν_μ-nucleus interactions at $\langle E_\nu \rangle = 1.86$ GeV using the NOvA Near Detector*, Phys. Rev. D **111**, 052009 (2025).

- M. A. Acero, B. Acharya, P. Adamson, N. Anfimov, A. Antoshkin, E. Arrieta-Diaz, L. Asquith, A. Aurisano, A. Back, N. Balashov, P. Baldi, B. A. Bambah, E. F. Bannister, A. Barros, A. Bat, K. Bays, R. Bernstein, T. J. C. Bezerra, V. Bhatnagar, D. Bhattarai, B. Bhuyan, J. Bian, A. C. Booth, R. Bowles, B. Brahma, C. Bromberg, N. Buchanan, A. Butkevich, S. Calvez, T. J. Carroll, E. Catano-Mur, J. P. Cesar, A. Chatla, R. Chirco, B. C. Choudhary, A. Christensen, M. F. Cicala, T. E. Coan, A. Cooleybeck, C. Cortes-Parra, D. Coveyou, L. Cremonesi, G. S. Davies, P. F. Derwent, P. Ding, Z. Djurcic, K. Dobbs, M. Dolce, D. Doyle, D. Dueñas Tonguino, E. C. Dukes, A. Dye, R. Ehrlich, E. Ewart, P. Filip, M. J. Frank, H. R. Gallagher, F. Gao, A. Giri, R. A. Gomes, M. C. Goodman, M. Groh, R. Group, A. Habig, F. Hakl, J. Hartnell, R. Hatcher, H. Hausner, M. He, K. Heller, V. Hewes, A. Himmel, T. Horoho, A. Ivanova, B. Jargowsky, J. Jarosz, M. Judah, I. Kakorin, A. Kalitkina, D. M. Kaplan, B. Kirezli-Ozdemir, J. Kleykamp, O. Klimov, L. W. Koerner, L. Kolupaeva, R. Kralik, A. Kumar, V. Kus, T. Lackey, K. Lang, J. Lesmeister, A. Lister, J. Liu, J. A. Lock, M. Lokajicek, M. MacMahon, S. Magill, W. A. Mann, M. T. Manoharan, M. Manrique Plata, M. L. Marshak, M. Martinez-Casales, V. Matveev, B. Mehta, M. D. Messier, H. Meyer, T. Miao, V. Mikola, W. H. Miller, S. Mishra, S. R. Mishra, A. Mislivec, R. Mohanta, A. Moren, A. Morozova, W. Mu, L. Mualem, M. Muether, D. Myers, D. Naples, A. Nath, S. Nelleri, J. K. Nelson, R. Nichol, E. Niner, A. Norman, A. Norrick, H. Oh, A. Olshevskiy, T. Olson, M. Ozkaynak, A. Pal, J. Paley, L. Panda, R. B. Patterson, G. Pawloski, R. Petti, R. K. Plunkett, L. R. Prais, M. Rabelhofer, A. Rafique, V. Raj, M. Rajaoalisoa, B. Ramson, B. Rebel, P. Roy, O. Samoylov, M. C. Sanchez, S. Sánchez Falero, P. Shanahan, P. Sharma, A. Sheshukov, A. Shmakov, **Shivam**, W. Shorrock, S. Shukla, D. K. Singha, I. Singh, P. Singh, V. Singh, E. Smith, J. Smolik, P. Snopok, N. Solomey, A. Sousa, K. Soustruznik, M. Strait, L. Suter, A. Sutton, K. Sutton, S. Swain, C. Sweeney, A. Sztuc, B. Tapia Oregui, N. Talukdar, P. Tas, T. Thakore, J. Thomas, E. Tiras, M. Titus, Y. Torun, D. Tran, J. Tripathi, J. Trokan-Tenorio, J. Urheim, P. Vahle, Z. Vallari, J. D. Villamil, K. J. Vockerodt, M. Wallbank, C. Weber, M. Wetstein, D. Whittington, D. A. Wickremasinghe, T. Wieber, J. Wolcott, M. Wrobel, S. Wu, W. Wu, W. Wu, Y. Xiao, B. Yaeggy, A. Yahaya, A. Yankelevich, K. Yonehara, S. Zadorozhnyy, J. Zalesak, R. Zwaska (NOvA Collaboration), *Dual-Baseline Search for Active-to-Sterile Neutrino Oscillations in NOvA*, Phys. Rev. Lett. **134**, 081804 (2025).

- M. A. Acero, B. Acharya, P. Adamson, L. Aliaga, N. Anfimov, A. Antoshkin, E. Arrieta-Diaz, L. Asquith, A. Aurisano, A. Back, N. Balashov, P. Baldi, B. A. Bambah, A. Bat, K. Bays, R. Bernstein, T. J. C. Bezerra, V. Bhatnagar, D. Bhattarai, B. Bhuyan, J. Bian, A. C. Booth, R. Bowles, B. Brahma, C.

Bromberg, N. Buchanan, A. Butkevich, S. Calvez, T. J. Carroll, E. Catano-Mur, J. P. Cesar, A. Chatla, **S. Chaudhary**, R. Chirco, B. C. Choudhary, A. Christensen, M. F. Cicala, T. E. Coan, A. Cooleybeck, C. Cortes-Parra, D. Coveyou, L. Cremonesi, G. S. Davies, P. F. Derwent, Z. Djurcic, M. Dolce, D. Doyle, D. Dueñas Tonguino, E. C. Dukes, A. Dye, R. Ehrlich, E. Ewart, P. Filip, J. Franc, M. J. Frank, H. R. Gallagher, F. Gao, A. Giri, R. A. Gomes, M. C. Goodman, M. Groh, R. Group, A. Habig, F. Hakl, J. Hartnell, R. Hatcher, M. He, K. Heller, V. Hewes, A. Himmel, Y. Ivaneev, A. Ivanova, B. Jargowsky, J. Jarosz, C. Johnson, M. Judah, I. Kakorin, D. M. Kaplan, A. Kalitkina, J. Kleykamp, O. Klimov, L. W. Koerner, L. Kolupaeva, R. Kralik, C. D. Kuruppu, V. Kus, T. Lackey, K. Lang, J. Lesmeister, A. Lister, J. Liu, J. A. Lock, M. Lokajicek, M. MacMahon, S. Magill, W. A. Mann, M. T. Manoharan, M. Manrique Plata, M. L. Marshak, M. Martinez-Casales, V. Matveev, B. Mehta, M. D. Messier, H. Meyer, T. Miao, V. Mikola, W. H. Miller, S. Mishra, S. R. Mishra, A. Mislivec, R. Mohanta, A. Moren, A. Morozova, W. Mu, L. Mualem, M. Muether, K. Mulder, D. Myers, D. Naples, A. Nath, S. Nelleri, J. K. Nelson, R. Nichol, E. Niner, A. Norman, A. Norrick, T. Nosek, H. Oh, A. Olshevskiy, T. Olson, M. Ozkaynak, A. Pal, J. Paley, L. Panda, R. B. Patterson, G. Pawloski, O. Petrova, R. Petti, L. R. Prais, A. Rafique, V. Raj, M. Rajaoalisoa, B. Ramson, M. Ravelhofer, B. Rebel, P. Roy, O. Samoylov, M. C. Sanchez, S. Sánchez Falero, P. Shanahan, P. Sharma, A. Shmakov, A. Sheshukov, S. Shukla, D. K. Singha, W. Shorrock, I. Singh, P. Singh, V. Singh, E. Smith, J. Smolik, P. Snopok, N. Solomey, A. Sousa, K. Soustruznik, M. Strait, L. Suter, A. Sutton, K. Sutton, S. Swain, C. Sweeney, A. Sztuc, B. Tapia Oregui, P. Tas, T. Thakore, J. Thomas, E. Tiras, Y. Torun, J. Tripathi, J. Trokan-Tenorio, J. Urheim, P. Vahle, Z. Vallari, J. Vasel, J. D. Villamil, K. J. Vockerodt, T. Vrba, M. Wallbank, M. Wetstein, D. Whittington, D. A. Wickremasinghe, T. Wieber, J. Wolcott, M. Wrobel, S. Wu, W. Wu, Y. Xiao, B. Yaeggy, A. Yahaya, A. Yankelevich, K. Yonehara, Y. Yu, S. Zadorozhnyy, J. Zalesak, R. Zwaska (NOvA Collaboration), *Search for CP-Violating Neutrino Nonstandard Interactions with the NOvA Experiment*, Phys. Rev. Lett. **133**, 201802 (2024).

- M. A. Acero, B. Acharya, P. Adamson, N. Anfimov, A. Antoshkin, E. Arrieta-Diaz, L. Asquith, A. Aurisano, A. Back, N. Balashov, P. Baldi, B. A. Bambah, A. Bat, K. Bays, R. Bernstein, T. J. C. Bezerra, V. Bhatnagar, D. Bhattarai,

B. Bhuyan, J. Bian, A. C. Booth, R. Bowles, B. Brahma, C. Bromberg, N. Buchanan, A. Butkevich, S. Calvez, T. J. Carroll, E. Catano-Mur, J. P. Cesar, A. Chatla, **S. Chaudhary**, R. Chirco, B. C. Choudhary, A. Christensen, T. E. Coan, A. Cooleybeck, L. Cremonesi, G. S. Davies, P. F. Derwent, P. Ding, Z. Djurcic, M. Dolce, D. Doyle, D. Dueñas Tonguino, E. C. Dukes, A. Dye, R. Ehrlich, M. Elkins, E. Ewart, P. Filip, J. Franc, M. J. Frank, H. R. Gallagher, F. Gao, A. Giri, R. A. Gomes, M. C. Goodman, M. Groh, R. Group, A. Habig, F. Hakl, J. Hartnell, R. Hatcher, M. He, K. Heller, V. Hewes, A. Himmel, B. Jargowsky, J. Jarosz, F. Jediny, C. Johnson, M. Judah, I. Kakorin, D. M. Kaplan, A. Kalitkina, J. Kleykamp, O. Klimov, L. W. Koerner, L. Kolupaeva, R. Kralik, A. Kumar, C. D. Kuruppu, V. Kus, T. Lackey, K. Lang, P. Lasorak, J. Lesmeister, A. Lister, J. Liu, J. A. Lock, M. Lokajicek, M. MacMahon, S. Magill, W. A. Mann, M. T. Manoharan, M. Manrique Plata, M. L. Marshak, M. Martinez-Casales, V. Matveev, B. Mehta, M. D. Messier, H. Meyer, T. Miao, V. Mikola, W. H. Miller, S. Mishra, S. R. Mishra, R. Mohanta, A. Moren, A. Morozova, W. Mu, L. Mualem, M. Muether, K. Mulder, D. Myers, D. Naples, A. Nath, S. Nelleri, J. K. Nelson, R. Nichol, E. Niner, A. Norman, A. Norrick, T. Nosek, H. Oh, A. Olshevskiy, T. Olson, A. Pal, J. Paley, L. Panda, R. B. Patterson, G. Pawloski, O. Petrova, R. Petti, R. K. Plunkett, L. R. Prais, A. Rafique, V. Raj, M. Rajaoalisoa, B. Ramson, B. Rebel, P. Roy, O. Samoylov, M. C. Sanchez, S. Sánchez Falero, P. Shanahan, P. Sharma, A. Sheshukov, S. Shukla, D. K. Singha, W. Shorrock, I. Singh, P. Singh, V. Singh, E. Smith, J. Smolik, P. Snopok, N. Solomey, A. Sousa, K. Soustruznik, M. Strait, L. Suter, A. Sutton, K. Sutton, S. Swain, C. Sweeney, A. Sztuc, B. Tapia Oregui, P. Tas, T. Thakore, J. Thomas, E. Tiras, Y. Torun, J. Trokan-Tenorio, J. Urheim, P. Vahle, Z. Vallari, K. J. Vockerodt, T. Vrba, M. Wallbank, T. K. Warburton, M. Wetstein, D. Whittington, D. A. Wickremasinghe, T. Wieber, J. Wolcott, M. Wrobel, S. Wu, W. Wu, Y. Xiao, B. Yaeggy, A. Yankelevich, K. Yonehara, Y. Yu, S. Zadorozhnyy, J. Zalesak, R. Zwaska (NOvA Collaboration), *Expanding neutrino oscillation parameter measurements in NOvA using a Bayesian approach*, Phys. Rev. D **110**, 011001 (2024).

- M. A. Acero, B. Acharya, P. Adamson, L. Aliaga, N. Anfimov, A. Antoshkin, E. Arrieta-Diaz, L. Asquith, A. Aurisano, A. Back, C. Backhouse, M. Baird, N. Balashov, P. Baldi, B. A. Bambah, S. Bashar, A. Bat, K. Bays, R. Bernstein,

V. Bhatnagar, D. Bhattarai, B. Bhuyan, J. Bian, A. C. Booth, R. Bowles, B. Brahma, C. Bromberg, N. Buchanan, A. Butkevich, S. Calvez, T. J. Carroll, E. Catano-Mur, A. Chatla, R. Chirco, B. C. Choudhary, **S. Chaudhary**, A. Christensen, T. E. Coan, M. Colo, L. Cremonesi, G. S. Davies, P. F. Derwent, P. Ding, Z. Djurcic, M. Dolce, D. Doyle, D. Dueñas Tonguino, E. C. Dukes, A. Dye, R. Ehrlich, M. Elkins, E. Ewart, G. J. Feldman, P. Filip, J. Franc, M. J. Frank, H. R. Gallagher, R. Gandrajula, F. Gao, A. Giri, R. A. Gomes, M. C. Goodman, V. Grichine, M. Groh, R. Group, B. Guo, A. Habig, F. Hakl, A. Hall, J. Hartnell, R. Hatcher, H. Hausner, M. He, K. Heller, V. Hewes, A. Himmel, B. Jargowsky, J. Jarosz, F. Jediny, C. Johnson, M. Judah, I. Kakorin, D. M. Kaplan, A. Kalitkina, J. Kleykamp, O. Klimov, L. W. Koerner, L. Kolupaeva, S. Kotelnikov, R. Kralik, Ch. Kullenberg, M. Kubu, A. Kumar, C. D. Kuruppu, V. Kus, T. Lackey, K. Lang, P. Lasorak, J. Lesmeister, S. Lin, A. Lister, J. Liu, M. Lokajicek, J. M. C. Lopez, R. Mahji, S. Magill, M. Manrique Plata, W. A. Mann, M. T. Manoharan, M. L. Marshak, M. Martinez-Casales, V. Matveev, B. Mayes, B. Mehta, M. D. Messier, H. Meyer, T. Miao, V. Mikola, W. H. Miller, S. Mishra, S. R. Mishra, A. Mislivec, R. Mohanta, A. Moren, A. Morozova, W. Mu, L. Mualem, M. Muether, K. Mulder, D. Naples, A. Nath, N. Nayak, S. Nelleri, J. K. Nelson, R. Nichol, E. Niner, A. Norman, A. Norrick, T. Nosek, H. Oh, A. Olshevskiy, T. Olson, J. Ott, A. Pal, J. Paley, L. Panda, R. B. Patterson, G. Pawloski, D. Pershey, O. Petrova, R. Petti, D. D. Phan, R. K. Plunkett, A. Pobedimov, J. C. C. Porter, A. Rafique, L. R. Prais, V. Raj, M. Rajaoalisoa, B. Ramson, B. Rebel, P. Rojas, P. Roy, V. Ryabov, O. Samoylov, M. C. Sanchez, S. Sánchez Falero, P. Shanahan, P. Sharma, S. Shukla, A. Sheshukov, I. Singh, P. Singh, V. Singh, E. Smith, J. Smolik, P. Snopok, N. Solomey, A. Sousa, K. Soustruznik, M. Strait, L. Suter, A. Sutton, S. Swain, C. Sweeney, A. Sztuc, B. Tapia Oregui, P. Tas, B. N. Temizel, T. Thakore, R. B. Thayyullathil, J. Thomas, E. Tiras, J. Tripathi, J. Trokan-Tenorio, Y. Torun, J. Urheim, P. Vahle, Z. Vallari, J. Vasel, T. Vrba, M. Wallbank, T. K. Warburton, M. Wetstein, D. Whittington, D. A. Wickremasinghe, T. Wieber, J. Wolcott, M. Wrobel, W. Wu, Y. Xiao, B. Yaeggy, A. Yallappa Dombara, A. Yankelevich, K. Yonehara, S. Yu, Y. Yu, S. Zadorozhnyy, J. Zalesak, Y. Zhang, R. Zwaska (NOvA Collaboration), *Monte Carlo method for constructing confidence intervals with unconstrained and constrained nuisance parameters in the NOvA experiment*, JINST **20**, T02001 (2025).

Please see ORCiD or iNSPIRE-HEP for full publication list.

Conference Presentations

- **POSTER** at International Neutrino Summer School (INSS) 2025 at Fermilab, US
  "First Joint Neutrino-Antineutrino Sterile Neutrino Search at NOvA Experiment" in Aug 2025
- **POSTER** at Users Meeting at Fermilab, US
  "Improved Joint FHC + RHC Sterile Analysis with $\nu \rightarrow$e Sample at NOvA Experiment" in July 2025
- **TALK** at New Perspectives Meeting at Fermilab, US
  "First Joint FHC-RHC Sterile Neutrino Search at NOvA Experiment" in July 2025
- **TALK** at Particle Physics and Cosmology (PPC) in IIT Hyderabad, India
  "Constraining Systematics for Future Sterile Neutrino Analysis at NOvA Experiment" in Oct 2024
- **TALK** at New Perspective Meeting at Fermilab, US
  "Sterile Neutrino Search at NOvA Experiment" in July 2024
- **POSTER** at Users Meeting at Fermilab, US
  "Constraining Systematics for Sterile Neutrino Search at NOvA in July 2024
- **POSTER** at NEUTRINO 2024 Conference at Milano, Italy
  "Constraining Cross Section and Beam Systematics for Future NOvA Sterile Neutrino Search" in June 2024
- **TALK** at XXV DAE BRNS High Energy Conference held at IISER Mohali, India
  "Sterile Neutrino Search at NOvA Experiment" in Dec 2022
- **POSTER** at XXV DAE BRNS High Energy Conference held at IISER Mohali, India
  "NOvA Experiment Detector Validation and Aging" in Dec 2022
- **TALK** at Vietnam School on Neutrinos
  "Sterile Neutrinos" in Sept 2021

Abstract

Neutrinos are among the most abundant fundamental particles in the universe, and yet they are so elusive that they pass through almost everything without leaving a trace. For decades, researchers have measured neutrino oscillations in great detail, refining our understanding of the theories. Yet, once again, neutrino shows their incredibly surprising nature through some recent experimental results, suggesting that our current understanding might be incomplete. Several experiments have observed an unexpected difference in the observed neutrino behaviour from what the Standard Model predicts, showing an excess in some cases (e.g. LSND, MiniBooNE) and a deficit of neutrino events in others (e.g. SAGE, GALLEX). These anomalies challenge our conventional theories of standard three neutrino flavors and phenomenologically motivate the sterile neutrino hypothesis, which does not interact through the usual weak force. While some results appear consistent with this idea, others have found no supporting evidence (e.g. MicroBooNE), leaving the question unanswered. NOvA is one such long-baseline neutrino experiment with its Near Detector (ND) at Fermilab and a Far Detector (FD) at 810 km in Minnesota. It uses the NuMI beam as its primary source of neutrinos for oscillation studies. Its two-detector setup, extended baseline, and ability to conduct combined ν-$\bar{\nu}$ analyses position it to explore these phenomena in new ways. We use the joint ν_μ and neutral current (NC) disappearance channels to probe active-sterile mixing in the 3+1 model. This analysis utilizes a data sample of 27×10^{20} protons on target (POT) in neutrino mode and 12.5×10^{20} protons on target (POT) in antineutrino mode. We found no evidence of sterile neutrino at 90% C.L. We present the limits in $\sin^2\theta_{24}$ vs Δm^2_{41}, $\sin^2\theta_{34}$ vs Δm^2_{41}, and $\sin^2 2\theta_{\mu\tau}$ vs Δm^2_{41} parameter spaces. The limits provided by this analysis are world leading in most of the parameter spaces.

Contents

List of Figures

List of Tables

Chapter 1

Neutrinos

"I have done a terrible thing. I have postulated a particle that cannot be detected."

Wolfgang Pauli

Introduction

It has been more than six decades since the first detection of the neutrino by Fred Reines and George Cowan; this elusive particle remains mysterious, and we still know very little about neutrinos. Being one of the most abundant particles in nature, after photons, it continues to surprise us with new information every day. In this chapter, we provide the fundamental concepts required for a clear understanding of neutrino physics. Over the past few decades, continuous advancements in detector technologies and theoretical development have significantly improved neutrino physics. Starting with the historical overview of neutrinos (Sec. 1.1), different sources of neutrinos (Sec. 1.2), neutrino anomalies (Sec. 1.3 and Sec. 1.4), this chapter ends with the theoretical development of the standard neutrino oscillation paradigm (Sec. 1.5).

1.1 Neutrinos and their History

Even after more than a century since Pauli's hypothesis, neutrinos continue to yield a series of surprising results, deviating from the theoretical description. Even today, with advanced technology, neutrinos cannot be directly detected due to their weak interactions and neutral charge. Neutrino studies have repeatedly exposed the limitations of existing theoretical frameworks, beginning with the anomalies in beta decay and continuing through the neutrino oscillation phenomenon and the discovery of non-zero masses.

In the early 1920s, the only known particles in nature were limited to negatively charged electrons, positively charged protons, and neutral photons. Several nuclear and atomic models were therefore constructed using these then-known particles. An atom with atomic number Z and mass number A was assumed to consist of A protons and Z orbital electrons. While this model initially described atomic structure, it soon encountered several difficulties, particularly in explaining beta decay processes.

One major flaw lies in the assumption that electrons pre-exist inside the nucleus, even before decay occurs, and are emitted during the beta decay process. The wave function of such an electron should be confined to a nuclear volume of size $\mathcal{O}(1\text{ fm})$. According to the Heisenberg uncertainty principle, the momentum of such a confined electron is approximately of the order of 100 MeV. This expectation contradicts experimental observations, which show that beta decay electrons typically possess maximum energies of only a few MeV (one order of magnitude smaller). This discrepancy strongly suggested that electrons could not exist as nuclear constituents prior to decay.

A second, more profound inconsistency arose from the observed energy spectrum of beta decay electrons. If beta decay were a two-body process of the form

$$(A, Z) \to (A, Z + 1) + e^- \tag{1.1}$$

According to the energy and momentum conservation laws, the energy spectrum of the emitted electron should be discrete. It can be calculated by the mass difference of the initial and final state nuclei $(m(A, Z) - m(A, Z + 1))$. However, experiments consistently reported a continuous energy spectrum ending at this mass difference. Fig. 1.1 shows the example of a beta decay where the blue curve is the continuous energy spectrum as reported in several experiments, and the red line represents the discrete energy as predicted by the theoretical models.

Niels Bohr, one of the most prominent physicists of the early twentieth century, went so far as to question the most "sacred" principles of physics: the conservation of energy. In an attempt to reconcile the surprising nature of beta decay, Bohr suggested that

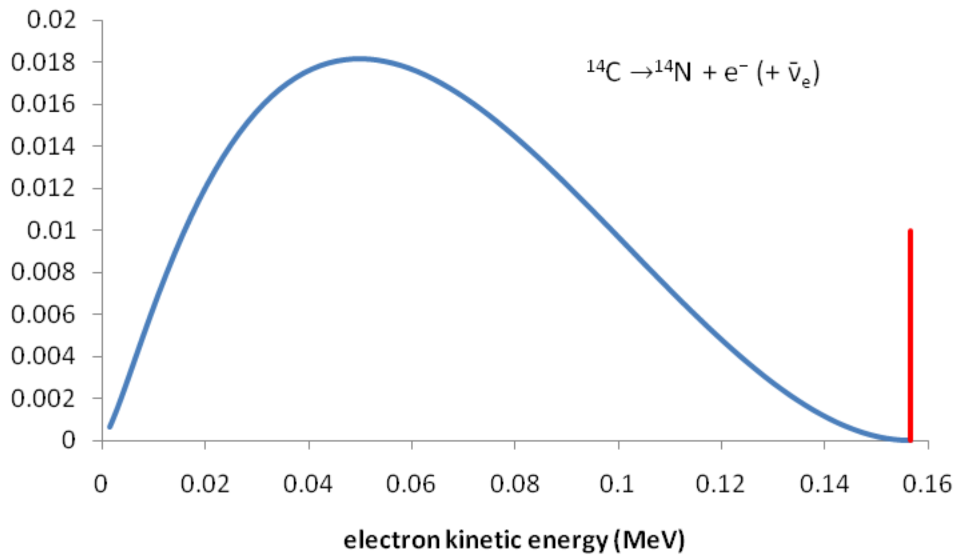

Figure 1.1: An example of the β-decay. The blue curve represents the measured energy spectrum, and the red line indicates the originally expected energy of the emitted electron, illustrating a clear difference between the observed and predicted spectrum [1].

energy conservation might not necessarily hold on an event-by-event basis but only statistically.

In 1930, Wolfgang Pauli took a bold step when he postulated the existence of an unknown, electrically neutral, and very light particle emitted alongside the electron in beta decay. Being charge-neutral, Pauli initially termed this particle the "neutron," proposing that it carried away the missing energy and momentum required for energy and momentum conservation. Following the discovery of the neutron by Chadwick in 1932 (two years later), Enrico Fermi later renamed Pauli's particle the "neutrino".

In 1933 and 1934, Fermi developed a quantitative theoretical framework for beta decay, and published his article titled *"Tentativo di una teoria dell'emissione dei raggi beta"* ("Attempt at a Theory of Beta-Ray Emission") [2]. Fermi advanced the hypothesis that electrons emitted in beta decay do not pre-exist within the nucleus but are instead created at the moment of decay together with a neutrino. This theoretical formulation, for the first time, provided a consistent explanation of both the continuous electron energy spectrum observed in beta decay experiments.

In modern notation, beta decay is represented as

$$n \to p^+ + e^- + \bar{\nu}_e, \tag{1.2}$$

where the symbols denote, respectively, the neutron (n), proton p^+, electron e^-, and electron antineutrino $(\bar{\nu}_e)$.

Despite the theoretical success of Fermi's model, the chances for experimental detection of the neutrino appeared bleak. Soon after the formulation of Fermi's theory of β decay, Bethe and Peierls reported the first neutrino–nucleus interaction cross section estimate, obtaining a value of order

$$\sigma \lesssim 10^{-44}\ \mathrm{cm}^2$$

at a few MeV neutrino energy [3]. This tiny cross-section corresponds to a penetrating power of 10^{16} km in solid matter, implying that neutrinos could travel through enormous amounts of material without interaction. Based on this result, Bethe and Peierls concluded that it was "therefore absolutely impossible to observe processes of this kind with neutrinos created in nuclear decays " [3].

Bruno Pontecorvo was the first physicist to propose an experimental approach to neutrino detection through the radiochemical method in 1946 [4]. Based on the groundwork by Pontecorvo, Frederick Reines and Clyde L. Cowan performed a series of experiments between 1953 and 1959 that became the first direct experimental evidence of neutrino existence [5]. They detected the electron antineutrinos produced in nuclear reactors, mainly those originating from beta decay of fission products at the Savannah River reactor. The detection relies on the measurement of the following process:

$$\bar{\nu}_e + p \rightarrow n + e^+, \tag{1.3}$$

1.2 Sources of Neutrinos

Neutrinos are produced in a wide range of natural and artificial processes, and cover energies from sub-eV to beyond the PeV scale as shown in Fig. 1.2. Neutrinos are one of the most abundant particles in nature after photons. Because of their weakly interacting nature, neutrinos can almost entirely escape the dense environments that are opaque to EM radiation. This makes neutrinos a perfect candidate for studying the physical processes that are otherwise impossible to probe. An overview of the primary artificial and natural neutrino sources is presented next.

1.2.1 Solar Neutrinos

Nuclear fusion inside the Sun is one of the most intense neutrino sources, producing a large flux of electron neutrinos, $2 \times 10^{38}\ \nu_e \mathrm{s}^{-1}$. Solar neutrinos are produced through several distinct processes (Fig. 1.3), primarily including the proton–proton (pp) chain [7, 8]. The resulting solar neutrino energy spectrum produced through several distinct processes is shown in Fig. 1.4 [9]. The main

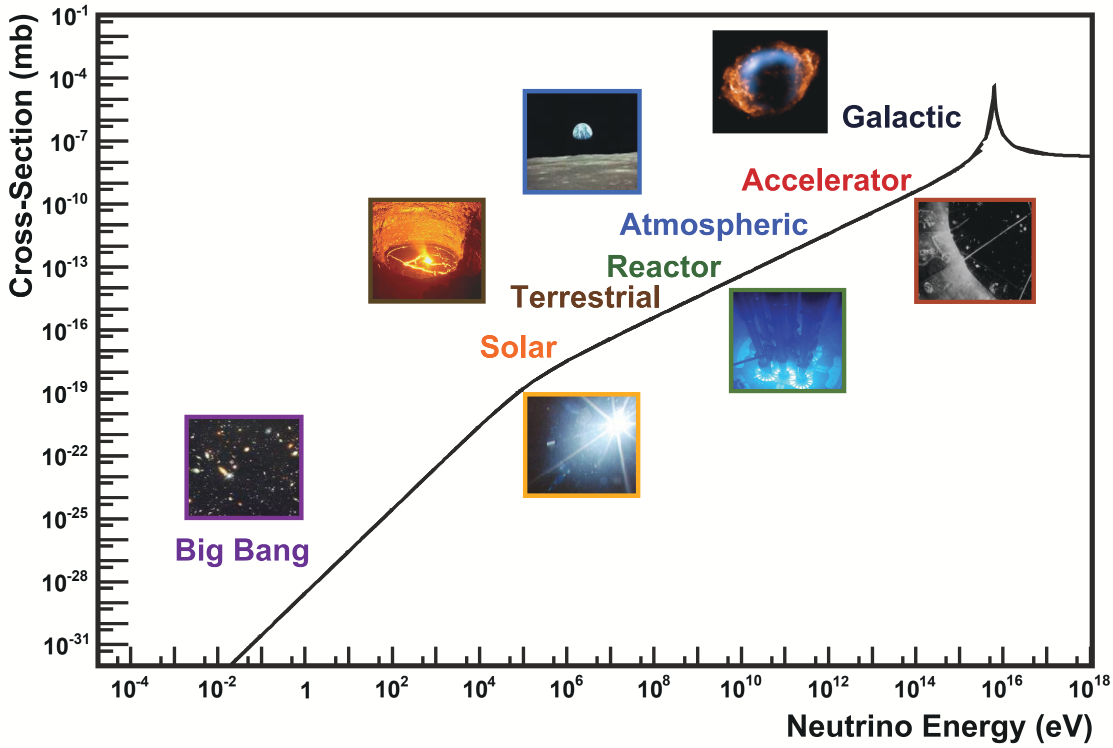

Figure 1.2: Figure showing different neutrino sources ranging from one-millionth of an eV (10^{-4}) to quintillion eV (10^{18}). On the y-axis is the neutrino cross section, which is a measure of how likely the neutrino is to be stopped by regular matter [6].

hydrogen-burning process, known as the pp cycle, proceeds through three steps:

$$
\begin{aligned}
p + p &\to D + e^{+} + \nu_e, \\
D + p &\to {}^{3}_{2}\mathrm{He} + \gamma, \\
{}^{3}_{2}\mathrm{He} + {}^{3}_{2}\mathrm{He} &\to {}^{4}_{2}\mathrm{He} + p + p.
\end{aligned}
$$

Because of low binding energy of ${}^{2}_{1}$D ($\sim$ 2.2 MeV), the neutrino produced through this process ($p+p \to D+e^{+}+\nu_e$) are low energy neutrinos with $E_\nu < 0.5$ MeV and hence are extremely difficult to detect. Therefore, for most of the experimental studies, higher energy neutrinos produced from the ^{7}Be and ^{8}B processes are used.

The highest energy solar neutrinos are produced from the β-decay of boron-8 (^{8}B), with energies up to 15 MeV.

$$
\begin{aligned}
{}^4_2\mathrm{He} + {}^3_2\mathrm{He} &\rightarrow {}^7_4\mathrm{Be} + \gamma, \\
{}^7_4\mathrm{Be} + p &\rightarrow {}^8_5\mathrm{B} + \gamma, \\
{}^8_5\mathrm{B} &\rightarrow {}^8_4\mathrm{Be}^* + e^+ + \nu_e,
\end{aligned}
$$

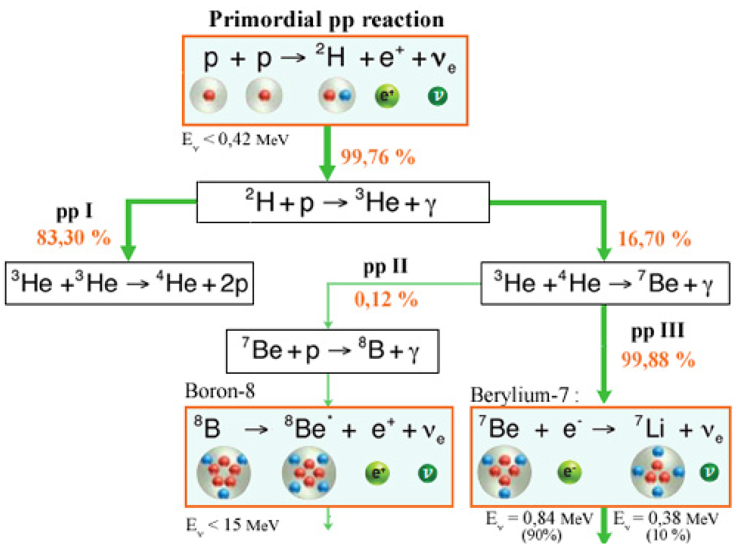

Figure 1.3: Several solar fusion processes producing the neutrinos. (Solar neutrino processes)

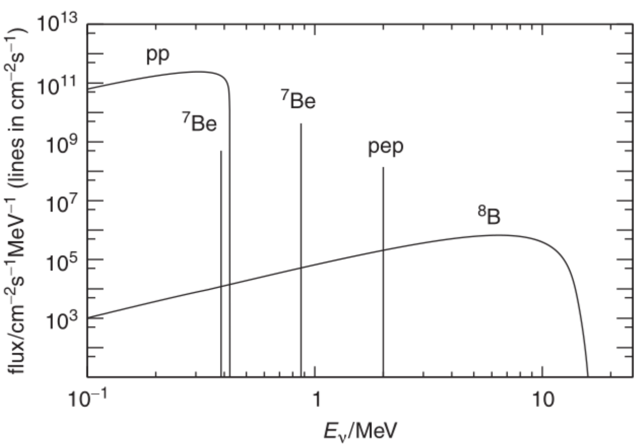

Figure 1.4: The flux of solar neutrinos from the main processes in the Sun [9].

1.2.2 Atmospheric Neutrinos

Atmospheric neutrinos are typically produced 15 km above the Earth's surface. High-energy cosmic-ray particles form the primary source of atmospheric neutrinos. When a highly energetic cosmic ray particle, such as a proton, interacts with the nuclei in Earth's atmosphere, it produces secondary mesons that primarily include pions and kaons. These pions, being unstable, are composed of a bound quark and an anti-quark pair, which decay to produce a muon and a muon neutrino. Due to the unstable nature of muons, they further decay to produce an electron, an electron (anti)neutrino and a muon (anti)neutrino [10]. Therefore, muon neutrinos and antineutrinos form two-thirds of the atmospheric neutrinos, while the rest are electron neutrinos and antineutrinos. In fact, it was the deviation from this ratio that provided some evidence of neutrino oscillation as they travel [11]. The typical energies of atmospheric neutrinos span a broad energy spectrum ranging from hundreds of MeV to several TeV.

1.2.3 Reactor Neutrinos

In 1956, the very first neutrino detected was from the reactor source. Reactor neutrinos are the by-products of the beta decay that comes from the nuclear fission process of unstable atomic nuclei. These are, therefore, a very intense source of electron antineutrinos, and because they come in only one flavor, electron antineutrinos are incredibly useful in determining neutrino properties. Beta decay of

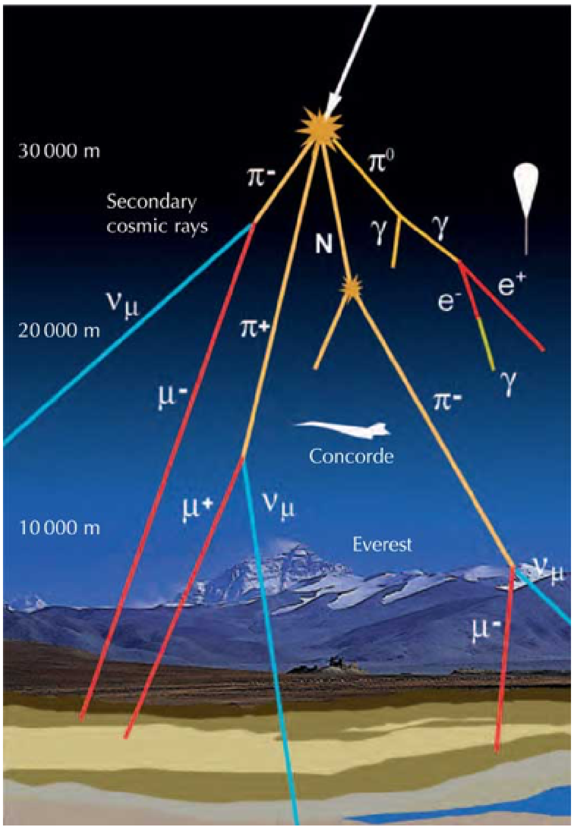

Figure 1.5: Production of atmospheric neutrinos through cosmic-ray interactions in the Earth's atmosphere.

neutron-rich fission fragments generated by the fission of isotopes such as ^{235}U, ^{238}U, ^{239}Pu, and ^{241}Pu [12] are primary source of reactor antineutrinos. The energies typically lie below 10 MeV and are primarily detected via inverse beta decay.

1.2.4 Accelerator Neutrinos

One of the most effective ways to study neutrinos is through intense neutrino beams, and particle accelerators are ideal candidates for generating highly energetic and intense neutrino beams. These are generated by directing high-energy protons onto a fixed solid target, such as graphite. The collision will produce secondary mesons

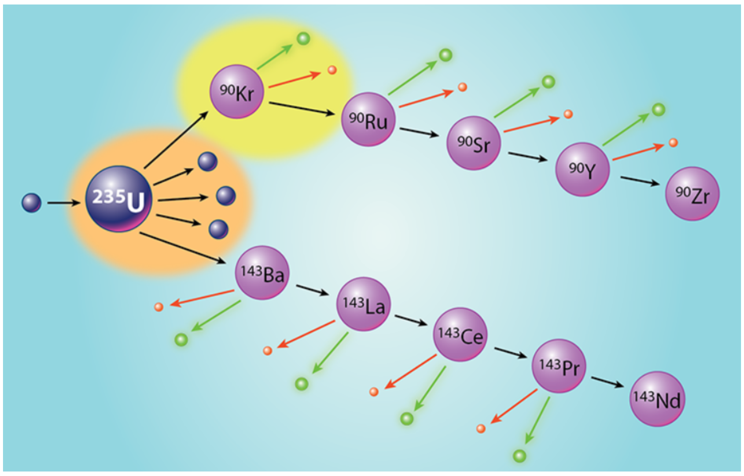

Figure 1.6: A neutron hits the Uranium nuclei producing the daughter nuclei, which further undergo beta decay producing an electron (in red) and an electron antineutrino (in green). (Reactor neutrino processes)

mainly pions ($\pi^{\pm}$) and kaons ($K^{\pm}$), which will then be focused using the magnetic horns. Based on the polarity of focused ($\pi^{\pm}$), the mesons then decay, allowing the creation of muon neutrinos (ν_μ) or antineutrinos ($\bar{\nu}_\mu$) with little contamination from electron neutrino or antineutrino [13].

1.3 Solar Neutrino Anomaly

As neutrino physics evolved, more experiments were built to study neutrinos. One particular measurement of interest was the observation of neutrino flux from the Sun. According to the Solar Model, the p-p chain in the Sun's core is the dominant source of ν_e flux on Earth with an approximate value of 6.5 $\times 10^{10}$ neutrinos per cm^2 s^{-1} (Sec. 1.2.1). Ray Davis and John Bahcall made one successful attempt to detect the solar neutrinos on Earth at the Homestack experiment [14]. However, contrary to their expectation, they observed a deficit in the number of ν_es at Earth compared to the Standard Solar Model. A similar deficit of solar neutrinos in the measured flux was also observed at the Kamiokande II experiment, in Japan [15], and at the Sudbury Neutrino Observatory (SNO), in Canada [16]. However, the SNO experiment shows the consistent result with the neutral current events, they observed the deficit only in the charged current events. These consistent deficit results are known as the Solar Neutrino Anomaly. Fig. 1.7 shows the predicted solar neutrino detection rate in Solar Neutrino Unit (SNU) from Bahcall's model in comparison with results from various experiments.

Gallium-based experiments (Gallex at Gran Sasso National Laboratory in Italy and SAGE at Baksan Neutrino Observatory in Russia) were developed to detect the low-energy solar electron neutrinos from the first step of the pp chain. These experiments use Gallium as the target material and leverage the low energy threshold of the $\nu_e +^{71} Ga \rightarrow^{71} Ge + e^-$ reaction (0.233 MeV). These experiments also observed a deficit of in the observed solar neutrino events. The results of these experiments are crucial, as they show that the deficit is not limited to the high-energy ^8B neutrinos and extends across the entire solar neutrino energy spectrum.

1.4 Atmospheric Neutrino Anomaly

Atmospheric neutrinos are produced in Earth's upper atmosphere when high-energy cosmic ray particle interacts with the atoms in the atmosphere. The primary production channels involve the decay of pions and kaons, resulting in the generation of muon neutrinos and antineutrinos. A subsequent decay of the resulting muons produces secondary electron neutrinos and antineutrinos. As a consequence of these processes, the expected flux ratio of atmospheric neutrinos is approximately

$$\frac{\nu_\mu + \bar{\nu}_\mu}{\nu_e + \bar{\nu}_e} \approx 2$$

However, experiments like Super Kamiokande [11] observed a significant deficit in the atmospheric muon neutrinos flux with no corresponding deficit in the electron neutrinos flux. This discrepancy cannot be explained solely by uncertainties in neutrino flux predictions or detector efficiencies; instead, it provided the first compelling experimental evidence of neutrino oscillations. Moreover, a strong zenith angle dependency is observed where the downward-going muon neutrinos, which traverse a relatively shorter distance, exhibit no such deficit, while the upward-going muon neutrinos, which travel long distances through the Earth's interior, exhibit the deficit as shown in Fig. 1.8.

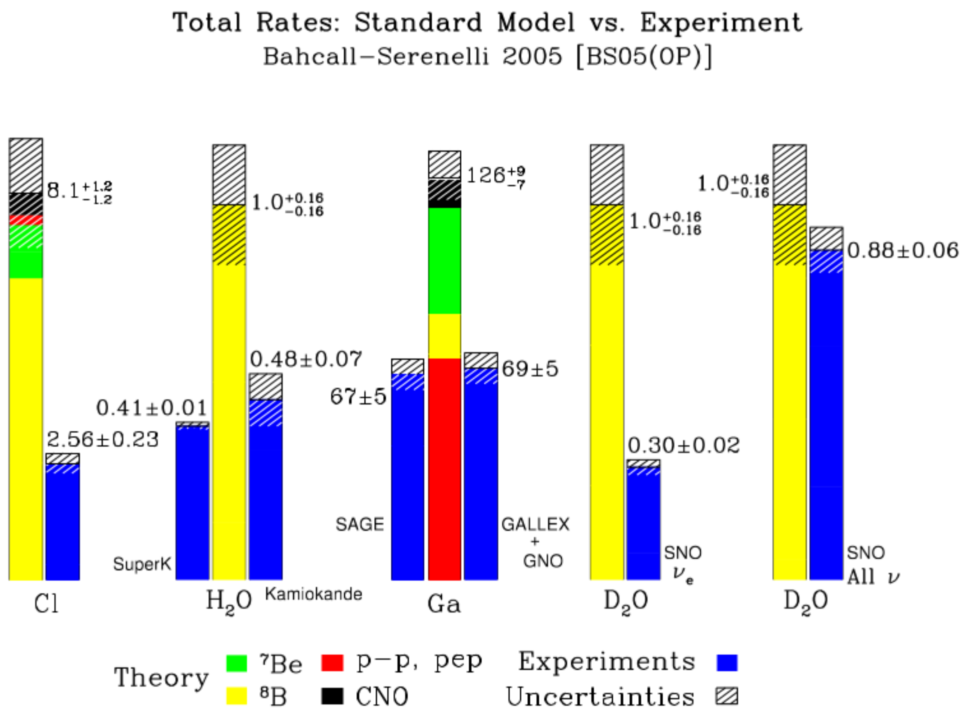

Figure 1.7: Solar neutrinos detection rates at various experiments, in units of SNU, are shown in this plot. The flux produced by different solar processes, as predicted by the Standard Solar Model, is shown in green, yellow, and black. The experimental results (in blue) with corresponding uncertainties are shown [17].

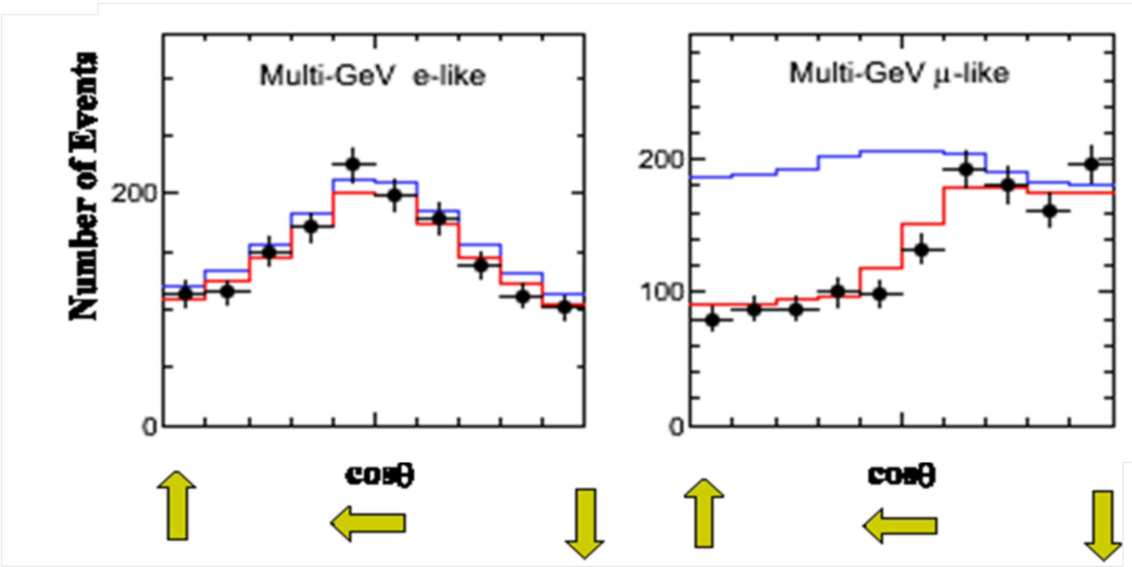

Figure 1.8: Zenith angle distribution of the muon neutrinos. The distribution on right-left(up-down) is symmetric and agrees with the expectation without neutrino oscillation (blue line) for electron neutrinos. In the right Figure, the observed upward-going muon neutrinos were half of the predictions. Theoretical expectation by assuming neutrino oscillation is given by the Red line (j-parc.jp/Neutrino/en/intro-t2kexp.html).

1.5 Neutrino Oscillations

In QM, the dynamics of a particle are described by the plane wave (the mass eigenstate), which is the solution of the Schrodinger equation. Pontecorvo suggested that the flavor eigenstate described above is a linear combination of the mass eigenstates, which implies that at a given instant of space and time, the state of being in any flavor state is probabilistic. So, as the neutrino travels, the component in the eigenstate changes, and we can observe a different eigenstate at some later point. Now, why are the mass and flavor eigenstates not the same? There is no reason to assume the two to be different, but since neither mass is precisely known nor has it been observed experimentally, the two are chosen to be different. To explain the Solar Neutrino Anomaly, let us say that the neutrino produced at the Sun's core is an electron neutrino, which is a linear combination of the three mass eigenstates. When this electron neutrino travels, its components change because the three mass eigenstates have different masses and travel at different frequencies. This will create a phase difference between the three, and at some point in time, a neutrino will be a muon or tau neutrino. Fig. 1.9 shows a ν_μ (combination of ν_1 and ν_2) oscillating to ν_e (a different combination of ν_1 and ν_2) and back to ν_μ (initial combination of ν_1 and ν_2). The two bases are related through a transformation matrix known as the **P**ontecorvo-**M**aki-**N**akagawa-**S**akata (PMNS) matrix.

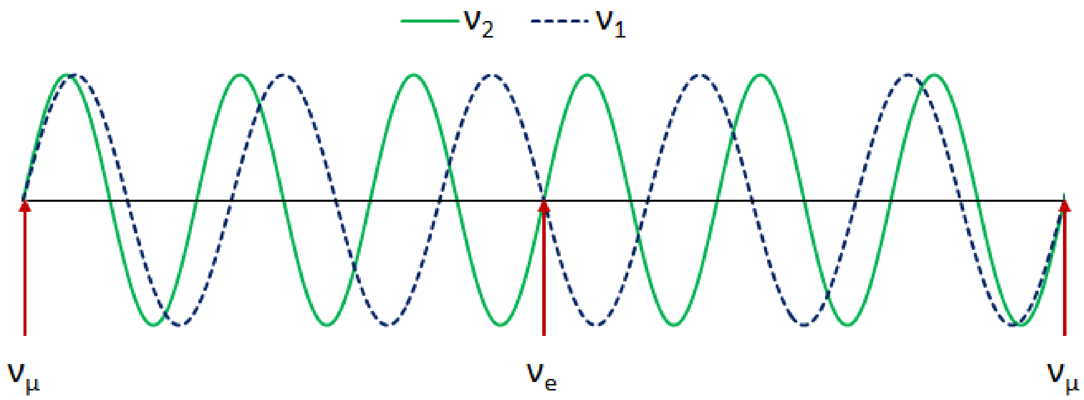

Figure 1.9: Figure showing neutrino oscillation in the two-flavor framework (https://lppp.lancs.ac.uk/neutrinos/en-GB/theory).

$$\begin{pmatrix} \nu_e \\ \nu_\mu \\ \nu_\tau \end{pmatrix} = \begin{pmatrix} U_{e1} & U_{e2} & U_{e3} \\ U_{\mu 1} & U_{\mu 2} & U_{\mu 3} \\ U_{\tau 1} & U_{\tau 2} & U_{\tau 3} \end{pmatrix} \begin{pmatrix} \nu_1 \\ \nu_2 \\ \nu_3 \end{pmatrix} \tag{1.4}$$

$$|\nu_f\rangle = U_{PMNS}|\nu_m\rangle \tag{1.5}$$

where $|\nu_f\rangle$ represents the flavor eigenstate, U_{PMNS} represent the unitary matrix also known as PMNS matrix and $|\nu_m\rangle$ is the mass eigenstate.

1.5.1 Two Flavor Oscillation

Consider the simple case of two generation neutrinos (ν_e and ν_μ) as flavour eigenstates and ν_1 and ν_2 as mass eigenstates. The time evolution of mass eigenstates is given by

$$\begin{aligned} |\nu_1(t)\rangle &= |\nu_1\rangle\, e^{i(\vec{p}_1\cdot\vec{x}-Et)} \\ |\nu_2(t)\rangle &= |\nu_2\rangle\, e^{i(\vec{p}_2\cdot\vec{x}-Et)} \end{aligned} \tag{1.6}$$

Eq. (2.5) in case of two-flavor oscillation is given by:

$$\begin{pmatrix} \nu_e \\ \nu_\mu \end{pmatrix} = \begin{pmatrix} U_{e1} & U_{e2} \\ U_{\nu 1} & U_{\nu 2} \end{pmatrix} \begin{pmatrix} \nu_1 \\ \nu_2 \end{pmatrix} \tag{1.7}$$

For a 2-D case, the simplest possible unitary matrix will be

$$U = \begin{pmatrix} \cos\theta & \sin\theta \\ -\sin\theta & \cos\theta \end{pmatrix} \tag{1.8}$$

Thus, for a neutrino in the initial state at t=0, it is considered to be created as an electron neutrino(ν_e), and thus the initial state is given as:

$$|\psi(0)\rangle = |\nu_e\rangle = \cos\theta|\nu_1\rangle + \sin\theta|\nu_2\rangle \tag{1.9}$$

As the particle propagates, the evolution of the wavefunction of mass eigenstates is given by:

$$|\psi(x,t)\rangle = \cos\theta|\nu_1\rangle e^{ip_1.x} + \sin\theta|\nu_2\rangle e^{ip_2.x} \tag{1.10}$$

Consider a neutrino has travelled over a distance L in time T, then, at this point, the wavefunction is given by:

$$|\psi(x,t)\rangle = \cos\theta|\nu_1\rangle e^{-i\phi_1} + \sin\theta|\nu_2\rangle e^{-i\phi_2} \tag{1.11}$$

where $\phi_i = ET - p_i.L$ is known as Lorent invariant phase. Furthermore, using the unitarity property of U, we find the matrix relation as:

$$\begin{pmatrix} \nu_1 \\ \nu_2 \end{pmatrix} = \begin{pmatrix} \cos\theta & -\sin\theta \\ \sin\theta & \cos\theta \end{pmatrix} \begin{pmatrix} \nu_e \\ \nu_\mu \end{pmatrix} \tag{1.12}$$

Moreover, this matrix relation gives:

$$\begin{aligned} |\nu_1\rangle &= \cos\theta\,|\nu_e\rangle - \sin\theta\,|\nu_\mu\rangle \\ |\nu_2\rangle &= \sin\theta\,|\nu_e\rangle + \cos\theta\,|\nu_\mu\rangle \end{aligned} \tag{1.13}$$

Now, back substituting these two relations in Eq. (1.11) we get:

$$\begin{aligned}|\psi(L,T)\rangle &= \cos\theta\big(\cos\theta|\nu_e\rangle - \sin\theta|\nu_\mu\rangle\big)e^{-i\phi_1} \\ &\quad + \sin\theta\big(\sin\theta|\nu_e\rangle + \cos\theta|\nu_\mu\rangle\big)e^{-i\phi_2} \\ &= e^{-i\phi_1}\Big[\big(\cos^2\theta + e^{-i\Delta\phi_{12}}\sin^2\theta\big)|\nu_e\rangle \\ &\quad + \big(e^{-i\Delta\phi_{12}} - 1\big)\cos\theta\sin\theta\,|\nu_\mu\rangle\Big]\end{aligned} \tag{1.14}$$

Now, this equation is similar to what we observe in quantum mechanics, where a particle has the possibility of existing in one of two given states, and the overall state is thus represented by a linear combination of these two. Thus, the probability of finding the neutrino to be in the muon neutrino state at a distance L and time T is given by:

$$P(\nu_e \to \nu_\mu) = |\langle\nu_\mu|\psi(L,T)\rangle|^2$$

$$\begin{aligned}P(\nu_e \to \nu_\mu) &= (1 - e^{-i\Delta\phi_{12}})(1 - e^{-i\Delta\phi_{12}})\cos^2\theta\sin^2\theta \\ &= \frac{1}{4}(2 - 2\cos\Delta\phi_{12})\sin^2 2\theta \\ &= \sin^2(2\theta)\sin^2\left(\frac{\Delta\phi_{12}}{2}\right).\end{aligned} \tag{1.15}$$

where $\Delta\phi_{12}$ is the phase difference between two mass eigenstates and varies with energy and distance, which can be deduced using the assumption that the momenta of the two mass eigenstates are equal, $p_1 = p_2 = p$. Thus, in this case:

$$\Delta\phi_{12} = (E_1 - E_2)T = \left[\sqrt{p_1^2 + m_1^2} - \sqrt{p_2^2 + m_2^2}\right]T \tag{1.16}$$

In the limit m<<E, we find using binomial expansion that

$$\sqrt{p^2 + m^2} \sim p\left(1 + \frac{m^2}{2p^2}\right)$$

$$\Delta\phi_{12} = \left[\frac{m_1^2 - m_2^2}{2p} L\right] \tag{1.17}$$

Thus, the probability of finding the neutrino to be a muon neutrino at distance L and time T with $p = E_\nu$ is found to be

$$P(\nu_e \to \nu_\mu) = \sin^2(2\theta)\sin^2\left(\frac{(m_1^2 - m_2^2)}{4E_\nu} L\right) \tag{1.18}$$

However, the generality of probability will not be lost even if we assume $E_1 = E_2$ and then calculate $\Delta\phi_{12}$. It is more convenient to express the probability in units that are easy to work with, such as length in kilometres and energy in electron volts. The probability expression turns out to be:

$$P(\nu_e \to \nu_\mu) = \sin^2(2\theta)\sin^2\left(1.27\frac{\Delta m^2[eV^2]L[km]}{4E_\nu[GeV]}\right) \tag{1.19}$$

This probability can also be thought of as the disappearance probability of electron neutrino, i.e., the probability that an electron neutrino(ν_e) disappears and is changed to muon neutrino(ν_μ). Similarly, we can express the appearance probability of electron neutrino(ν_e) as:

$$P(\nu_e \to \nu_e) = 1 - \sin^2(2\theta)\sin^2\left(1.27\frac{\Delta m^2[eV^2]L[km]}{4E_\nu[GeV]}\right) \tag{1.20}$$

1.5.2 Three Flavor Oscillations

Now, if we consider all three generations of neutrinos, then, together with electron and muon neutrinos, the tau neutrino also comes into play, resulting in an extra dimension to the PMNS matrix. Therefore, the general relation between mass and flavor eigenstates will be used while calculating the disappearance and survival probabilities.

$$\begin{pmatrix} \nu_1 \\ \nu_2 \\ \nu_3 \end{pmatrix} = \begin{pmatrix} U^*_{e1} & U^*_{\mu_1} & U^*_{\tau_1} \\ U^*_{e_2} & U^*_{\nu 2} & U^*_{\tau_2} \\ U^*_{e_3} & U^*_{\nu_3} & U^*_{\tau 3} \end{pmatrix} \begin{pmatrix} \nu_e \\ \nu_\mu \\ \nu_\tau \end{pmatrix} \tag{1.21}$$

The unitarity condition gives $UU^\dagger = I$, considering a neutrino at t=0 to be completely an electron neutrino, which is a linear combination of three mass eigenstates and is given by:

$$|\psi(0)\rangle = |\nu_e\rangle = U^*_{e1}|\nu_1\rangle + U^*_{e2}|\nu_2\rangle + U^*_{e3}|\nu_3\rangle \tag{1.22}$$

The time evolution of this wavefunction results from the time evolution of mass eigenstates and is given as:

$$|\psi(x,t)\rangle = U^*_{e1}|\nu_1\rangle e^{-i\phi_1} + U^*_{e2}|\nu_2\rangle e^{-i\phi_2} + U^*_{e3}|\nu_3\rangle e^{-i\phi_3} \tag{1.23}$$

where again ϕ_i represents the phase of the plane wave representing the mass eigenstates. Using Eq. (1.21) and substituting the value of $|\nu_1\rangle, |\nu_2\rangle$ and $|\nu_3\rangle$ we get the following result:

$$\begin{aligned} |\psi(x,t)\rangle = U^*_{e1}(U_{e1}|\nu_e\rangle + U_{\mu 1}|\nu_\mu\rangle + U_{\tau 1}|\nu_\tau\rangle)e^{-i\phi_1} \\ +U^*_{e2}(U_{e2}|\nu_e\rangle + U_{\mu 2}|\nu_\mu\rangle + U_{\tau 2}|\nu_\tau\rangle)e^{-i\phi_2} \\ +U^*_{e3}(U_{e3}|\nu_e\rangle + U_{\mu 3}|\nu_\mu\rangle + U_{\tau 3}|\nu_\tau\rangle)e^{-i\phi_3} \end{aligned}$$

$$\begin{aligned} |\psi(x,t)\rangle = (U^*_{e1}U_{e1}e^{-i\phi_1} + U^*_{e2}U_{e2}e^{-i\phi_2} + U^*_{e3}U_{e3}e^{-i\phi_3})|\nu_e\rangle \\ +(U^*_{e1}U_{\mu 1}e^{-i\phi_1} + U^*_{e2}U_{\mu 2}e^{-i\phi_2} + U^*_{e3}U_{\mu 3}e^{-i\phi_3})|\nu_\mu\rangle \\ +(U^*_{e1}U_{\tau 1}e^{-i\phi_1} + U^*_{e2}U_{\tau 2}e^{-i\phi_2} + U^*_{e3}U_{\tau 3}e^{-i\phi_3})|\nu_\tau\rangle \end{aligned}$$

This expression is similar to what we write in the QM for a particle that has a finite probability of being in any of the given states, such that

$$|\psi(x,t)\rangle = c_e|\nu_e\rangle + c_\mu|\nu_\mu\rangle + c_\tau|\nu_\tau\rangle$$

Thus, the disappearance probability for e^- neutrino (ν_e) to muon neutrino (ν_μ) is found to be

$$P(\nu_e \rightarrow \nu_\mu) = |\langle \nu_\mu | \psi(x,t) \rangle|^2 = c_\mu^* c_\mu$$

$$P(\nu_e \rightarrow \nu_\mu) = |U_{e1}^* U_{\mu_1} e^{-i\phi_1} + U_{e2}^* U_{\mu_2} e^{-i\phi_2} + U_{e3}^* U_{\mu_3} e^{-i\phi_3}|^2 \quad (1.24)$$

The fact that three mass eigenstates exhibit a phase difference gives rise to the oscillation among different flavors can be understood from the above expression; if we assume all the mass eigenstates have the same phase, i.e., $\phi_1 = \phi_2 = \phi_3$ then, the probability will have $U_{e1}^* U_{e1} + U_{e2}^* U_{e2} + U_{e3}^* U_{e3}$ which is zero from the unitary condition of PMNS matrix and imply no oscillation. The expression of probability in Eq. (1.24) can be solved using the complex number properties i.e. $|z_1 + z_2 + z_3|^2 = |z_1|^2 + |z_2|^2 + |z_3|^2 + 2\,\mathrm{Re}(z_1 z_2^* + z_2 z_3^* + z_1 z_3^*)$. This gives the oscillation probability as

$$\begin{aligned} P(\nu_e \rightarrow \nu_\mu) = {} & |U_{e1}^* U_{\mu 1}|^2 + |U_{e2}^* U_{\mu 2}|^2 + |U_{e3}^* U_{\mu 3}|^2 \\ & + 2\ \mathrm{Re}\Big(U_{e1}^* U_{\mu 1}\, U_{e2} U_{\mu 2}^*\, e^{-i(\phi_1 - \phi_2)}\Big) \\ & + 2\ \mathrm{Re}\Big(U_{e1}^* U_{\mu 1}\, U_{e3} U_{\mu 3}^*\, e^{-i(\phi_1 - \phi_3)}\Big) \\ & + 2\ \mathrm{Re}\Big(U_{e2}^* U_{\mu 2}\, U_{e3} U_{\mu 3}^*\, e^{-i(\phi_2 - \phi_3)}\Big) \end{aligned}$$

Using the complex number property and equation. above we can show that the disappearence probability of ν_e to ν_μ is given by

$$\begin{aligned} P(\nu_e \rightarrow \nu_\mu) = {} & 2\,\mathrm{Re}[U_{e1}^* U_{\mu_1} U_{e2}^* U_{\mu_2} \{e^{-i(\phi_1 - \phi_2)} - 1\}] \\ & + 2\,\mathrm{Re}[U_{e1}^* U_{\mu_1} U_{e3}^* U_{\mu_3} \{e^{-i(\phi_1 - \phi_3)} - 1\}] \\ & + 2\,\mathrm{Re}[U_{e2}^* U_{\mu_2} U_{e3}^* U_{\mu_3} \{e^{-i(\phi_2 - \phi_3)} - 1\}] \end{aligned} \quad (1.25)$$

where ϕ_i are the respective phases of mass eigenstates, and the difference can be calculated as

$$\begin{aligned}\mathrm{Re}\{e^{-i(\phi_j-\phi_k)}-1\} &= \cos(\phi_j-\phi_k)-1 \\ &= -\sin^2\left(\frac{\phi_j-\phi_k}{2}\right) \\ &= -\sin^2\Delta_{jk} \end{aligned} \tag{1.26}$$

where Δ_{jk} is same as defined earlier

$$\Delta_{jk} = \frac{\phi_j-\phi_k}{2} = \frac{(m_j^2-m_k^2)}{4E_\nu}L$$

The disappearance (or appearance) probability involves phase factors that depend on the neutrino masses' mass-squared terms, which makes our experiments sensitive to mass-squared terms instead of individual masses. Apart from explaining the Solar Neutrino Problem, neutrino oscillation could help solve the problems of Charge-Parity (CP) violation, the neutrino mass hierarchy, dark matter, and many other issues.

1.5.3 Mass Hierarchy and CP Violation

One of the main points of discussion in high-energy physics is to decide the order in which masses m_1, m_2 and m_3 exist. Since the disappearance or survival probability involves only the squared mass difference, it will be independent of the order of masses. Experimentally, it is observed that these squared mass differences are $\Delta m_{21}^2 \sim 8\times10^{-5}eV^2$ and $\Delta m_{32}^2 \sim 2\times10^{-3}eV^2$. However, this does not show whether $m_1 \sim m_2 > m_3$ (inverted hierarchy) or $m_3 > m_1 \sim m_2$ (normal hierarchy). Current experiments are not sensitive enough to distinguish between the two, which will be one of the many challenges for experimental physicists.

We know that charge conjugation and parity are maximally violated from the V-A structure of the weak interaction vertex. The effect of charge conjugation is to replace a particle with an antiparticle and vice versa. At the same time, the parity operator will keep track of the helicity of the particles and antiparticles. This means that the weak interactions respect the combined CP symmetry. So far, the best possible explanation for observed matter anti-matter asymmetry is via CP violation. T represents the time-reversal transformation, which implies that a process that can occur forward in time must also occur in the same manner. e.g., If an electron neutrino transforms into a muon neutrino, then time-reversal symmetry states that the muon neutrino must also transform into an electron neutrino in exactly a similar way. It can be shown that all Lorentz-invariant field theories are invariant under the combined CPT transformation. One of the consequences of CPT transformation is that the particles and antiparticles have the same mass, magnetic moments, etc. As a result, CPT is considered to be the exact symmetry of nature, which implies that if one of these symmetries is violated in a process, the other must also, so that the combined effect results in no overall change.
If time-reversal symmetry exists then, $P(\nu_e \to \nu_\mu)$ must be same as $P(\nu_\mu \to \nu_e)$. The oscillation probability for $\nu_\mu \to \nu_e$ can be

obtained from Eq. (1.25) just by replacing e by μ such that

$$\begin{aligned} P(\nu_\mu \to \nu_e) &= 2\,\mathrm{Re}[U^*_{\mu 1} U_{e1} U^*_{\mu 2} U_{e2} \{e^{-i(\phi_1 - \phi_2)} - 1\}] \\ &+ 2\,\mathrm{Re}[U^*_{\mu 1} U_{e1} U^*_{\mu 3} U_{e3} \{e^{-i(\phi_1 - \phi_3)} - 1\}] \\ &+ 2\,\mathrm{Re}[U^*_{\mu 2} U_{e2} U^*_{\mu 3} U_{e3} \{e^{-i(\phi_2 - \phi_3)} - 1\}] \end{aligned} \tag{1.27}$$

From Eq. (1.25) and Eq. (1.27), we can conclude that these two can be the same only if elements of the PMNS matrix are real, but these are complex, which implies that the two expressions are not the same. This suggests the possibility of time symmetry violation, which in turn hints at CP violation in neutrino oscillations. The effect of CP transformation gives: $\nu_e \to \nu_\mu \longrightarrow \bar{\nu}_e \to \bar{\nu}_\mu$. To get a measure of the CP violation, we measure the difference between the two expressions such that:

$$\begin{aligned} P(\nu_e \to \nu_\mu) - P(\bar{\nu}_e \to \bar{\nu}_\mu) = 16\,\mathrm{Im}\{U^*_{e1} U_{\mu_1} U_{e2} U^*_{\mu_2}\} \times \\ \sin\Delta_{12} \sin\Delta_{13} \sin\Delta_{23} \neq 0 \end{aligned} \tag{1.28}$$

This difference is observed to be at most a few per cent.
The PMNS matrix can be described in terms of three real parameters and a single phase, where each angle represents the rotation about the axis, and the phase will be a complex phase factor. The PMNS matrix is given by [18]

$$U = \begin{pmatrix} U_{e1} & U_{e2} & U_{e3} \\ U_{\nu 1} & U_{\nu 2} & U_{\nu 3} \\ U_{\tau 1} & U_{\tau 2} & U_{\tau 3} \end{pmatrix} = \begin{pmatrix} 1 & 0 & 0 \\ 0 & c_{23} & s_{23} \\ 0 & -s_{23} & c_{23} \end{pmatrix} \begin{pmatrix} c_{13} & 0 & s_{13}e^{-i\delta} \\ 0 & 1 & 0 \\ -s_{13}e^{i\delta} & 0 & c_{13} \end{pmatrix} \begin{pmatrix} c_{12} & s_{12} & 0 \\ -s_{12} & c_{12} & 0 \\ 0 & 0 & 1 \end{pmatrix}$$

1.5.4 Matter Effects on Neutrino Oscillation

Consider the vacuum Hamiltonian as H_0. In the case of matter, what happens is that the neutrino, when it travels, gets scattered by the constituents of electrically neutral matter (like protons, neutrons, or electrons). Furthermore, the time evolution of mass eigenstates also depends on the effective Hamiltonian of the medium (through e^{-iHt}). The effective Hamiltonian experienced by the neutrino is given by [19]

$$H = H_0 + \sqrt{2}G_F N_e \begin{pmatrix} 1 & 0 \\ 0 & 0 \end{pmatrix} + ... \tag{1.29}$$

where H_0 is the effective vacuum Hamiltonian, G_F Fermi constant, N_e electron density. The higher terms are proportional to the identity matrix and are generally less effective. Consider the vacuum Hamiltonian defined as:

$$H_0 = \frac{U^\dagger \hat{m}^2 U}{4E} \tag{1.30}$$

where U is the PMNS matrix and $\hat{m}$ is the diagonal matrix in mass eigenbasis given as

$$\hat{m} = \begin{pmatrix} m_1 & 0 \\ 0 & m_2 \end{pmatrix}$$

Consider the case of two flavour oscillations, and using the matrix form of Eq. (1.8), we found the Hamiltonian to be

$$H_0 = \frac{1}{4E} \begin{pmatrix} \cos\theta_0 & -\sin\theta_0 \\ \sin\theta_0 & \cos\theta_0 \end{pmatrix} \begin{pmatrix} m_1^2 & 0 \\ 0 & m_2^2 \end{pmatrix} \begin{pmatrix} \cos\theta_0 & \sin\theta_0 \\ -\sin\theta_0 & \cos\theta_0 \end{pmatrix}$$

$$H_0 = \frac{\Delta m_0^2}{4E}\begin{pmatrix} -\cos 2\theta_0 & \sin 2\theta_0 \\ \sin 2\theta_0 & \cos 2\theta_0 \end{pmatrix}$$

Now, including the matter effect and assuming the same form of Hamiltonian, such that:

$$H = \frac{\Delta m^2}{4E}\begin{pmatrix} -\cos 2\theta & \sin 2\theta \\ \sin 2\theta & \cos 2\theta \end{pmatrix}$$

where the matter effect can be seen in the different parameters as

$$\frac{A}{2E} = \sqrt{2} G_F N_e$$

$$\sin^2 2\theta = \frac{\sin^2 2\theta_0}{\sin^2 2\theta_0 + \left(\cos 2\theta_0 - \frac{A}{\Delta m_0^2}\right)^2}$$

$$\Delta m^2 = \Delta m_0^2 \sqrt{\sin^2 2\theta_0 + \left(\cos 2\theta_0 - \frac{A}{\Delta m_0^2}\right)^2}$$

Now, there will be maximal oscillation if $A = \Delta m_0^2 \cos 2\theta_0$ which implies $\sin^2\theta = 1$ (the maximum amplitude of the neutrino oscillation). This condition is known as the resonance condition.

Neutrino oscillations in the matter form the basis for various experiments like NOvA, where a beam of neutrinos is allowed to pass through the matter before being detected.

1.6 Summary

This chapter provides an overview of neutrino physics, tracing the theoretical origins and experimental discoveries that have led to our current understanding of these particles. We further presented a detailed overview of neutrino sources, with a primary focus on both natural (such as solar and atmospheric) and artificial (reactor and accelerator) sources. The experimental observations of solar and atmospheric neutrinos have revealed discrepancies in the observed and predicted fluxes, referred to as the solar and atmospheric neutrino anomalies, respectively. These anomalies played a central role in establishing the neutrino oscillations and thus provided the first compelling experimental evidence of massive neutrinos.

The chapter further presents a detailed mathematical formalism of neutrino oscillations, starting with the simplest case of the two-flavour approximation and extending it to the complete three-flavour framework. We introduced and discussed the important oscillation parameters, which include mass ordering and CP-violating phase. Matter effects that modify the neutrino oscillation probabilities as neutrinos propagate through the matter are also discussed. These concepts formed the basis of modern long-baseline experiments, such as NOvA, which will be discussed in the subsequent chapters.

Chapter 2

Sterile Neutrinos

"Everything should be made as simple as possible, but no simpler."

Albert Einstein

Introduction

2.1 Motivation

From the measurement of the Z-boson decay width rate at LEP [18], it has been a proven fact that neutrinos exist in three active flavors with masses less than $\frac{m_z}{2}$. Sec. 1.5 explains the study of three flavor oscillation which assumes a 3×3 PMNS matrix and this matrix has been parameterised by three mixing angles $(\theta_{13}, \theta_{23}, \theta_{12})$ and one CP-violating phase (δ) [20]. Standard three-flavor neutrino oscillation experiments, involving solar, atmospheric, reactor, and accelerator neutrinos, have established the oscillation parameters.

$$7.05 \times 10^{-5} eV^2 \leq \Delta m^2_{21} \leq 8.34 \times 10^{-5} eV^2,$$
$$2.07 \times 10^{-3} eV^2 \leq |\Delta m^2_{31}| \leq 2.75 \times 10^{-3} eV^2,$$
$$0.25 \leq \sin^2\theta_{12} \leq 0.37, 0.36 \leq \sin^2\theta_{23} \leq 0.67, \sin^2\theta_{13} < 0.056 \text{ at}$$
$$90\% \text{ CL}$$

All these parameters have been measured in multiple experiments, except δ_{CP} [11, 21, 22], as we are still unable to constrain this parameter. The current three-flavors mixing model has successfully explained most of the experimental data. However, experiments such as LSND, MiniBooNE, KARMEN, and others have yielded some anomalous results that cannot be explained based on the current three-flavor theory.

As already discussed in the standard model, there are three generations of leptons, each corresponding to a distinct flavor generation, and a neutrino accompanies each flavor generation. It is also observed that each particle has both left- and right-handed components, except for the neutrino. Neutrinos are all left-handed, and antineutrinos are right-handed; however, the opposite has not been experimentally observed yet, and no process that could support this possibility has been observed. As predicted by SM, neutrinos are massless, which clearly shows the non-existence of right-handed neutrino states [23]. The mass term as predicted by the SM is given as [23]

$$\mathcal{L}_l = h_e \bar{\ell}_L e_R \Phi + H.c. \tag{2.1}$$

where the mass of the lepton is given by $m_\ell = h_\ell v$, which shows that to have mass, a lepton should have a right-handed component too.

However, the problem arises for neutrinos, where neutrino oscillation confirms them to have mass, but no right-handed component.

Furthermore, the cosmological events also predict the existence of one additional mass eigenstate for neutrinos, and other results from the LSND and MiniBooNE experiments also provide a hint of this extra neutrino state. The question that then comes to our mind is what this fourth state could be. This right-handed neutrino state can explain various anomalies both at the theoretical and experimental levels. This fourth eigenstate is known as the Sterile Neutrino. Again, the question would be, shouldn't it affect the decay width of Z and W bosons? The answer is NO because this fourth state is completely sterile, which interacts only through gravity and thus gives sterile neutrinos the following properties:

1. No Interaction : Zero electric charge.
2. No Weak interaction: Zero Hypercharge.
3. No strong interaction: Zero colour charge.

2.2 How to observe Sterile Neutrinos ?

There is no direct way to observe sterile neutrinos similar to the neutrinos. However, there are a few indirect ways to observe them, which are also the basis of various experiments:

1. We know that neutral current interactions remain unaffected in the three-flavor neutrino oscillation. So, a deficit or excess in the rate of events in the neutrino oscillation should be expected if there is any sterile neutrino.

2. With the addition of the fourth mass eigenstate of neutrino, the PMNS matrix would now be 4×4. This is given by:

$$V = \begin{pmatrix} V_{3\times3} & K_{3\times1} \\ U_{1\times3} & M_{1\times1} \end{pmatrix} \tag{2.2}$$

Now, in case there is a possible oscillation from active to sterile neutrinos, the non-diagonal terms can never be zero, and thus in order for V to be unitary, $V_{3\times3}$ should never be unitary. Thus, the unitarity of the PMNS matrix can provide direct evidence for the existence of sterile neutrinos.

3. Neutrinoless double beta decay should be possible only if the neutrino is a Majorana particle and the mass of the unstable nuclei is given by:

$$m_{\beta\beta} = |\sum_i V_{ei}^2 m_i| \tag{2.3}$$

Moreover, this is sensitive to the mass of the fourth state and V_{e4}.

2.3 Experimental Hints for Sterile Neutrinos

In the initial days when experiments by Kamiokande [24, 25] and IMB [26, 27] observed the atmospheric muon neutrino deficit, the explanation for this deficit was given in terms of muon neutrino oscillation into sterile neutrino [28, 29]. A similar kind of explanation has also been given for the solar neutrino problem [30, 31, 32, 33]. However, it has been firmly established that these two problems can be solved within the present three-flavor oscillation model. However, several experimental anomalies remain unexplained in terms of active neutrino mixing and necessitate an extension of the model.

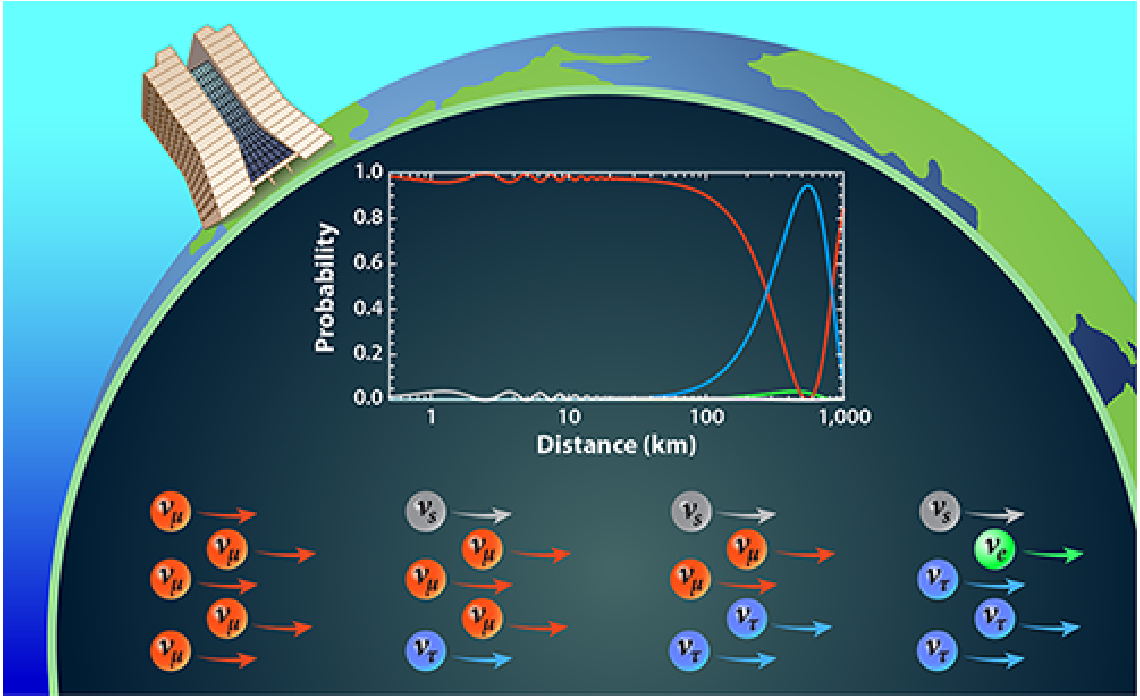

Figure 2.1: The neutrino oscillates as it travels through the matter. This figure shows how a muon neutrino produced at Fermilab changes its flavor during its course of motion to the far detector into electron(green), tau(blue) and hypothetical sterile(grey) neutrino (https://physics.aps.org/articles/v13/123).

2.3.1 LSND

The **L**iquid **S**cintillator **N**eutrino **D**etector (LSND) was operated at Los Alamos National Laboratory from 1993 to 1998 [34]. The experiment used a beam composed of ν_μ, $\bar{\nu}_\mu$ and ν_e, and since most of the pions (π^-) were absorbed via strong interaction before decaying, the beam is almost free of $\bar{\nu}_e$. This made the experiment ideally suitable for $\bar{\nu}_\mu \to \bar{\nu}_e$ oscillation studies. $\bar{\nu}_e$ interactions ($\bar{\nu}_e + p \to n + e^+$) have been characterised by a coincident observation of a prompt positron signal with a delayed photon signal produced by neutron capture by a proton. Fig. 2.2 shows the result of the LSND experiment with varying baseline and energy. It shows that LSND observes a significant (3σ) excess compared to the estimated background. The best possible explanation for this excess is given in terms of active-sterile neutrino oscillation. However, there are other possible explanations for this as well, which are less probable, and these are:

- **Decay in Flight**:: π^- decaying in flight before they can be absorbed in the matter are an obvious source of $\bar{\nu}_e$ but since the design of the target is so perfect that it is almost difficult to imagine where these estimates could have gone wrong.

- **Accidental Backgrounds**: There is a possibility that cosmic-induced neutrons and electrons or positrons can mimic the charged current ν_e interaction from the beam. These backgrounds can be estimated directly and are negligible due to the very low probability of both temporal and spatial coincidence between random neutrons and random electrons or positrons.

- **Knock-on neutrons**: When a ν_e interacts with the Carbon nucleus inside the detector via QE scattering, it will convert to an electron and eject a proton. On its way out of the nucleus, the proton may transfer energy to a neutron so that the final state will contain an electron and a neutron. This final state is indistinguishable from a positron and a neutron of $\bar{\nu}_e$ interaction. However, it is found that the energy required for such an interaction is so high that most events fall below the 200MeV cut that LSND has imposed on the reconstruction of positron energy.

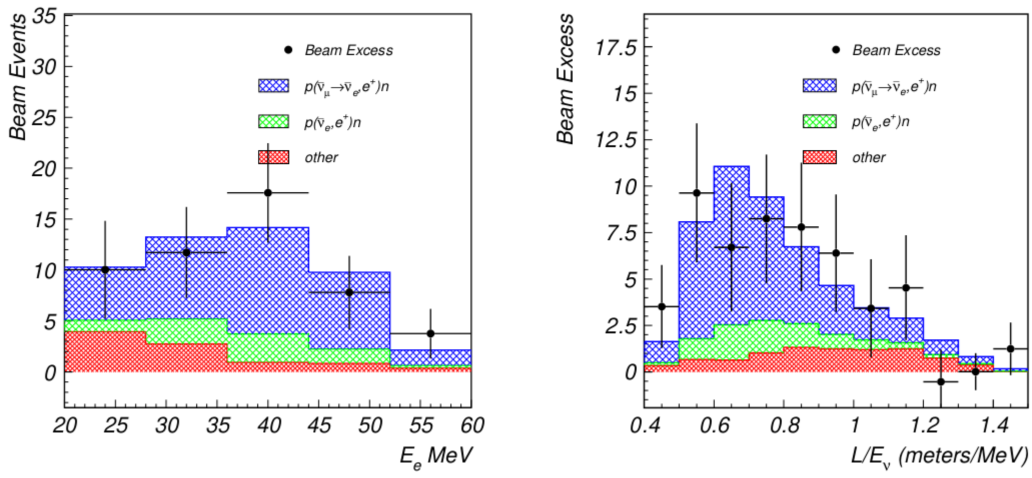

Figure 2.2: The distribution of observed events in LSND as a function of positron energy (left) and as a function of L/E (right) [35]

2.3.2 MiniBooNE

This experiment at Fermilab was designed independently to test the results from the LSND experiment. The detector was located at 541m downstream of the primary pion production target and shaped in the form of a spherical vessel containing 818 tons of mineral oil [36, 37]. The detectors were optimised to identify the charged current interactions (ν_μ, $\bar{\nu}_\mu$, ν_e, and $\bar{\nu}_e$) characterised by the emission of corresponding charged leptons in the final state. It used approximately 18.25×10^{20} in the neutrino mode and 11.27×10^{20} in the antineutrino mode, producing the results as shown in Fig. 2.3. An apparent excess of 4.7σ significance for the neutrino mode and 4.8σ for the combined neutrino and antineutrino mode was observed. Like the LSND excess, MiniBooNE results can also be explained in terms of active-sterile neutrino mixing, and, similar to LSND, they have alternative explanations, which are again less probable.

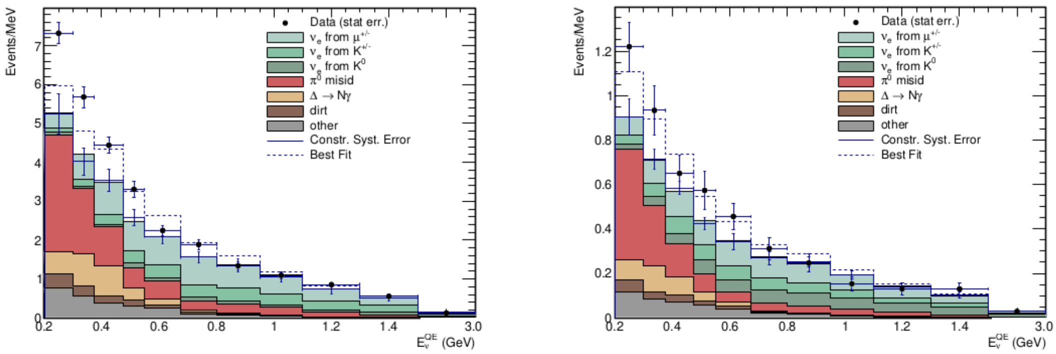

Figure 2.3: The observed event spectra by MiniBooNE for neutrino mode [38] (left) and antineutrino mode [39] (right).

- **Neutral Pions**: If the neutral current pion (π^0) background was larger than predicted by a factor of 2, then it could explain the observed excess of neutrino events quite well. However, this is unlikely to be true because the prediction of π^0 background is data-driven.

- **Decays of heavier mesons to photons**: Theoretically speaking, heavier neutral mesons such as η can decay to produce a diphoton in the detector in the same way as π^0. Now, if the decay products are reconstructed as a single photon because one of them is lost or because the invariant mass is small, this could mimic the ν_e signal. However, such a case is implausible because the likelihood of two photons having a small invariant mass is much smaller.

2.3.3 Reactor Anomaly

Nuclear reactors have been a prime source of neutrinos since the initial days of neutrino experiments [40, 41]. Besides various long-baseline experiments that contributed to the precise measurement of oscillation parameters, short-baseline experiments were still being carried out, where no oscillation was expected in the standard three-flavor framework. It was the theoretical prediction of Mueller [42] and Huber [43] that created a new spark, as the experimental results do not agree with their predictions. This disagreement corresponds to a 3σ significance level and has been known as the reactor antineutrino anomaly. Similar to the previous two experiments, the reactor anomaly also requires a sterile neutrino to explain the disagreement between the two results Fig. 2.4. Earlier flux calculations were made using Huber-Mueller reactor flux models, which resulted in the disagreement. This anomaly was thought to be resolved in 2021 through flux recalculations, but a more recent reactor antineutrino flux calculation result published by the French group [44] and recently used for oscillation study in [45], which revives the reactor neutrino anomaly.

2.3.4 Gallium Anomaly

The gallium-based experiments, such as GALLEX [47, 48] and SAGE [49], used neutrinos from highly intense radioactive sources, such as ^{51}Cr and ^{37}Ar. These radioactive sources are placed inside the detectors where they decay via electron capture through $e^- +^{51} Cr \rightarrow^{51} V + \nu_e$ and $e^- +^{37} Ar \rightarrow^{37} Cl + \nu_e$ to produce the neutrinos. These neutrinos were detected using the same reaction as used in the solar neutrino detection ($\nu_e +^{71} Ga \rightarrow^{71} Ge + e^-$) because of the low-energy threshold for the reaction. Both GALLEX and SAGE

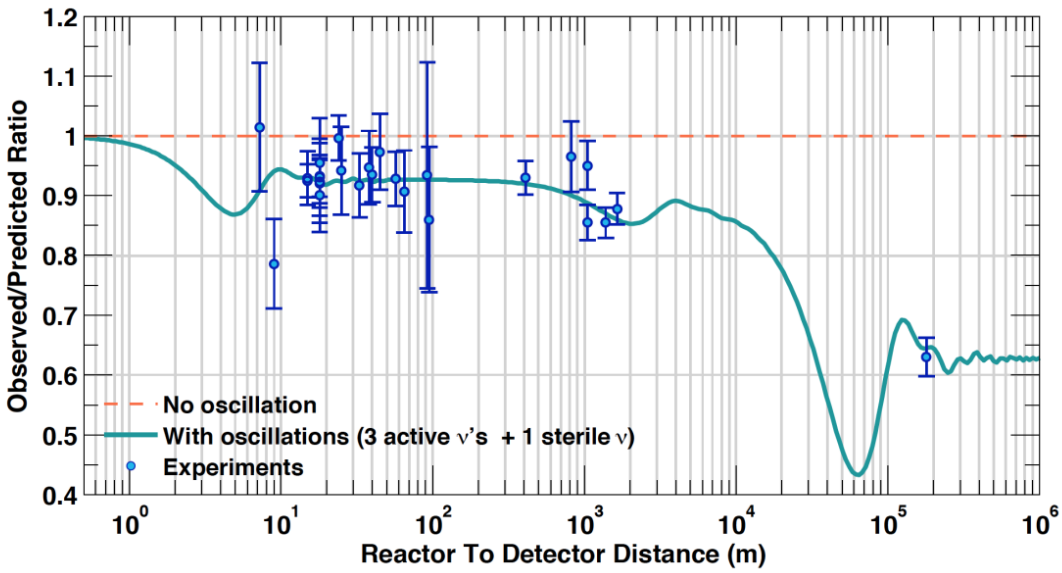

Figure 2.4: Comparison of measured and predicted $\bar{\nu}_e$ event rates from nuclear reactors. Results from a long list of present experiments are shown as a function of baseline [46].

observed an event deficit, with the observed-to-predicted event ratio (R) around 0.8 [50, 51]. These suggest possible electron-neutrino disappearance at short baselines and a possible hint of active-sterile neutrino mixing.

2.3.5 Cosmological Constraints

Sterile neutrinos are a natural extension of the standard model as a solution to the short-baseline anomalies. However, the sterile neutrino scenario is constrained by the cosmological model. To address the short-baseline anomalies using the sterile neutrino interpretation requires the mass splitting $\Delta m^2 \sim \mathcal{O}(eV^2)$ and $|U_{\alpha 4}| \approx 10^{-2}$. Furthermore, CMB+BAO data robustly found the limits on the $|U_{\alpha 4}| \approx 10^{-3}$, which is much stronger than that observed from the short-baseline experiments. Additional limits on the effective electron neutrino masses ($m_\beta < 0.09$ eV) from the CMB data are also in serious tension with the direct experimental measurements [?].

2.4 Active-Sterile Oscillations

In Sec. 1.5.2, we have discussed how neutrino oscillation occurs in the three-flavor scenario of the Standard Model. However, to explain the aforementioned anomalies observed in various experiments, we need to extend our model. The simplest extension of such a model is to add a new neutrino state (3+1 model). Adding a new flavor and mass eigenstate will also increase the dimensionality of the PMNS matrix from 3 to 4, thereby introducing additional parameters. The flavor and mass eigenstates are related in the same way as the three-flavor case

$$|\nu_l\rangle = U_{4\times 4}|\nu_i\rangle \tag{2.4}$$

where l corresponds to the neutrino flavor (e, μ, τ, s) and i to the mass eigenstates (1,2,3,4). While the addition of this single neutrino does not describe the global data well, this model has become a standard way to compare data across experiments, assuming that new physics takes the form of modifications to the oscillation probability that go as a function of L/E_ν. The 4×4 PMNS matrix can be parameterized as $U = R_{34}S_{24}S_{14}R_{23}S_{13}R_{12}$, where R_{ij} represents the rotation through mixing angle θ_{ij} and S_{ij} represents the complex rotation through θ_{ij} and phase δ_{ij}. This introduces several new oscillation parameters: one mass-squared splitting, Δm^2_{41}, three mixing angles, θ_{14}, θ_{24}, and θ_{34}, and two CP violating phases, δ_{14} and δ_{24}. Considering the above parameterization, the extended form of the PMNS matrix can be written as:

$$U = \begin{pmatrix} U_{e1} & U_{e2} & e^{-i\delta_{13}} s_{13} c_{14} & e^{-\delta_{14}} s_{14} \\ U_{\mu 1} & U_{\mu 2} & -e^{-i(\delta_{13}-\delta_{14}+\delta_{24})} s_{13} s_{14} s_{24} + c_{13} s_{23} c_{24} & e^{-i\delta_{24}} c_{14} s_{24} \\ U_{\tau 1} & U_{\tau 2} & -e^{i\delta_{24}} c_{13} s_{23} s_{24} s_{34} + c_{13} c_{23} c_{34} - e^{-i(\delta_{13}-\delta_{14})} s_{13} s_{14} c_{24} s_{34} & c_{14} c_{24} s_{34} \\ U_{s1} & U_{s2} & -e^{i\delta_{24}} c_{13} s_{23} s_{24} c_{34} - c_{13} c_{23} s_{34} - e^{-i(\delta_{13}-\delta_{14})} s_{13} s_{14} c_{24} c_{34} & c_{14} c_{24} c_{34} \end{pmatrix} \tag{2.5}$$

Furthermore, using the unitary property of PMNS matrix which suggest that $\Sigma_{k=1}^{4} U_{ak} U_{bk}^{*} = \delta_{ab}$, the elements of this matrix can be written in terms of mixing angles and phases with shorthand notations of $\cos\theta_{ij} = c_{ij}$ and $\sin\theta_{ij} = s_{ij}$. The general expression for oscillation probability is given as:

$$\begin{aligned} P(\nu_\alpha \to \nu_\beta) = P_{\alpha\beta} = \delta_{\alpha\beta} &+ 2 \sum_{i(>j)} \sum_{j} \mathrm{Im}\left[U_{\beta j}^{*} U_{\beta j} U_{\alpha i}^{*} U_{\alpha j} \sin\left(\frac{\Delta m_{ij}^2 L}{2E}\right)\right] \\ &- 4 \sum_{i(>j)} \sum_{j} \mathrm{Re}\left[U_{\beta j}^{*} U_{\beta j} U_{\alpha i}^{*} U_{\alpha j} \sin\left(\frac{\Delta m_{ij}^2 L}{4E}\right)\right] \end{aligned} \tag{2.6}$$

While the exact matrix and probabilities calculation are performed by the PMNS_Sterile class, which describes the implementation of oscillations of neutrinos in matter in a n-neutrino framework, it is useful to have some approximation of the 4F sterile neutrino appearance probability to understand which parameters are important. The derivation of the probability expressions in this thesis assumes $\Delta_{21} = 0$, which further implies $\Delta_{31} = \Delta_{32}$ and $\Delta_{41} = \Delta_{42}$. A validation study of this approximation has been explicitly performed [52]. Furthermore, δ_{14} primarily come into play for ν_e appearance case, so it's not expected to affect ν_μ and NC disappearance at the first order.

NOvA is sensitive to probe the oscillations over the mass-squared splitting range 10^{-3} eV$^2 \leq \Delta m^2_{41} \leq 100$ eV^2. Above $\Delta m^2_{41} = 100$ eV^2, oscillations become very rapid and cannot be resolved, leading to an overall normalisation effect in both the near and far detectors, which is difficult to distinguish from our normalisation uncertainties. At the opposite extreme, which is below $\Delta m^2_{41} = 10^{-3}$ eV^2, the sterile-driven oscillations develop so slowly to produce an observable effect, even at the long baseline of the FD. For $\Delta m^2_{41} \gtrapprox 0.5$ eV^2, oscillations begin to develop over the 1 km between the NuMI target and the NOvA ND, resulting in characteristic spectral distortions in the near-detector energy spectrum. NOvA experiment is well positioned to probe the parameter space where several short-baseline anomalies have been reported, notably around $\Delta m^2_{41} \sim$1eV^2.

NOvA's dual-baseline sterile neutrino search investigates the existence of sterile neutrinos under a 3+1 model using both the ν_μ and **N**eutral **C**urrent (NC) disappearance channels. On one hand, the NC channel provides a very clean probe of active-sterile mixing due to its flavor independence. On the other hand, any additional ν_μ disappearance beyond the expected three-flavour prediction can also be manifested as sterile neutrino oscillations.

Under the 3+1 framework, we can approximate the NC disap-

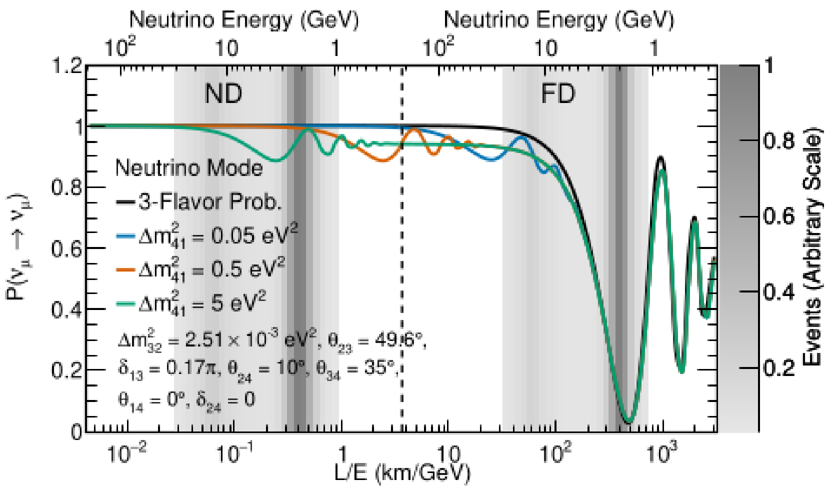

Figure 2.5: Oscillogram showing the oscillation probablity for ν_μ disappearance for 3F oscillations without sterile neutrinos (black), and with sterile neutrinos with $\Delta m^2_{41} = 0.05$ eV^2 (blue), $\Delta m^2_{41} = 0.5$ eV^2 (orange) and $\Delta m^2_{41} = 5$ eV^2 (green). The other sterile oscillation parameters are shown in the image.

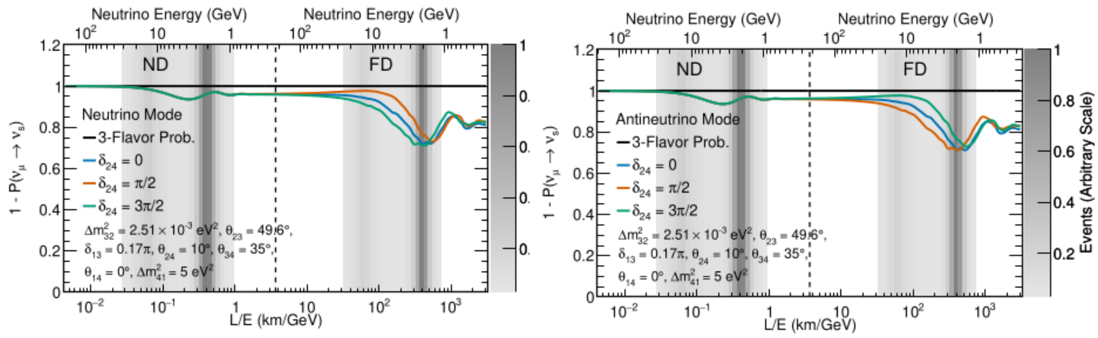

Figure 2.6: Oscillograms showing the oscillation probability for NC survival probability under a 3+1 model for neutrinos (left) and antineutrinos (right), for different values of δ_{24}. The effect of δ_{24} has an opposite effect for neutrinos and antineutrinos, with $\delta_{24} \sim \pi/2$ leading to smaller amounts of disappearance compared to $\delta_{24} \sim 3\pi/2$ for neutrinos, and the opposite being the case for antineutrinos.

pearance probability as:

$$\begin{aligned} 1 - P(\nu_\mu \to \nu_s) \approx 1 &- \cos^4\theta_{14}\cos^2\theta_{34}\sin^2 2\theta_{24}\sin^2\Delta_{41} \\ &- \sin^2\theta_{34}\sin^2\theta_{23}\sin^2\Delta_{31} \\ &\pm \frac{1}{2}\sin\delta_{24}\sin\theta_{24}\sin 2\theta_{23}\sin\Delta_{31}. \end{aligned} \tag{2.7}$$

where the $\pm$ is for neutrinos and antineutrinos. The ν_μ disappearance probability under 3+1 approximation is determined as:

$$\begin{aligned} P(\nu_\mu \to \nu_\mu) \approx 1 &- \sin^2 2\theta_{23} \sin^2 \Delta_{31} \\ &+ 2 \sin^2 2\theta_{23} \sin^2 \theta_{24} \sin^2 \Delta_{31} \\ &- \sin^2 2\theta_{24} \sin^2 \Delta_{41}. \end{aligned} \tag{2.8}$$

The ν_μ CC disappearance sample is sensitive to the sterile oscillations only driven by θ_{24} and Δm^2_{41}, and is particularly insensitive to θ_{14}, θ_{34} and δ_{24}. The NC disappearance sample, on the other hand, gives us access to θ_{14}, θ_{24}, θ_{34}, δ_{24}, and Δm^2_{41}. Because the first term in Eq. (2.7) contains a $\sin^2 2\theta_{24}$, our sensitivity to θ_{34} in the ND NC sample is limited (because we can always make θ_{24} small to turn off sterile oscillations), meaning that sensitivity to θ_{34} primarily comes from the second term, which oscillates at the atmospheric frequency. From this, we understand that our sensitivity to θ_{34} is driven primarily by the FD NC sample.

The inclusion of the RHC data for this analysis gives us an additional constraint on the value of δ_{24}, since there are opposite signs for the last term in the Eq. (2.7), the approximate NC disappearance equation, and as shown in Fig. 2.6. This parameter does not affect oscillations in the ND or in the ν_μ samples. The RHC data sample and period 11-14 of the FHC data sample will reduce statistical uncertainty in the FD relative to the previous analysis, thereby improving our limit at low values of Δm^2_{41}, which is currently dominated by FD data.

2.5 Summary

This chapter has presented a comprehensive overview of sterile neutrinos, beginning with their theoretical motivation. We have also discussed some experimental methods for probing sterile neutrinos and reviewed some experimental hints, including anomalous results from various experiments such as LSND, MiniBooNE, and the Reactor Anomaly. Finally, we presented the theoretical framework of sterile neutrino phenomenology required for this analysis in the NOvA experiment.

Chapter 3

NOvA Experiment

"With the advancement of accelerator technology, we can now produce intense neutrino beams, allowing us to explore the nature of neutrinos in unprecedented detail."

Takaaki Kajita

Introduction

Since the first experimental detection of neutrinos in 1956 by Clyde Cowan and Frederick Reines using a nuclear reactor, the field of neutrino physics has advanced significantly. Developing new detector technologies and neutrino sources has enabled scientists to study neutrinos across a range of energy scales and for various physics goals. All experiments share the common goal of studying neutrino oscillations despite the differences in their setups and analysis techniques, which provide insights into CP violation in the leptonic sector. In this chapter, a detailed overview of the NOvA experiment will be presented in Sec. 3.1 that includes the neutrino beamline (Sec. 3.2) and the detectors (Sec. 3.3).

3.1 NOvA Experiment

NOvA (NuMI Off-axis ν_e Appearance) is a long-baseline neutrino experimental setup at **F**ermi **N**ational **A**ccelerator **L**aboratory (**FNAL** or Fermilab) in the United States [53]. The experiment uses the **NuMI** (**N**eutrinos at the **M**ain **I**njector) beam and two detectors positioned off-axis to the neutrino beam with the primary goal of investigating the oscillation of muon neutrinos into electron neutrinos at a distant detector (Fig. 3.1).

3.1.1 Research Goals of NOvA

1. $\nu_\mu \to \nu_e$ **Oscillation**: The MINOS experiment is the first-generation long-baseline neutrino experiment [54], primarily aimed to study the ν_μ disappearance at Fermilab. NOvA is designed as the successor of MINOS, focusing on ν_e appearance in addition to the ν_μ disappearance. NOvA aims to observe $\nu_\mu(\bar{\nu}_\mu) \to \nu_e(\bar{\nu}_e)$ oscillations and the precise measurements of the oscillation parameters.

2. **Neutrino Mass Hierarchy**: The oscillation experiments measure neutrino oscillations in terms of mass-squared differences rather than absolute masses. NOvA aims to determine the neutrino mass hierarchy, as discussed in Sec. 1.5.3. The FD is placed 810km from the neutrino source, allowing neutrinos

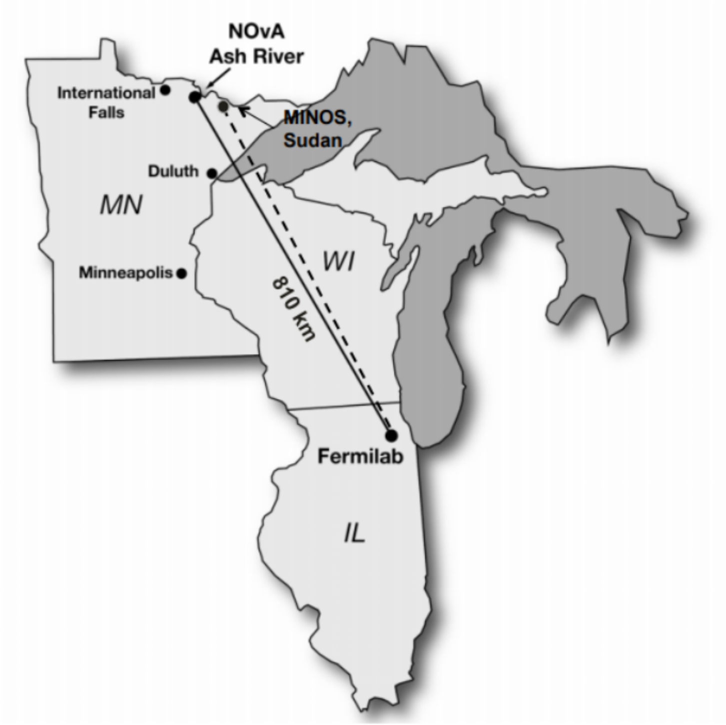

Figure 3.1: Schematic representation of the NOvA's baseline. The neutrino source and the near detector (ND) are based at Fermilab, Illinois, while the far detector (FD) is placed 810 Km away at Ash River, Minnesota.

to travel through the Earth, where the oscillations get modified by the matter effects due to the $\nu - e$ coherent forward scattering. NOvA exploits the difference in oscillation probabilities of $\nu_\mu \to \nu_e$ and $\bar{\nu}_\mu \to \bar{\nu}_e$ to shed light on this mass ordering.

3. **Matter-Antimatter Asymmetry**: Neutrino oscillations exhibit differences between neutrinos and antineutrinos, which can reveal CP violation and the ordering of neutrino masses. This asymmetry is crucial for addressing the matter-antimatter imbalance observed in the universe. Different oscillation channels are sensisitve to different oscillation parameters such as $\nu_\mu(\bar{\nu}_\mu)$ disappearance channel, on one hand, is primarily sensi-

tive to the atmospheric oscillation parameters Δm^2_{32} and $\sin^2\theta_{23}$. On the other hand, the $\nu_e(\bar{\nu}_e)$ appearance channel is sensitive to the CP-violating phase δ_{CP}. NOvA aims to investigate the matter-antimatter asymmetry through the CP-violating phase term.

With the new advanced analysis techniques and broader physics program, NOvA is not limited to the standard three-flavor oscillation analyses. The collaboration is also pursuing various new analyses, including sterile neutrino searches, magnetic monopole searches, dark matter searches, neutrino-nucleus cross-section analyses, and many more.

3.2 NuMI Beam

3.2.1 Fermilab Accelerator Complex

The **Fermilab Accelerator Complex** is one of the world's most advanced particle accelerator facilities, located at the **F**ermi **N**ational **A**ccelerator **L**aboratory (Fermilab or FNAL) in Batavia, Illinois. The accelerator complex provides high-energy particle beams for experiments like NOvA, Mu2e, MicroBooNE, and others. The key components of the complex are listed below.

1. **Linac (Linear Accelerator)**: The first acceleration stage is Linac, which accelerates the protons generated from H^- ions to an energy of about 400 MeV (million electron volts), making them intense enough for further acceleration.

2. **Booster**: The high-intensity proton beam from Linac is sent to the Booster, which is the circular accelerator that increases the protons' energy from 400 MeV to 8 GeV. The Booster is a crucial component of Fermilab's complex in supplying the high-energy protons for subsequent stages and various experiments.

3. **Recycler**: The Recycler is a storage ring essential to Fermilab's upgrade to support high-intensity neutrino experiments. It accumulates protons from the Booster and prepares them for further acceleration by the Main Injector.

4. **Main Injector**: The Main Injector (**MI**) accelerates protons (or antiprotons) from 8 GeV to 120 GeV [55, 56]. These high-energy protons are crucial for producing high-energy neutrino beams, which are used for various Fermilab experiments, such as NOvA, MINOS, and MicroBooNE. The Main Injector can accelerate beams to even higher energies, depending on the experiment.

3.2.2 NuMI Beamline

The **N**eutrinos at the **M**ain **I**njector (**NuMI**) beamline [57] at Fermilab was initially constructed to generate neutrinos for the MINOS experiment [58], which aimed to study long-baseline neutrino oscillations. Over time, the NuMI beam has been utilised for several other Fermilab-based experiments, including NOvA [56], MINERvA [59], and others.

The MI was initially designed for a beam power of 400 kW and

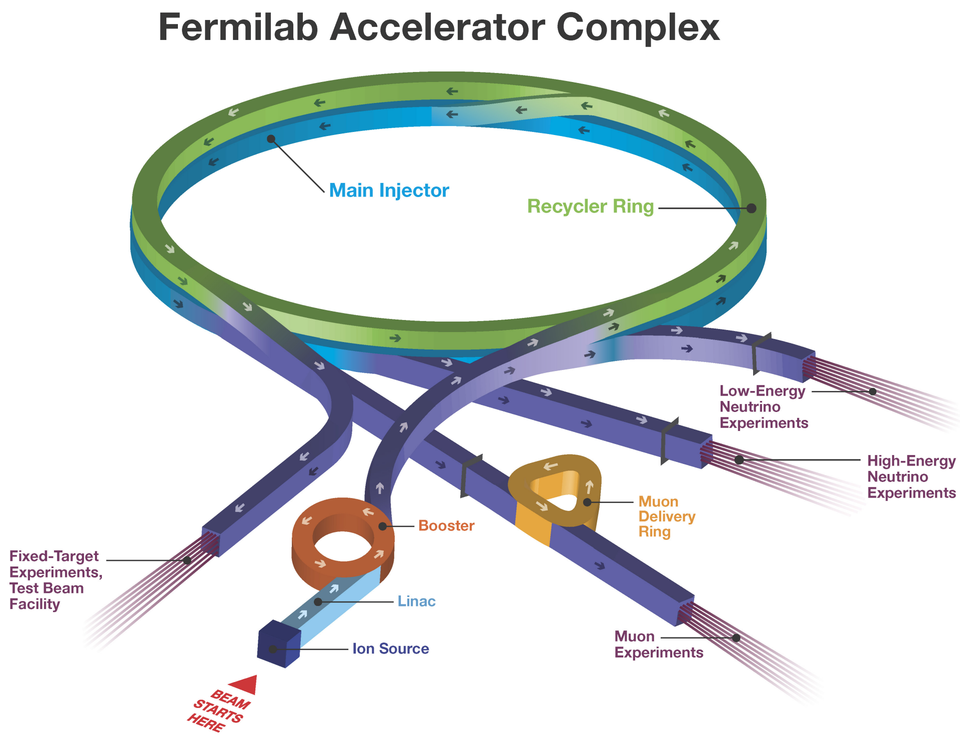

Figure 3.2: Schematic diagram of the Fermilab Accelerator Complex. The beam is followed to the Linac, Booster and main injector from the ion source. The neutrino beam is transferred to various experiments.

is upgraded so that the proton beam achieves an average power of 800 kW or higher, corresponding to approximately $5{\times}10^{13}$ protons delivered in a 10 μs spill window, repeated at an average interval of 1.1 seconds. This is further directed to the NuMI beamline. In June 2024, the NuMI beamline achieved a significant milestone by operating at 1.011 MW for a continuous hour.

Protons (or H^- ions) are accelerated to around 120 GeV in Fermilab's Main Injector and directed onto a narrow graphite target ($\rho = 1.68 g/cm^3$), about 1.25 meters long, through a collimating baffle [60]. The collision produces various hadrons, primarily pions ($\pi^{\pm}$) and kaons ($K^{\pm}$), which are then focused forward and sorted by charge using two toroidal magnetic horns (Fig. 3.3). The magnetic horns can be configured to focus either positive or negative mesons, depending on the direction of the current flow. These two modes, referred to as Forward Horn Current (FHC) and Reverse Horn Current (RHC), focus on the positively charged mesons and the negatively charged mesons, respectively. These forward-focused mesons decay in a 675 m long decay tunnel to produce respective $\nu_\mu/\bar{\nu}_\mu$ beams. The decay pipe is filled with helium gas to maximise the interaction length and provide a reasonable time for the charged mesons to decay. This avoids the interaction of mesons with the air. A small fraction of ν_e contamination intrinsic to the beam comes from the tertiary $\mu^{\pm}$ decays and the kaon decay. Furthermore, the charged mesons passing through the centre of the horns do not get focused, resulting in the "wrong-sign" neutrinos ($\bar{\nu}_\mu$ in ν and vice versa) in the beam.

Tab. 3.1 outlines the decay processes of pions and kaons for a ν_μ beam. The resulting neutrino beam typically consists of approximately 96.3 % ν_μ, 2.7 % $\bar{\nu}_\mu$ and 1.1 % $\nu_e + \bar{\nu}_e$ (Fig. 3.4). To ensure a muon neutrino or antineutrino-enriched beam, muons produced through pion decay are stopped using a rock shield, preventing further decay into electrons. Additionally, the absorber stops the primary beam protons (those that did not interact with the NuMI target), electrons, neutrons, and γ rays produced from the beam and target collision.

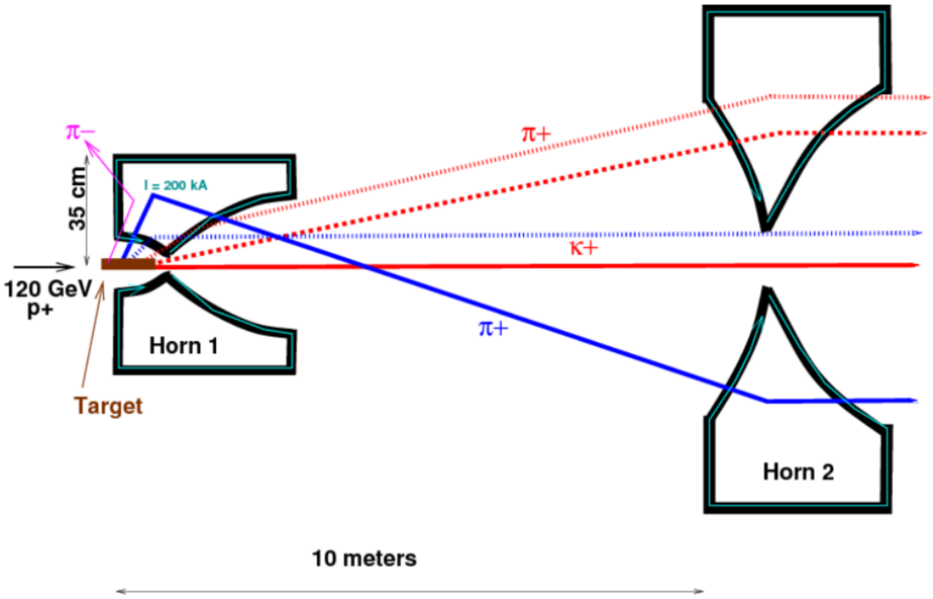

Figure 3.3: Schematic diagram of magnetic horns used for the NuMI beam to focus the produced hadrons. An example of positively charged hadrons produced by collision and focused by horn one and horn two, being used for trajectory corrections.

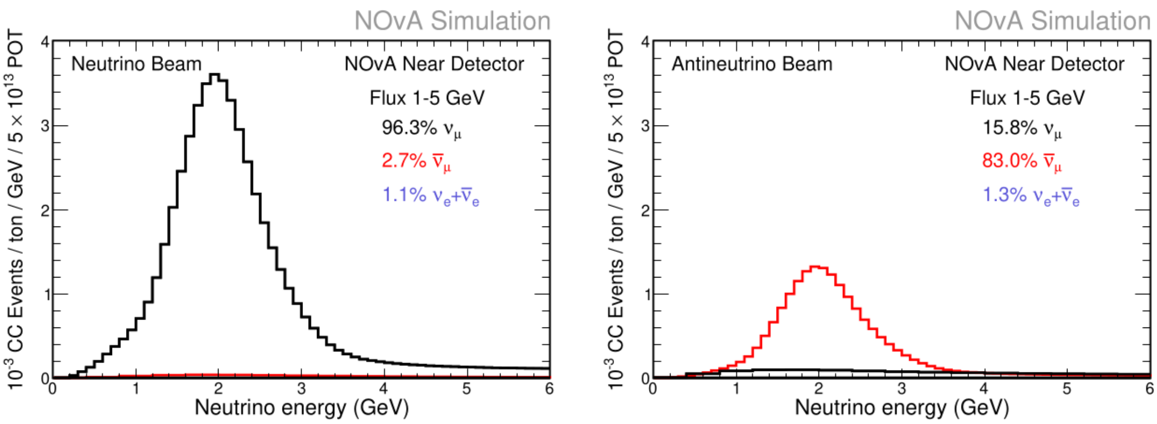

Figure 3.4: Distributions showing the MC CC neutrino events at the NOvA near detector in neutrino (FHC) on the left and antineutrino (RHC) mode on the right.

A diagram illustrating the process of generating a muon neutrino beam is shown in Fig. 3.5.

Decay Mode	Branching Ratio
$K^+ \rightarrow \mu^+\nu_\mu$	63.6
$K^+ \rightarrow \pi^+\pi^0$	20.6
$K^+ \rightarrow \pi^+\pi^+\pi^-$	5.59
$K^+ \rightarrow \pi^+\pi^0\pi^0$	1.76
$K^+ \rightarrow \pi^0e^+\nu_e$	5.07
$K^+ \rightarrow \pi^0\mu^+\nu_\mu$	3.35
$\pi^+ \rightarrow \mu^+\nu_\mu$	99.9
$\pi^+ \rightarrow e^+\nu_e$	.01
$\pi^+ \rightarrow \pi^0e^+\nu_e$	0.000001
$\mu^+ \rightarrow e^+\nu_e\bar{\nu}_\mu$	100

Table 3.1: Decay modes of π^+ and K^+ to produce ν_μ beam

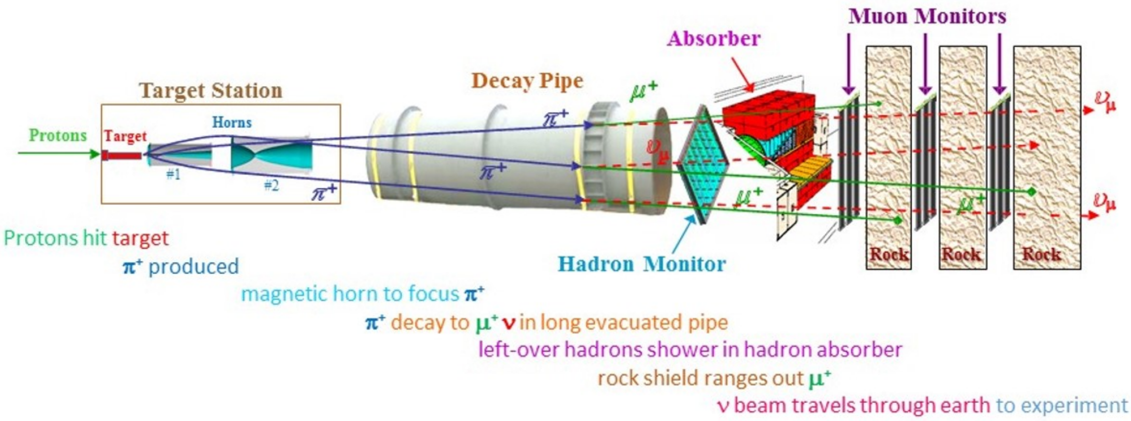

Figure 3.5: A schematic representation of the NuMI beamline [56].

3.3 NOvA Detectors

NOvA uses two functionally identical detectors: a Near Detector (ND) located 1 km from the neutrino source and a Far Detector (FD) situated 810 km away. These detectors are placed in an off-axis configuration to optimise the best detected ν_e at the far detector. The hadronic decays generate the mono-energetic daughter neutrinos. The energy (E_ν) and flux (F) of these mono-energetic neutrinos depend on the angle (θ) between the pions ($\pi^{\pm}$) and the neutrino trajectories. The neutrino energy and flux, observed at a detector of area A, located at a distance L, and produced from hadron decay of energy E_h, is given by [61]:

$$F = \left(\frac{2\gamma}{1+\gamma^2\theta^2}\right)^2 \frac{A}{4\pi L^2} \tag{3.1}$$

$$E_\nu = \frac{E_h}{1+\gamma^2\theta^2}\left(1 - \frac{m_\mu^2}{m_h^2}\right) \tag{3.2}$$

The detectors are positioned approximately 14.6 mrad off-axis from the NuMI beam direction to ensure that they receive an intense beam with energy peaks at 2 GeV. This energy is approximately equal to 1.6 GeV, close to the first oscillation maximum energy for $\nu_\mu \rightarrow \nu_e$ oscillation probability for a baseline of 810 km. Fig. 3.6 and Fig. 3.7 show the MC neutrino flux, energy, and number of CC events at the NOvA FD for the different off-axis configurations [62].

NOvA detectors (Fig. 3.8a) are liquid scintillator calorimeters with sets of PVC plastic cells arranged perpendicularly. The length of each cell is 4m for the near detector (ND) and 15.5m for the far detector (FD), which spans the entire detector. The rectangular structure of each cell is shown in the Fig. 3.8b with a cross-section of 3.9×5.9 cm^2. One unit is formed by glueing 16 PVC cells, and two units are stuck together to create a module. These modules, each with 32 cells, are glued side by side to create a layer of cells known as the detector planes. The adjacent planes are mutually orthogonal, as seen in Fig. 3.9 for proper 3D reconstruction of tracks. Overall, 344,064 cells in FD and 18,342 in ND contain the active

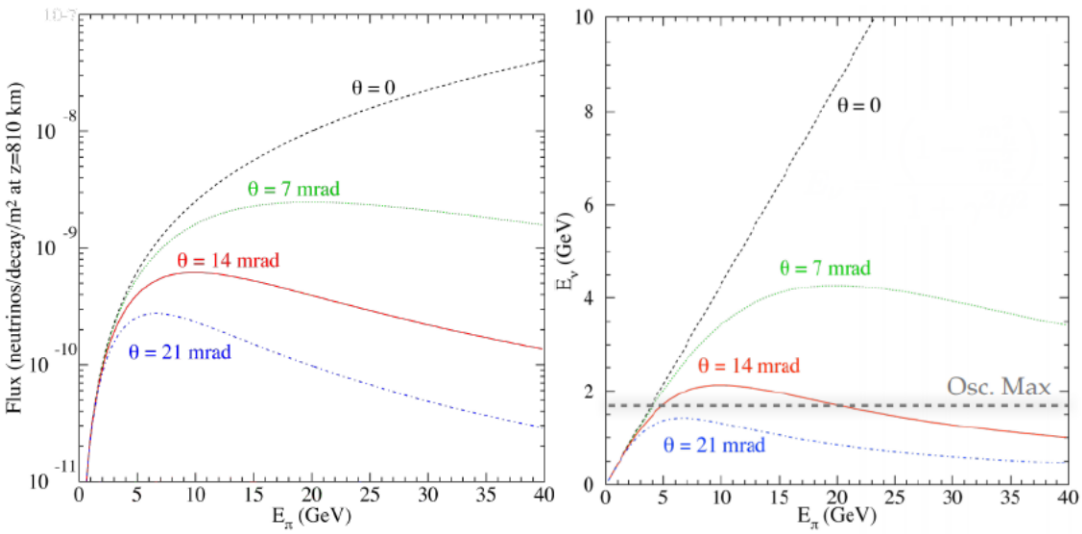

Figure 3.6: The neutrino flux as a function of pion energy corresponding to different angles (θ) on the left and the energy of daughter neutrinos produced at an angle θ with respect to the mother pion direction as a function of pion energy on the right.

detector material, accounting for approximately 65% of the total detector mass. Furthermore, the detectors utilise pseudocumene as a scintillating material to generate photons after interaction. The UV range (270-320 nm) photons are produced during the interactions, which are then converted to the visible range using two **W**avelength **S**hifting **F**ibre (WLS). Tab. 3.2 lists the full composition of the active detector material.

3.3.1 Near Detector

The Near Detector or ND (Fig. 3.10) is nearly 1 km from the neutrino source and about 105 m beneath the surface. It is 15.9 m long, consisting of a fully active region (12.9 m long) and a partially active muon catcher region (3.1 m) in the beam direction. The fully active region measures the neutrino-nucleus interaction,

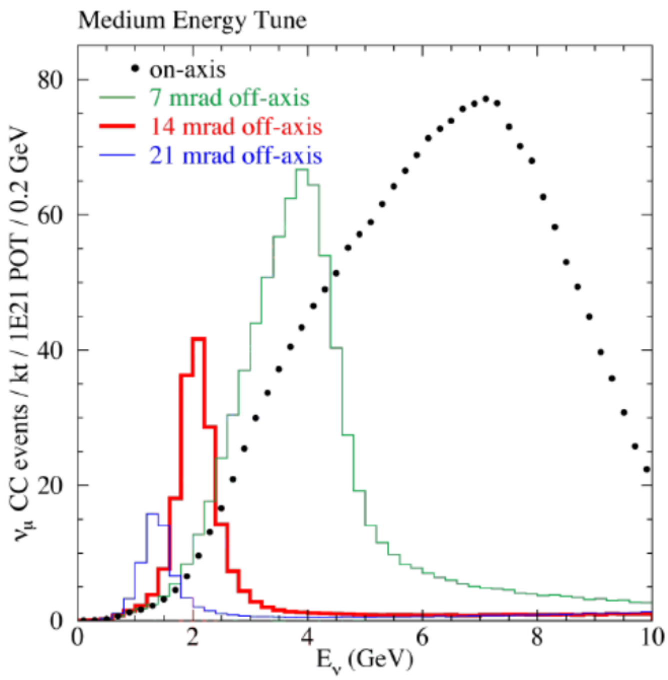

Figure 3.7: Simulated energy spectra of NOvA Far Detector

Component	Purpose	Mass Fraction(%)	Mass(Kg)
Mineral Oil	Solvent	94.63	7,658,656
Pseudocumene	Scintillant	5.23	423,278
PPO	waveshifter	0.14	11,331
bis-MSB	waveshifter	0.0016	129
Stadis-425	antistatic	0.001	81
Vitamin E	antioxidant	0.001	78

Table 3.2: Table showing the composition of the liquid scintillator used in the NOvA cell. The purpose, mass fraction in %, and mass in kg of each component is shown together [63].

while the muon catcher captures the muons leaving the active region. ND contains about 192 planes with dimensions 4.1×4.1×12.8 m^3 in the form of 8 blocks, with each block containing 24 planes. The 192 planes are organised into three blocks of 64 planes each. The neutrino beam passes through the fully active region, where

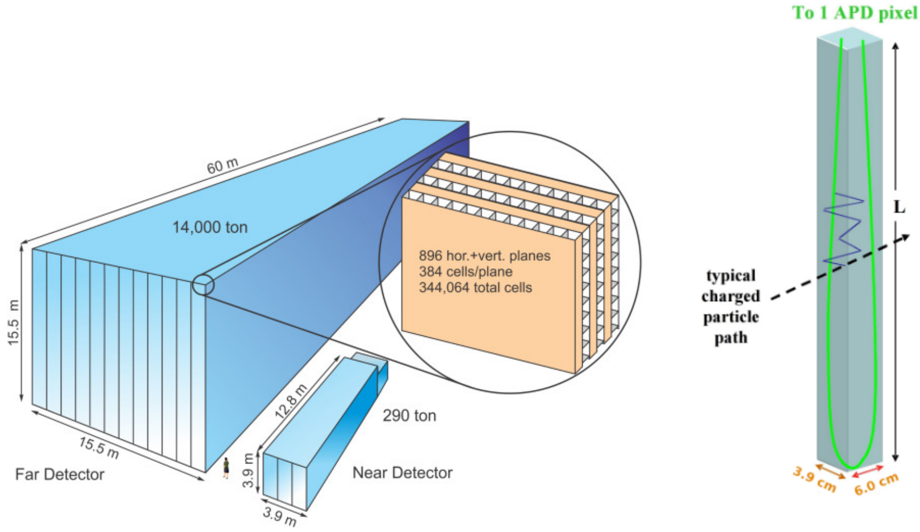

(a) (b)

Figure 3.8: Figure (a) showing the NOvA near and far detector with a person standing showing the scale of the size of the detector, and (b) showing the internal structure of the basic unit Cell used in the detectors.

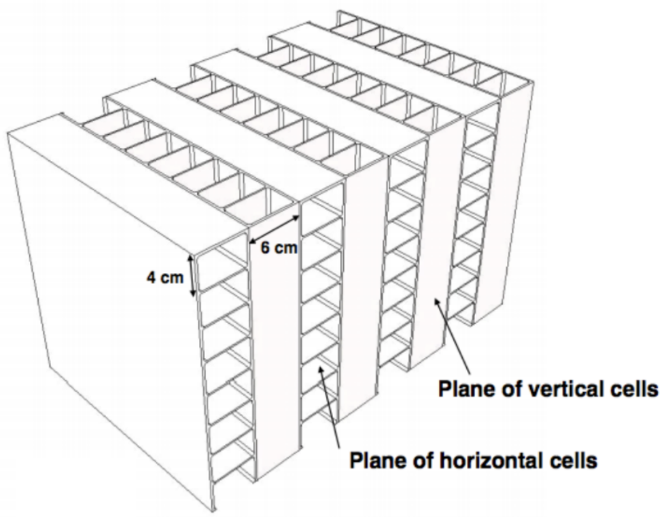

Figure 3.9: The detector planes consisting of the cells are shown connected orthogonal to each other.

it interacts, and then enters the muon catcher, where muon energy can be measured with high precision. The total mass of the ND is 300 tons, with 130 tons from the scintillator, 78 tons from the steel planes and the remaining 92 tons from PVC [61].

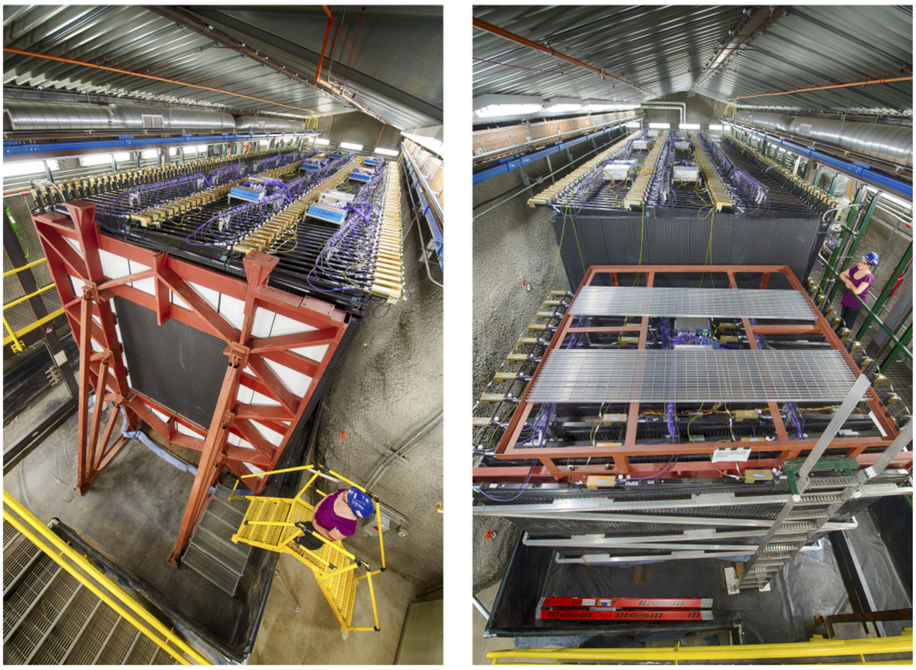

Figure 3.10: The NOvA's ND with an active region on the left and muon catcher on the right, with Dr Louise Suter present as a measure of the scale. (https://vms.fnal.gov/)

3.3.2 Far Detector

The Far Detector, or FD (Fig. 3.11), is functionally identical to the ND except it is much larger in size. It is located about 810 km from the source on the surface in Ash River, MN, USA. Since the FD is located on the surface, it is continuously exposed to the cosmic rays, posing a significant challenge for the event selection, especially for neutral current (NC) events. The FD receives the cosmic particles at a ∼130 kHz flux. Therefore, for Sterile Neutrino Analysis, which is NC-based, the cosmics contribute primarily to the background events. The FD consists of 14 blocks, each diblock consisting of 64 planes. The FD is covered in 4 feet of concrete and 6 feet of barite, shielding around 14 radiation lengths. Furthermore,

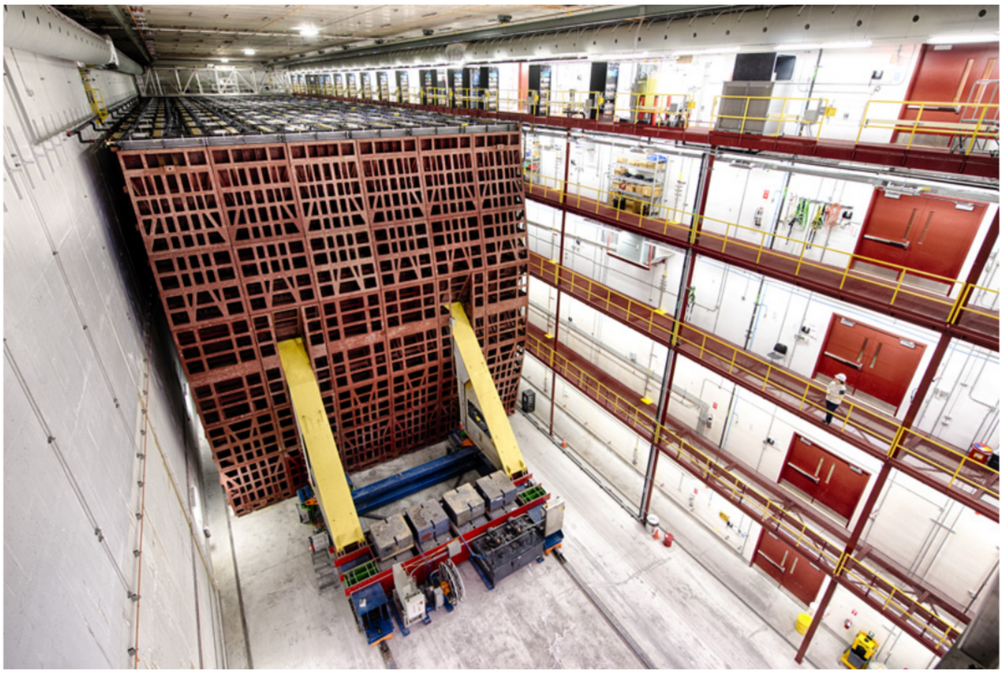

Figure 3.11: The NOvA's far detector. (https://vms.fnal.gov/)

loose graphite shot rocks are used on the sides as detector enclosure walls. The FD weighs around 14 kton, with scintillator consisting of ∼65% and the remaining 35% from PVC [61].

3.4 Interaction to Electronics

The two-detector setup offers the advantage of 3D reconstruction of particle tracks. Several secondary particles, including electrons, muons, or hadrons, are produced whenever a neutrino interacts inside the detector via a weak interaction. These particles propagate through the detector material and deposit their energies through ionisation or excitation of material molecules inside the detector. The energy transfer results in the excitation and subsequent de-excitation of scintillating material molecules, which produce visible to near-UV light. This light is further collected by thin flexible WLS fibres, which are then re-emitted at the end connected to APD with a longer wavelength. These APDs are the first step in converting light signals into electrical signals.

3.4.1 Avalanche Photodiodes

APDs are specialised semiconductor devices that detect highly sensitive but low light levels and convert them into electric signals. When a light signal from WLS reaches the surface of the APD, an electron-hole pair gets generated through the *photoelectric effect*. These electron (or holes) accelerates in the presence of a significant voltage (375 V) applied inside the APD. These accelerated electrons collide with nearby molecules, generating secondary electron-hole pairs through impact ionisation and therefore amplify the signal. These APDs need to operate at $\sim$ -15°C to minimise the noise from the thermally generated electron-hole pairs, making the APDs more sensitive to the scintillation light.

Furthermore, Thermoelectric Coolers (TECs) are also placed directly upon each APD to maintain the required temperature. These TECs absorb the heat produced during the process and remove it through the water circulating across all the TECs. Dry ice is constantly circulated through the APDs to avoid ice formation due to the condensation caused by these TECs.

3.4.2 NOvA DAQ System

Data **A**cquisation **S**ystem (**DAQ**) is responsible for recording the data available from the large number of APDs into a single stream of data for storage and analysis. The signal from the APD is sent to the front-end board (FEB), which is connected to the APDs. The signal is further amplified, multiplexed, digitised and time-stamped in the FEB. Each FEB consists of **A**pplication **S**pecific **I**ntegrated **C**ircuit (**ASIC**), **A**nalog-to-**D**digital **C**onverter (**ADC**), and **F**ield **P**rogrammable **G**ate **A**rray (**FPGA**). The signal is pre-amplified by the ASIC and passed on to the ADC to be digitised and multiplexed. This digitised and multiplexed signal is then fed into the FPGA responsible for time-stamping each signal.

The time-stamped and digitised data is then delivered to the **D**ata **C**oncentrator **M**odules (**DCMs**), which is further organised into small 50 μs time blocks (micro-slices). Each DCM has an "event-builder" that organises the data into 5-ms "millislices" out of 100 micro-slices and routes them to the buffer nodes. The data is temporarily (20-30 minutes) stored in the buffer node until a trigger decides whether to discard it or permanently save it. NOvA utilises clock-based and data-driven triggers, where the clock-based trigger obtains information about the NuMI beam, and the data-driven trigger examines the topologies in the data stream [64]. The clock-based trigger selects a time window for the NuMI beam spill when a beam spill occurs at Fermilab. This is particularly useful in removing the cosmic rays at the far detectors. The NuMI spill triggers the buffers to save 550 μs continuous data centred around the NuMI's 10 μs on the arrival of a NuMI beam spill every $\sim$1.3 s [65].

3.5 Summary

This chapter summarises the key components and objectives of the NOvA experiment, providing a detailed overview. We began outlining the primary physics goals of the experiment. We presented a detailed description of the Fermilab accelerator complex, which is used to produce high-energy particle beams for various physics experiments at Fermilab. Additionally, we presented the detailed design and operation of the NuMI beamline that delivers the neutrino beam to the NOvA experiment. We end this chapter by detailing the two detectors used for the neutrino oscillation analyses in the NOvA experiment. In the subsequent chapters, we will explain the analysis strategy and methodology used to determine sterile neutrino analysis results.

Chapter 4

NOvA Simulation and Reconstruction

"It's the memory of particles that detector records and we reconstruct."

4.1 Introduction

The simulation and reconstruction are the keys to the neutrino oscillation experiments. Neutrinos, being neutral and weakly interacting, are invisible to the detectors, and hence difficult to reconstruct. NOvA follows the simulation and reconstruction chains to identify the particles interacting inside the detector. However, before the data is used for the analysis, the proper validation should be done for both the simulation and the reconstruction chains. This chapter will discuss such a validation framework developed for the NOvA experiment at the hit level. The validation analysis modules themselves are split conceptually into simulation validation (running on data products which are *only* present in the simulation), reconstruction validation (running on data products which are present for both simulation and data).

4.2 Simulation

The purpose of simulation is to create a simulated analogue to the data extracted from our detector. In order to give us something that looks like the data, we must run through four stages including the event generation, particle propagation, energy deposition, and electronics modeling. The simulation validation modules cover all these data products which are only available for simulation Art files: generator MC truth, Geant4 particles and true energy depositions, and true photon signals incident on the APDs. The particle-level distributions in the generator and Geant4 steps break distributions down into individual particle types, neutrino interaction modes, etc. where appropriate.

4.2.1 GENIE Validation

NOvA's GENIE simulation models neutrino interactions using the NuMI beam flux, which in forward horn current (FHC) mode consists of primarily ν_μ, with some contamination from wrong-sign $\bar{\nu}_\mu$ and intrinsic ν_e, and a small amount of $\bar{\nu}_e$, as demonstrated in Fig. 4.1a. For reverse horn current (RHC), the same is true but with ν and $\bar{\nu}$ exchanged.

Neutrinos from the NuMI beam interacting in the NOvA detectors and their surroundings produce a neutrino energy spectrum in the few-GeV energy regime, spanning a range of interaction modes including quasielastic scattering (QE), resonant pion production (Res), deep inelastic scattering (DIS), coherent (Coh), coherent elastic, electron scattering, meson exchange currents (MEC) and diffractive events. Simple validation distributions including the neutrino sign and flavour, interaction mode and current, and the true energy of the neutrino and primary lepton are demonstrated in Fig. 4.1.

Beyond these simple interaction variables, plots are also produced of the true neutrino momentum (Fig. 4.2) and true neutrino interaction vertex within the detector (Fig. 4.3), as well as various kinematic variables such as q_0, q_3, W, x, y, and Q^2. q_0 and q_3 represent the energy and momentum transferred from the incoming lepton to the target nucleon. The invariant mass of the final-state hadronic system is given by $W^2 = (p + q)^2$, where p represents the initial four momentum of the nucleon. Q^2 which is basically negative of the four-momentum squared ($-q^2$) characterises the interaction scale of scattering process. The variable y, known as the inelasticity, is referred to as the amount of incoming lepton's energy transferred to the nucleon. At the same time, Bjorken (x) represents the nucleon's momentum carried away by the struck parton.

In the example nonswap near detector file (file using the nominal flux from the beam), interactions are dominated by charged current (Fig. 4.1c) through the QE, resonant, and DIS modes (Fig. 4.1b). From Fig. 4.1e, it is observed that the neutrino energy distribution peaks around 2 GeV, which should be expected because our detectors are in off-axis configuration and we expect a large neutrino flux around 2 GeV. In case our detectors were on-axis, then the distribution should peak around 7 GeV. In addition, since the interactions are charged current and mostly dominated by DIS, after the interaction most of the neutrino energy gets carried away with the corresponding leptons which are clearly understood from Fig. 4.1f distribution.

Since the z dimension corresponds to the direction of the beam, true neutrino momenta are strongly boosted in the z direction, as can be observed in Figs. 4.2a to 4.2d. The distribution of neutrino interaction vertices within the detector is shown in Figs. 4.3a to 4.3f

Furthermore, since we have confined our interactions within the geometry of our detector i.e. $-200-200$ cm in the x and y dimensions and $0-1000$ cm in the z dimension, we have observed that the distribution doesn't vary much and most of the interactions occur near the start of the detector instead of the very end (Fig. 4.3a). 2D distributions of vertex coordinates are also plotted which show the confined interaction vertices (Fig. 4.3b). For inelastic scattering, we know that the invariant mass W of the hadronic system depends on the 4-momentum of the virtual particle, which is also clear from the W distribution Fig. 4.4c. Furthermore, the elasticity of scattering (Bjorken x) is also in the range $0 \leq x \leq 1$ which should be as expected

$$x = \frac{Q^2}{Q^2 + W^2 - m^2} \tag{4.1}$$

$W^2 > m^2$ and $Q^2 > 0$, which implies that x should only be in the given range as also observed from Fig. 4.4d. In addition to this, the fractional energy lost by the incoming neutrino (expressed by y) has been observed to be in the range $0 \leq y \leq 1$ as expected (Fig. 4.4e). Furthermore, it is observed that neutrons pre-FSI (Fig. 4.5) are more, whereas for all other particles, it is less.

All GENIE truth distributions are provided as both inclusive plots across all simulated events and as a set of exclusive plots for event subcategories. Plots are provided for every neutrino flavour & sign combination, and then subdivided into charged or neutral currents within each of those, and then further subdivided by interaction mode.

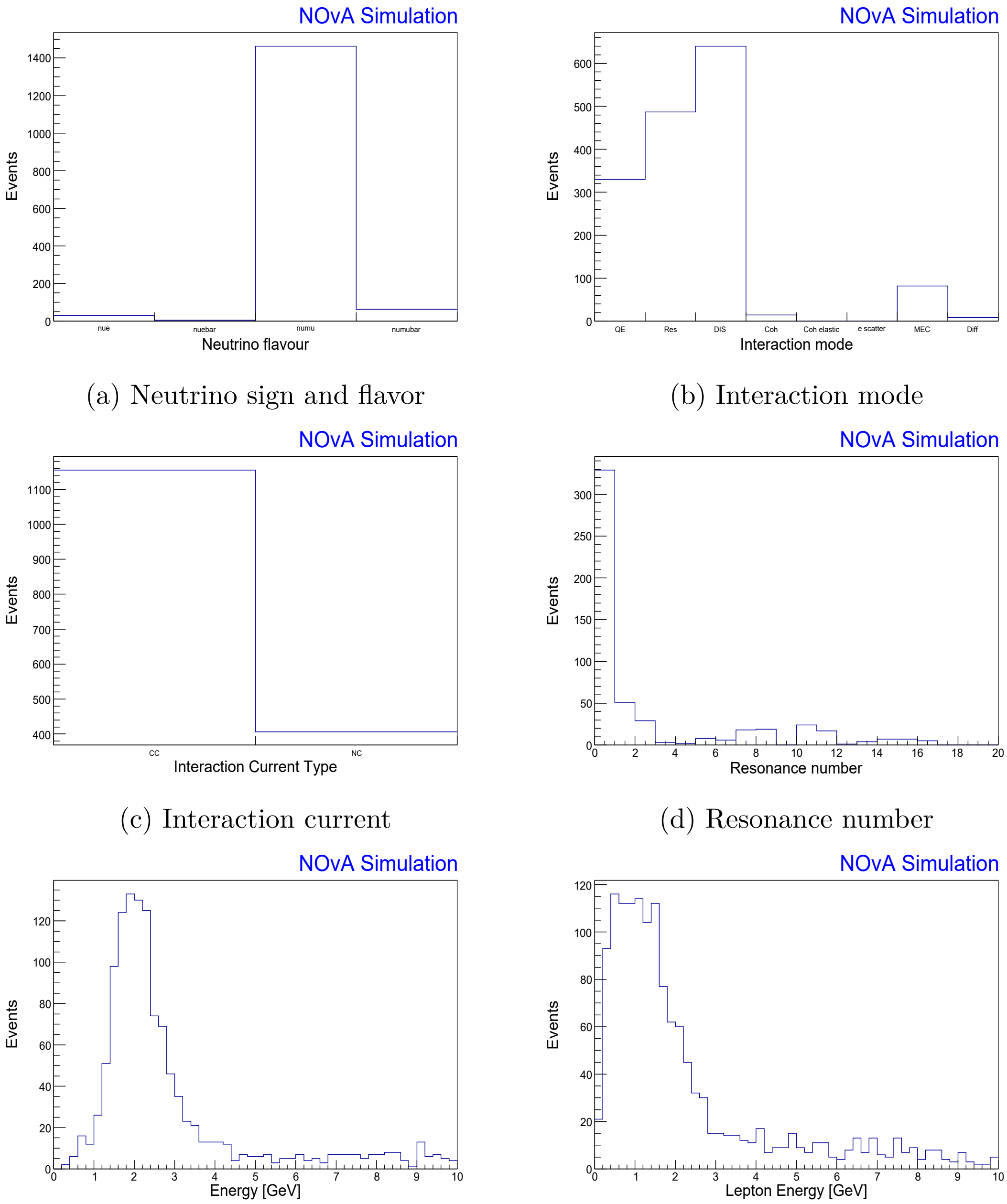

(a) Neutrino sign and flavor

(b) Interaction mode

(c) Interaction current

(d) Resonance number

(e) Neutrino energy

(f) Primary lepton energy

Figure 4.1: Distribution showing the basic interaction variables characterizing different events. These information comes directly from the GENIE modeling.

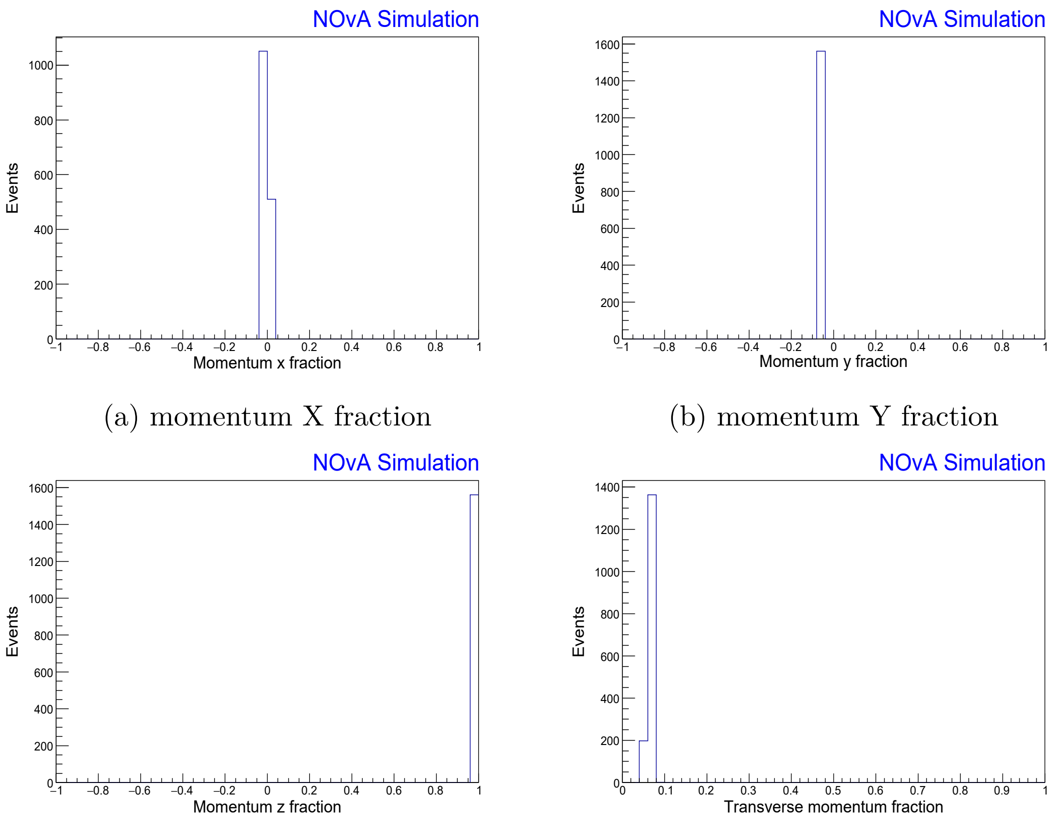

(a) momentum X fraction

(b) momentum Y fraction

(c) momentum Z fraction

(d) Transverse momentum fraction

Figure 4.2: x, y, z, and transverse GENIE momentum distribution

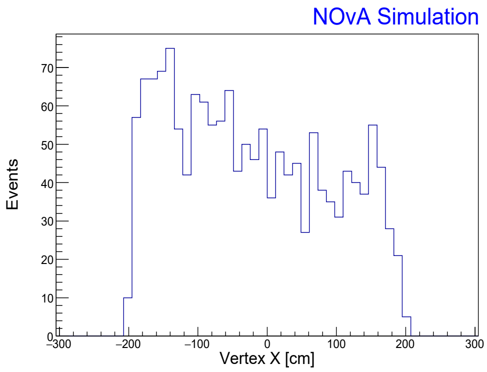

(a) Vertex X coordinate

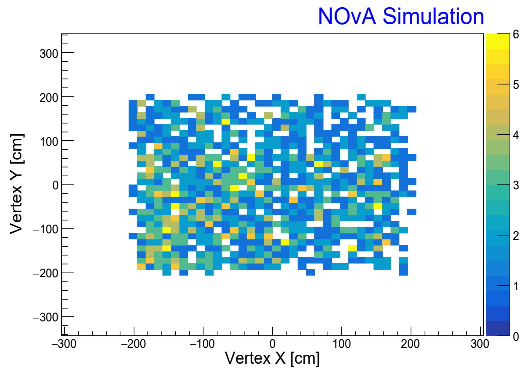

(b) Vertex X and Y coordinates

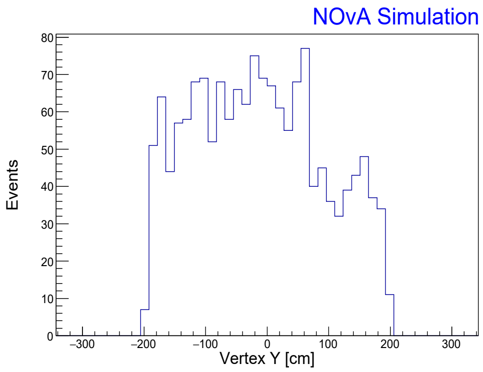

(c) Vertex Y coordinate

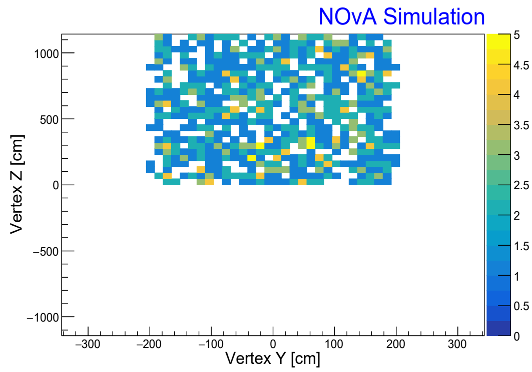

(d) Vertex Y and Z coordinates

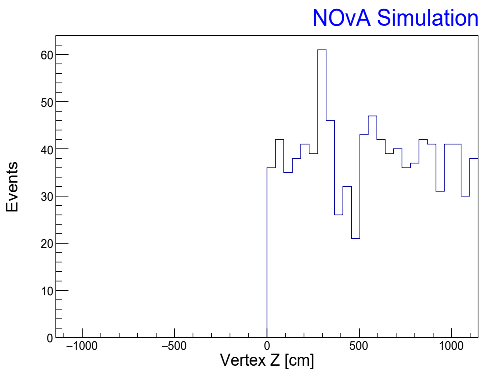

(e) Vertex Z coordinate

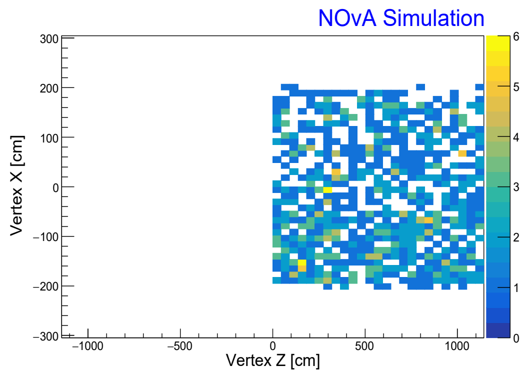

(f) Vertex X and Z coordinates

Figure 4.3: 1D vertex distribution showing the event distribution for the MC simulated particles and 2D vertex distributions showing the distribution of MC particles.

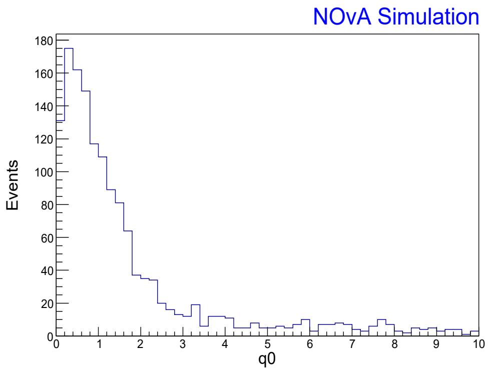

(a) Interaction q_0

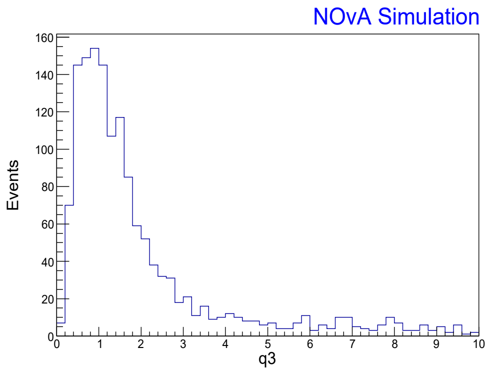

(b) Interaction q_3

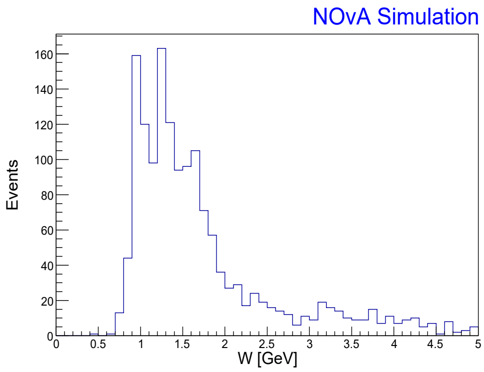

(c) Interaction W

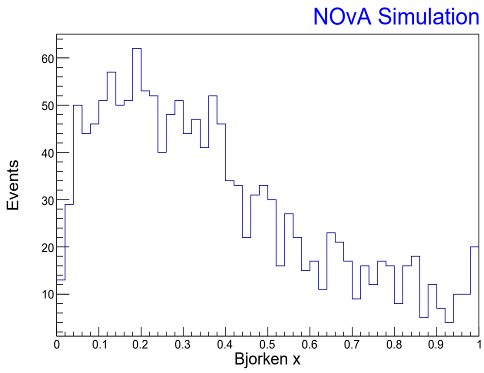

(d) Bjorken x

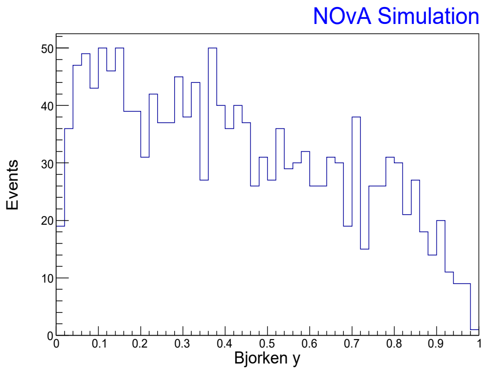

(e) Inelasticity

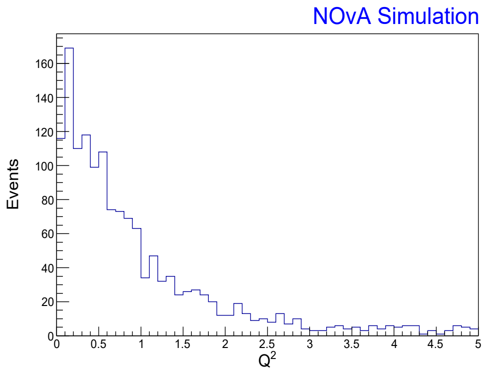

(f) Q^2

Figure 4.4: Distributions for different variables characterizing the kinematics of simulated MC events.

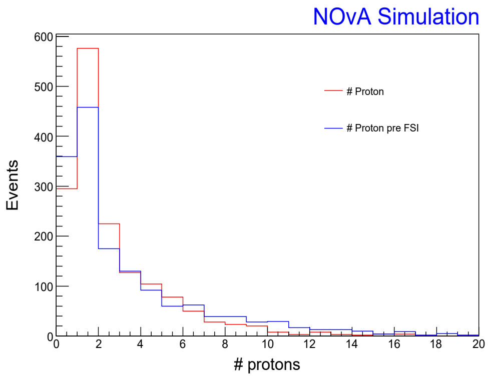

(a) Final state protons

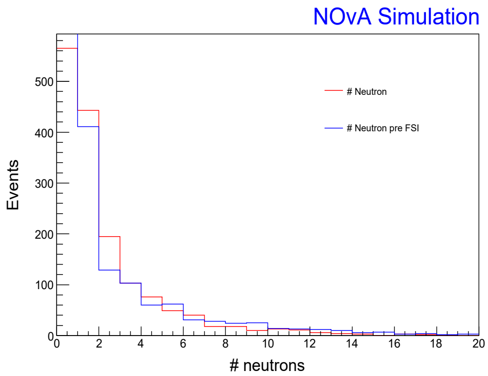

(b) Final state neutrons

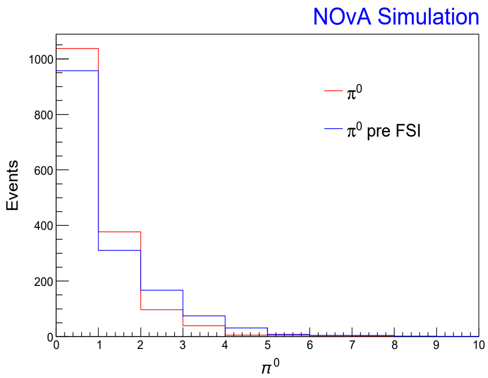

(c) Final state π^0s

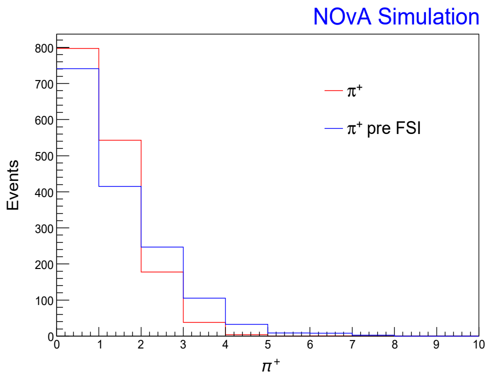

(d) Final state π^+s

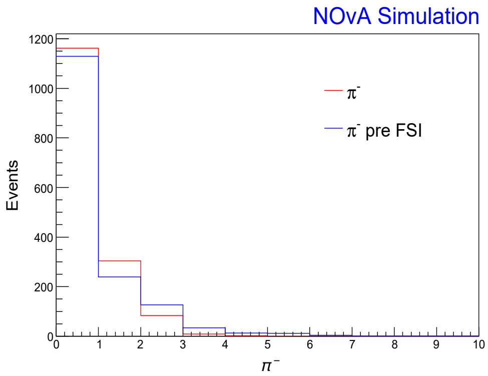

(e) Final state π^-s

Figure 4.5: GENIE distributions shown for different particles before and after the final state interactions.

4.2.2 Geant4 Validation

As discussed in Sec. 4.2.1, many simulated neutrino interactions are higher-energy deep inelastic scattering events, which produce a range of hadronic primary particles that propagate through the detector and reinteract. This module visualises the propagation of the MC truth particles simulated by Geant4. As with the GENIE validation module, simple distributions such as particle counts and energy (Fig. 4.6), vertex position (Fig. 4.7) and momentum (Figs. 4.8 to 4.11) are produced, both as inclusive plots across all particle types and separated out into exclusive plots for certain common particle types.

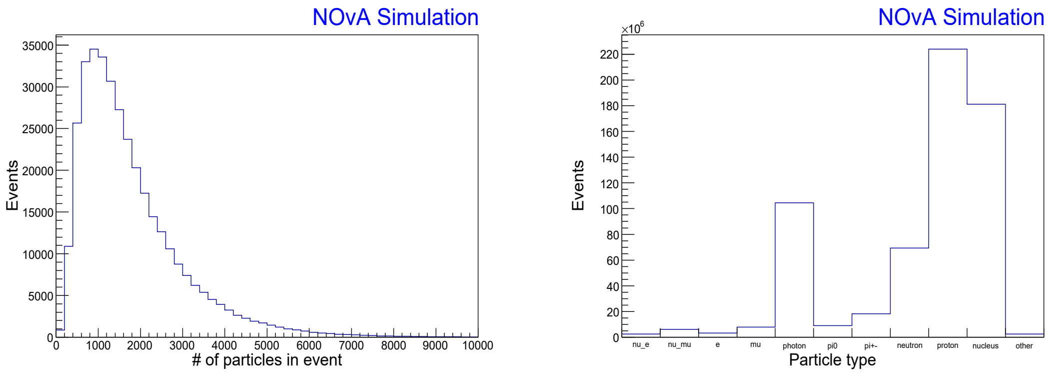

(a) Number of particles (b) Particle type counts

Figure 4.6: Distributions showing the particle number and different particles characterized through the GEANT4.

From the previous GENIE distributions, it is clear that most of the incoming neutrinos are strongly boosted in the positive z direction, and consequently the final state particles emerging from neutrino interactions will be similarly boosted, as demonstrated in Fig. 4.12. Correspondingly, the p_z component of Geant4 particles is enhanced in Fig. 4.11a compared to the x and y components in

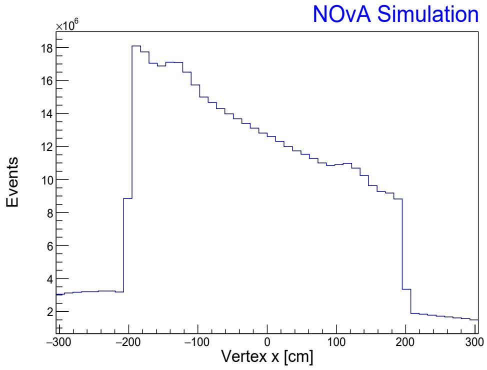

(a) Vertex X coordinate

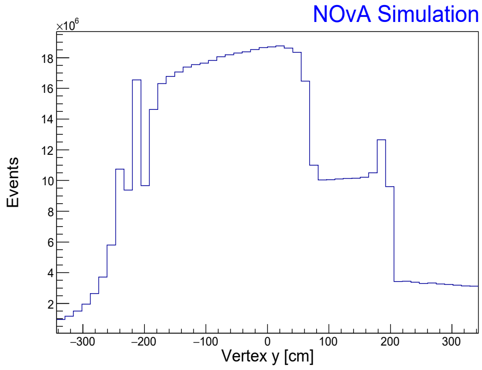

(b) Vertex Y coordinate

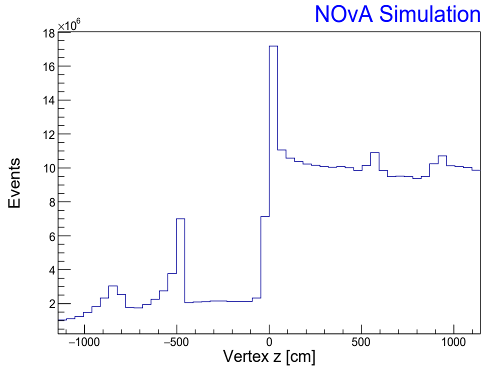

(c) Vertex Z coordinate

Figure 4.7: Vertex x, y, and z distribution for particles at the GEANT4 level.

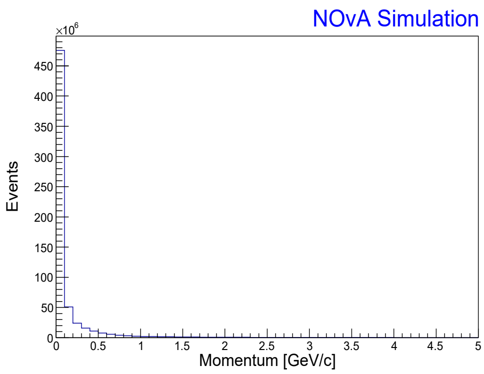

(a) Particle momentum

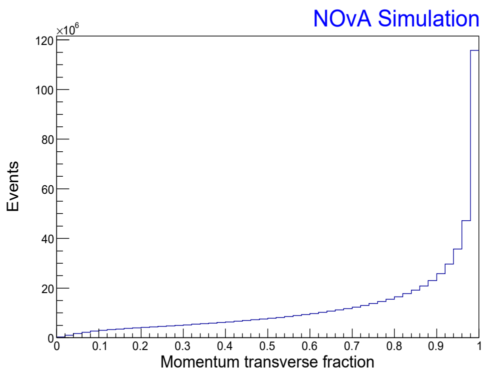

(b) Transverse momentum fraction

Figure 4.8: Total and transverse momentum fraction distribution for the particles are shown.

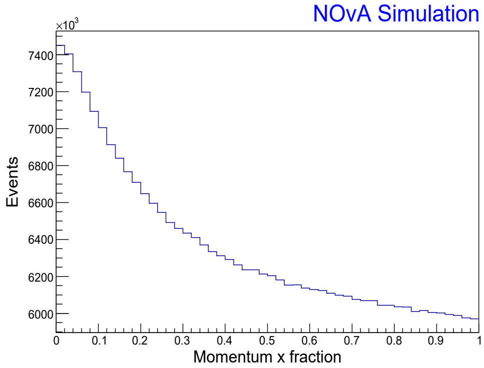

(a) Momentum X fraction

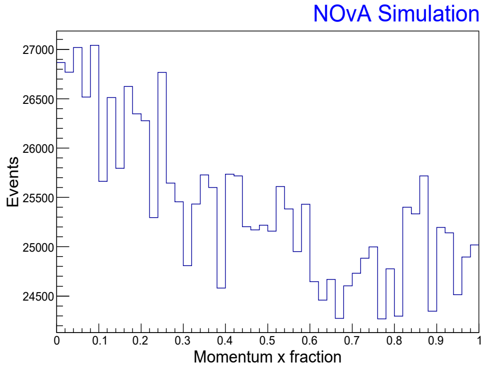

(b) ν_e momentum X fraction

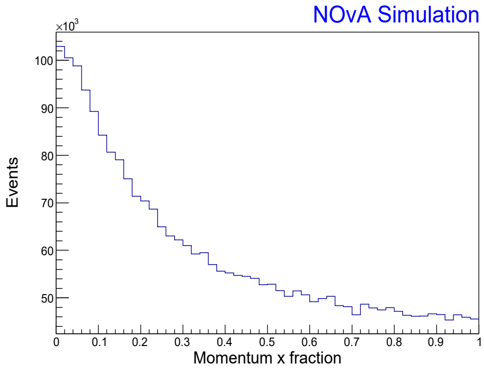

(c) ν_μ momentum X fraction

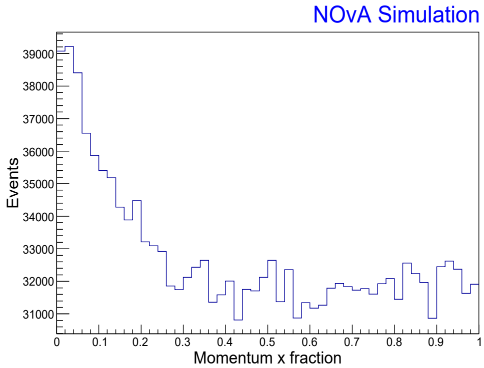

(d) e momentum X fraction

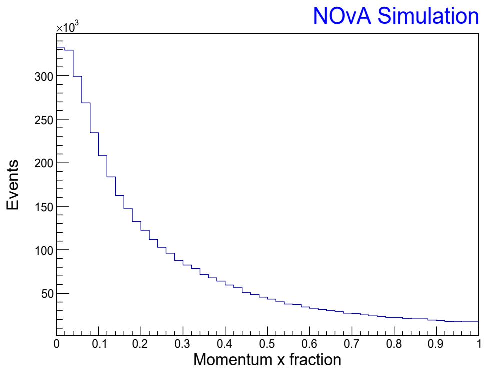

(e) μ momentum X fraction

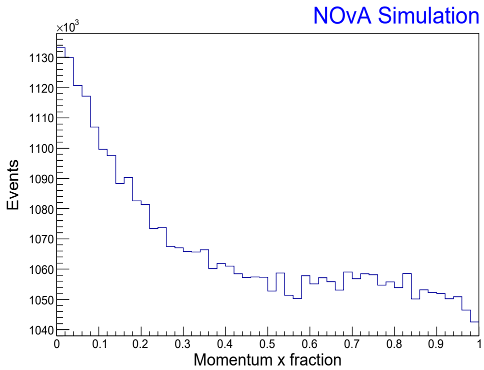

(f) γ momentum X fraction

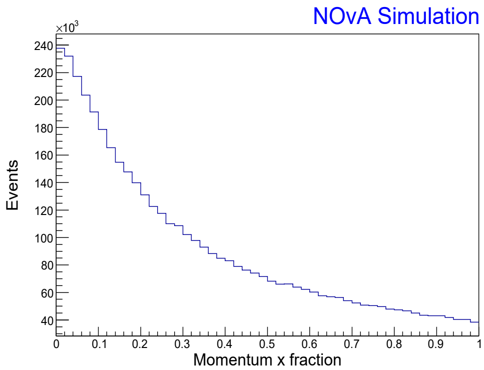

(g) π^0 momentum X fraction

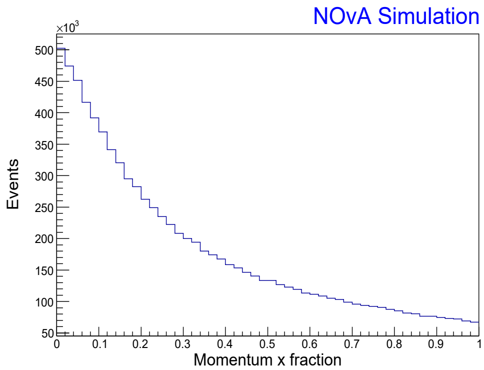

(h) π^+ momentum X fraction

Figure 4.9: Geant4 X momentum distributions

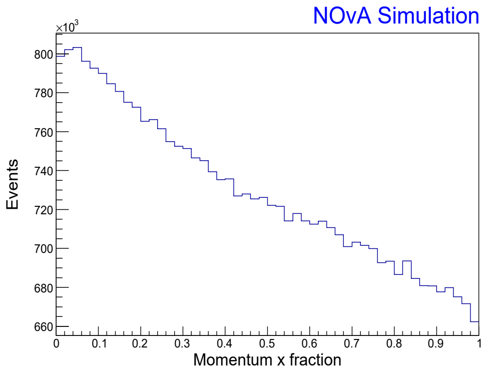

(i) Neutron momentum X fraction

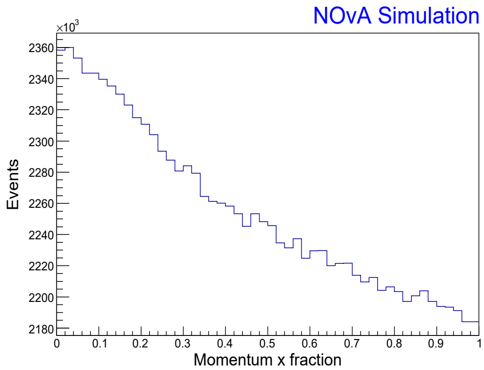

(j) Proton momentum X fraction

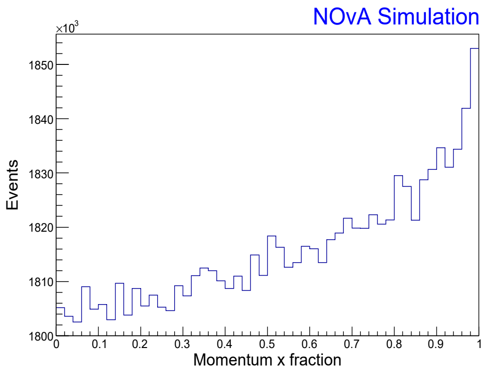

(k) Nucleus momentum X fraction

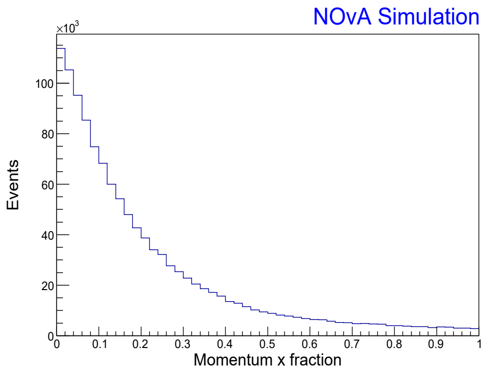

(l) Others momentum X fraction

Figure 4.9: X momentum fraction distribution of all the particles processed through GEANT4

Figs. 4.9a and 4.10a.

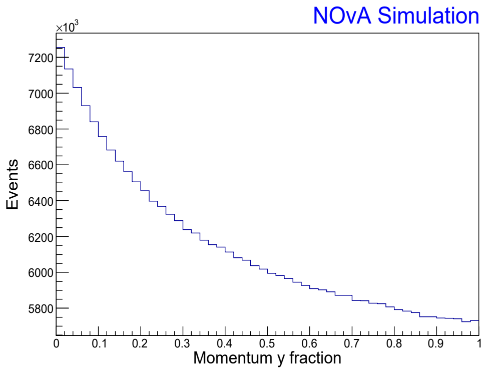

(a) Momentum Y fraction

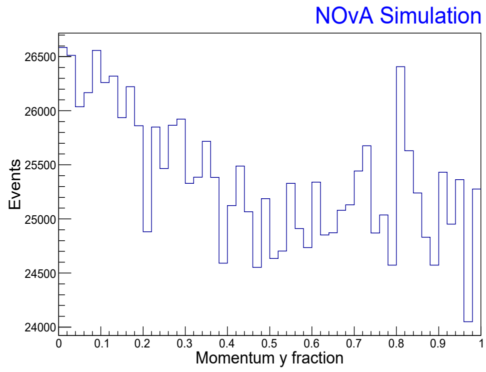

(b) ν_e momentum Y fraction

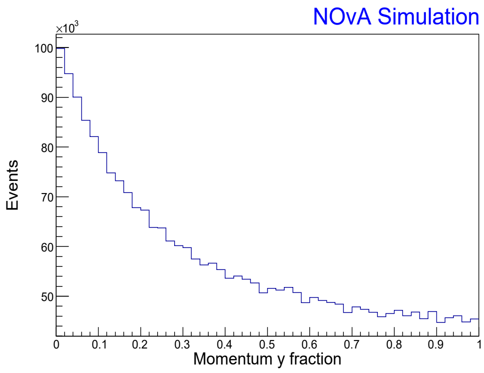

(c) ν_μ momentum Y fraction

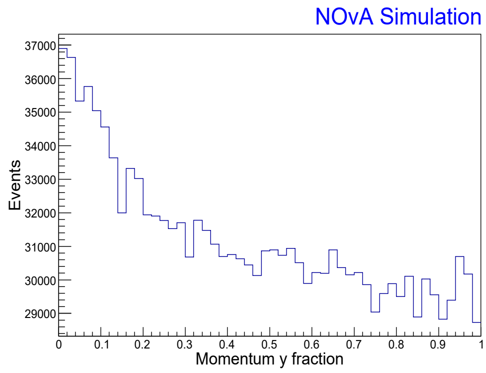

(d) e momentum Y fraction

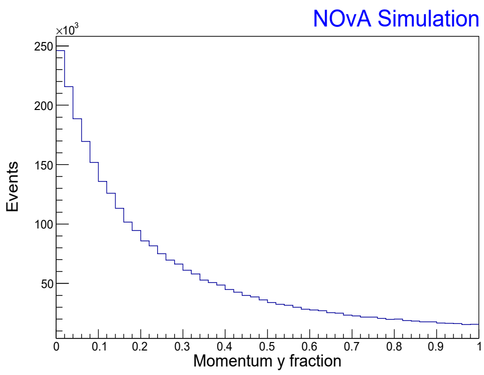

(e) μ momentum Y fraction

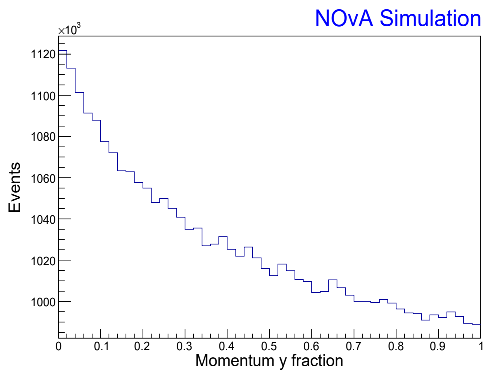

(f) γ momentum Y fraction

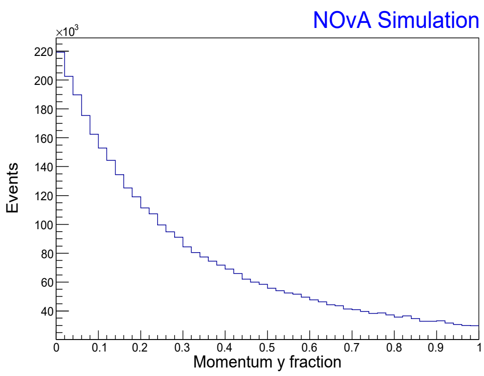

(g) π^0 momentum Y fraction

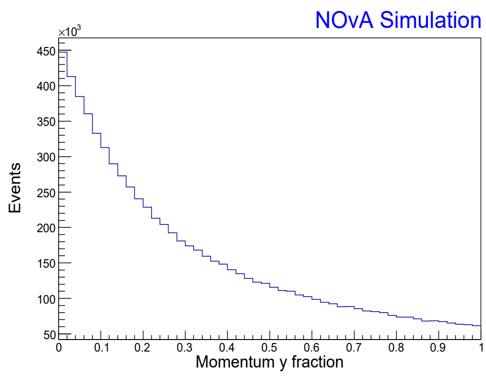

(h) π^+ momentum Y fraction

Figure 4.10: Geant4 Y momentum distributions

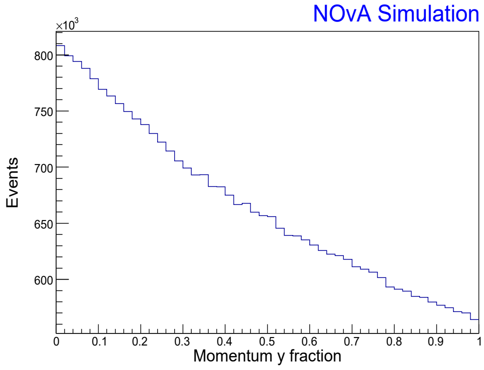

(i) Neutron momentum Y fraction

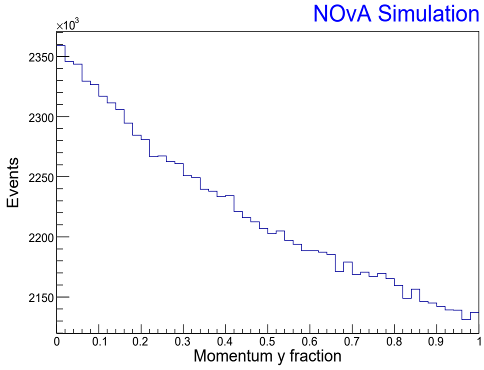

(j) Proton momentum Y fraction

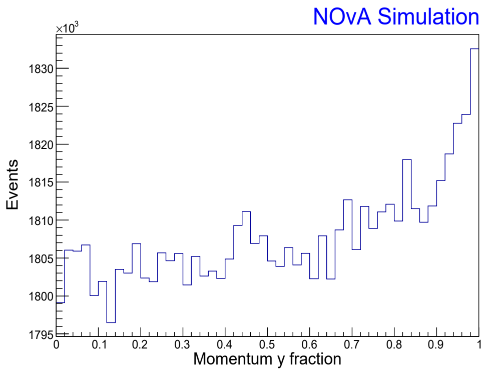

(k) Nucleus momentum Y fraction

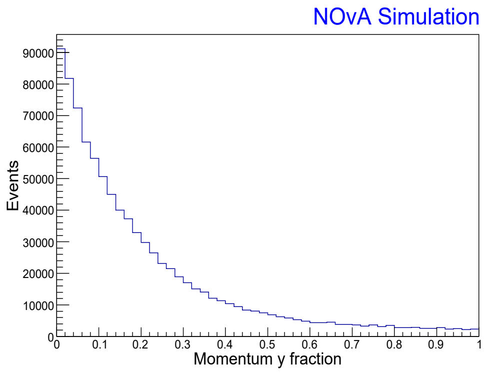

(l) Others momentum Y fraction

Figure 4.10: X momentum fraction distribution of all the particles processed through GEANT4

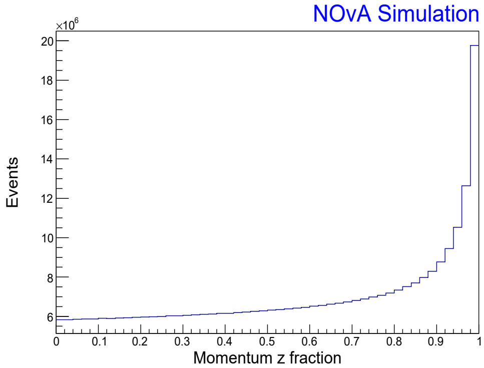

(a) Momentum Z fraction

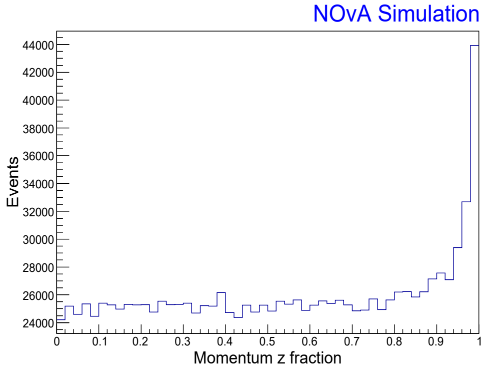

(b) ν_e momentum Z fraction

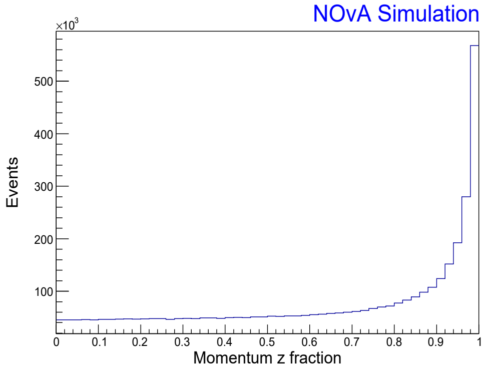

(c) ν_μ momentum Z fraction

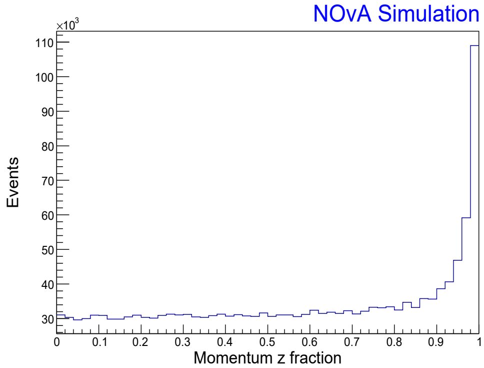

(d) e momentum Z fraction

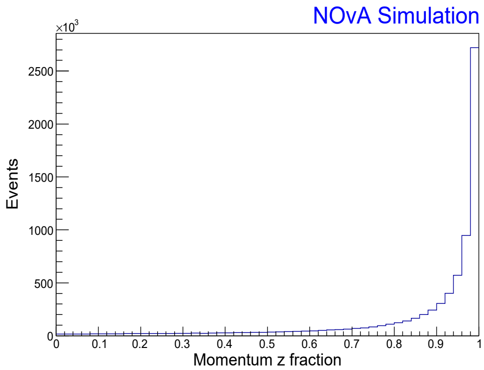

(e) μ momentum Z fraction

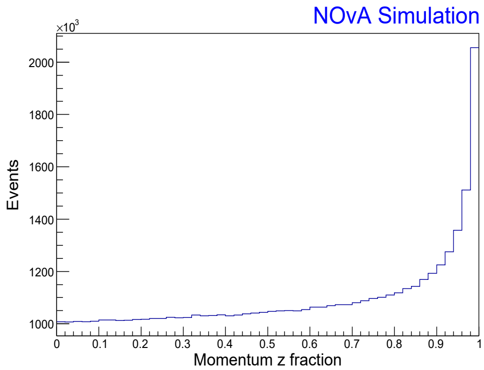

(f) γ momentum Z fraction

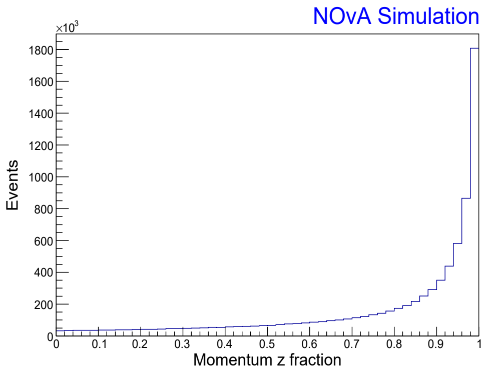

(g) π^0 momentum Z fraction

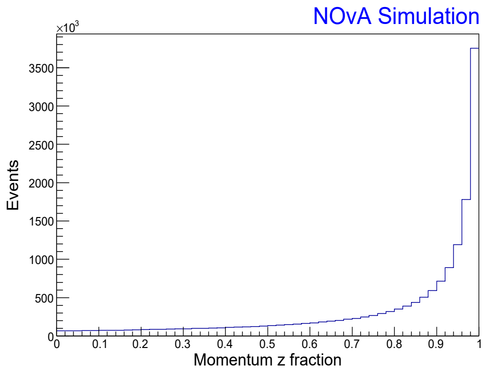

(h) π^+ momentum Z fraction

Figure 4.11: Geant4 Z momentum distributions

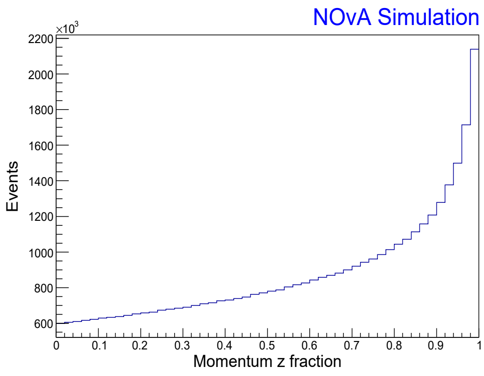

(i) Neutron momentum Z fraction

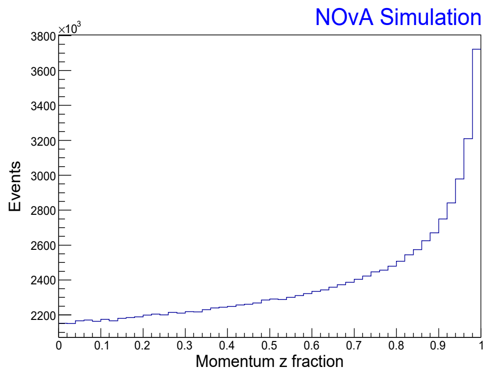

(j) Proton momentum Z fraction

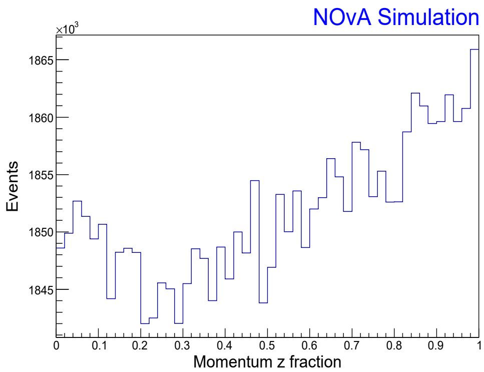

(k) Nucleus momentum Z fraction

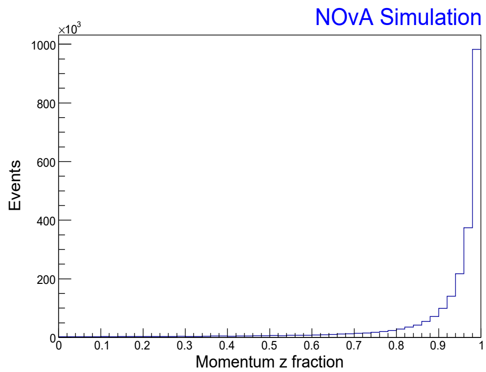

(l) Others momentum Z fraction

Figure 4.11: X momentum fraction distribution of all the particles processed through GEANT4

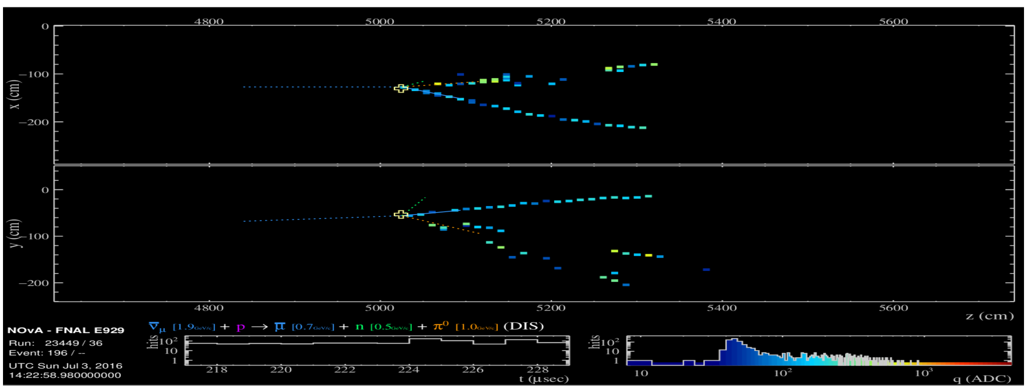

Figure 4.12: Sample interaction for DIS scattering showing the momentum distribution

4.2.3 Fibre in a Liquid Scintillator (FLS) Hits Validation

As Geant4 simulated the trajectory of particles through the detector geometry, it records FLS hit objects which record true energy depositions in NOvA detector cells. Each FLS hit contains the position and time coordinates for particle cell entry and exit, and the particle's energy when it entered and exited the cell. FLS hit validation plots these entry and exit coordinates, and also the difference between entry and exit values. True energy deposition in the cell is recorded inclusively for all hits, and also exclusively for specific true particle types.

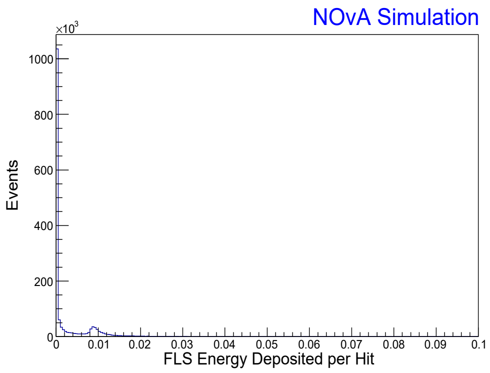

(a) Energy deposited per hit

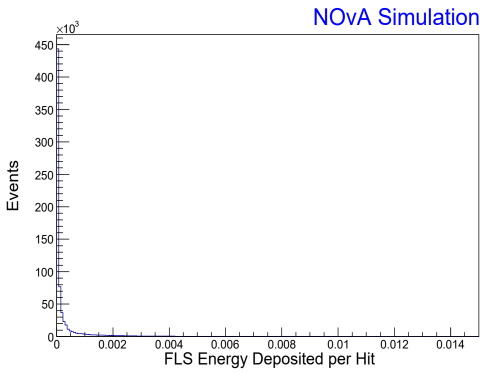

(b) Energy deposited per e^- hit

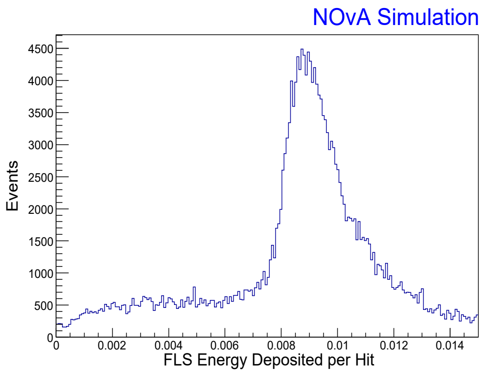

(c) Energy deposited per μ^- hit

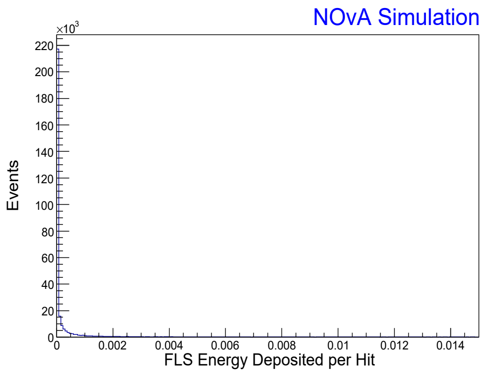

(d) Energy deposited per proton hit

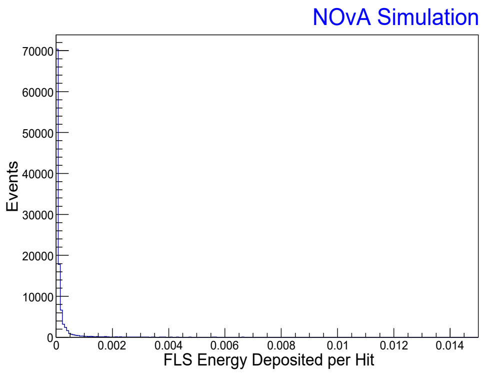

(e) Energy deposited per γ hit

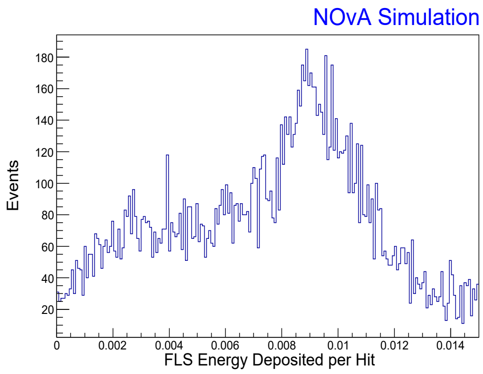

(f) Energy deposited per π hit

Figure 4.13: FLS hit energy deposition distributions for different particles

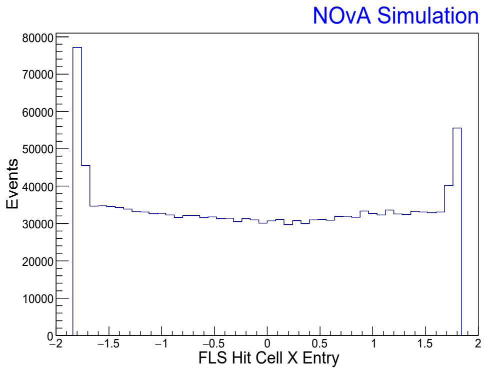

(a) Cell entry X coordinate

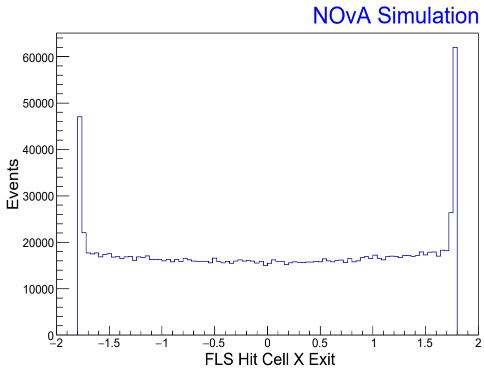

(b) Cell exit X coordinate

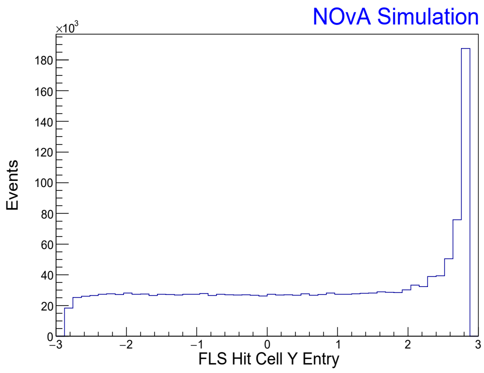

(c) Cell entry Y coordinate

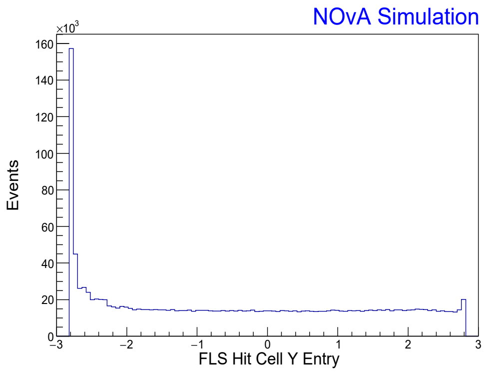

(d) Cell exit Y coordinate

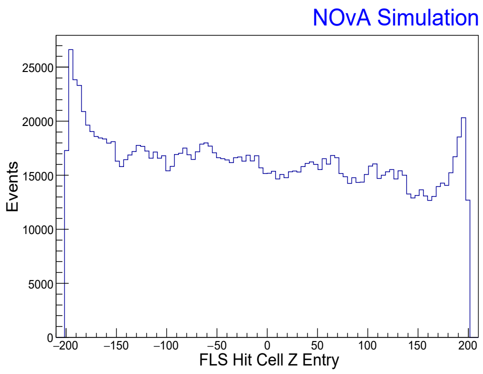

(e) Cell entry Z coordinate

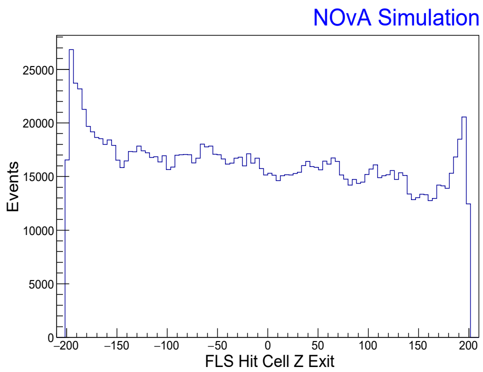

(f) Cell exit Z coordinate

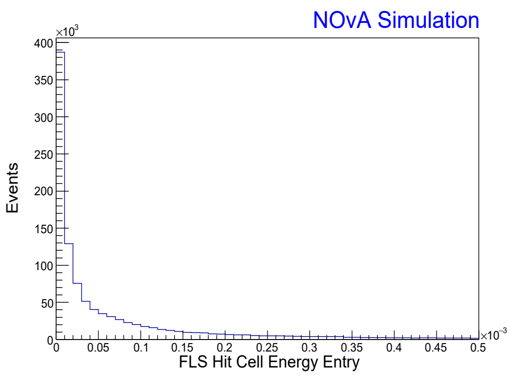

(g) Cell entry energy

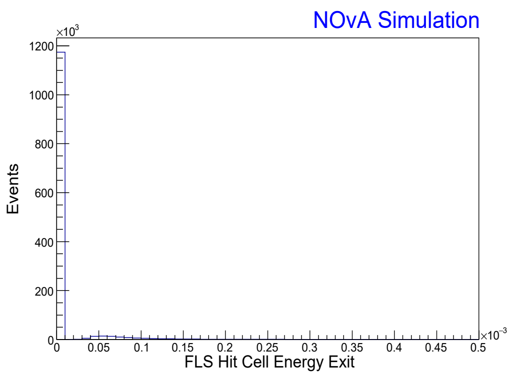

(h) Cell exit energy

Figure 4.14: Entry and exit distributions of the particles from the cell in the detector.

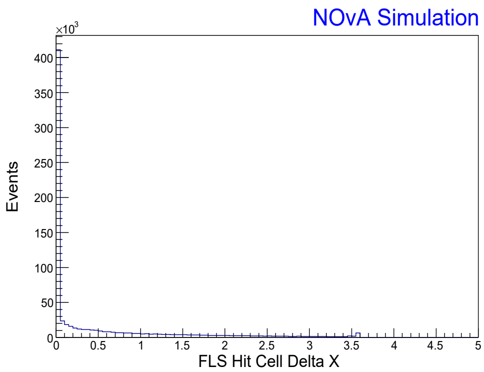

(a) Δx across cell

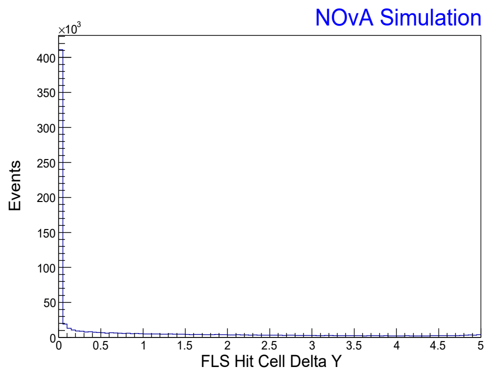

(b) Δy across cell

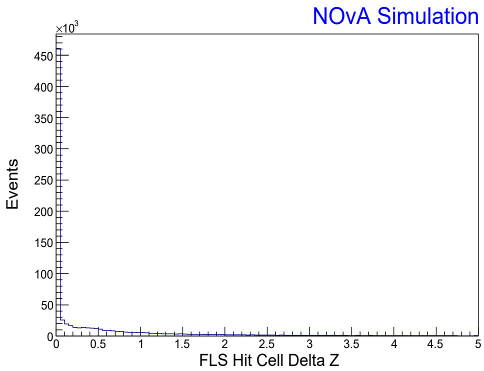

(c) Δz across cell

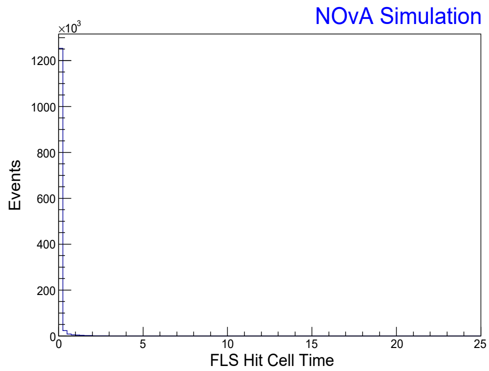

(d) Δt across cell

Figure 4.15: FLS hit distance distributions

4.2.4 Photon Transport Validation

Photon transport is responsible for taking the true energy depositions simulated by Geant4 as FLS hits (Sec. 4.2.2), and modelling scintillator light yield, Cherenkov light and fiber attenuation in order to produce PhotonSignal objects which describe the number of photons incident on cell APDs. The light response is characterised using a parameterised model

$$N_\gamma = F_{\text{view}}(Y_s E_{\text{Birks}} + \epsilon_C C_\gamma), \tag{4.2}$$

where F are overall scaling factors for the X and Y views in each detector, Y_s is an overall scaling for scintillation energy, E_{Birks} is the Birks energy, ϵ_C is an overall scaling factor for Cherenkov energy, and C_γ is energy deposited due to Cherenkov photons.

The number of photons incident on the APD is subject to statistical variations, and so for each photon signal, the number of photons is drawn from a Poisson distribution centred around the output of the parameterised light model. The number of photons before and after statistical fluctuations are shown in Fig. 4.16b and Fig. 4.16a, respectively.

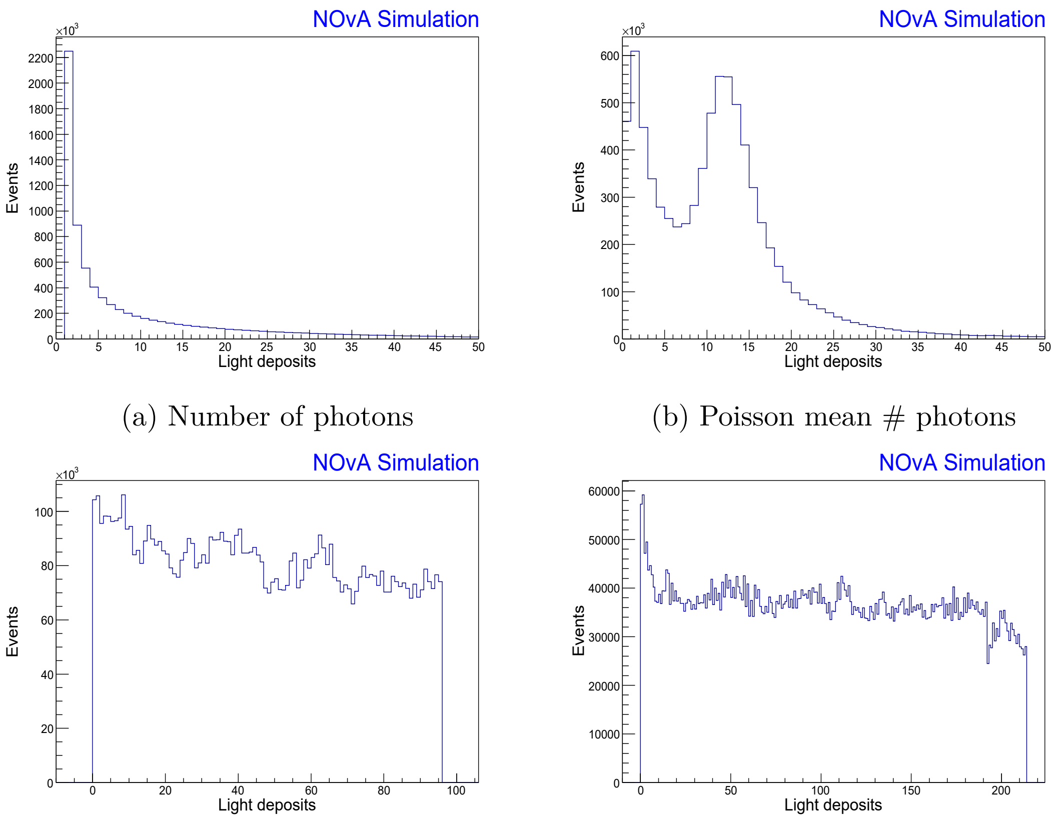

(a) Number of photons

(b) Poisson mean # photons

(c) Light deposit cell

(d) Light deposit plane

Figure 4.16: Photon transport distributions are shown

4.3 Reconstruction

4.3.1 Raw Digit Validation

This module visualises the raw readout information from the detector. Each RawDigit consists of an ADC value, a TDC value, and a channel index. For simulated events, the readout simulation reads in photon signals from the photon transport stage, simulates the effects of electronics, and then saves the result as RawDigit objects; for data events, RawDigit objects are the real raw output from the detector. ADC and TDC are signal amplitude and time measurements which are expressed in arbitrary units from our electronics. These signals are then converted into a measure of number of photoelectrons at the CellHit stage in Sec. 4.3.2, and then reconstructed in 3D and calibrated to form energy measurements in Sec. 4.3.3.

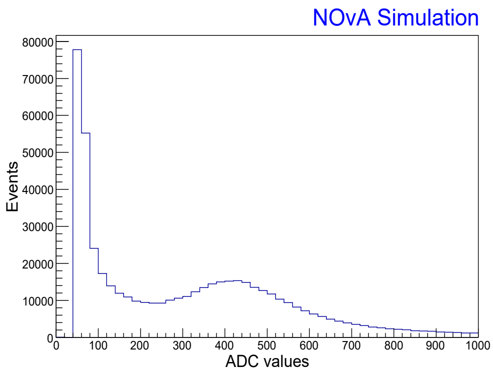

(a) Raw digit ADC

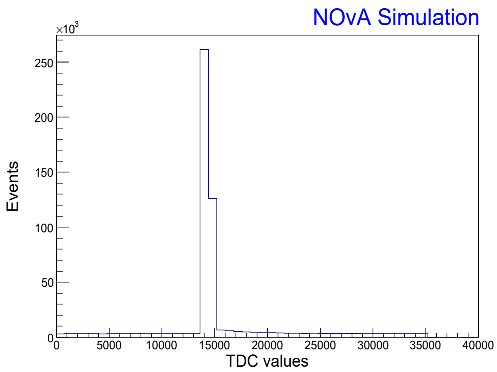

(b) Raw digit TDC

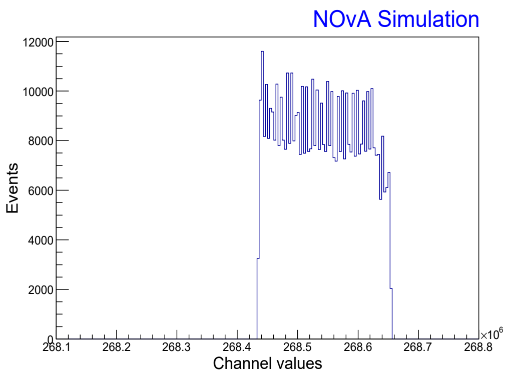

(c) Raw digit channel

Figure 4.17: These are the raw data distribution from the detector.

4.3.2 Cell Hit Validation

This module visualises cell hit objects, which are discrete detector hits formed from the RawDigit objects described in Sec. 4.3.1. The quantities stored in each cell hit include the plane, view and cell indices, the raw ADC and TDC measurements from the raw digit, and the photoelectron and TNS measurements derived from those.

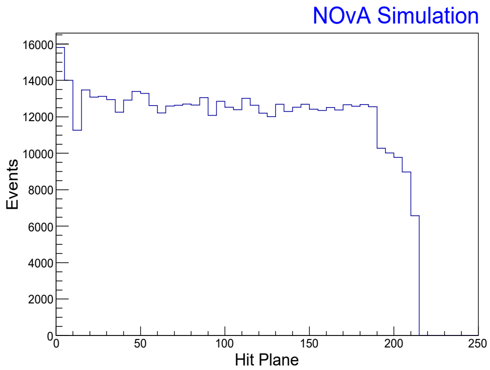

(a) Cell hit plane

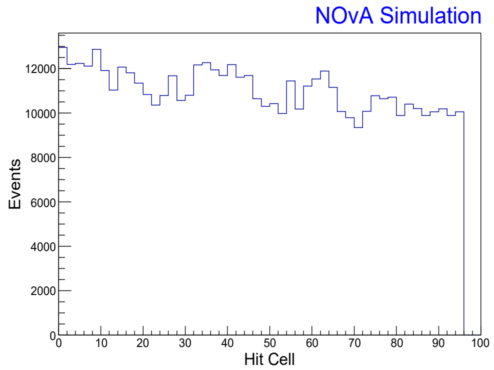

(b) Cell hit cell

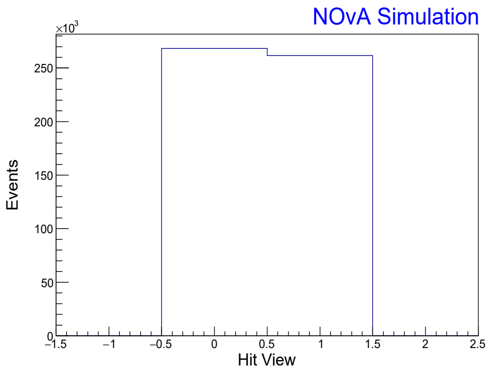

(c) Cell hit view

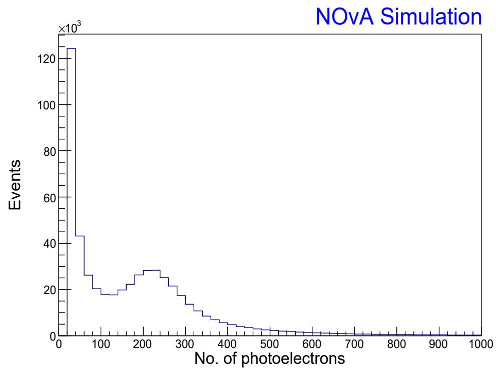

(d) Cell hit PE

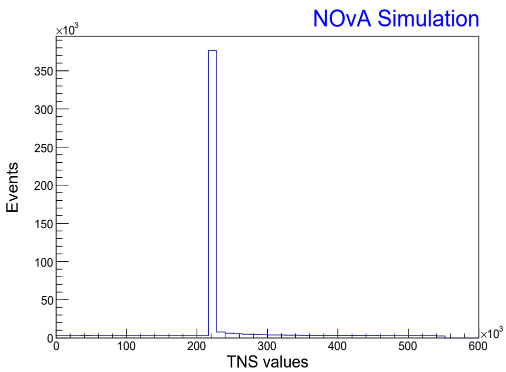

(e) Cell hit time

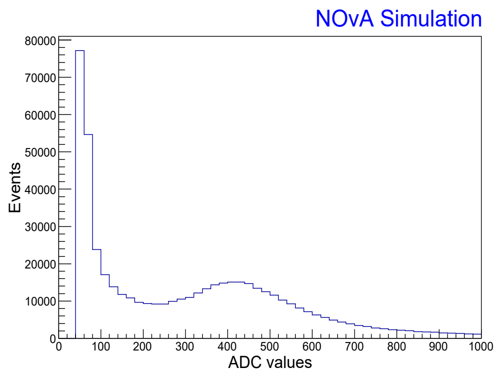

(f) Cell hit ADC

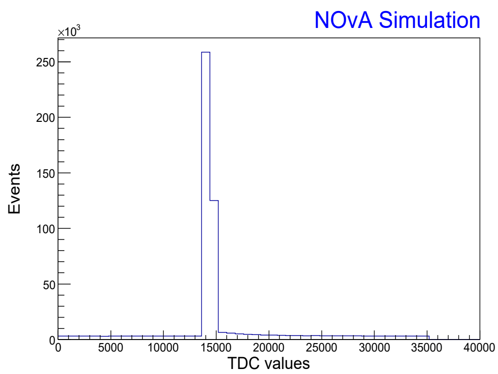

(g) Cell hit TDC

Figure 4.18: These distributions show the cell hit information processed from the raw data.

4.3.3 Reconstructed hit Validation

Reco hit objects are derived from the cell hits described in Sec. 4.3.2. In order for a reconstructed hit to be formed from a cell hit, that hit must have been reconstructed into a slice. The reconstructed hits are stored in the Art event record as children of the slice data product, and store information on whether the hit was successfully calibrated, the number of photoelectrons corrected for attenuation (PECorr), the deposited energy in GeV, and the 3D coordinates and time of the hit.

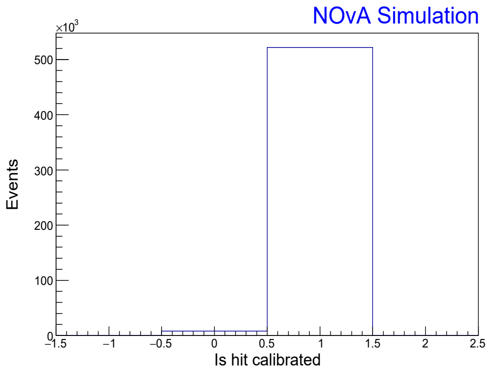

(a) Number of hits

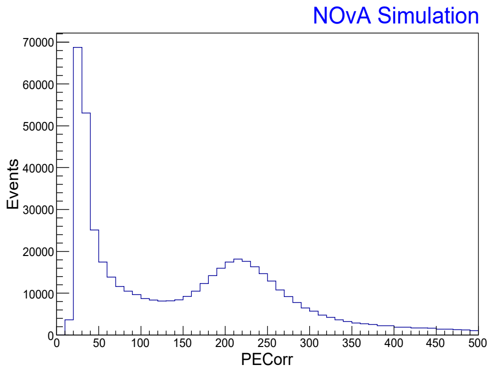

(b) Hit PECorr

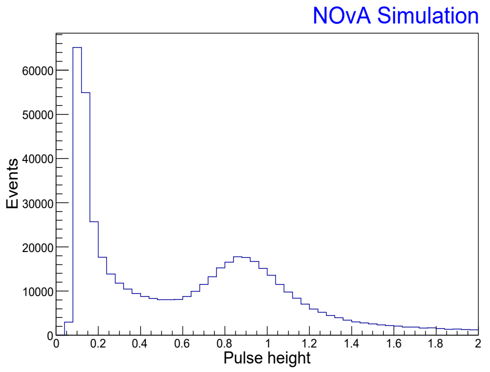

(c) MIP-normalised pulse height

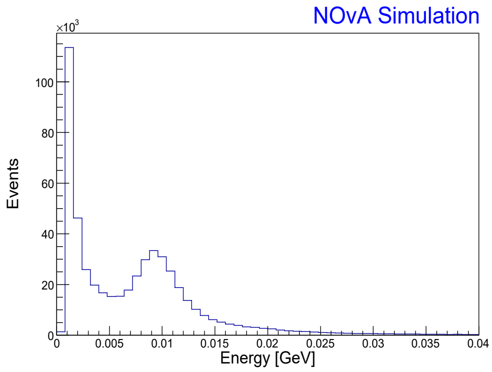

(d) Energy deposited

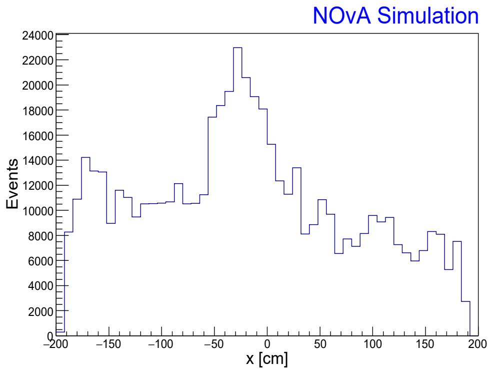

(e) Hit X coordinate

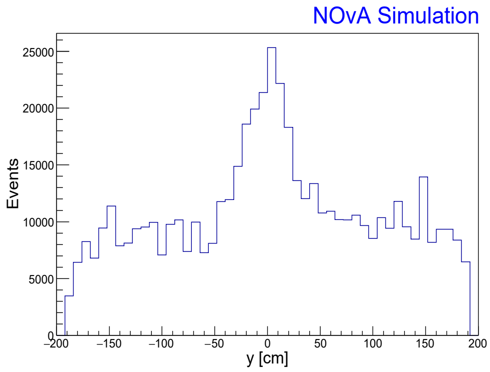

(f) Hit Y coordinate

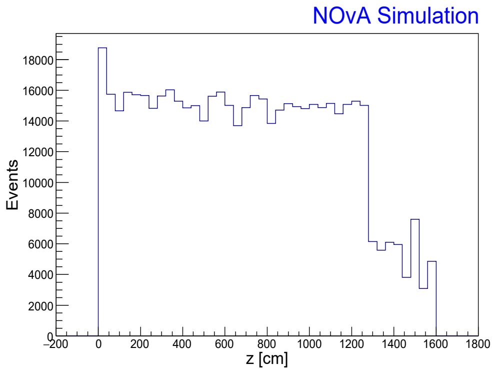

(g) Hit Z coordinate

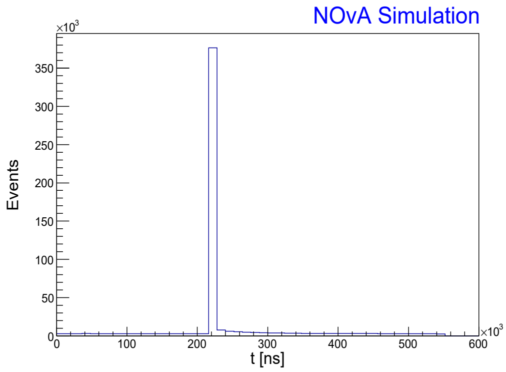

(h) Hit time

Figure 4.19: Reco hit distributions

4.3.4 Vertex Validation

Vertex reconstruction is responsible for identifying the true spatial position at which the neutrino interaction occurred. This module reads in the reconstructed position of the neutrino interaction vertex, and also the true interaction vertex from MC truth. It then visualises the 3D position of the reconstructed vertex, and the distance between the reconstructed and true positions of the vertex (Fig. 4.20).

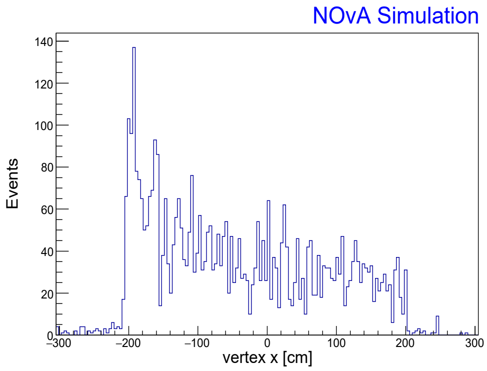

(a) Vertex X coordinate

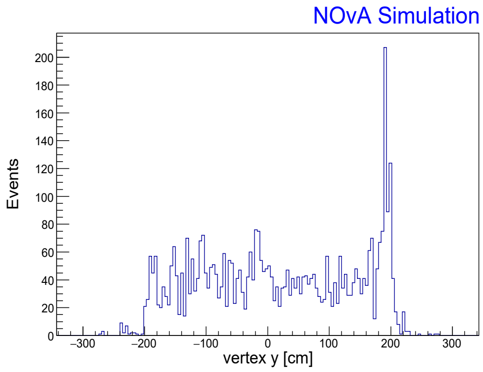

(b) Vertex Y coordinate

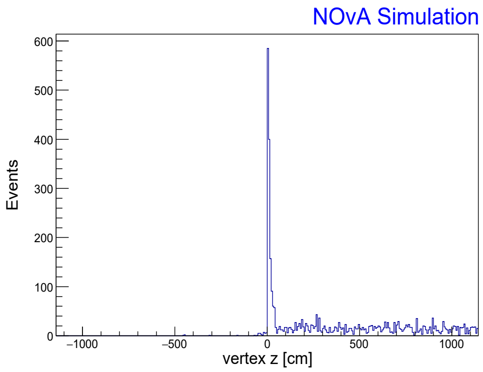

(c) Vertex Z coordinate

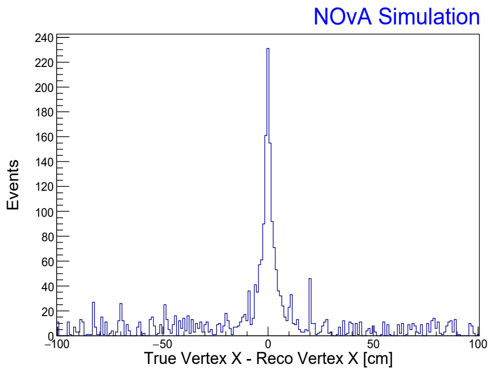

(d) Vertex true X - reco X

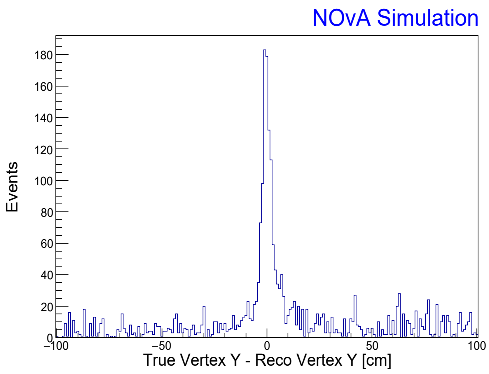

(e) Vertex true Y - reco Y

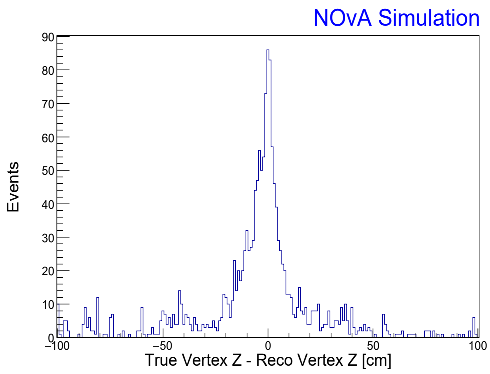

(f) Vertex true Z - reco Z

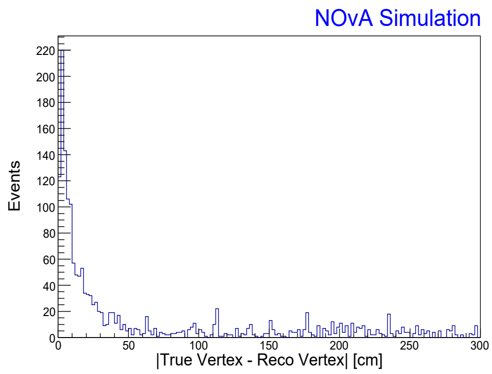

(g) Vertex resolution

Figure 4.20: Distribution showing the vertex resolution of the reconstructed particles.

4.4 Summary

This chapter presents a detailed overview of the validation framework developed for the NOvA experiment. The framework has been designed to validate both simulated and reconstructed objects at the hit level to ensure the reliability of the simulated and observed data. Furthermore, a collection of essential validation plots is also presented to serve as the benchmark for expected physics. In the following chapters, we will discuss the details of the sterile neutrino analysis built upon the work so far.

Chapter 5

Event Selection and Energy Estimation

"Through careful selection and precise reconstruction, we turn noise into knowledge to discover nature's secret."

5.1 Introduction

This chapter is dedicated to event selection and energy reconstruction, which are critical components of the physics analysis in an experiment. We begin with an overview and introduction of the different event topologies in Sec. 5.2. The selection criteria for ν_μ and NC events, which form the foundation of the complete analysis, are discussed in Sec. 5.3 and Sec. 5.4, respectively. In Sec. 5.5 we discuss the energy reconstruction for the ν_μ (Sec. 5.7) and NC events (Sec. 5.6). While the detailed information on NC event selection and energy reconstruction is the primary focus, the information on ν_μ-CC events is provided in this chapter.

5.2 Event Topologies

NOvA Neutrino oscillation analyses rely on counting how many neutrino events are recorded at both the Near and Far Detectors. To achieve this, events originating from neutrino interactions must be identified within the full detector activity. The process of event and energy reconstruction primarily involves identifying the group of raw cell hits originating from the same single particle.

Primarily, a neutrino oscillation analysis targets the identification of events originating from different neutrino interactions. The interest in choosing a particular type of interaction depends on the physics analysis you wish to perform. Sterile neutrino analysis being the joint ν_μ- NC disappearance, the primary interaction type would be ν_μ ($\bar{\nu}_\mu$) CC and NC. There are several interaction modes for the CC and NC, of which, Quasi Elastic (QE) is presented as an example.

- **ν_μ ($\bar{\nu}_\mu$) CC**: These interactions are generally characterized by the charged leptons. An incoming muon neutrino (ν_μ) or antineutrino ($\bar{\nu}_\mu$) interacts with the **proton/neutron** leading to the production of ***neutron/proton*** and ***muon*** ($\mu^\pm$) via charged current process defined through the Feynman diagram in Fig. 5.1.

$$\nu_\mu + p \longrightarrow \mu^+ + n \tag{5.1}$$

$$\bar{\nu}_\mu + n \longrightarrow \mu^- + p \tag{5.2}$$

- **ν_e ($\bar{\nu}_e$) CC**: These interactions are similar to the ν_μ-CC and are also characterised by the charged leptons, which generally

(a) Charged-Current (CC)
$\nu_\mu + X \rightarrow \mu^- + X'$

(b) Neutral-Current (NC)
$\nu_\mu + X \rightarrow \nu_\mu + X$

Figure 5.1: (a) Charged-current (CC) neutrino interaction and (b) neutral-current (NC) neutrino interaction.

have shorter tracks. An incoming electron neutrino (ν_e) or antineutrino ($\bar{\nu}_e$) interacts with the **proton/neutron** leading to the production of ***neutron/proton*** and ***electron*** ($e^{\pm}$) via a charged current process (Fig. 5.2).

$$\nu_e + p \longrightarrow e^{+} + n \tag{5.3}$$

$$\bar{\nu}_e + n \longrightarrow e^{-} + p \tag{5.4}$$

- **NC:** These interactions are quite challenging to detect in the detectors due to the absence of any charged lepton in the final state. An incoming neutrino (antineutrino) interacts with a proton/neutron, leading to the proton/neutron and neutrino in the final state. The interactions are governed by the exchange of a Z boson, illustrated in the Feynman diagram in Fig. 5.1.

$$\nu(\bar{\nu}) + p(n) \longrightarrow \nu(\bar{\nu}) + p(n) \tag{5.5}$$

Given that we use ν_μ-CC and NC disappearance channels for the sterile neutrino analysis, the primary focus of reconstruction is on these channels. However, we will describe the ν_e events for the sake of completeness here. Before moving to the discussion of selection and reconstruction, let us develop an intuition about the topologies of these events inside the detector.

Fig. 5.2 shows the topologies of different neutrino interactions at the NOvA ND. It is essential to comprehend the topology of various processes, particularly when the incoming particle is a neutrino, which is neutral. Identifying the final state particles is necessary for energy reconstruction and event identification. At the top in Fig. 5.2 is the ν_μ-CC interaction, which is primarily identified with the outgoing ***muon*** (μ). The outgoing μ is characterised by a very ***long track*** inside the detector. On the other hand, ν_e-CC interactions are also identified through the outgoing lepton (electron). However, an electron, in contrast to a muon, has a ***shorter-wider fuzzy track*** (middle). At the bottom, we have the NC interactions, which are not associated with any charged lepton in the final state and hence are difficult to reconstruct. One of the primary signatures of the NC interactions is the π^0 decaying to two photons. A major difference between the ν_e-CC and NC is the starting point of the shower. In the case of ν_e-CC, the shower starts at the vertex, whereas in NC interactions, there is usually a gap between the shower starting point and the vertex.

5.3 Neutral Current Event Selection

In general, we apply preselection cuts to ensure that the neutral current selection remains mutually exclusive from the ν_μ and ν_e selections. The primary reason to have the NC selection exclusive of ν_μ-CC and ν_e-CC selection is to avoid double counting. Basically, the selection strategy ensures that each event exist only in one sample. These cuts are applied uniformly across both the near and far detectors for both the FHC and RHC modes. The preselection criteria impose minimal constraints on events and include the following:

- **Fiducial volume:** A loose fiducial volume cut is applied to reconstructed events, with a 10 cm buffer zone from the edges of the detector.
- **Decaf cut:** A relaxed CVN score threshold is applied to identify neutrino and antineutrino events.
- To maintain exclusivity from the ν_μ and ν_e analyses, we apply the "not ν_μ" and "not ν_e" selection cuts, ensuring no duplicate events exist across the selections.

5.3.1 True NC Events and Background

A true signal event is defined as a true neutral current (NC) event with a true vertex located inside the detector. The background consists of all selected true charged-current (CC) events, as well as NC events with a true vertex located outside the detector.

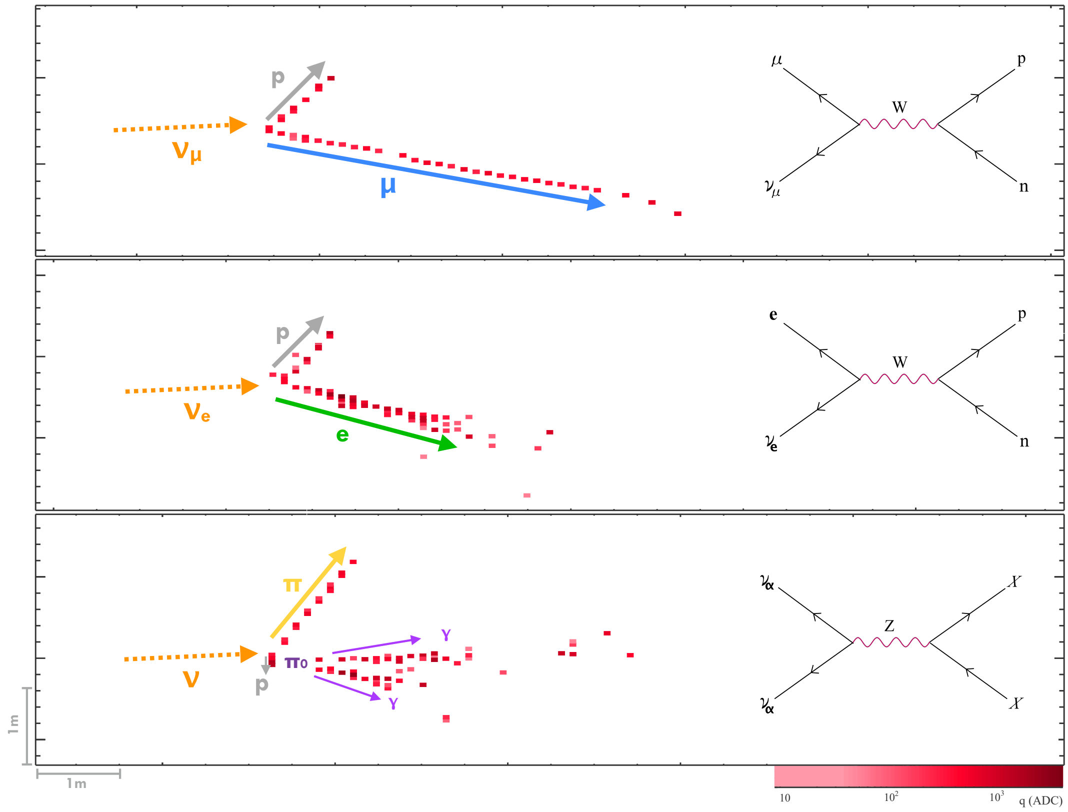

Figure 5.2: Topologies of different neutrino events from NOvA data at ND. At the top, we have ν_μ -CC interaction producing a straight long track representing the outgoing muon. In the middle is the ν_e-CC interaction, producing a short, fuzzy track characterising the outgoing electron. At the bottom is ν-NC interaction resulting in the production of a π^0, which further decays into two photons.[66]

5.3.2 Near Detector Selection

This section provides an overview of the neutral current selection for the Near Detector (ND). The ND selection criteria are broadly categorised into three main groups: Quality, Containment, and Selection.

5.3.2.1 Quality Cuts

The quality cuts ensure that only well-reconstructed events are selected, while poorly reconstructed events are rejected. These cuts are primarily applied to the slice. A slice is a cluster of hits, associated/correlated between themselves and each slice should correspond to one neutrino interaction. The following criteria are applied to ensure proper event reconstruction:

- The slice must have a properly reconstructed vertex (**kIsElastic > 0**).
- The event should not terminate prematurely, requiring a minimum number of planes for accurate reconstruction. Poorly reconstructed events will have a low or discontinuous number of planes (**kNContPlanes > 2**).
- Each slice must contain at least one reconstructed prong (**kNFuzzyProng > 0**).

Fig. 5.3 and Fig. 5.4 present the data/MC comparisons for the FHC and RHC modes, respectively. These distributions, which include preselection and quality cuts, show no significant discrepancies between the data and Monte Carlo simulations in terms of shape or behaviour.

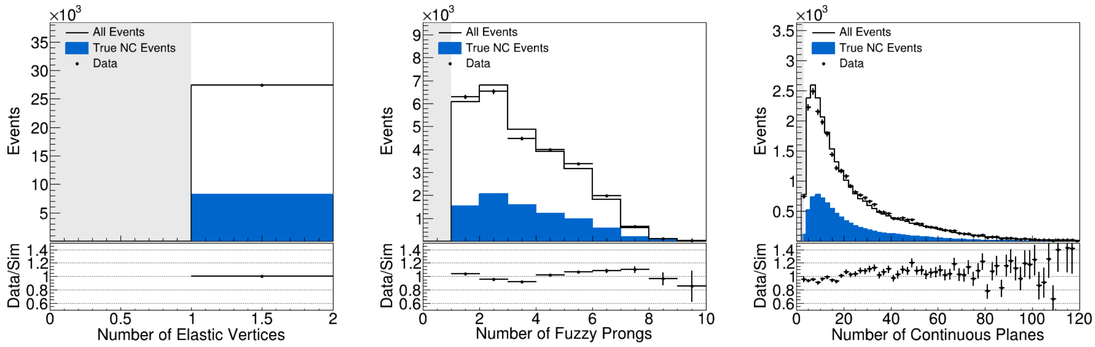

Figure 5.3: Data/simulation comparisons for the ND quality requirements for **neutrino (FHC)** mode. The true NC events are highlighted in blue, and the proposed regions to remove are shown as grey boxes. The simulation is area-normalised to the data.

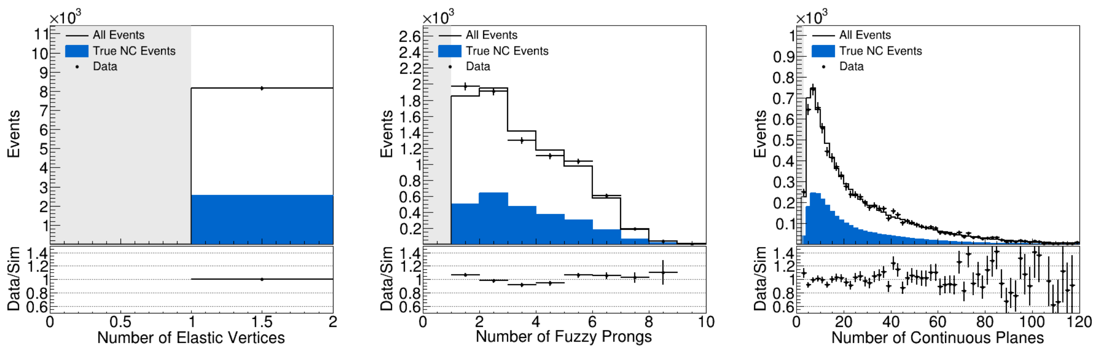

Figure 5.4: Data/simulation comparisons for the ND quality requirements for **antineutrino (RHC)** mode. The true NC events are highlighted in blue, and the proposed regions to remove are shown as grey boxes. The simulation is area-normalised to the data.

5.3.2.2 Containment

Containment Cuts are required to ensure the events have the properly contained energy. This is achieved in two ways, primarily by placing the cut on the fiducial volume and the interaction vertex.

5.3.2.3 Vertex Containment Cut

Particles entering the detector from outside are expected to have reconstructed vertices near the edges of the detector. To mitigate such background events, a requirement is imposed that the reconstructed vertex position lies well within the detector boundaries. Fig. 5.5 and Fig. 5.6 show the vertex position distributions for FHC and RHC modes, respectively, after applying preselection and quality selection criteria. While most rock-induced events are effectively rejected through vertex cuts, they still constitute a significant fraction of the background in the Near Detector (ND) neutral current (NC) sample.

Given that a looser CVN was already planned for the Near Detector in this analysis to avoid the rock contamination issue found during the last analysis [67], we had the flexibility to impose tighter vertex cuts to reduce rock-induced background events further. Tab. 5.1 shows the cut values applied for the vertex position. A detailed rock study can be found in [68].

Cut Type	**Cut Name**	**Cut Value (cm)**
Vertex Cuts		
	kVtxX	> -60 && < 100
	kVtxY	> -100 && < 60
	kVtxZ	> 300 && < 1000

Table 5.1: ND Vertex Cuts applied for the analysis.

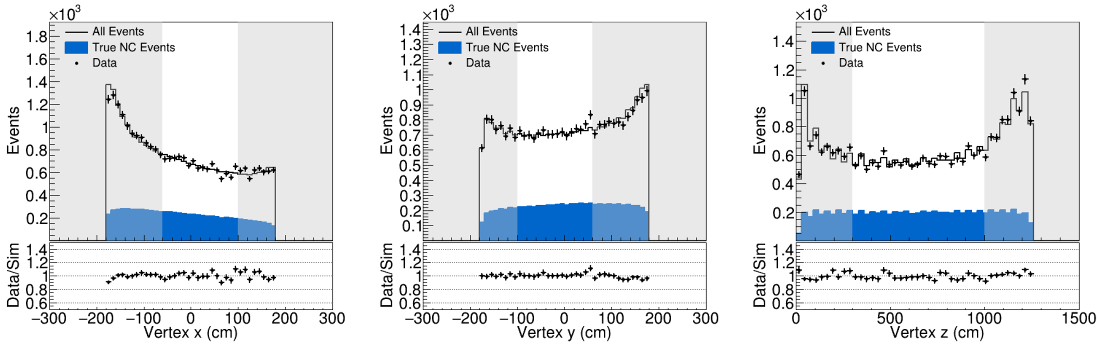

Figure 5.5: Data/simulation comparisons for the vertex position from each side of the detector for **FHC** mode. Here, the true NC events are in blue, and the suggested regions to remove are shown as grey boxes. Note that the simulation has been area-normalised to match the data. In these plots, the quality requirements (Sec. 5.3.2.1) have been applied.

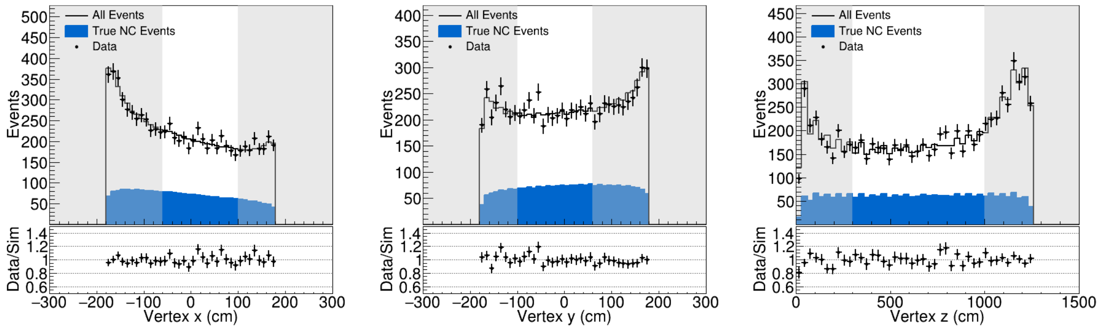

Figure 5.6: Data/simulation comparisons for the vertex position from each side of the detector for **RHC** mode. Here, the true NC events are in blue, and the suggested regions to remove are shown as grey boxes. Note that the simulation has been area-normalised to match the data. In these plots, the quality requirements (Sec. 5.3.2.1) have been applied.

5.3.2.4 Fiducial Volume Containment Cut

A reconstructed prong can be considered a proxy for a reconstructed particle and is defined by a collection of hits associated with a vertex (point), direction, and length. However, there are events where the prongs deposit part of their energy outside the detector, which can ruin the overall energy resolution and the reconstruction of the sample. A prong to distance from the edge cut is applied to contain such events. A detailed analysis of this strategy can be found in [69]. Fig. 5.7 shows the distribution of prong distance from each edge of the detector.

Cut Type	**Cut Name**	**Cut Value (cm)**
Fiducial		
	kDistAllTop	> 20
	kDistAllBottom	> 20
	kDistAllEast	> 20
	kDistAllWest	> 20
	kDistAllFront	> 150
	kDistAllBack	> 50

Table 5.2: ND Fiducial Volume Cuts applied for the analysis.

5.3.2.5 CVN Requirement

Differentiating NC events from CC events is essential for accurate NC disappearance analysis. To achieve this, we used a trained Convolutional Visual Network (CVN) algorithm to distinguish the NC signal from the CC background. Events with a CVN score exceeding a specific threshold are classified as NC events, while those below the threshold are identified as CC backgrounds.

Our analysis has evaluated various CVN score thresholds and previously identified an optimal threshold value of 0.98 for effective event selection. However, this high CVN score threshold, while effective at removing CC backgrounds, also eliminates many true NC signals and retains numerous signal-like events from the rock

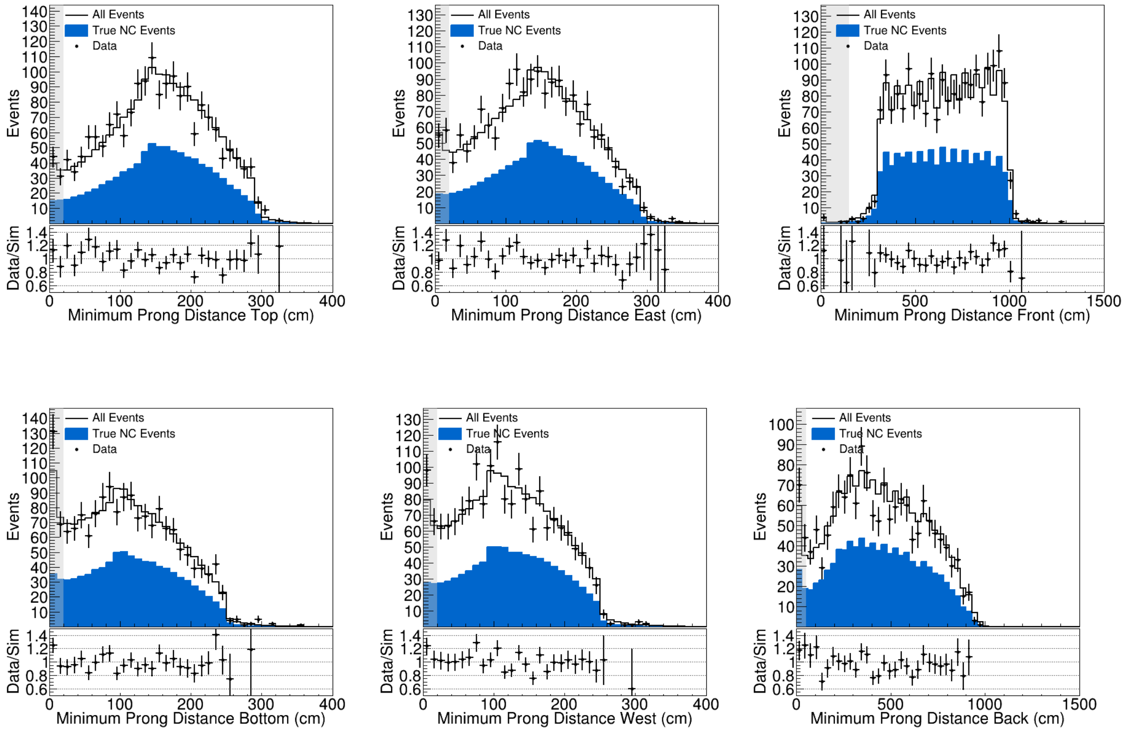

Figure 5.7: Data/simulation comparisons for the minimum distance of any prong to each detector edge for **FHC** mode. Here, the true NC events are in blue, and the suggested regions to remove are shown as grey boxes. Note that the simulation has been area-normalised to match the data. In these plots, the quality requirements (Sec. 5.3.2.1) and vertex (Sec. 5.3.2.3) have been applied.

near the detector. Although this approach successfully reduces CC backgrounds, it significantly impacts signal efficiency, necessitating the exploration of alternative CVN score thresholds.

Fig. 5.9a shows the data/MC comparison for the CVN distribution and Fig. 5.9b shows the FOM distribution overlaid on the CVN distribution. The FOM is almost flat around the 0.4 to 0.5 range, hence keeping a value of 0.5 makes sense.

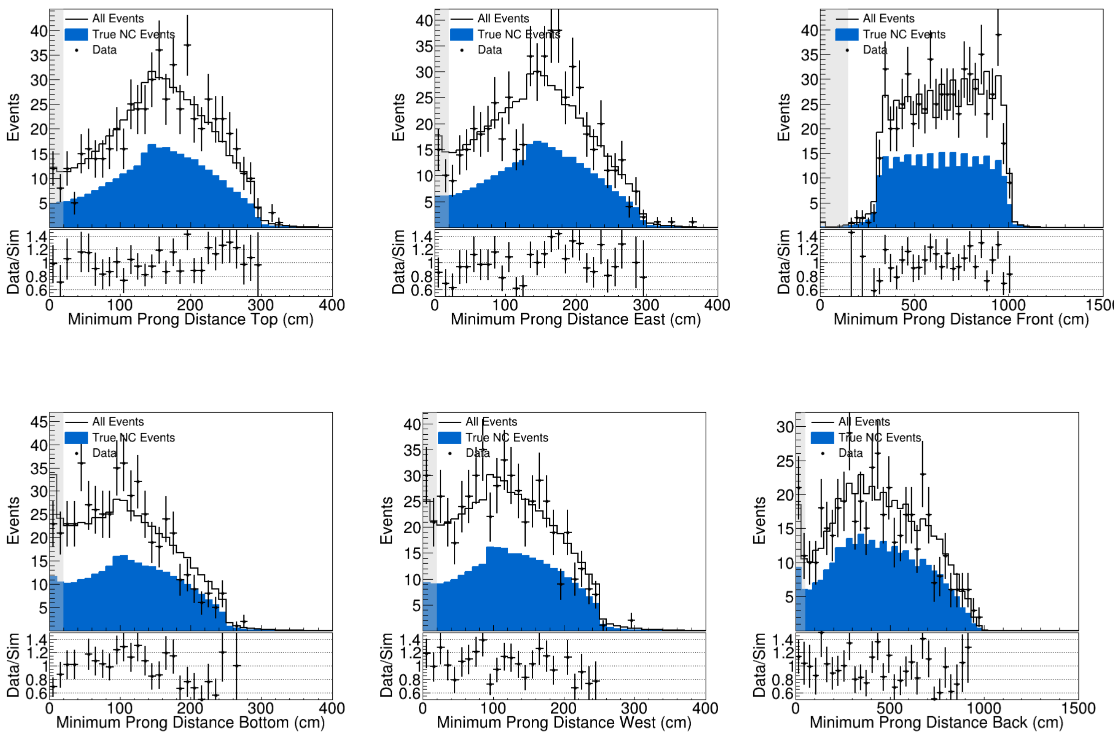

Figure 5.8: Data/simulation comparisons for the minimum distance of any prong to each detector edge for **RHC** mode. Here, the true NC events are in blue, and the suggested regions to remove are shown as grey boxes. Note that the simulation has been area-normalised to match the data. In these plots, the quality (Sec. 5.3.2.1) and vertex (Sec. 5.3.2.3) requirements have been applied.

5.3.2.6 Full Selection

Fig. 5.10a presents the distribution of uncorrected calorimetric energy, while Fig. 5.10b displays the reconstructed energy distribution for the FHC mode. A detailed study on energy estimation has been conducted specifically for this analysis and is discussed in Sec. 5.6. The final selection achieves a purity of 76% for FHC mode and 80.6% for the RHC, relative to all true NC events with a true vertex inside the detector that meet the preselection criteria. Tab. 5.3 (Tab. 5.4) provides the number of selected events for

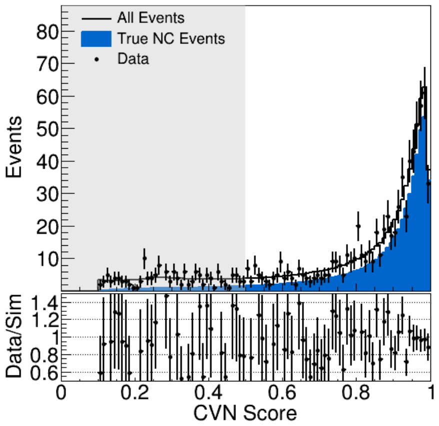

(a) CVN Distribution

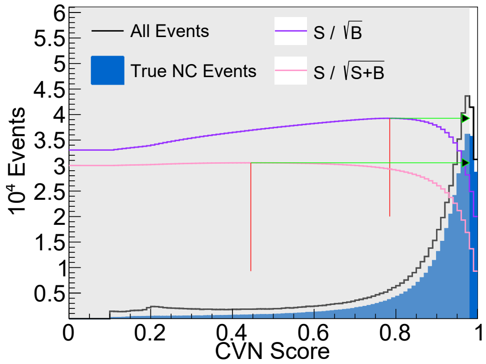

(b) FOM overlaid on the CVN distribution

Figure 5.9: Data/simulation comparisons for the CVN distribution on the left and FOM distribution for **FHC** mode. Here, the true NC events are in blue, and the suggested regions to remove are shown as grey boxes. Note that the simulation has been area-normalised to match the data. In these plots, the quality requirements (Sec. 5.3.2.1), vertex (Sec. 5.3.2.3), and fiducial (Sec. 5.3.2.4) volume criteria have been applied.

Cuts	All Events	True NC Events	CC Backgrounds	Rock Background
PreSelection	5.21e+7	1.55e+7(29.6%)	2.22e+7(42.6%)	1.45e+7(27.8%)
Quality	5.19e+7	1.55e+7(29.9%)	2.22e+7(42.6%)	1.42e+7(27.3%)
Fiducial	1.60e+6	1.04e+6(65%)	402219(25.13%)	161728(10.10%)
All Cuts	1.19e+6	904249(76%)	204384(17.2%)	84596.9(7.1%)

Table 5.3: FHC CutFlow table

FHC (RHC), along with purity values at each stage of the analysis. Furthermore, using a tighter cut on the vertex has reduced the rock background from around 11% to 8%.

Cuts	All Events	True NC Events	CC Backgrounds	Rock Background
PreSelection	1.01e+7	3.12e+6(30.9%)	4.25e+6(42.1%)	2.73e+6(27.0%)
Quality	1.00e+7	3.12e+6(31.2%)	4.25e+6(42.5%)	2.70e+6(27.0%)
Fiducial	293643	210087(71.5%)	50368.9(17.2%)	33186.3(11.3%)
All Cuts	219440	176873(80.6%)	26722.4(12.2%)	15844.9(7.2%)

Table 5.4: RHC CutFlow table

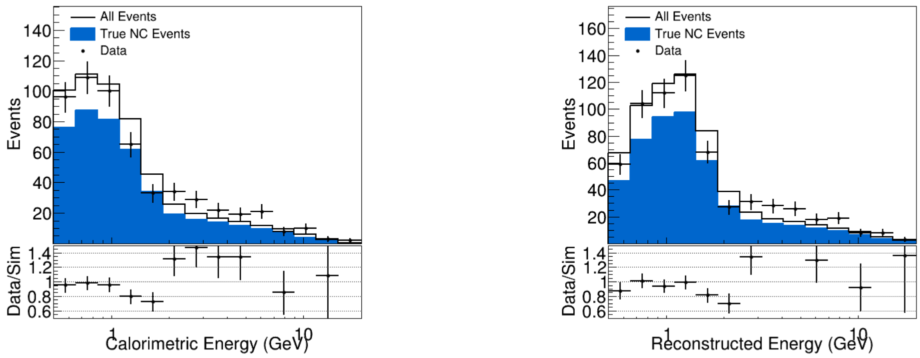

(a) Uncorrected Calorimetric Energy

(b) Corrected Energy

Figure 5.10: Data/simulation comparisons for the uncorrected calorimetric energy on the left and the corrected energy on the right for **FHC** mode. Here, the true NC events are in blue, and the suggested regions to remove are shown as grey boxes. Note that the simulation has been area-normalised to match the data. In these plots, the quality requirements (Sec. 5.3.2.1), vertex (Sec. 5.3.2.3), fiducial (Sec. 5.3.2.4) volume, and CVN (Sec. 5.3.2.5) criteria have been applied.

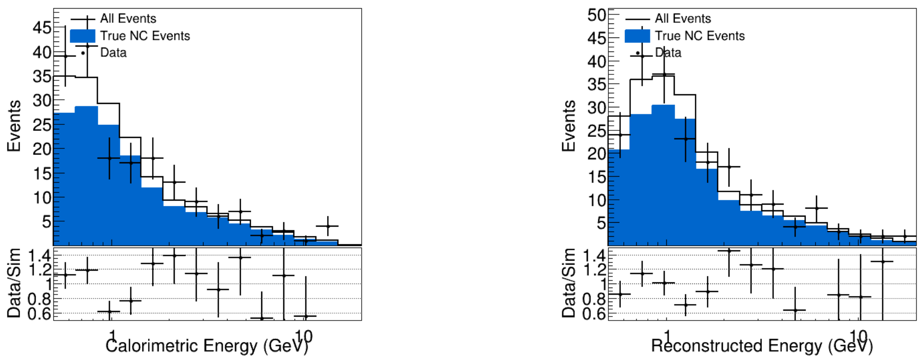

(a) Uncorrected Calorimetric Energy

(b) Corrected Energy

Figure 5.11: Data/simulation comparisons for the uncorrected calorimetric energy on the left and the corrected energy on the right for **RHC** mode. Here, the true NC events are in blue, and the suggested regions to remove are shown as grey boxes. Note that the simulation has been area-normalised to match the data. In these plots, the quality requirements (Sec. 5.3.2.1), vertex (Sec. 5.3.2.3), fiducial (Sec. 5.3.2.4) volume, and CVN (Sec. 5.3.2.5) criteria have been applied.

5.3.3 Far Detector

While the NC events are not affected by the 3-Flavor oscillations, the CC background in there does get impacted; hence, 3F oscillations need to be considered when discussing the FD selections. Similar to the ND, the FD selection cuts can also be broadly classified into Quality, Containment, Selection, and Cosmic Rejection. The cosmic statistics are much larger than the POT-scaled Monte Carlo, so we drop them from the plots for the early parts of the selection. However, we will keep the cosmic in the final cutFlow table for completeness.

5.3.3.1 Quality

We have used the same set of quality cuts for the FD as we have used for ND. The distributions for the selection variables do look normal for both FHC (Fig. 5.12) and RHC (Fig. 5.13).

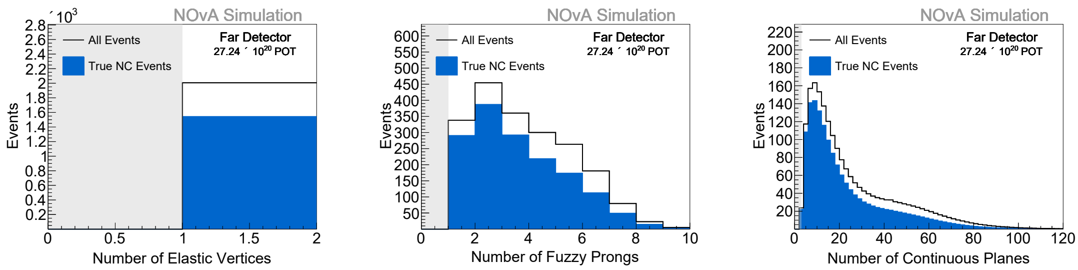

Figure 5.12: Distributions for the Quality Selection Variables for the FHC (ν) mode. The true NC events are highlighted in blue, and the proposed regions to remove are shown as grey boxes.

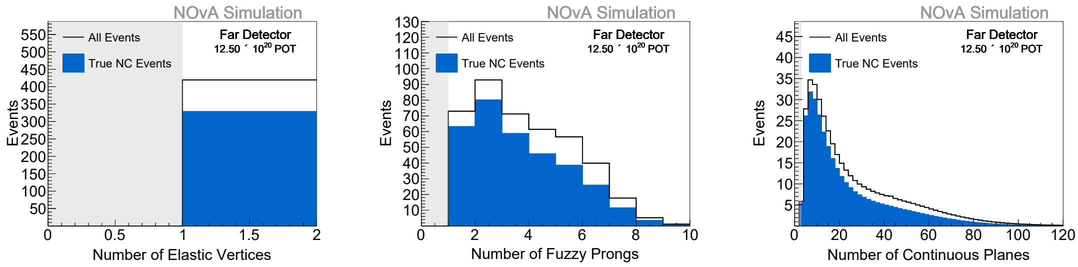

Figure 5.13: Distributions for the Quality Selection Variables for the RHC ($\bar{\nu}$) mode. The true NC events are highlighted in blue, and the proposed regions to remove are shown as grey boxes.

5.3.3.2 Containment

Unlike the ND, only the fiducial volume variable is used to select events at FD. There will be no separate cut applied to the vertex position, as it will be used as the Boosted Decision Tree (BDT) training variable for cosmic rejection. Being on the surface, FD is continuously exposed to the cosmic background, and the vertex is one of the significant distinguishing variables for rejecting the cosmic. The distance of the prong from each side of the FD is shown in Fig. 5.14 for FHC and Fig. 5.15 for RHC.

Cut Type	**Cut Name**	**Cut Value (cm)**
Fiducial		
	kDistAllTop	> 100
	kDistAllBottom	> 100
	kDistAllEast	> 100
	kDistAllWest	> 100
	kDistAllFront	> 160
	kDistAllBack	> 160

Table 5.5: FD Fiducial Volume Cuts applied for the analysis.

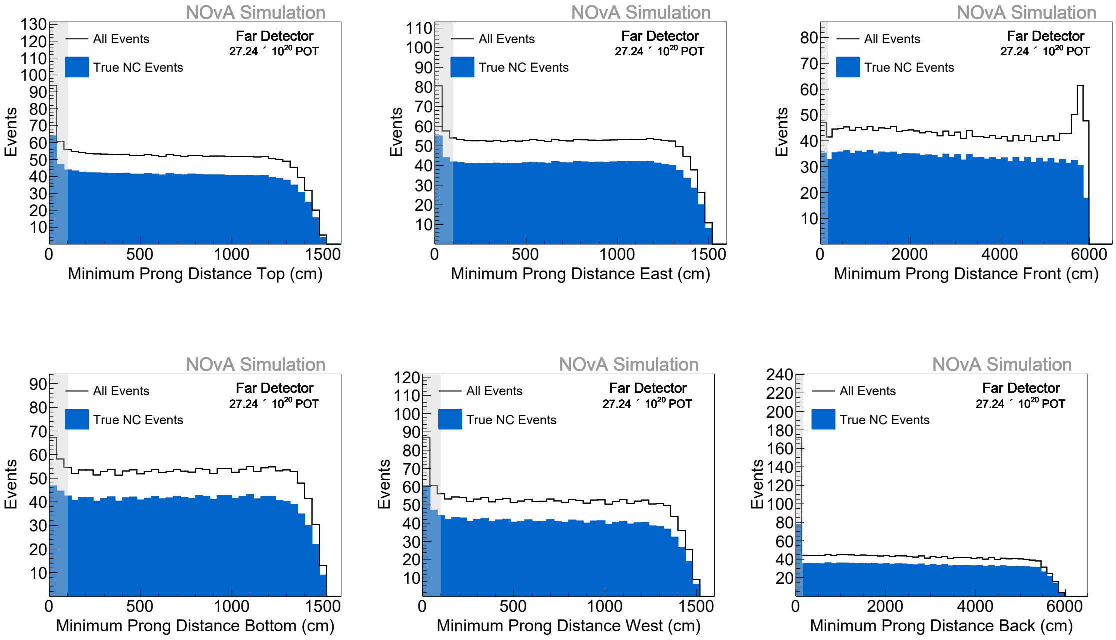

Figure 5.14: Distributions for the Quality Selection Variables for the FHC (ν) mode. The true NC events are highlighted in blue, and the proposed regions to remove are shown as grey boxes.

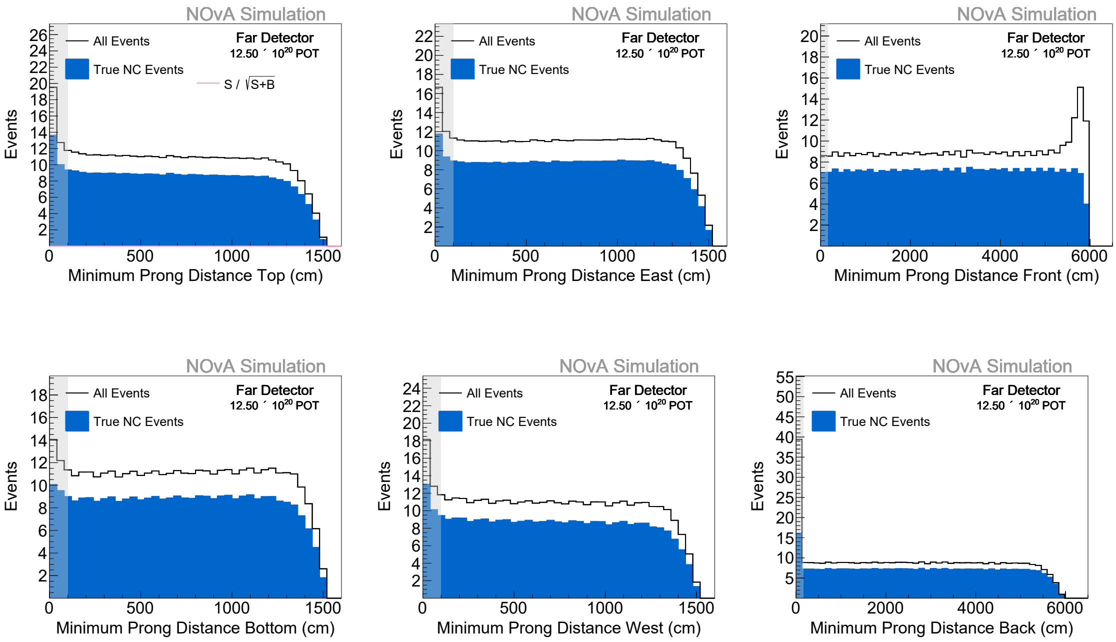

Figure 5.15: Distributions for the distance of prong from the sides of the detector for the RHC ($\bar{\nu}$) mode. The true NC events are highlighted in blue, and the proposed regions to remove are shown as grey boxes.

5.3.3.3 CVN Selection

Similar to the previous analysis, two separate selections are used for cosmic rejection and the MC background rejection. CVN score is used to reject the MC background from the true NC signal, and we have used the 0.1 value for the selection. The LoosePTP CVN distribution is shown in Fig. 5.16a for FHC and Fig. 5.16b for RHC.

Cut Type	Cut Name	Cut Value
Fiducial		
	kCVNnc_looseptp	> 0.1

Table 5.6: FD NC Selection Cuts applied for the analysis.

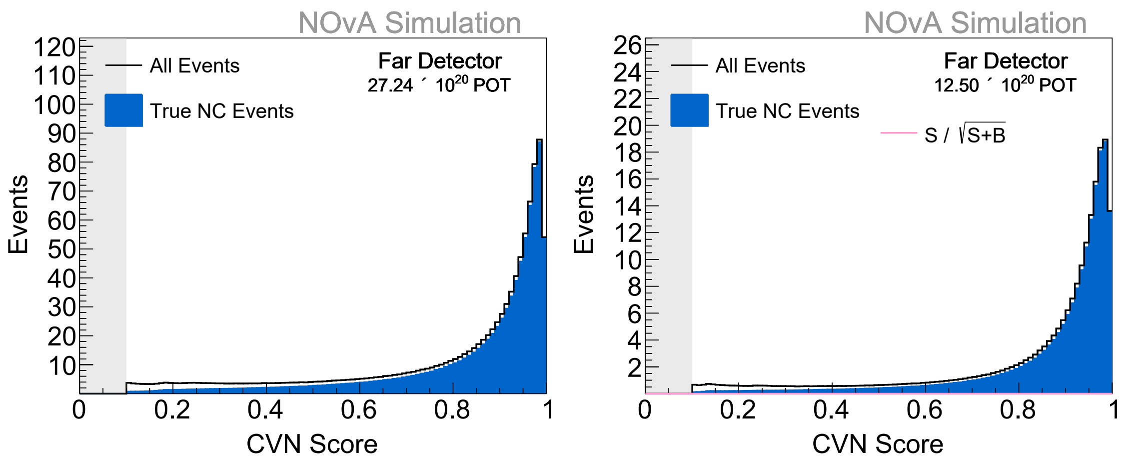

(a) FHC (ν) mode

(b) RHC ($\bar{\nu}$) mode

Figure 5.16: Distributions of LoosePTP CVN for FHC (ν) in (a) and RHC ($\bar{\nu}$) mode in (b). The true NC events are highlighted in blue, and the proposed regions to remove are shown as grey boxes.

5.3.3.4 Cosmic Rejection BDT

Being on the surface, the FD is constantly exposed to the cosmic, which makes it one primary source of the background for the analysis. The list of variables used for the BDT training is shown in Tab. 5.8.

Cut Type	**Cut Name**	**Cut Value**
Fiducial		
	kNus5p1CosRej	> 0.85

Table 5.7: FD Cosmic Rejection BDT Cuts applied for the analysis.

Variable name	**Description**
vtxx	Vertex X Position
vtxy	Vertex Y Position
vtxz	Vertex Z Position
ncontplanes	number of continuous planes
nhitsperslice	number of hits in the slice
nhitsperplane	Average number of hits per plane
nmiphits	Number of MIP-like hits
closestslicetime	Closest slice in time to this slice
closestslicemindist	Closest slice in distance to this slice
nshowers	Number of Reconstructed showers
showercale	Shower Calorimetric Energy
showergap	distance between reconstructed vertex and start of shower
showerdirycosine	Shower Y direction cosine
showerlength	Shower Length
showerwidth	Shower Width
shwhitx	number of hits in the shower in X plane
shwhity	number of hits in the shower in Y plane
shwhittot	Total number of hits in the shower
shwhitasymm	shower hit X - Shower hit Y
shwhitratio	shower hit X / Shower hit Y

Table 5.8: Variable names and description used for BDT training

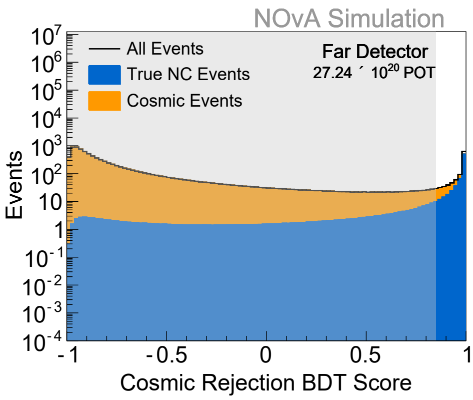

(a) FHC Cosmic Rejection BDT

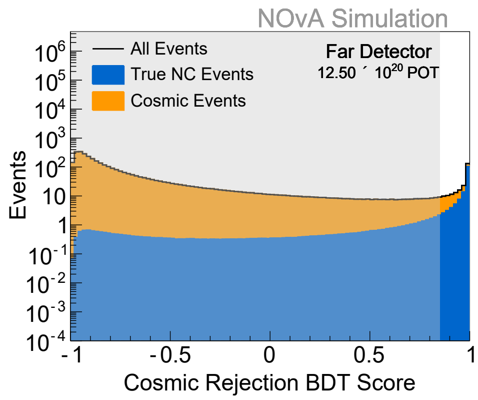

(b) RHC Cosmic Rejection BDT

Figure 5.17: Simulation distributions of the Cosmic Rejection BDT for FHC on the left and RHC on the right. Here, the true NC events are in blue, and the cosmic events are displayed in orange. These plots have the quality, prong distance to edge, and CVN requirements.

Cuts	All Events	True NC Events	MC bkg	Cosmic bkg
PreSelection	78067.8	1545.73(1.98%)	463.22(0.59%)	76058.8(97.42%)
Quality	77696.5	1543.16(1.98%)	463.049(0.59%)	75690.3(97.42%)
Fiducial	10667.5	890.3(8.34%)	146.71(1.38%)	9630.47(90.28%)
CVN	10667.5	890.3(8.34%)	146.71(1.38%)	9630.47(90.28%)
All Cuts	913.252	646.089(70.75%)	123.179(13.49%)	143.984(15.8%)

Table 5.9: FHC CutFlow table. The numbers in the brackets are the respective numbers divided by the total number of selected events.

5.3.3.5 Full Selection

The final Calorimetric Energy and reconstructed energy distribution for FD are shown in Fig. 5.18 for FHC and Fig. 5.19 for RHC. Furthermore, the BDT distributions are shown for FHC in Fig. 5.17a and RHC in Fig. 5.17b. Tab. 5.9 (Tab. 5.10) provides the number of selected events for FHC (RHC), along with purity values at each stage of the analysis.

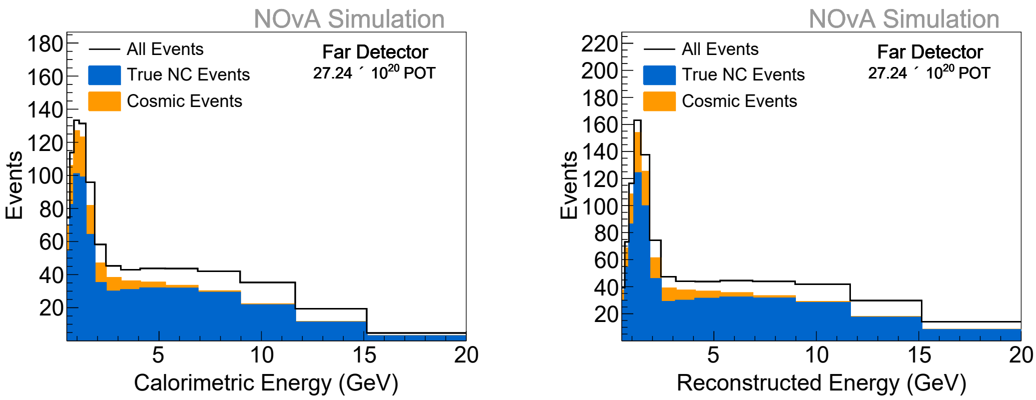

(a) Uncorrected Calorimetric Energy (b) Corrected Energy

Figure 5.18: Simulation distributions for the uncorrected calorimetric energy, the left, and the corrected energy on the right for **FHC** mode. Here, the true NC events are in blue, and the cosmic events are displayed in orange. These plots meet the quality, prong distance to edge, and CVN requirements, as well as the cosmic BDT.

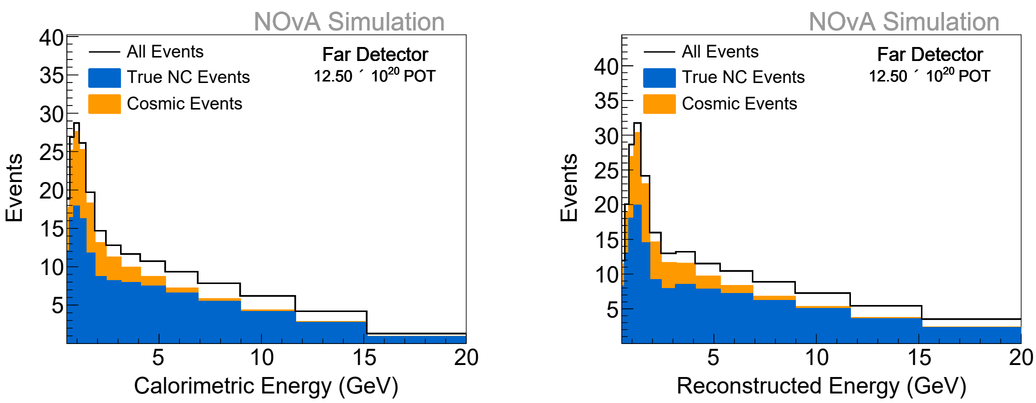

(a) Uncorrected Calorimetric Energy (b) Corrected Energy

Figure 5.19: Simulation distributions for the uncorrected calorimetric energy, the left, and the corrected energy on the right for **RHC** mode. Here, the true NC events are in blue, and the cosmic events are displayed in orange. These plots meet the quality, prong distance to edge, and CVN requirements, as well as the cosmic BDT.

Cuts	All Events	True NC Events	MC bkg	Cosmic bkg
PreSelection	28819.4	329.287(1.14%)	90.9075(0.31%)	28399.2(98.54%)
Quality	28679.4	328.633(1.14%)	90.8707(0.31%)	28259.9(98.53%)
Fiducial	3818.86	188.868(4.95%)	26.2026(0.68%)	3603.79(94.37%)
CVN	3818.86	188.868(4.95%)	26.2026(0.68%)	3603.79(94.37%)
All Cuts	205.878	130.976(63.62%)	21.578(10.5%)	53.3233(25.9%)

Table 5.10: RHC CutFlow table. The numbers in the brackets are the respective numbers divided by the total number of selected events.

5.4 ν_μ CC Event Selection

For the ν_μ disappearance channel, we adopt the same selection cuts, energy binning, and energy estimator as described in [70]. The cut flow chart for ν_μ CC selection is shown in Fig. 5.20 which is followed by a detailed summary of each selection cut.

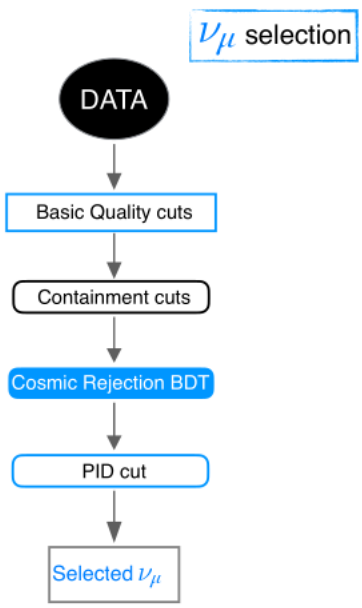

Figure 5.20: Flowchart showing the cut flow for the ν_μ-selection.

5.4.1 Spill and Data Quality Cuts

During data-taking, there are occasional beam failures and detector instability that result in degraded data quality. To mitigate such effects, the detector and beam quality cuts were applied at the spill level. To ensure a good quality beam, the spill POT must exceed 2×10^{12} within the beam spill duration of less than $0.5\times10^9\ ns$. Additionally, the following cuts should also be imposed to ensure a good beam.

- The horn current for the beam should be in the range $-202 < I_{horn} < -198$.
- The range of X beam position is $-2 <$ xpos < 2.
- The range of Y beam position is $-2 <$ ypos < 2.
- The X width of the beam is $0.57 <$ xwidth < 1.58.
- The Y width of the beam is $0.57 <$ xwidth < 1.58.

In addition to the beam quality requirements, we also require the detector to be in a stable condition to obtain good-quality events for reliable reconstruction. The detector quality cuts are applied to remove any events with one or more issues in the data concentrator module (DCM). We first check the discontinuities in the hit patterns at the boundaries of the DCM to catch out-of-sync DCMs. We therefore check for any non-functioning DCM during the spill that cease to record hits during the spill. The following set of cuts needs to be applied to ensure the proper detector conditions.

- No missing DCM signal in the FD.

- Fraction of allowed DCM edge matching in the FD is greater than 0.2.
- Fraction of 3 consecutive DCM hits in the ND must be less than 0.45.

Finally, the timing peak of the beam must be within the 217-229 µs beam spill window of the 550 ns NuMI trigger. Only data within this window is used in the analysis. This timing cut is expected to reduce approximately 0.2% of the total FHC POT, which is allocated to the uncertainty budget, and to reduce the total livetime by about 7%.

5.4.2 Quality Cut

ν_μ events are characterised by the outgoing μ which we need to reconstruct. In general, the selection of the ν_μ sample is fairly simple compared to the NC or ν_e events. The basic quality cuts are imposed to ensure a properly reconstructed ν_μ event. The following selection criteria constitute the quality cuts:

- no. of reconstructed prong ≥ 1,
- no. of hits in the slice > 20,
- Track Energy > 0,
- no. of contiguous planes > 4.

In addition to these selection criteria, there must be a reconstructed Kalman track that can be used for ν_μ energy estimation, and the reconstructed energy must be below 5 GeV for a ν_μ CC event.

5.4.3 Containment Cuts

The idea of imposing the containment cut for ν_μ CC events is the same as that of the NC selection, which is to reduce the rock-induced ν_μ events in the ND and cosmic events in the FD. The idea is to keep the events inside the detector fiducial volume to ensure proper energy reconstruction without missing energy. A selection cut is applied on the distance of reconstructed prongs from each side of the detector, which are given in Tab. 5.11.

Cut Type	**Cut Name**	**Cut Value**
Fiducial		
	kDistAllTop	> 63
	kDistAllBottom	> 12
	kDistAllEast	> 12
	kDistAllWest	> 12
	kDistAllFront	> 18
	kDistAllBack	> 18

Table 5.11: Prong distance from each side of the detector.

A special containment cut is made for the identified muon track to reconstruct the track length in the energy estimation. Furthermore, to ensure the proper reconstruction of the track length in the energy estimation, a special cut is applied to identify the muon track. The prongs must extend to at least two active detector planes to the front and three from the back of the detector. Furthermore, the forward and background projections of the track must pass through at least six planes before nearing the edges of the detector. An additional cut of the shower vertex is also applied ($z_{min} > 40$ cm) at the ND.

5.4.4 Signal Selection and Cosmic Rejection

Similar to NC events, the ν_μ events are also prone to contamination from rock-induced events at ND and cosmics at FD. There are three different PIDs used to select the ν_μ CC signal events, which include event CVN, ReMId, and a BDT for cosmic rejection. Cosmic ray muons can easily be misidentified as the muon produced by NuMI ν_μ CC interactions. However, it has certain features that are used to identify and reject such events. These features are used to train the BDT for cosmic rejection.

In addition to the cosmic BDT, we use the **C**onvolutional **N**eural **N**etwork trained variables as well to identify different particles such as event CVN and ReMId score. CVN is trained to take the event slice and assign a score to each event, regardless of whether it is a ν_μ, ν_e, or cosmic event. Furthermore, **R**econstructed **M**uon **Id**entifier (ReMId) is another method used to identify the muon tracks based on the k-Nearest-Neighbour (kNN) algorithm, dE/dx, track's scattering length, and non-hadronic plane fraction [71].

- Cosine of the track angle with respect to the direction of the NuMI beamline (z-direction).
- Track length of the muon.
- Maximum vertical coordinates of particle's track.

- Distance of particle's track from the detector walls.
- Cosine of the track's angle with respect to the vertical axis (y-axis).
- Hits in the track compared to the entire event.
- Normalized transverse momentum (P_i/P) of the particle.

FOM optimisation was performed simultaneously for all three PIDs. Table 5.12 shows the event classifiers and corresponding scores used for both polarities. With all three PIDs, the FHC and the RHC selection of ν_μ CC events achieves a purity of 96% and 97%, respectively.

PID Classifier	Minimum Score
CosRej BDT	0.45
ReMId	0.30
EventCVN	0.80

Table 5.12: Three PID Classifiers and their minimum PID scores for ν_μ CC interaction for both FHC and RHC modes.

5.5 Energy Reconstruction

In general, neutrino oscillation experiments involve comparing observed event distributions with predicted ones, assuming no oscillations. The oscillation probabilities are particularly dependent on two factors: neutrino energy and the baseline. For NOvA, the baseline is kept fixed at 810 km, making the measurements particularly sensitive to true neutrino energy. A critical aspect of the oscillation analysis is an accurate estimation of the energy of neutrino signal candidates.

The energy reconstruction is basically done in three steps. The first step is calibration, which includes evaluating and adjusting the raw data to ensure consistent energy translation among hits, over time, and comparability to the simulation. The second step includes the event reconstruction, where the calibrated hits are grouped into events and prongs. In the final step, an energy estimator is constructed, which varies from analysis to analysis.

5.6 Neutral Current Energy Estimator

Neutral Current (NC) interactions occur when a neutrino interacts with a target nucleus via the exchange of a Z-boson, resulting in no outgoing charged lepton. Instead, these interactions produce a cascade of secondary particles, primarily hadrons and, to a lesser extent, electromagnetic (EM) particles. The energy of the incoming neutrino (E_ν) is partially transferred to these secondary particles, leading to what we term deposited energy (E_{Dep}).

The deposited energy, E_{Dep}, is the energy imparted to the detector by the resulting hadronic and EM showers. This can be mathematically represented as $E_{Dep} = y \times E_\nu$, where E_ν is the incoming neutrino energy, and y is the inelasticity parameter, indicating the fraction of the neutrino's energy transferred to the showers. The value of y varies depending on the specifics of the interaction and the particles' kinematics. Since directly determining E_ν is not feasible, we aim to estimate the deposited energy through calorimetric energy derived from reconstructed quantities.

We use the difference $\Delta E = (E_{Dep} - E_{cal/est})/E_{Dep}$ as a measure of the energy estimator's efficiency. The closer this value is to zero, the more accurate the estimator is. Additionally, a narrower spread of ΔE indicates better resolution and a more precise estimator. The energy estimator should be developed using true NC events with the interaction vertex contained within the detector. Therefore, we focus on events that meet our selection criteria, as those that escape the detector could lead to an overestimation of deposited energy. We must also consider true NC events, as neutrons in NC interactions may cause an underestimation of the energy.

5.6.1 First Order Scaling

The energy estimator is developed in two primary steps. The first step involves scaling the hadronic and EM-dominated events using a Gaussian fit. In contrast, the second step corrects any remaining bias through a functional fit (an example is provided in Eq. (5.8)). As shown in Fig. 5.21, ΔE significantly deviates from zero, underestimating the deposited energy for the selected events.

To address this, the events are categorised into hadronic and EM-like groups. An event is classified as hadronic if it contains at least one neutron or charged pion but no neutral pions. In contrast, an event is considered EM-like if it has at least one neutral pion and no neutrons or charged pions. The bias distributions for each sample's

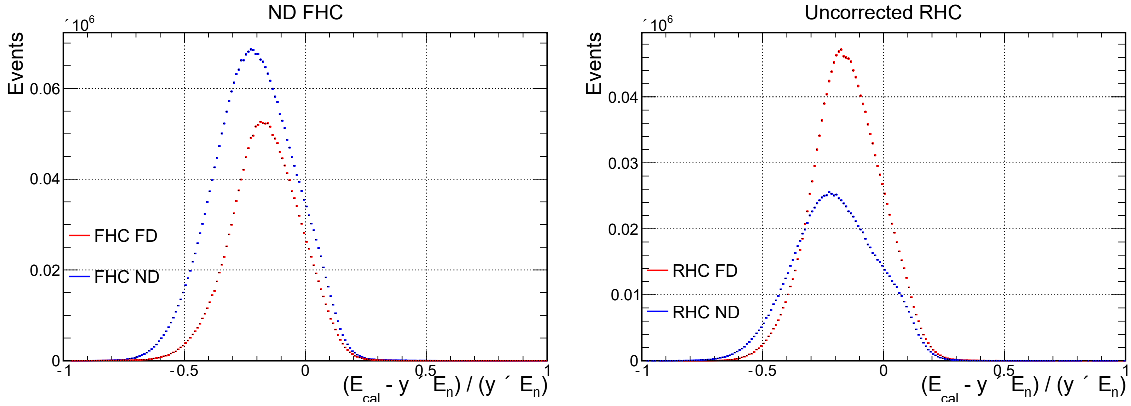

Figure 5.21: These distributions show the uncorrected energy distribution for FHC on the left and RHC on the right.

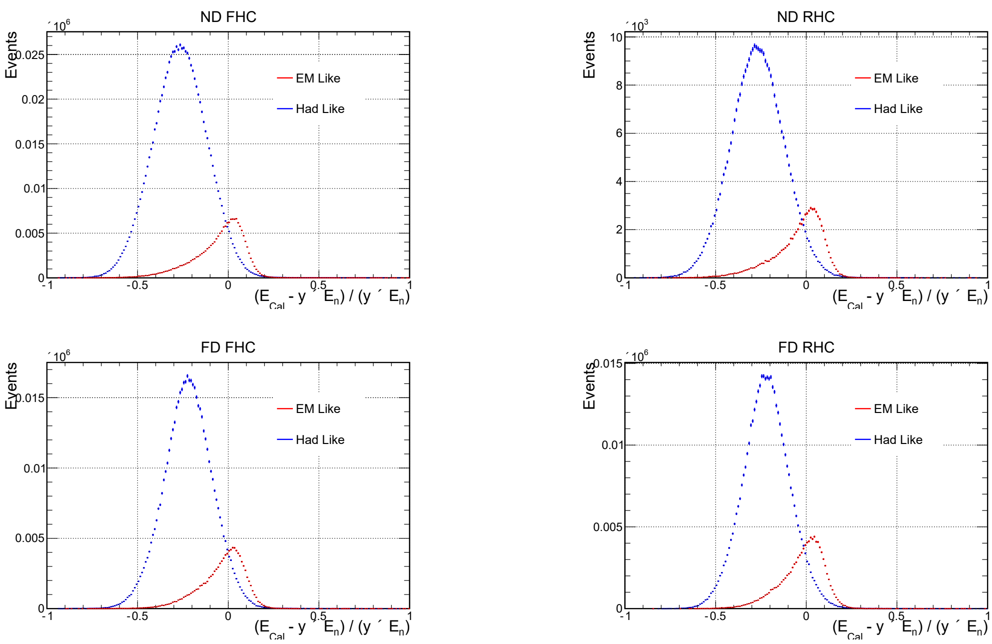

Figure 5.22: These distributions show the hadronic and electromagnetic dominated events for ND FHC on the top left, ND RHC on the top right, FD FHC on the bottom left, and FD RHC on the bottom right.

hadronic and EM-dominated events are illustrated in Fig. 5.22.

A Gaussian fit is applied to each distribution, concentrating on the region where the bias values reach 75% of their maximum. This 75% threshold is chosen empirically, as the distributions maintain a Gaussian shape within this range but deviate from it outside. The means (μ) derived from these fits are then used to define the first-order corrected energy estimator as follows:

$$E_{first\,correction} = \frac{E_{EM}}{A} + \frac{E_{had}}{B} \tag{5.6}$$

Here, E_{EM} represents the total energy deposited by the EM prongs, while $E_{had} = E_{Cal} - E_{EM}$ denotes the total hadronic energy associated with the selected events. A and B coefficients are determined through a Gaussian fit (Eq. (5.7)) and are used to scale the energy according to the event characteristics. Events with a bias already close to zero require minimal scaling. At the same time, those with a significant bias necessitate more substantial scaling corrections. Tab. 5.13 presents the parameter values alongside the Gaussian fit means.

$$A = \frac{1}{1+\mu_{EM}}, \quad B = \frac{1}{1+\mu_{had}} \tag{5.7}$$

	ND		FD	
	FHC	RHC	FHC	RHC
A	1.023	1.029	1.022	1.032
B	0.735	0.730	0.779	0.778

Table 5.13: Table showing the values of first-order scaling corrections.

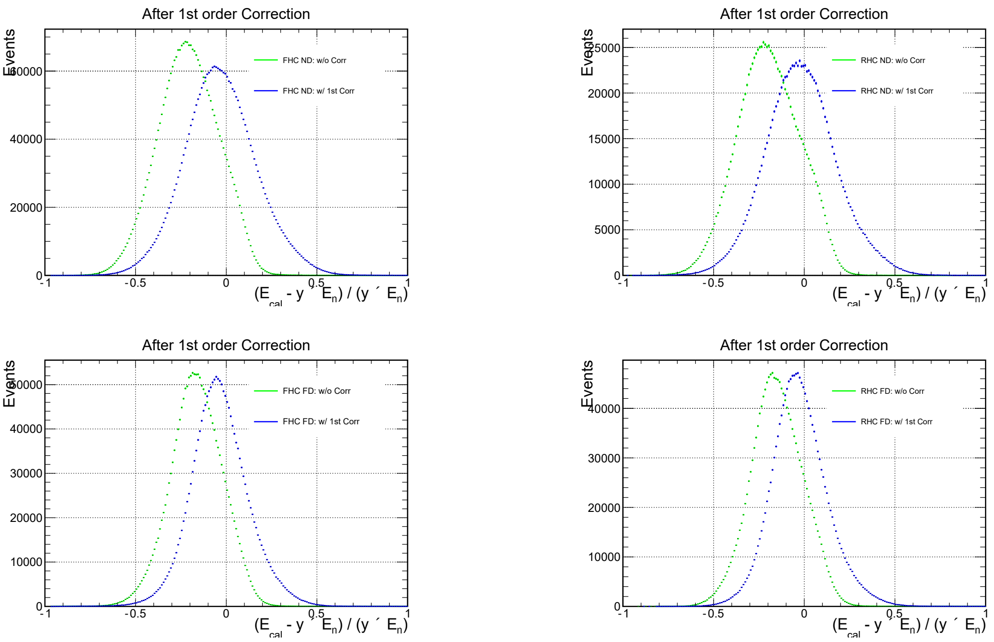

Figure 5.23: These distributions show the first-order corrected bias for ND FHC on the top left, ND RHC on the top right, FD FHC on the bottom left, and FD RHC on the bottom right.

5.6.2 Second Order Correction

After the first-order correction, we then calculate the remaining bias using the first-order corrected energy, $\Delta E_{Corr} = (E_{Corr} - E_{Dep})/E_{Dep}$, where E_{Corr} is the first-order corrected energy. Fig. 5.24 shows the remaining bias after the correction for each sample. We use the same functional form for the second-order correction as in the previous analysis.

$$f(E_{Cal}) = P(E_{Cal} + Q)^2.exp(-R * E_{Cal}) + S \qquad (5.8)$$

However, this functional form does not perform uniformly well across all loose ND CVN values. For this analysis, a loose ND CVN score (ND CVN $>$ 0.5) will be employed (Fig. 5.9b). It has been observed that the function inadequately captures the remaining bias,

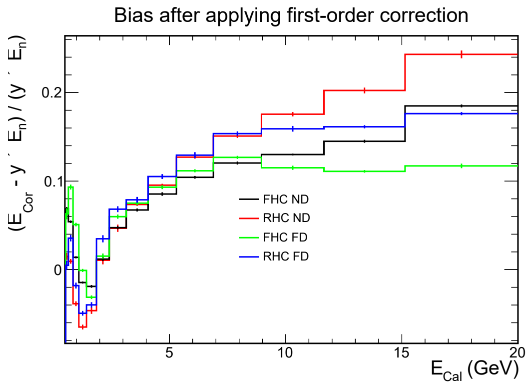

Figure 5.24: Distribution showing the remaining bias for each of the samples.

particularly at low energies and notably within the RHC samples. The remaining bias exhibits a non-curved structure at low energies, which we fit with an exponential (Fig. 5.25). Therefore, we explored alternative fit functions capable of accurately modelling all samples across the entire energy range, examining different energy bins. In this note, we focus on the specific function that was ultimately used, with details on the other approaches provided in the Appendix.

5.6.3 TGraphSmooth Fit

This analysis employs the TGraphSmooth fit class to address the remaining bias. TGraphSmooth is a ROOT class that utilises various algorithms to smooth a graph. This approach is helpful in situations where the fluctuations in the fit points are significant, and no clear underlying trend exists in the data points.

5.6.4 Lowess Algorithm

LOWESS (Locally Weighted Scatterplot Smoothing), or LOESS (Locally Estimated Scatterplot Smoothing), is a non-parametric

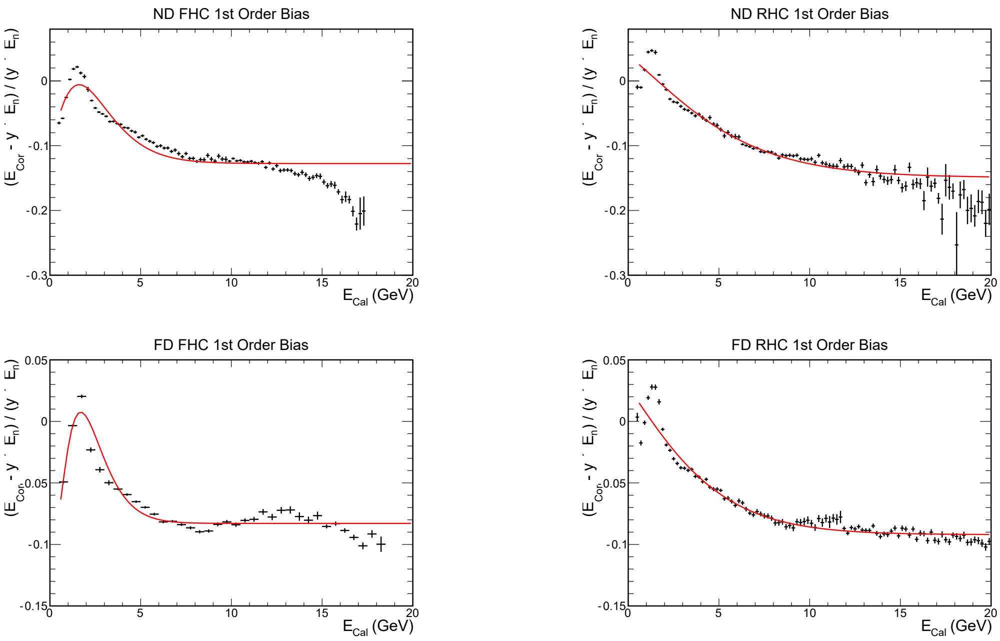

Figure 5.25: These distributions show the remaining first-order bias fitted with the functional form in Eq. (5.8) for ND FHC on the top left, ND RHC on the top right, FD FHC on the bottom left, and FD RHC on the bottom right.

method to fit a smooth curve to scatterplot data. It is valuable when the relationship between variables is complex and does not follow a simple linear or polynomial pattern. This algorithm operates by fitting simple models (typically linear or quadratic) to localised subsets of data rather than applying a single model across the entire dataset. It considers a small neighbourhood of nearby data points for each point and fits a model to this subset, focusing on the local context. A weighted regression is performed for each data point using nearby points, with more weight given to those closer to the target point.

The weight given to each neighbouring point is based on its distance from the target point, with points closer to the target receiving more influence. This weighting is often done using a tri-cube weight function:

$$W(x_i) = \left(1 - \left(\frac{|x_i - x|}{D}\right)^3\right)^3 \tag{5.9}$$

Here, x_i represents a point in the local neighbourhood, x is the target point, and D is the maximum distance within the neighbourhood.

In Lowess smoothing, one of the critical parameters is the span, also known as the bandwidth, which determines the fraction of data points included in each local regression. A larger span results in a smoother curve by incorporating more data points in each fit, which can smooth out local variations but might miss finer details. Conversely, a smaller span captures more intricate patterns in the data but may introduce noise.

In this context, a span value of 0.1 GeV is chosen to strike a balance between smoothness and detail for the given data. After calculating the weights, a weighted least squares regression is applied within the local neighbourhood, from which the smoothed value for the target point is obtained. This process is repeated for each data point, generating a smooth curve that accurately reflects the overall trend in the dataset.

Another important parameter in Lowess is the number of iterations used to refine the smoothing process. In this case, the number of iterations is set to 3, which typically offers a good compromise between precision and computational efficiency. While increasing the number of iterations can yield a more refined fit, it also significantly increases the computational resources and time required.

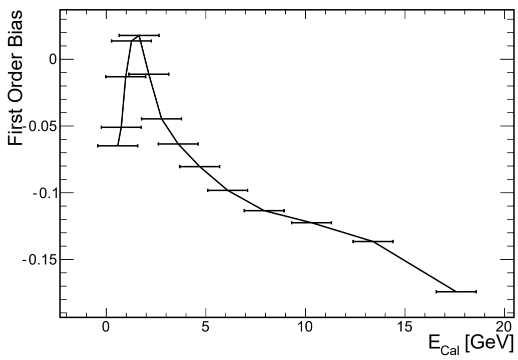

Figure 5.26: This distribution shows the TGraphSmooth fit function

Fig. 5.26 illustrates the TGraphSmooth fit function applied using the specified parameter values. Additionally, Fig. 5.27 displays the smoothed curve superimposed on the original data points, highlighting an excellent fit. In this analysis, we maintained the 30% energy resolution binning, consistent with prior studies, while evaluating alternative binning strategies. The final corrected energy is the combination of both first-order scaling and second-order correction done using the TGraphSmooth, which is given by:

$$E_{Corr} = \frac{E_{first\,correction}}{1 + ogs} \tag{5.10}$$

Here, $E_{first\,correction}$ is the first order corrected energy given in Eq. (5.6), and the ogs is the TGraphSmooth algorithm fit.

For the first-order bias fit, we will use the binning defined as:

$$\begin{aligned} Binning = 0.5, 0.65, 0.85, 1.10, 1.43, 1.86, 2.41, 3.14, \\ 4.08, 5.30, 6.89, 8.96, 11.65, 15.14, 20 \end{aligned}$$

5.6.5 Final Estimated Energy

The final corrected estimated energy is given by Eq. (5.10), and Fig. 5.25 represents the first-order corrected energy. We observe

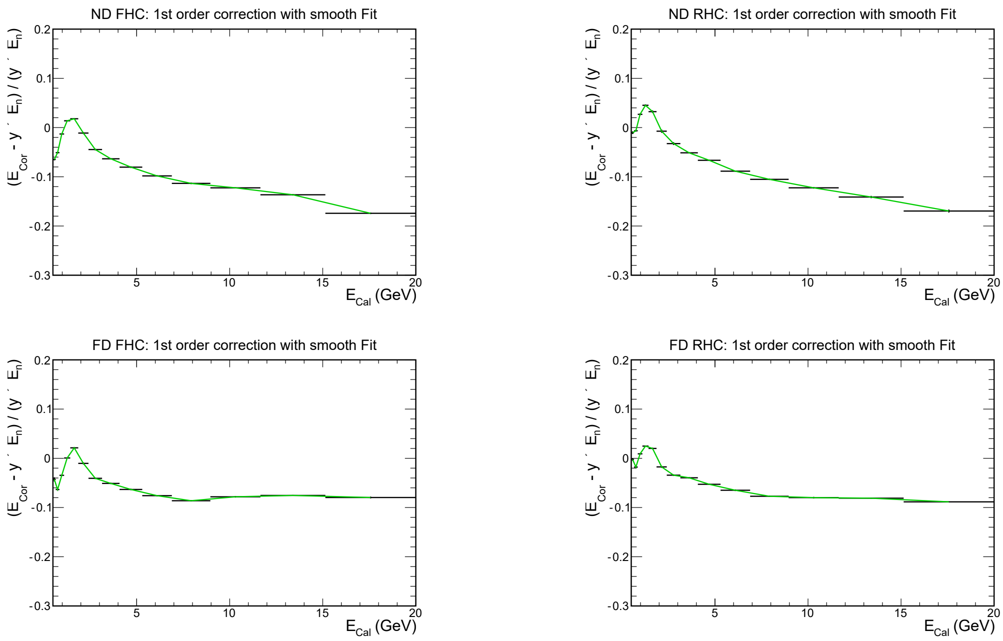

Figure 5.27: These distributions show the TGraphSmooth fit overlaid with the data points for ND FHC on the top left, ND RHC on the top right, FD FHC on the bottom left, and FD RHC on the bottom right.

that the hadronic and EM scaling still leave a bias, which requires further correction. Using the TGraphSmooth to fit the first-order bias leaves almost zero bias to correct with (Fig. 5.28). The final corrected energy distribution is shown in Fig. 5.29. Furthermore, Tab. 5.14 shows the corrected mean energy and the corrected distribution width compared to the uncorrected ones. We found that the corrected energy distribution is very closely peaked at 0, implying a good energy estimator.

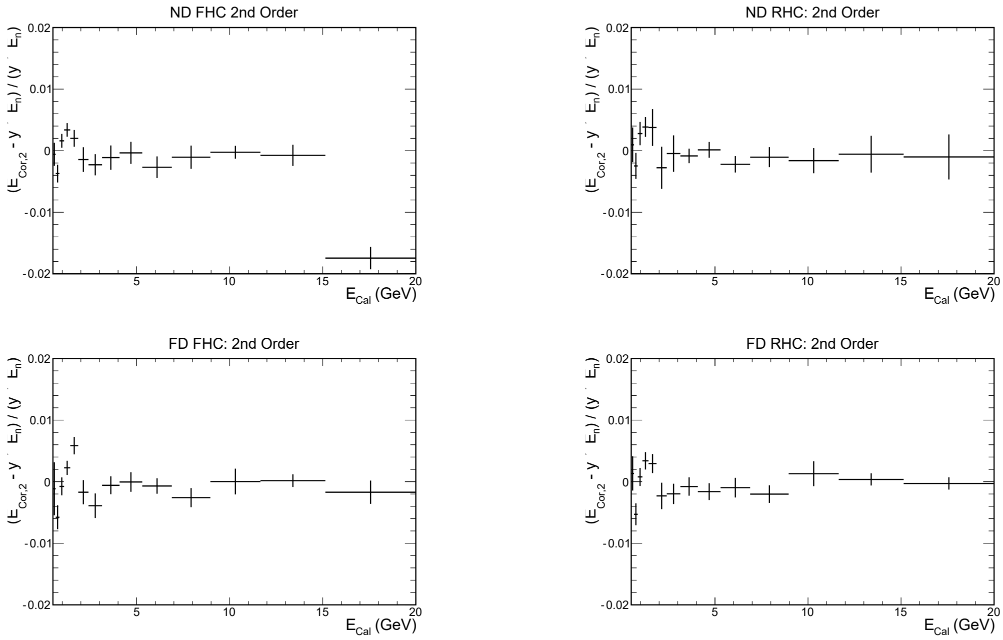

Figure 5.28: These distributions show remaining bias after fitting with TGraphSmooth for all the samples

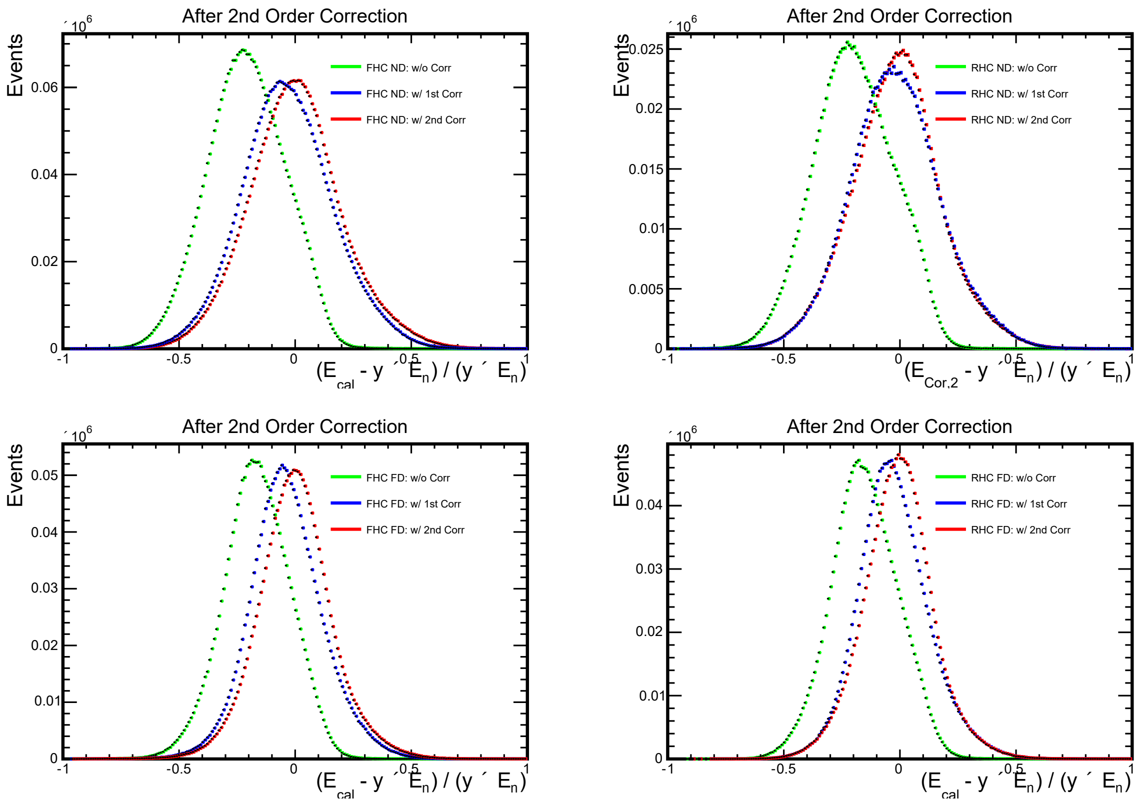

Figure 5.29: Distributions showing the final corrected energy for all the samples, compared with the uncorrected and first-order corrected energy.

Sample	ND		FD	
	FHC	RHC	FHC	RHC
Uncorrected Energy mean	**-0.217**	**-0.214**	**-0.169**	**-0.165**
Corrected Energy mean	0.0016	0.0039	-0.0009	0.0006
Uncorrected Energy width	**0.40**	**0.42**	**0.31**	**0.32**
Corrected Energy width	0.41	0.39	0.3	0.29

Table 5.14: Table showing the width and energy of corrected and uncorrected distributions

5.7 ν_μ Energy Reconstruction

For ν_μ oscillation analysis, the energy range of 1–3 GeV is of particular interest, as the ν_μ oscillation probability at the FD is maximal within this region. ν_μ CC events are primarily identified by an outgoing muon (μ), which typically produces a long, straight track inside the detector and is straightforward to reconstruct. This muon track constitutes a significant amount of energy for the events, while the remaining energy originates from hadronic activity resulting from the non-leptonic particles of the interaction. Therefore, the incoming neutrino (E_ν) energy is estimated as the sum of the muon and hadronic energy components, expressed as:

$$E_\nu = E_\mu + E_{Had} \tag{5.11}$$

where E_ν is the energy of incoming neutrino, E_μ is the reconstructed muon energy, and E_{Had} is the energy of reconstructed hadrons. Fig. 5.30 shows the example of a selected ν_μ event with reconstructed neutrino energy of 2.94 GeV.

The muon energy denoted by E_μ is estimated based on its re-

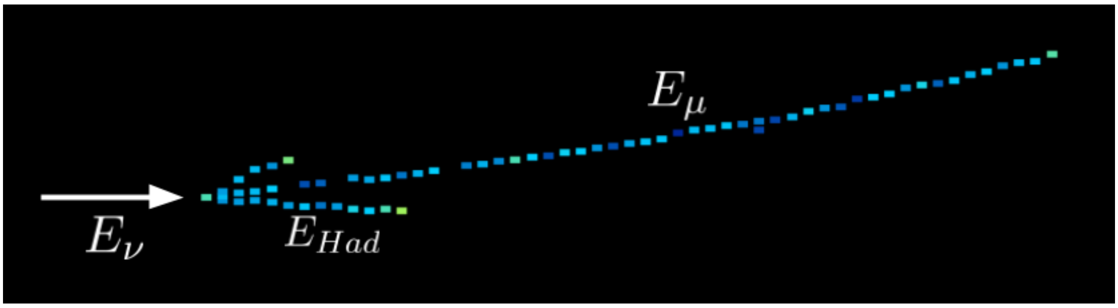

Figure 5.30: An example of the FHC event selected by the numu 2024 analysis. The CVN score for this event is 0.999912, and the reconstructed energy is 2.94707 GeV. The arrow shows the incoming muon neutrino from left and outgoing hadronic (E_{had}) and leptonic (E_μ) energy components [72].

constructed track length. In contrast, the hadronic energy E_{Had} is calculated by subtracting the muon energy (E_μ) from the total energy deposited in the detector. A critical component in reconstructing the E_μ is the identification of outgoing muon (μ), which is accomplished using the *Reconstructed Muon Identifier (ReMId)*. The ReMId is a Boosted Decision Tree (BDT) algorithm used in the NOvA to classify reconstructed muons as being consistent with charged current (CC) interactions or other muon-like signatures [73, 74]. ReMId exploits the characteristic long, straight tracks for muon, which are typically well-reconstructed and identified using a Kalman filter-based algorithm. The energy associated with the hits along this Kalman track constitutes the reconstructed muon energy. The reconstructed track length from the muon is plotted against simulated true muon energy. A piecewise linear spline fit is performed at each track length bin in this parameter space through a Gaussian means procedure [75]. The spline fit achieves an approximate 3% energy resolution for estimating E_μ.

The reconstruction of the hadronic component E_{Had} follows a similar approach but differs in the implementation due to the nature of hadronic showers. Unlike muons, hadronic showers do not have clean, long tracks. Instead, the reconstruction relies on the total calorimetric energy deposition in the event slice. To estimate the hadronic energy, the previously determined energy (E_μ) is subtracted from the total deposited energy in the slice event. This comprises what is called the visible hadronic energy, and this method prevents energy overestimation, for example, from the overlapping of the muon track near the interaction vertex. The visible hadronic energy is then plotted against the true E_ν - E_μ energy, with an additional spline fit performed. This method yields an energy resolution of approximately 26%. Combined with the precise resolution from the reconstruction of E_μ, the total incoming energy resolution for events at the FD is found to be 9.1%(8.2%) for neutrinos(antineutrinos) [76]. Fig. 5.31 displays the spline fits for each of the E_μ and $E_{\ rmHad}$ estimations, for both neutrinos (FHC) and antineutrinos (RHC).

5.8 Summary

This chapter provides a comprehensive overview of the selection and the energy reconstruction of the selected events. It begins with the discussion of event topology forming the basis of event selection strategy. Following this, a detailed description of the neutral current event selection and energy reconstruction for this analysis is presented. Finally, an overview of the ν_μ event selection and energy

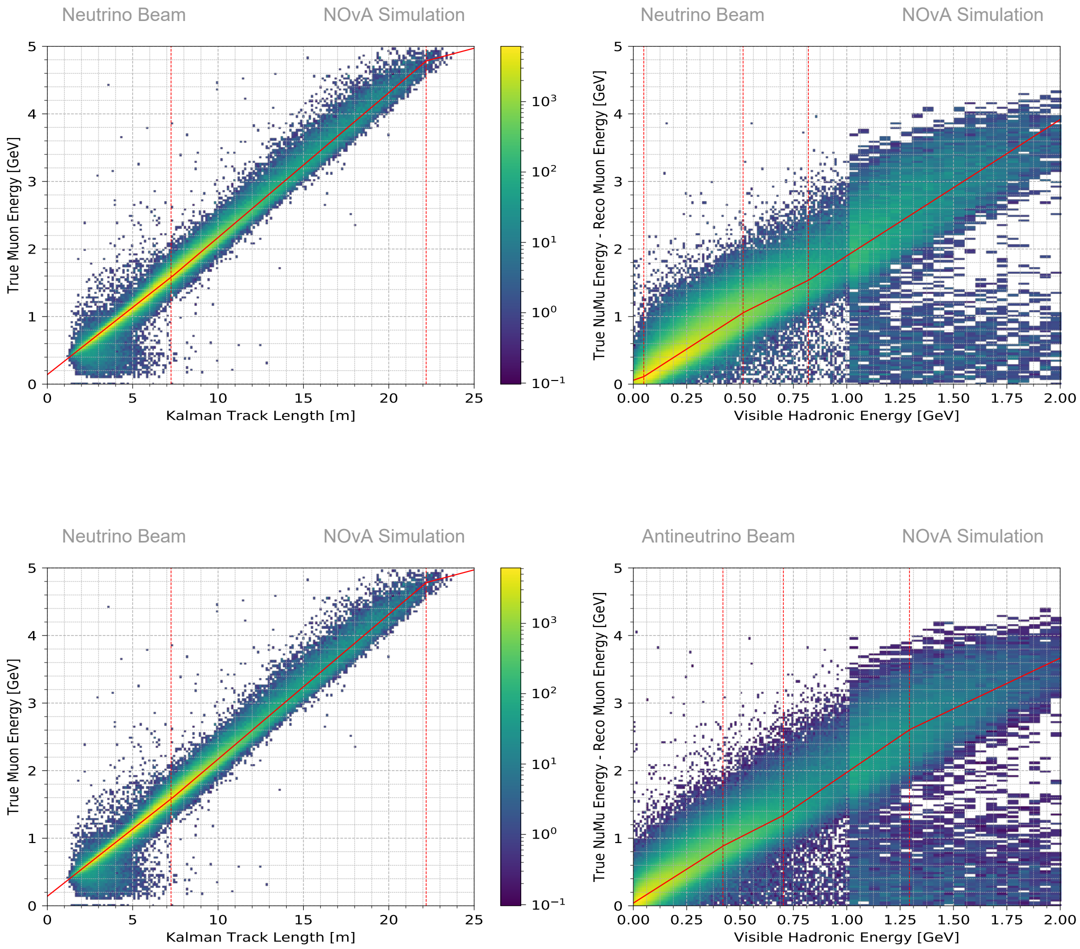

Figure 5.31: The true muon (μ) energy is plotted against reconstructed Kalman Track Length on the left for outgoing muon as part of the resolution estimation of $E_{\mu/\bar{\mu}}$. In contrast, the plot on the right shows the true simulated energy minus the muon reconstructed energy as a function of visible hadronic energy. The top row represents the plots for the neutrino (FHC) mode, while the bottom ones are for the antineutrino (RHC) mode. The red dotted lines represent the boundaries between which each separate spline fit is performed [77].

reconstruction is presented.

Chapter 6

Analysis Framework

"In the presence of uncertainty, the goal of inference is not certainty, but consistency."

George E. P. Box

Introduction

In this chapter, we will present the framework used for this analysis. NOvA typically uses an extrapolation approach for the nominal three-flavor oscillation analyses, where the FD prediction is corrected using ND spectra. However, the extrapolation technique is unsuitable for this analysis since the active-sterile analysis is sensitive to oscillations at the ND. Sec. 6.1 introduces the joint ND-FD framework and the systematic uncertainties (Sec. 6.2) considered in this analysis. Particular focus is given to the MEC systematic uncertainty, specifically designed for this analysis, which is discussed in Sec. 6.3. Finally, Sec. 6.4 summarises this chapter to provide the foundation for the analysis results presented in the next chapter.

6.1 PISCES Framework

PISCES stands for **P**arameter **I**nference with **S**ystematic **C**ovariance and **E**xact **S**tatistics. It employs a hybrid test statistic, combining a Gaussian multivariate approach for systematic uncertainties (Sec. 6.1.1) with a Poisson likelihood ratio treatment for statistical uncertainties (Sec. 6.1.2). PISCES introduces a novel technique for performing covariance matrix-based fits using a Poisson likelihood. In this technique, systematic uncertainties are encoded into a covariance matrix, enabling a Gaussian multivariate technique to provide the fits without treating systematic uncertainties as nuisance parameters to be profiled over. The statistical uncertainties are handled using a Poisson likelihood method.

$$\chi^2_{total} = \chi^2_{Systs} + \chi^2_{Stats} \tag{6.1}$$

The total χ^2_{total} is a combination of χ^2_{Systs} and χ^2_{Stats}, where the former is derived from the Gaussian Multivariate treatment of systematic uncertainty and the latter from the Poisson likelihood for statistical uncertainty.

6.1.1 Gaussian Multivariate Treatment

Dealing with systematic uncertainties is a critical component in the analysis of high-energy experiments, especially in neutrino experiments. In most neutrino experiments, the neutrino flux, interaction cross-section, and detector resolution constitute the central portion. The systematic uncertainties used for this analysis are discussed in Sec. 6.2. In quantifying these uncertainties, we must consider how different uncertainties are related to one another, whether they are correlated (affecting different samples in the same way) or anti-correlated.

In the PISCES framework, we encode all systematics in a covariance matrix that not only contains the magnitude of systematics but also the correlation among different systematics. The diagonal elements of this covariance matrix give the variances (σ^2) of each systematic, while the off-diagonal elements represent the covariance/correlation between pairs of uncertainties (Eq. (6.2)).

$$V = \begin{pmatrix} Var(x_1) & cov(x_1, x_2) & \cdots & cov(x_1, x_n) \\ cov(x_2, x_1) & Var(x_2) & \cdots & cov(x_2, x_n) \\ \vdots & \vdots & \ddots & \vdots \\ cov(x_n, x_1) & cov(x_n, x_2) & \cdots & Var(x_n) \end{pmatrix} \tag{6.2}$$

The likelihood is calculated using the covariance matrix as:

$$\chi^2_{cov} = \sum_{ij}(x_i - \mu_i)V_{ij}^{-1}(x_j - \mu_j) \tag{6.3}$$

where x_i is the data, μ_i is the nominal prediction in i^{th} bin, and V_{ij} is the covariance matrix Eq. (6.2).

6.1.2 Poisson Likelihood Ratio Treatment

In analyses such as neutrino oscillation, where the statistics are very low, the treatment of statistical uncertainty becomes particularly critical. The Gaussian Multivariate technique discussed in Sec. 6.1.1 is well-suited for systematics but breaks down at low statistics. To avoid this breakdown, we need to use the Poisson likelihood method. The profile likelihood using the Poisson likelihood can be calculated as:

$$\chi^2_{pull} = 2\sum_i^N \left(m_i - x_i + x_i \log \frac{x_i}{m_i} \right) + \sum_i^K \alpha_j^2 \qquad (6.4)$$

where $m_i = \Sigma_j^K (1 + \alpha_j s_{ji})\mu_i$ is the prediction in each bin with systematic weights applied, α_j is the fit parameter for systematic uncertainty j, s_{ji} is the reweight for systematic uncertainty j in analysis bin i and K is the number of sources of systematic uncertainty [78].

Each of the two approaches has its own advantages and disadvantages, with Gaussian convergence being the faster of the two. In comparison, Poisson is more time-expensive due to the way the two approaches treat the systematics. In the Gaussian multivariate technique, systematic uncertainties are not profiled over but instead stored in a covariance matrix, in contrast to the Poisson treatment. Since the systematic pulls are not calculated explicitly in the Gaussian treatment, their impact and exact values can not be visualised. However, the profile likelihood can calculate the pulls explicitly and is also well-suited for low stats bins. The PISCES framework is developed using a hybrid approach that leverages both techniques [79].

6.1.3 Calculation of χ^2

The hybrid test statistic is the sum of the Gaussian and Profile likelihoods, which also avoids the explicit profiling over the systematic pulls.

$$\begin{aligned}\chi^2_{\text{Hybrid}} &= 2\sum_{i}^{N}\left[S_i - x_i + x_i \log\frac{x_i}{S_i}\right] \\ &+ \sum_{ij}^{N}\sum_{\alpha\beta}^{M}(s_{\alpha i}-1)F^{-1}_{\alpha i\beta j}(s_{\beta j}-1)\end{aligned} \tag{6.5}$$

where x_i is the observed data, $S_i = \sum_\alpha \mu_{\alpha i}s_{\alpha i}$ is the predicted value, $\mu_{\alpha i}$ is nominal expectation, $s_{\alpha i}$ is the fractional systematic shift for spectrum component α and i^{th} bin, and F is the full covariance matrix. The covariance matrix, $F_{\alpha i\beta j}$, encodes the systematics uncertainties and their correlations across different oscillation channels (α, β) and analysis bins (i, j) [80].

At each point in the parameter space, a fit is performed in two phases. At first, we minimise the χ^2 with respect to the systematic pulls. Levenberg-Marquardt Algorithm [81] is applied to evaluate the roots of the gradient of χ^2 with respect to each systematic pull by solving the Hessian matrix for the pair of systematic pulls. The gradient of χ^2 is given by:

$$\frac{\partial\chi^2}{\partial s_{\gamma k}} = 2\left(\mu_{\gamma k} - \frac{\mu_{\gamma k}x_k}{\sum_{\alpha}^{M}\mu_{\alpha k}s_{\alpha k}} + \sum_{\alpha i}^{MN}(s_{\alpha i}-1)F^{-1}_{\alpha i\gamma k}\right) \tag{6.6}$$

The Hessian for the pair of systematic pulls is given by:

$$\frac{\partial^2\chi^2}{\partial s_{\gamma k}\partial s_{\delta l}} = 2(1+\delta_{\gamma\delta}\delta_{kl}\lambda)\left(\frac{\mu_{\gamma k}x_k}{(\sum_{\alpha}^{M}\mu_{\alpha k}s_{\alpha k})^2}\delta_{kl} + F^{-1}_{\gamma k\delta k}\right) \tag{6.7}$$

where λ is the stabilising factor used in LMA for a stable minimisation by interpolating between gradient descent and Newton's method, it starts at 0.1 and is reduced repeatedly by a factor of 1.5 until it reaches a minimum and becomes negligible. At this point, the pure Newton method is reached.

Sometimes, the content of the bin is so small that the gradient becomes negative and LMA fails to converge. Hence, for the initial minimisation, we temporarily remove such bins, and once the minimisation is done, we reintroduce these bins and repeat the minimisation until the minimum is reached.

In the second phase, once the systematic penalty term is determined, χ^2 is recomputed as the sum of the penalty term and the Poisson likelihood term as in Eq. (6.5). These two phases are repeated iteratively until χ^2 between the subsequent iterations reaches the value of 10^{-10}, at which point the minimum is achieved within the tolerance set in the MINUIT.

6.2 Systematic Uncertainties

There are several components to the complex neutrino oscillation analyses, and each comes with different limitations, which are attributed to different uncertainties. NOvA is a complex experiment that has certain limitations, including detector inefficiency and calibration issues. For this analysis, we consider approximately 178 systematic uncertainties, grouped into various categories. The broad systematic categories considered for this analysis are beam flux, detector, cross-section, meson exchange current (MEC), normalisation, and Geant4. The complete set of systematics is listed in Appendix B.

Some systematics are easy to handle, allowing us to use reweighing functions to reweight the energy distribution of nominal predictions. For other systems that have a larger effect on the reconstruction, new predictions are made from scratch. A complete reconstruction chain is performed for these dedicated samples to generate systematically shifted simulations. Each systematics is generated within $\pm 1\sigma$ shift band. .

6.2.1 Flux Systematics

The flux systematics uncertainty encompasses the uncertainties from beam production and transport. This basically covers the mismodeling in the production and transport of hadrons, which eventually decay to produce the neutrino beam Sec. 3.2. The **P**ackage to **P**redict **F**lux [82] applies data-driven constraints to the G4NuMI simulation. It employs a multiverse technique to generate event weights from randomly fluctuating interaction cross-sections. In addition to the correction on the hadrons, a list of uncertainties on the beam is also applied. The list of beam-related uncertainties is:

- Horn Current: ± 2 kA
- Horn Position: ± 3 mm for X and Y axis.
- Beam Position on Target: ± 1 mm for X and Y axis.
- Beam Spot Size: ± 2 mm for X and Y axis.
- Water layered thickness on horns: ± 1 mm.
- Carbon target position: ± 7 mm along z-axis.
- Beam divergence: 54 μrad.

To derive the systematic shifts from the multiverse weights of PPFX, we perform the **P**rinciple **C**omponent **A**nalysis (PCA) on the randomly fluctuated universes. Each universe creates a covariance matrix, which then decomposes into eigenvalues and eigenvectors, generating a series of $\pm 1\sigma$ shifts that decorrelate the hadron and flux dependencies.

Kaon Uncertainty

In the MINOS+ joint ν_μ and NC sterile analysis, it was observed that the PPFX hadron production prediction significantly improved the data-MC agreement at low energies. In contrast, no corresponding effect was observed at high energies. This suggests that the corrections to the neutrino flux coming from parent Kaon decay might require additional systematic uncertainty beyond what is provided by PPFX. Since both NOvA and MINOS+ use the same beam (though NOvA is off-axis and MINOS+ is on-axis), a study is performed using the Horn off ND sample to determine the effect and level of this uncertainty. An additional 10(30)% uncertainty for the FHC(RHC) sample on the kaon component is used in this analysis.

6.2.2 Detector Systematics

Detector systematic uncertainties are among the significant uncertainties related to modelling the detector response and calibration process. The uncertainties require a full re-simulation of the MC files for ND and FD, as any change in the underlying detector parameters will have a direct impact on the reconstruction chain.

The calibration uncertainties include absolute calibration, calibration shape and detector drift uncertainty.

Absolute calibration energy uncertainty arises from the detector energy response of protons and muons, as evaluated through the data/MC discrepancies. The standard set of variables, such as beam muon and proton $\frac{dE}{dx}$, π^0 mass, and Michel electrons, are used to define the level of uncertainty. Historically, NOvA uses a 5% uncertainty on the energy scale for ND and a relative 5% calibration uncertainty for FD as well. Calibration shape uncertainty accounts for those parts of the detectors that are not very well modelled. This results in variations in reconstructed and true energies near the detector edges.

Detector drift reflects the degradation of detector components over time and is modelled as a steady decrease in light output. Since the detector response over time only decreases, only the variation of this systematics is considered. A 4.5% per year reduction for detector aging effects is considered for NOvA analyses.

Furthermore, the detector response uncertainties are characterised by Cherenkov and light-level uncertainty. The level of these uncertainties is determined through the light-level tuning. A 6.2% for the Cherenkov light and 5% for the light level are used in this analysis.

6.2.3 Cross-section Systematics

Neutrino-nucleus cross-sections are one of the major sources of systematic uncertainties in neutrino oscillation analyses. These uncertainties arise due to the complexity of neutrino interactions and the lack of experimental cross-section data, which makes it challenging to reduce these uncertainties. In general, cross-section uncertainties come from the GENIE, which are tuned to data from several different experiments at different baselines. This also renders it insensitive to any potential sterile neutrinos. These uncertainties are evaluated by reweighting the nominal simulation event rate according to the frequency of different interaction types. These reweighs are generally described as GENIE "knobs". The primary set of interactions available in GENIE is Quasi-Elastic Scattering (QES), Resonance (RES), Deep Inelastic Scattering (DIS), and Meson Exchange Current (MEC). There are 78 systematic GENIE knobs, of which the 30 largest are listed with their brief descriptions.

- **ZNormCCQE**: Normalisation parameter in the CCQE z-expansion axial form factor.
- **ZExpAxialFFSyst2020_EV1,2,3,4**: Four correlated CCQE z-expansion axial vector shape variations.
- **MECEnuShape2020Nu**: E_ν dependence of MEC for neutrinos.
- **MECEnuShape2020AntiNu**: $E_{\bar{\nu}}$ dependence of MEC for antineutrinos.
- **MECShape2024Nu**: $(q_0, |\vec{q}|)$ dependence of MEC for neutrinos.
- **MECShape2024AntiNu**: $(q_0, |\vec{q}|)$ dependence of MEC for antineutrinos.

- **MECInitStateNPFrac2020Nu**: Fraction of MEC interactions on neutron-proton pairs for neutrinos.
- **MECInitStateNPFrac2020AntiNu**: Fraction of MEC interactions on neutron-proton pairs for antineutrinos.
- **MaCCRES**: Mass parameters in axial form factors for resonant production in CC events.
- **MvCCRES**: Mass parameters in vector form factors for resonant production in CC events.
- **MaNCRES**: Mass parameters in axial form factors for resonant production in NC events.
- **MvNCRES**: Mass parameters in vector form factors for resonant production in NC events.
- **RPAShapeenh2020**: Higher-Q^2 enhancement for Random Phase Approximation in CCQE
- **RPAShapesupp2020**: Low-Q^2 suppression for Random Phase Approximation in CCQE.
- **LowQ2RESSupp2020**: Low-Q^2 suppression in RES events.
- **RESvpvnRatioNuXSecSyst**: Relative RES cross-section scaling of $\frac{\sigma(\nu+p)}{\sigma(\nu+n)}$.
- **RESvpvnRatioNubarXSecSyst**: Relative RES cross-section scaling of $\frac{\sigma(\bar{\nu}+p)}{\sigma(\bar{\nu}+n)}$.

- **RESDeltaScaleSyst**: Scales the normalization of RES interactions which produces a Δ.
- **RESOtherScaleSyst**: Scales the normalisation of RES interactions, which produces higher order resonances.
- **DISvnCC1pi_2020**: Normalisation factor of 1π final states in DIS scattering of neutrinos from neutrons.
- **DISNuHadronQ1Syst**: Relative scaling of ν DIS interactions with 2 final state hadrons with total Q=1.
- **DISNuBarHadronQ0Syst**: Relative scaling of $\bar{\nu}$ DIS interactions with 2 final state hadrons with total Q=0.
- **hNFSI_MFP_2024**: Neutrino mean free path in FSI.
- **hNFSI_FateFracEV1_2024**: Largest of three correlated 'fate fraction' shifts.
- **radcorrnue**: ν_e/ν_μ cross-section differences from radiative corrections.
- **radcorrnuebar**: $\bar{\nu}_e/\bar{\nu}_\mu$ cross-section differences from radiative corrections.
- **2ndclasscurr**: Cross-section differences from second-class currents.

NOvA tunes its cross-section model to ND data, which results in improved data/mc agreement and a suite of uncertainties that we cannot use. However, for sterile neutrino analyses, we employ a joint Near and Far Detector (ND-FD) fit approach that accounts for possible oscillations in the ND. As a result, cross-section uncertainties for NuX analyses must be treated differently. While standard GENIE uncertainties are applicable in most NOvA analyses, this does not hold for MEC uncertainties, as GENIE does not define any MEC uncertainties. Consequently, sterile-specific MEC systematics need to be developed independently of ND data, which will be discussed in a later section.

6.2.4 Normalisation Systematics

Normalisation systematics account for multiple minor effects, including uncertainties in POT, differences in detector masses, and event pile-up in the ND, with separate values assigned to FHC and RHC. Lastly, the normalisation systematic also includes simulation uncertainty, which accounts for the FD air bubbles that GEANT did not simulate.

- POT uncertainty: 0.55%
- Near/Far detector mass uncertainty: 0.19%
- Simulation normalisation uncertainty: 0.4%
- ND pile-up systematics: ν_μ FHC - 0.21%, ν_μ RHC - 0.48%

The quadrature sum of these uncertainties is 0.74(0.85)% for ν_μ FHC(RHC).

6.2.5 Geant4

This is a new systematic added recently in the NOvA analysis. Geant4Reweight is an event reweighing framework used to incorporate uncertainties in hadron production in neutrino interactions, aiming to avoid rerunning computationally expensive simulations. 11 systematic knobs cover the uncertainties due to the elastic scattering of hadrons produced in the primary and subsequent secondary neutrino interactions. These include 5 for π^+, 5 for π^-, and 1 for the proton, and these are incorporated through the PCA in the analysis.

6.3 MEC Systematics

Meson Exchange Current (MEC) systematics refer to the uncertainties arising from the mismodelling of Meson Exchange Current (MEC) interactions. In MEC processes, a neutrino interacts not just with a single nucleon but simultaneously with multiple nucleons, such as protons and neutrons, within a nucleus. Often, this interaction occurs with a correlated pair of nucleons, resulting in the ejection of both nucleons in the final state. These events resemble quasi-elastic interactions because energy is transferred without the production of new particles, though two nucleons are ejected rather than one. As a result, these interactions are known as two-particle two-hole (2p2h) processes. MEC interactions are crucial in neutrino physics, as they can significantly influence observed cross-sections, especially in the energy ranges relevant to many neutrino

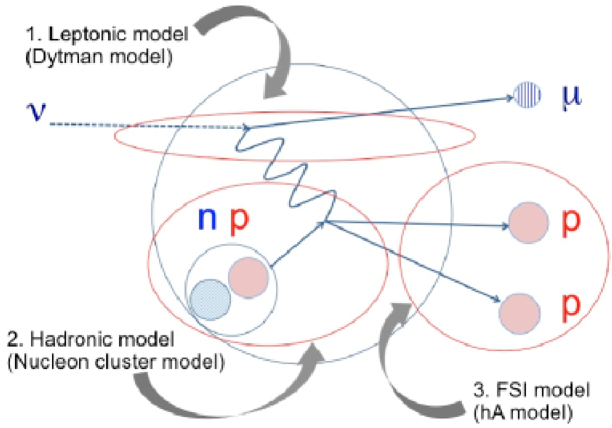

Figure 6.1: This figure shows the neutrino interacting with a pair of nucleons (np). The final state includes the lepton and nucleons that mimic the quasi-elastic interactions [83].

oscillation experiments. However, the complexities of MEC processes, combined with limited understanding compared to simpler interaction types, contribute to significant uncertainties, or MEC systematics, in the analysis. These systematics require careful consideration, particularly when widely-used models like GENIE do not fully incorporate MEC effects.

Although these events resemble quasi-elastic interactions, they involve scattering from correlated nucleon pairs. Misclassifying them as quasi-elastic during reconstruction can lead to significant errors in energy estimation, as standard reconstruction methods typically assume single-particle interactions. This misclassification can result in an underestimation of the actual energy involved. To address this, we utilise two key uncertainties associated with Charged Current MEC events: the initial state composition of nn-np pairs and the Neutrino Energy Dependent Model Spread Uncertainty. These uncertainties are particularly advantageous because

Samples	GENIE Tune	GENIE Version
Dytman	G18_01a_02_11a	v3_00_06
Valencia	G18_10a_02_11a	v3_00_06
SuSA	G21_11a_00_000	v3_04_00

Table 6.1: Table listing the different GENIE tunes and versions used for generating the MEC CC events.

they do not depend on the Near Detector (ND) [84].

6.3.1 Model Uncertainties

The new uncertainties are divided into model-based shape uncertainties and overall normalisation uncertainties. To develop the shape uncertainties, we employ three models, one of which is Valencia, NOvA's default simulation model. The models used are:

- Dytman
- SuSA
- Valencia (NOvA's base model)

We develop the shape systematics in True $q_0 - q_3$, derived from inputs from different GENIE tunes and versions available in NOvA (Tab. 6.1). We generated approximately 1 million CC MEC events for each model.

Weights are generated using the True $q_0 - q_3$ distributions derived from the previous step. The weighting process is as follows:

1. Normalize the True $q_0 - q_3$ distributions for ν and $\bar{\nu}$ to unit area.

2. Generate three random scaling factors.

3. Apply these scaling factors to the ν and $\bar{\nu}$ distributions, ensuring that both sets of weights are generated within the same universe.

4. Combine the scaled distributions to create a unique composite model from the three GENIE models.

5. Divide this composite distribution by the Valencia distribution (NOvA's default model) to obtain the final MEC weights.

6. Repeat this procedure 1000 times to generate 1000 unique models, producing a range of weights.

This process yields 1000 distributions of weights in $q_0 - q_3$ space. For each event (depending on ν and $\bar{\nu}$), a weight is drawn based on its true $q_0 - q_3$ value, leading to a spread of possible universes, as illustrated.

6.3.2 Normalization

We will use an overall normalisation uncertainty on the MEC events in addition to the model-spread uncertainties. We will add the 100% normalisation uncertainty as used in the previous analysis. Additional details on the normalisation uncertainties can be found here [84]. This represents a conservative estimate of the uncertainty in the total number of MEC events within the sample. Although this estimate may be overly cautious, given our confidence in the

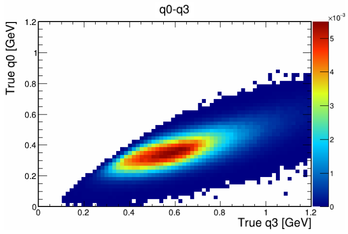

(a) Dytman Model

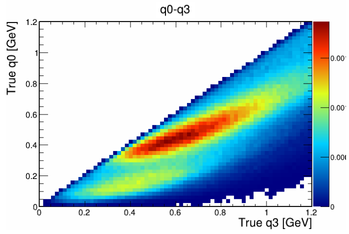

(b) Valencia Model

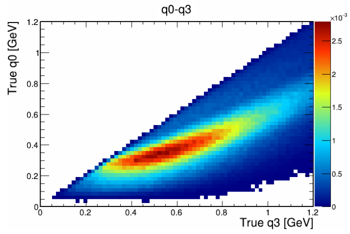

(c) SuSA Model

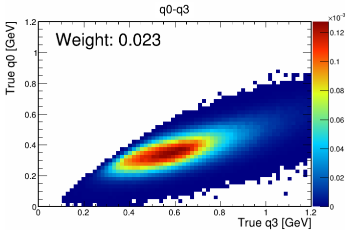

(d) Dytman Model

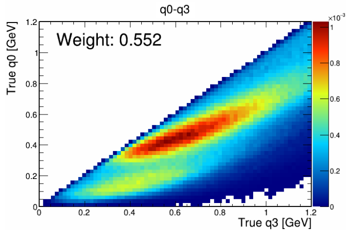

(e) Valencia Model

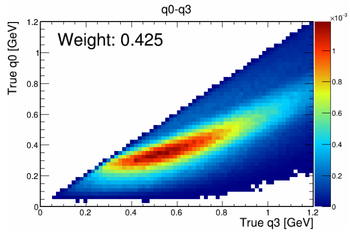

(f) SuSA Model

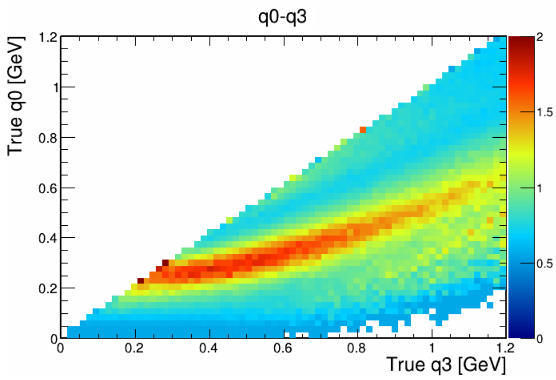

Figure 6.2: One of the 1000 examples of True $q_0 - q_3$ distributions for ν**-mode** showing the weighing procedure. The first row represents the unweighted distribution, and the second row represents the first row distributions getting multiplied by the random weights. The third row shows the final reweighted distributions.

presence of MEC events, it effectively accounts for the variations between the models.

6.3.3 Principal Component Analysis (PCA)

A PCA is then performed on the 1000 MEC universes generated in Sec. 6.3.1, where an eigenvalue decomposition of the fractional Covariance matrix is done. The detailed PCA procedure has already

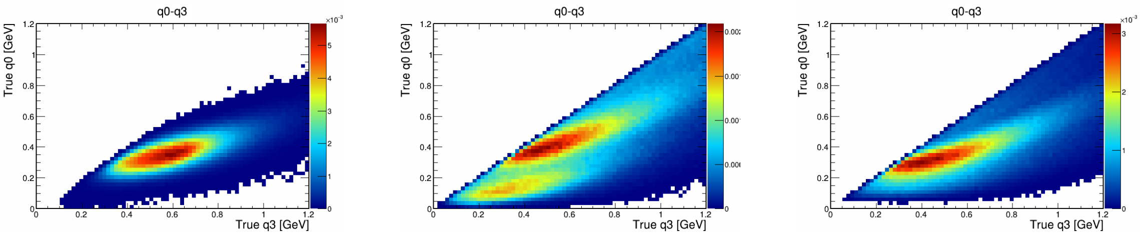

(a) Dytman Model (b) Valencia Model (c) SuSA Model

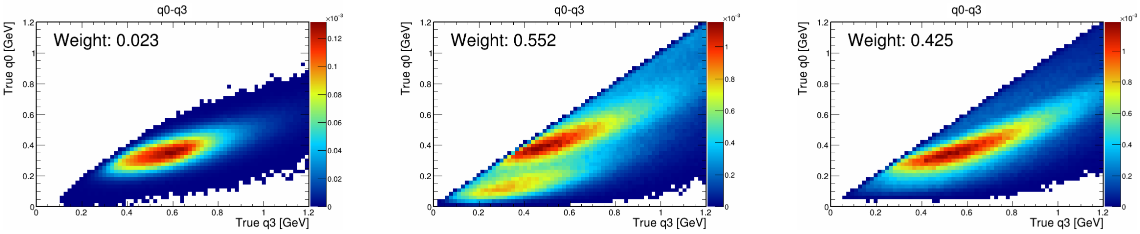

(d) Dytman Model (e) Valencia Model (f) SuSA Model

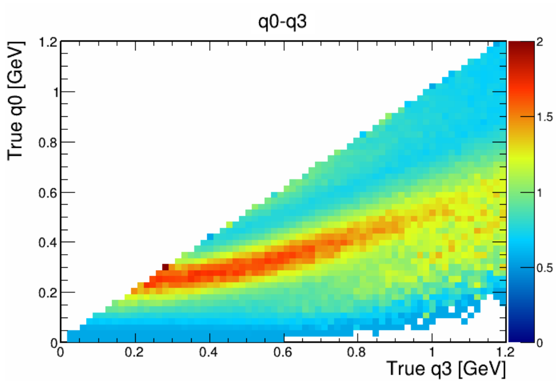

Figure 6.3: One of the 1000 examples of True $q_0 - q_3$ distributions for $\bar{\nu}$**-mode** showing the weighing procedure. The first row represents the unweighted distribution, and the second row represents the first row distributions getting multiplied by the random weights. The third row shows the final reweighted distributions.

been explained in the previous version of the technote [84]. The FHC, RHC, and FHC-RHC covariance matrices used for the PCA decomposition are shown in Fig. 6.4. The eigenvalues of the ten most significant components for FHC, RHC, and joint FHC-RHC are shown in Tab. 6.2. The only appreciable eigenvalues are the top two for FHC, RHC, and the joint FHC-RHC mode.

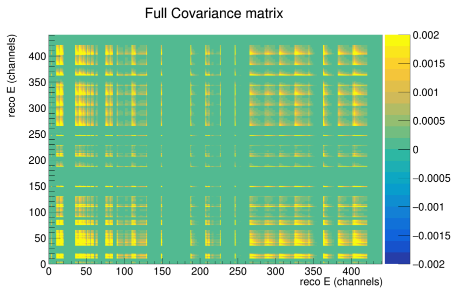

(a)

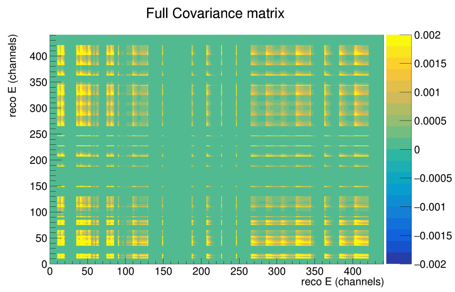

(b)

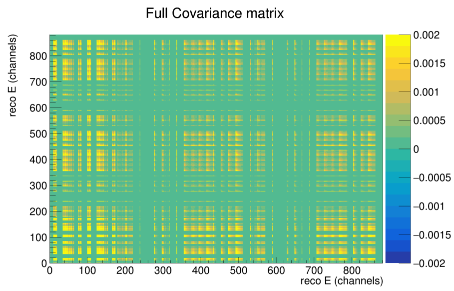

(c)

Figure 6.4: Covariance matrix produced from 1000 MEC universe weights for ν (Fig. 6.4a), $\bar{\nu}$ (Fig. 6.4b), and joint $\nu - \bar{\nu}$ (Fig. 6.4c). This matrix is symmetric, and each axis is a linearisation of multiple axes. In order, this axis combines the integrated ν_μ selection, and the NC selection for 30% energy resolution schemes.

FHC	RHC	FHC-RHC
3.44091e+06	2.05021e+06	5.47e+06
634477	3691.58	651166
0.028579	0.002272	0.0309944
1.29e-09	6.27e-10	4.1e-09
7.33e-10	5.32e-10	2.71e-09
5.19e-10	5.17e-10	1.25e-09
4.45e-10	4.16e-10	1.13e-09
3.99e-10	2.91e-10	8.42e-09
2.68e-10	2.56e-10	6.87e-09
1.52e-10	1.90e-10	5.87e-09

Table 6.2: Eigenvalues for the ten largest principal components derived from the MEC shape covariance matrix

6.3.4 Systematic Spectra

For this analysis, we have been using separate, sterile, focused MEC weights; therefore, we do not want to use the MEC weights in the cross-section CV weights. Therefore, a MEC with a less cross-section CV weight tune is used for this analysis, which basically includes the FSI and Genie Skew Fix weights. Fig. 6.5 shows that the $\pm 1\sigma$ MEC uncertainty band very well covers the 3F XSec Tune. The distribution on the left is for the FHC, and on the right, it is for the RHC.

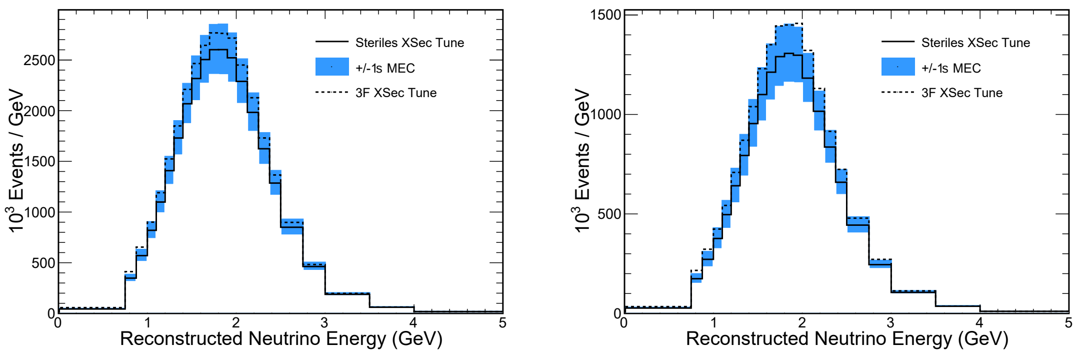

(a) (b)

Figure 6.5: This plot shows the 3-flavor cross section tune, including the standard GENIE weights and the 3-flavor MEC weights (dashed), sterile specific XSec tune in solid black, and $\pm 1\sigma$ MEC uncertainty band (in blue). The distribution on the right is RHC, and on the left is for the FHC.

6.4 Summary

This chapter provides a detailed overview of the PISCES framework used for sterile neutrino searches. The chapter begins with a detailed description of the statistical methodology employed in the PISCES framework, which includes the treatment of statistical and systematic uncertainties. We further discuss the different systematic effects and their impact on the analysis. A detailed description of the MEC systematics and their impact on the predicted spectra is presented in this chapter.

Chapter 7

Results

"Nature does not reveal her secrets once and for all."

Werner Heisenberg

7.1 Introduction

This chapter summarizes the results from this analysis. Before analyzing the real data we will discuss some preliminary studies that includes the sideband region studies to check and validate the our analysis framework (Sec. 7.2). Furthermore, we will discuss the sensitivities that include Asimov and pseudo-experiment surface fits to validate the robustness and efficiency of the fitter (Sec. 7.3.1 and Sec. 7.3.2). We will end this chapter with the final result derived from this analysis Sec. 7.4.

7.2 Sideband Studies

7.2.1 Near Detector NC Selection Sidebands

This analysis is the dual-baseline search where we consider the possible oscillation at the ND, so we can not use the ND data without any restriction and is subject to the blindness. However, we do need some ND data to ensure that the selections [85] and energy estimators [86] we have developed are behaving in the same way for simulation and data.

We make a small sample from the real data such that oscillations and statistical fluctuations are not distinguishable in the sample [87]. We have used 0.1% of the full dataset for the NC selection studies [88] considering around 10% statistical uncertainty. This burner sample will not be a part of the final dataset.

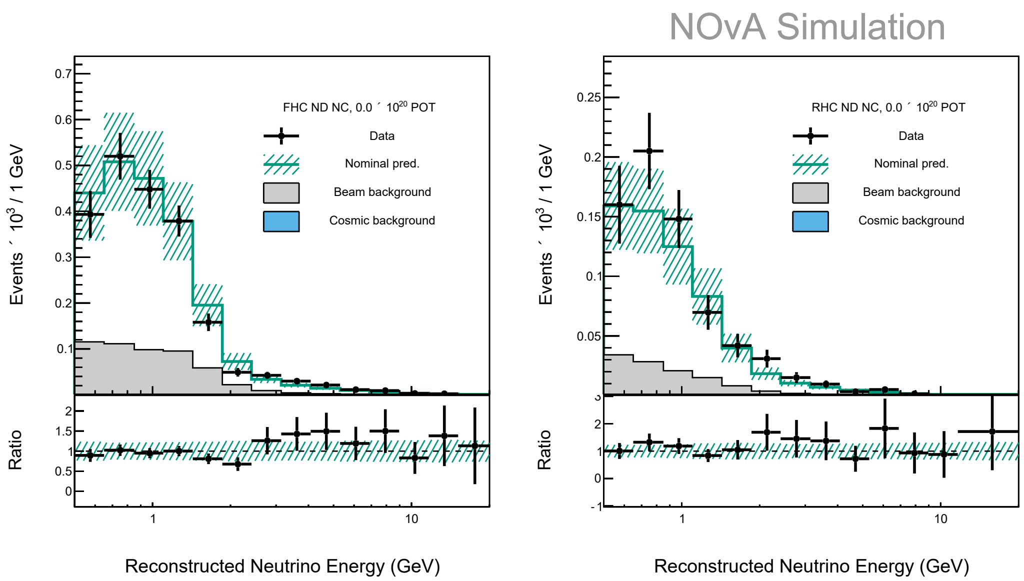

Figure 7.1: Data/simulation comparisons of the reconstructed energy with the burner sample. On the left, we have ND NC FHC, while on the right, we have the ND NC RHC. Here, the black are the data points and the green is the nominal distribution.

Fig. 7.1 shows comparisons of data and simulation in terms of the reconstructed neutrino energy. Both show good agreement between prediction and data, with the RHC distribution having slightly worse agreement which could be accounted for by the low statistics in the burner sample. Fig. 7.2 shows the data/MC comparison for the CVN variable. The distributions look sensible.

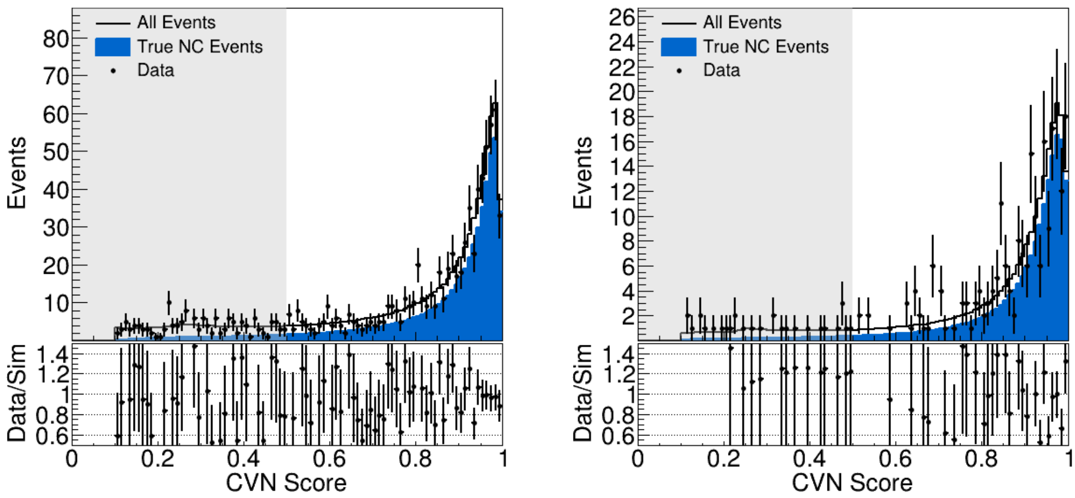

(a) (b)

Figure 7.2: Data/simulation comparisons for the CVN distribution. On the left (a), we have FHC, while on the right (b), we have the RHC. Here, the true NC events are in blue, and the CVN cut rejects the grey area. Note that the simulation has been area-normalised to match the data. The quality requirements, vertex, and fiducial volume criteria have been applied in these plots.

7.2.2 Near Detector ν_μ CC Selection Sidebands

For the same reasons as outlined in Sec. 7.2.1, a burner sample [89] is used as a sanity check of the ND ν_μ selection. The size of the burner sample should be such that the statistical uncertainties are comparable to the size of the effect being sought. We have used a 0.06% sample as the burner sample for FHC, considering around 10% statistical uncertainty, and 0.1% for RHC (Tab. 7.1). When selecting the burner sample, we ensure that the events are randomly selected across all periods, not just from specific periods, to avoid any bias. We were able to use the same burner set for the RHC data that was used for the NC ND burner dataset. However, the FD sample is a dedicated sample, and we need to remake the other burner samples.

Mode	**Fraction (in %)**	**Burner POT** ($\times 10^{18}$)	**Number of files**
FHC	0.06	0.8	10
RHC	0.1	1.1	10

Table 7.1: Table showing the details of the burner sample, including the number of files, fraction of the full data sample, and corresponding burner POT

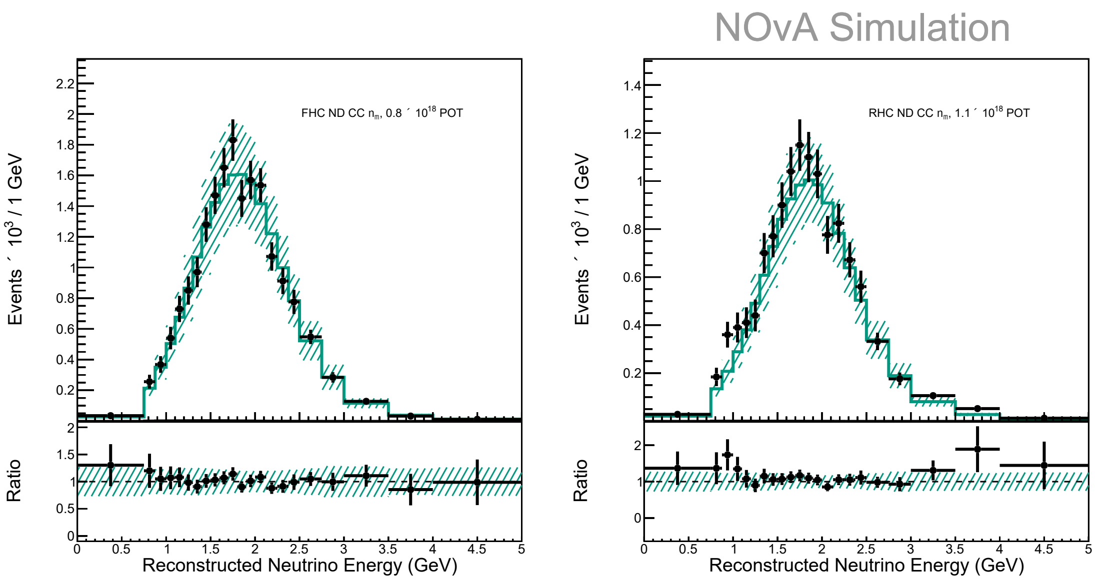

Figure 7.3: Data/simulation comparisons of the Reconstructed Energy with the Burner Sample. On the left, we have ND CC FHC, while on the right, we have the ND CC RHC. Here, the black are the data points and the green is the nominal distribution.

Fig. 7.3 shows the data/MC comparison for the burner sample (FHC on the left and RHC on the right). The distributions do not show any discrepancy, and the data/MC ratio is within the expected uncertainty band over the whole energy range.

7.3 Sensitivities Assuming No Sterile Neutrino

Limit Calculation:

- We have constructed a 50×50 grid of the parameter space ($\sin^2\theta_{24}$ vs Δm^2_{41}) and at each point in the parameter space, a χ^2 minimization is performed by comparing the predicted and observed data using the pisces method (as described in Chapter 6).
- This process is repeated for all the grid points in the parameter space. A global minimum is extracted from all the calculated values to compute the $\Delta\chi^2$ for each grid point.
- Exclusion contours will then be drawn comparing the $\Delta\chi^2$ at the grid point with the critical-value needed. The points which has larger $\Delta\chi^2$ than the critical value will fall into the exclusion region (in this case the exclusion region is on the right side of the contour).
- Assuming the Wilk's theorem, the 90% Confidence Level (C.L.) critical value is 4.61. However, due to violation of Wilk's theorem in Neutrino Oscillation Analysis, the Feldman-Cousins correction is used for the exact critical-value calculation.

FC Correction

The final results obtained from the fits to the real data will be drawn using the Feldman-Cousins Unified Approach. The FC procedure is computationally expensive and the resources will be provided by National Energy Research Scientific Computing Center (NERSC) suplied in collaboration with the SciDAC-4 "HEP Data Analytics on HPC" project. However, due to the limited resources and NERSC allocated hours an approximate Feldman Cousins corrected value of test-statistic is used ($\Delta\chi^2_{crit} = 8.87$) is used for the Asimov and Median Sensitivities. This is calculated using a set of 1500 pseudoexperiments. Fig. 7.4 shows the $\Delta\chi^2$ distribution for the three-flavor point where $\Delta\chi^2$ is calculated as the difference between the 3F and 4F χ^2 values. In the Magenta, it's the $\Delta\chi^2_{crit}$ from the Wilks' theorem, while in the blue is the value calculated from the pseudoexperiments.

The FC critical-value is derived using the following the method:

- At each point on the grid of parameter space, we perform 5000 pseudoexperiments by keep the x and y-values of the grid parameters fixed and alllowing the rest of the parameters to float. This is known as the constrained fit.

- For each pseudoexperiment, a global fit is also performed where all the parameters are allowed to float. This is known as the unconstrained fit.

- A $\Delta\chi^2 = \chi^2_{const} - \chi^2_{unconst}$ is calculated for each point on the grid using all the PseudoExperiments and is used to evaluate the critical value for each point to construct the exclusion contours.

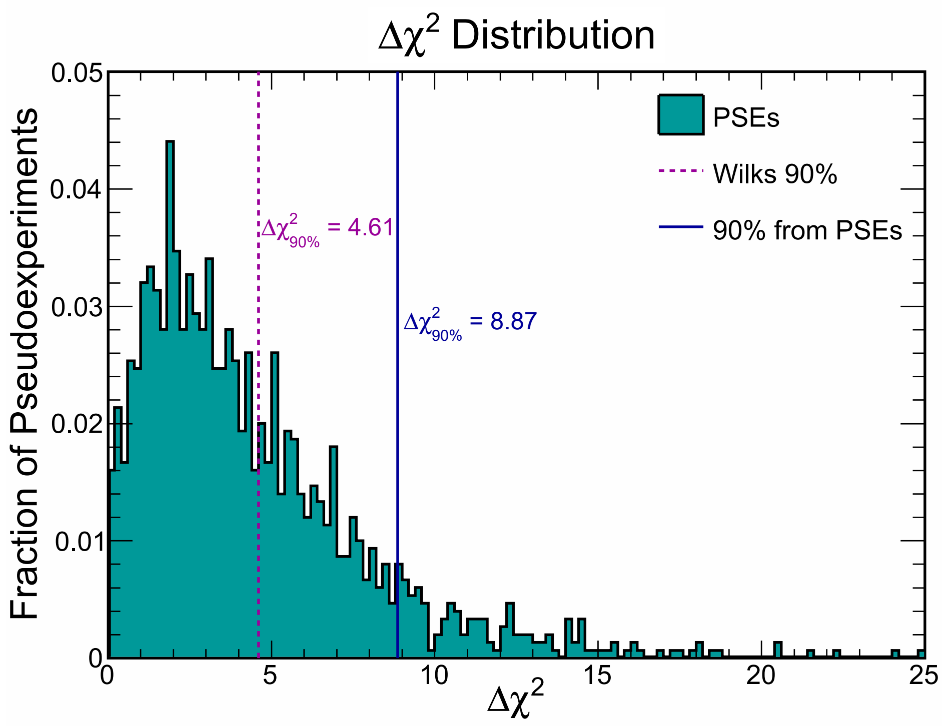

Figure 7.4: $\Delta\chi^2$ distribution for the three-flavor point calculated as $\Delta\chi^2 = \chi^2_{3F} - \chi^2_{4F}$.

7.3.1 Asimov Sensitivities

Asimov sensitivities are obtained from predictions derived from high-statistics Monte Carlo (MC) simulations. The Asimov sample is characterised by minimal statistical uncertainty and assumes no systematic shifts. For each point on the sensitivity surface of $\sin^2\theta_{24}$ versus Δm^2_{41}, the likelihood is profiled over $\sin^2\theta_{34}$, δ_{24}, θ_{23}, and Δm^2_{31}. The reconstructed energy spectra that are taken into account for generating the sensitivity contours are in Fig. 7.5 for the neutrino mode and Fig. 7.6 for the antineutrino mode. The distributions show predictions for the ν_μ CC and NC samples in the ND and FD with a systematic uncertainty band summarising the effect of all 177 systematics. To properly understand the effect of each systematic, we have divided these into different groups, mainly cross-section, flux, mec, ν_μ, normalisation, detector, and miscellaneous (Neutron, Kaon, and Tau).

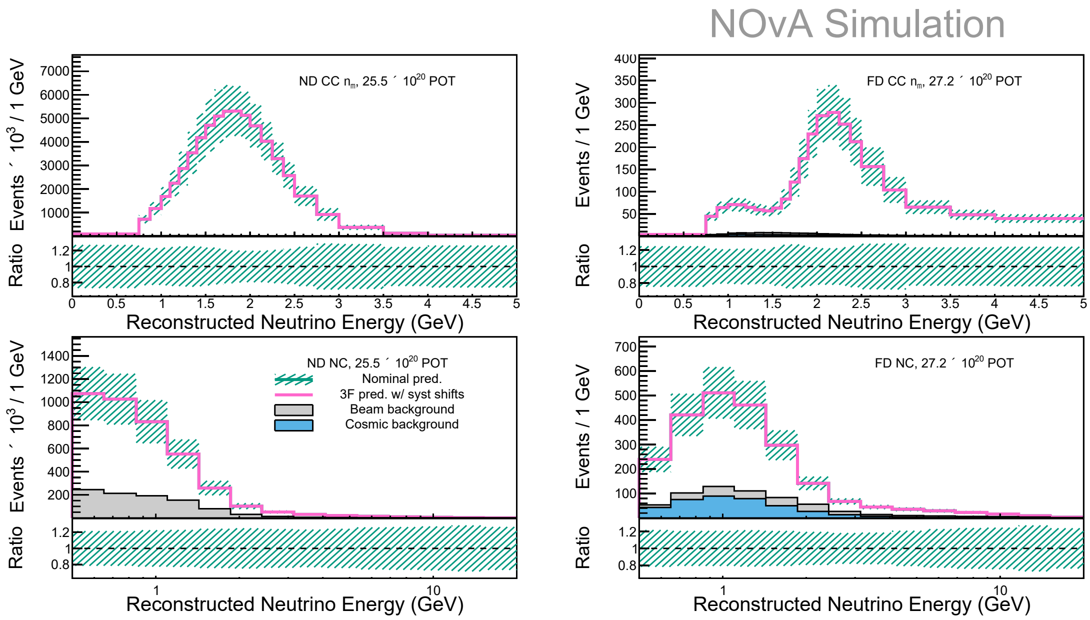

Figure 7.5: Reconstructed neutrino energy of the selected ν_μ-CC and NC events at Near and Far Detector for the beam in FHC mode.

Fig. 7.7 shows the asimov sensitivity for $\sin^2\theta_{24}$ vs Δm^2_{41} at 99% C.L. The parameter space can be considered low and high Δm^2 ranges. The sensitivity in the high Δm^2 region is driven by the ND sample, while the FD sample drives the low Δm^2 region. For $\Delta m^2_{41} > 0.05$ ev^2, the FD sensitivity is flat because at high Δm^2, the oscillations are too rapid to resolve. Furthermore, the difference between the ND+FD and FD-only is due to a systematic constraint through the ND sample. We can also see that the sensitivity of $\sin^2\theta_{24}$ is primarily driven by the ν_μ-CC sample, which is likely because the NC-only fit has no constraint on θ_{23} at all. At very low

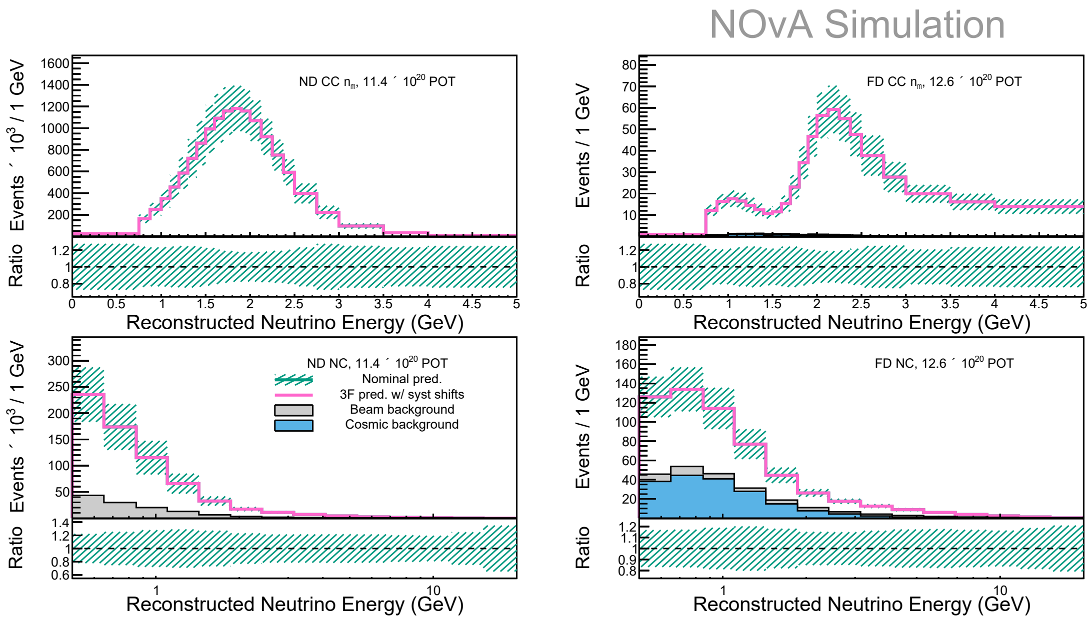

Figure 7.6: Reconstructed neutrino energy of the selected ν_μ-CC and NC events at Near and Far Detector for the beam in RHC mode.

Δm^2, the sensitivity falls sharply, which is due to the degeneracy between atmospheric and sterile-driven oscillations at this Δm^2. The small island at $\sim 2 \times \Delta m^2$ is an allowed region where θ_{23} and θ_{24} swap their roles.

Fig. 7.8 shows the effect of $\bar{\nu}$ sample. The sensitivity at small Δm^2 is largely driven by FD, a statistically limited region. With additional $\bar{\nu}$ data, the sensitivity is expected to be enhanced. Furthermore, due to the CP phase difference in ν and $\bar{\nu}$ sample, the addition of $\bar{\nu}$ will provide additional constraint on the sensitivity in the high Δm^2 region, which is systematically dominated.

7.3.2 Sensitivities Using Systematically Fluctuated Fake Data

In addition to the Asimov sensitivity discussed in Sec. 7.3.1, we have also conducted an extensive pseudo-experiment study. A

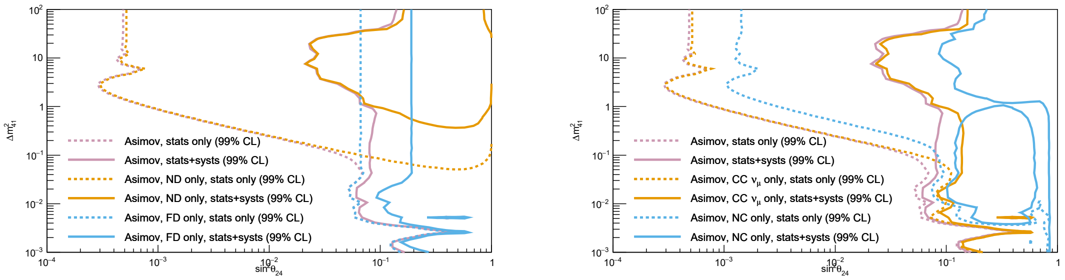

Figure 7.7: Asimov sensitivities for $\sin^2\theta_{24}$ vs Δm^2_{41} at 99% CL with dashed contours representing the stats only and solid ones for stats with systematics. Left: A comparison of the two-detector sensitivity (pink) with the ND-only (orange) and FD-only (blue) sensitivities. Right: A comparison of the full sensitivity (pink) with the ν_μ CC-only (orange) and the NC-only (blue) sensitivities.

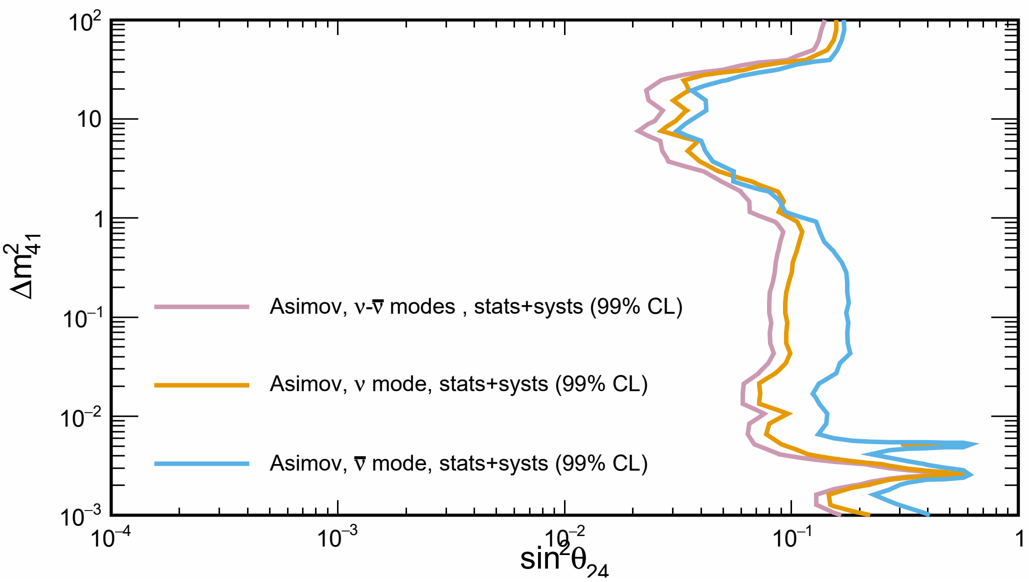

Figure 7.8: Asimov sensitivities for $\sin^2\theta_{24}$ vs Δm^2_{41} at 99% CL. A comparison of the full sensitivity (pink) with the FHC (ν) (orange) and the RHC ($\bar{\nu}$) (blue) sensitivities.

pseudo-experiment is characterised by statistical and systematic fluctuation that fakes the real data, which serves the purpose of confirming the robustness of the fitter. This will also help us derive the median sensitivity. For this study, we used 100 pseudo-experiments to derive the median sensitivities. Despite this, the parameter space is too large ($\sim$ five orders of magnitude in Δm^2_{41}), and hence it is not uncommon for some fluctuation to be mistaken for oscillation effects.

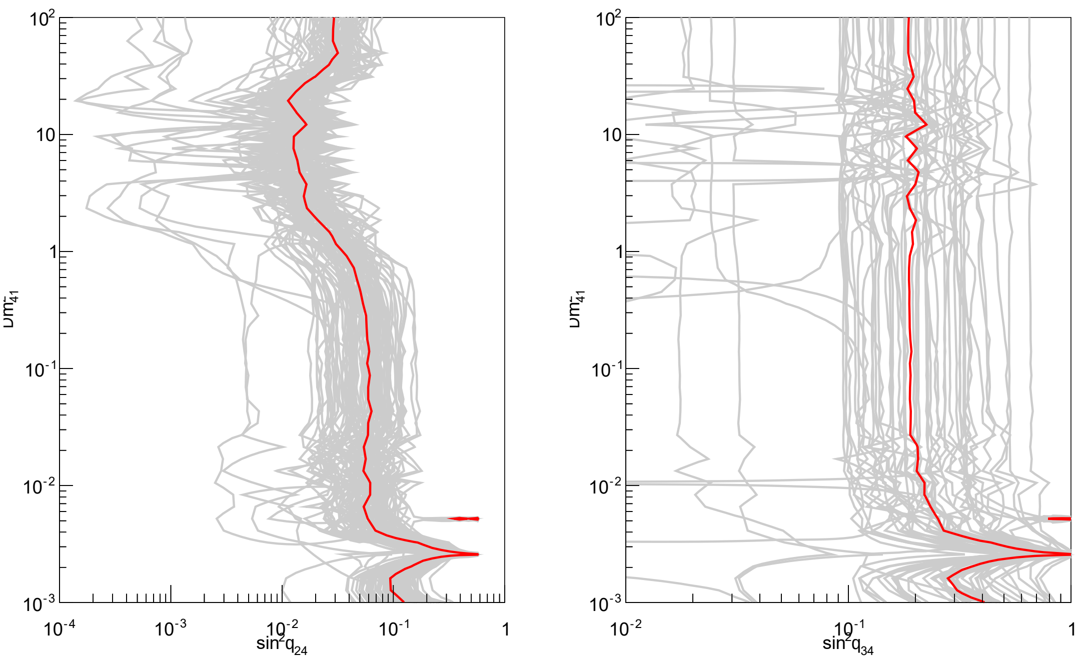

Figure 7.9: Median sensitivities at 90% CL (red) with individual pseudoexperiment sensitivity contours at 90% CL (grey). Left: $\sin^2\theta_{24}$ vs Δm^2_{41} , Right: $\sin^2\theta_{24}$ vs Δm^2_{41}.

7.4 Results and Discussion

Following the discussion of Asimov Sensitivity Sec. 7.3.1 and Fake Data Sec. 7.3.2 sensitivity, this section presets the results from the NOvA data using the POT for different samples as listed in Tab. 7.2.

Sample	POT ($\times 10^{20}$)
ND FHC	13.8
FD FHC	27.2
ND RHC	11.4
FD RHC	12.5

Table 7.2: This table presents the POT value for different samples used in the analysis. The corresponding ND samples does not contain the respective burner sample POT used in the sideband studies Sec. 7.2

7.4.1 Data/MC Comparison

Tab. 7.3 and Tab. 7.4 show the predicted and observed data for neutrino and antineutrino modes, respectively. Fig. 7.10 and Fig. 7.11 show the reconstructed energy spectra compared with the data for this analysis. The figures show the nominal prediction in grey, the 4F best-fit with systematics effect in blue, and the 3F best-fit with systematics included, along with the data points in black. The backgrounds are stacked histograms, with light grey representing the beam background and dark grey representing the cosmic background, which is only visible in the FD spectra. The data spectrum is well within the uncertainty range for both the neutrino and antineutrino mode, showing no significant excess/deficit of the data. Any discrepancy between the data and the simulation can be accounted for by the systematic uncertainties.

7.4.2 Data Results

We present the 90% limits on the most relevant $\sin^2\theta_{24}$ vs Δm^2_{41}, $\sin^2\theta_{34}$ vs Δm^2_{41}, and $\sin^2 2\theta_{\mu\tau}$ vs Δm^2_{41} parameter spaces. This

Mode	ND		FD	
FHC	ν_μ CC	NC	ν_μ CC	NC
Predicted	3.5e+06±650735	577601±108477	377.377±71.1263	917.878±144.726
Observed	3.59e+06	546921	384	889

Table 7.3: Predicted and observed number of NC and ν_μ events in the neutrino mode (FHC) in ND and FD.

Mode	ND		FD	
RHC	ν_μ CC	NC	ν_μ CC	NC
Predicted	1.4e+06±241867	180459±41401.7	91.02±15.02	205.164±31.22
Observed	1.47e+06	180540	106	222

Table 7.4: Predicted and observed number of NC and ν_μ events in the antineutrino mode (RHC) in ND and FD.

analysis presents a significant improvement in the sensitivity of all parameter spaces, providing world-leading limits in several regions of the sterile parameter space. For each fit, a $\Delta\chi^2$ surface is constructed for the required parameter space while profiling over the remaining parameters.

Fig. 7.12 shows NOvA's FC corrected 90% C.L. results (in black) in the $\Delta m^2_{41} - \sin^2\theta_{24}$ space compared with the previous results in Fig. 7.12a and with other experiments in Fig. 7.12b. The sensitivity for $\sin^2\theta_{24}$ comes largely from the muon-disappearance channel, and at high Δm^2_{41}, it is mostly driven by the ND data, which is systematically limited. The improvement in high Δm^2_{41} is accounted for by the constraint on systematics through the joint FHC-RHC fit. NOvA presents world-leading limits in several regions of $\sin^2\theta_{24}$ space and excludes most of the IceCube allowed region in the 1.5 eV^2 $\leq$ Δm^2_{41} $\leq$10 eV^2 range. The low Δm^2_{41} region is primar-

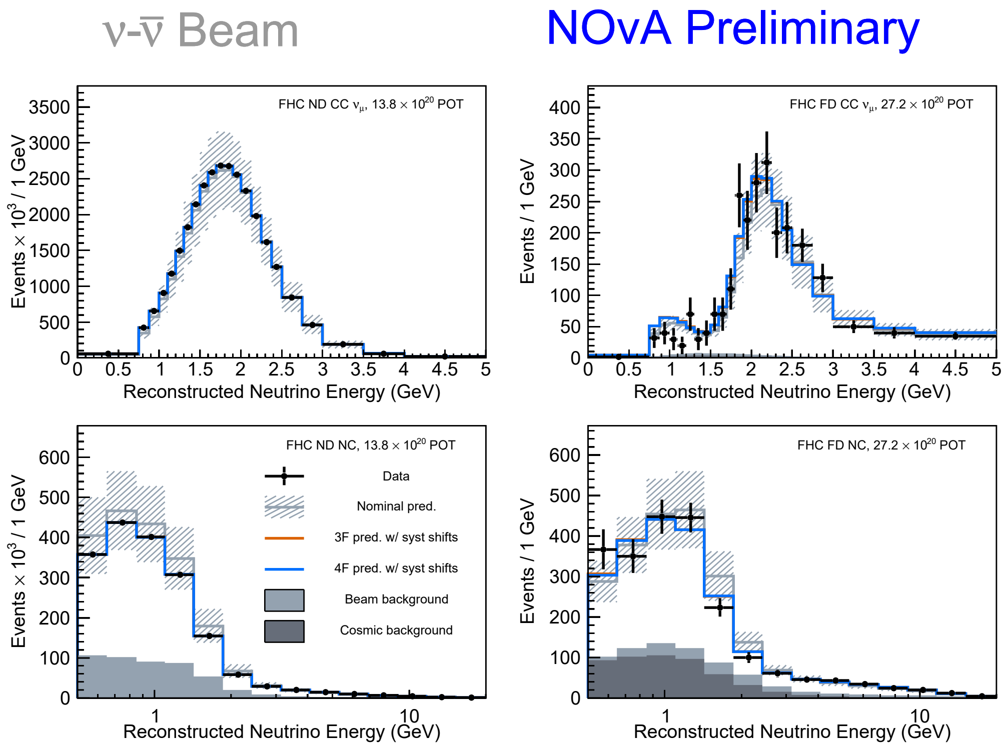

Figure 7.10: Reconstructed neutrino energy of the selected ν_μ-CC and NC events at Near and Far Detector for the beam in FHC mode. NOvA data shown as black points with Nominal prediction shown as a gray histogram with shaded uncertainty bands. The backgrounds are shown as a stacked histogram in each panel, and are separated into cosmic data and simulated backgrounds under a 3F model with $\Delta m^2_{32} = 2.51 \times 10^{-3}$ eV^2 and $\theta_{23} = 49.6°$. The 3F best fit prediction is shown in orange while the 4F best fit prediction is presented in blue.

ily driven by the FD data, which is statistically limited, and the improvement is the result of additional FHC (2×) and RHC data.

NOvA's FC corrected 90% C.L. results (in black) in the $\Delta m^2_{41} - \sin^2\theta_{34}$ space compared with the previous results in Fig. 7.13a and with other experiments in Fig. 7.13b. This analysis presents the world leading limits for $\sin^2\theta_{34}$ throughout the entire Δm^2_{41} range compared to the previous analysis where we were leading only in Δm^2_{41} <0.1 eV^2. The sensitivity to this parameter space is independent of the neutral current disappearance channel and is driven

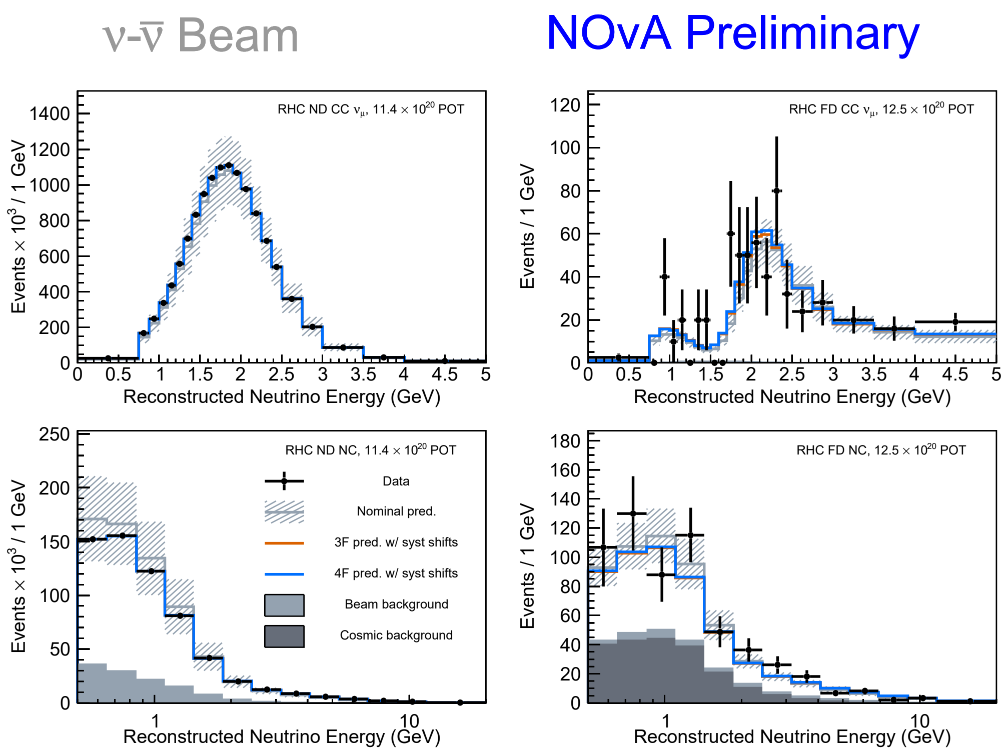

Figure 7.11: Reconstructed neutrino energy of the selected ν_μ-CC and NC events at Near and Far Detector for the beam in RHC mode. NOvA data shown as black points with Nominal prediction shown as a gray histogram with shaded uncertainty bands. The backgrounds are shown as a stacked histogram in each panel, and are separated into cosmic data and simulated backgrounds under a 3F model with $\Delta m^2_{32} = 2.51 \times 10^{-3}$ eV^2 and $\theta_{23} = 49.6°$. The 3F best fit prediction is shown in orange while the 4F best fit prediction is presented in blue.

solely by the FD sample (Eq. (2.7)). The FD region is statistically dominated, so any improvement in this comes from the additional neutrino (FHC) and antineutrino (RHC) dataset.

Furthermore, we present our results in terms of an effective mixing angle parameter, $\sin^2 2\theta_{\mu\tau} = \sin^2 2\theta_{24} \sin^2 \theta_{34}$, which can be thought of as describing anomalous sterile-driven ν_τ appearance. When considering ν_μ disappearance alone, one could define an effective atmospheric mixing angle to account for both sterile and standard oscillations by combining the first two terms in Eq. (2.8)

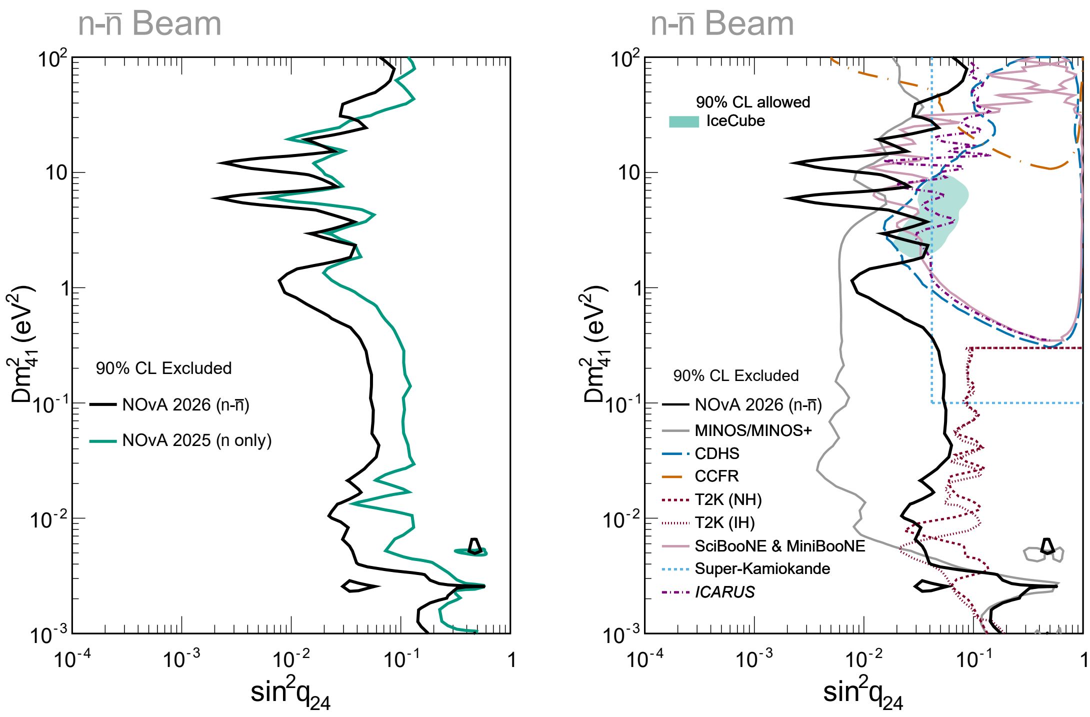

(a) (b)

Figure 7.12: NOvA's Feldman-Cousins corrected 90% confidence limits in $\sin^2\theta_{24}$ vs Δm^2_{41} space in green on the left compared with the previous analysis and with allowed regions and exclusion contours from other experiments on the right [90, 91, 92, 93, 94, 95, 96, 97, 98]. Regions to the right of the contours are excluded. Closed counter by IceCube represent the allowed region.

to give effective mixing angle ($\sin^2 2\theta_{23}^{\text{eff}} = \sin^2 2\theta_{23}\cos^2\theta_{24}$). One of the advantages of ν_μ disappearance channel is to disambiguate between θ_{24} and θ_{34} but it simultaneously provide an in-situ constraint on atmospheric mixing angle ($\sin^2 2\theta_{23}^{\text{eff}}$). In this parameter space, we significantly improved our sensitivity and present the world's most stringent limits for ν_τ appearance in $\Delta m^2 \lesssim 10$ eV^2.

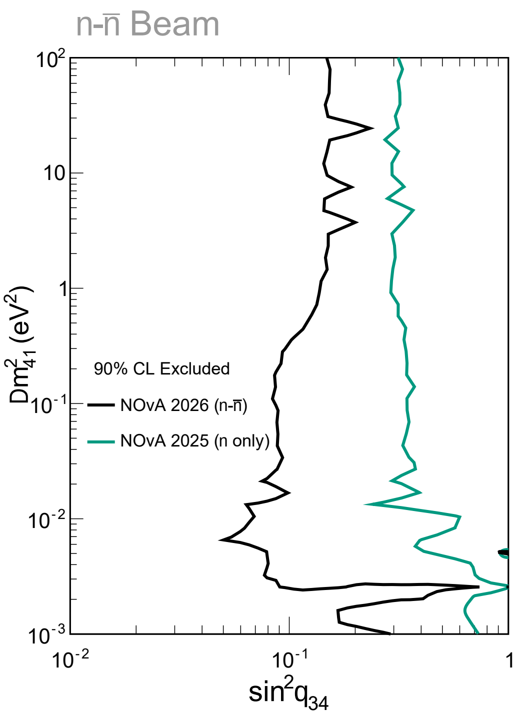

(a)

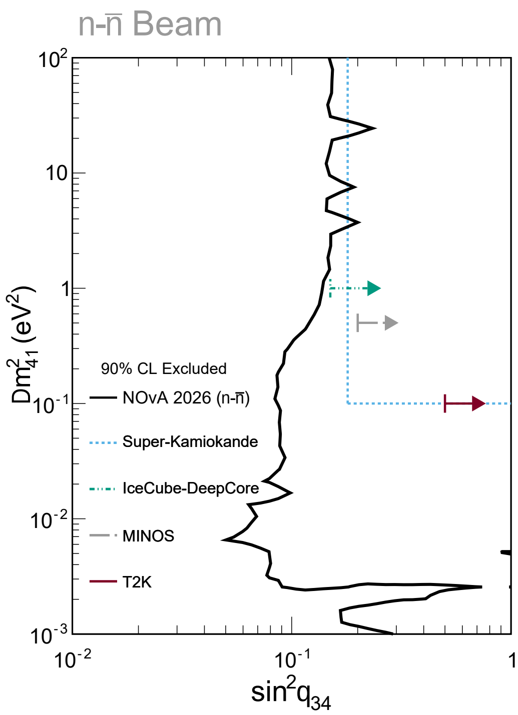

(b)

Figure 7.13: NOvA's FC corrected 90% confidence limits in $\sin^2\theta_{34}$ vs Δm^2_{41} space in green on the left compared with the previous analysis and with exclusion regions from other experiments on the right [93, 96, 97]. Regions to the right of the contours are excluded, and arrows represent the constraint on $\sin^2\theta_{34}$ at a single value of Δm^2_{41}.

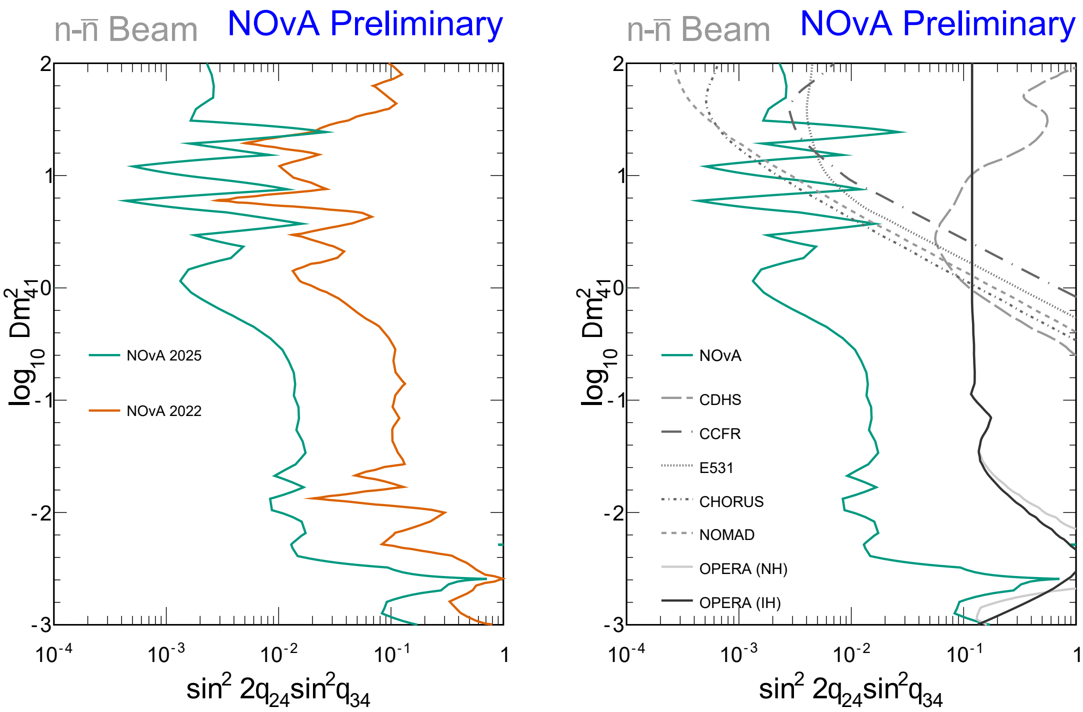

(a) (b)

Figure 7.14: NOvA's 90% confidence limits in $\sin^2 2\theta_{24} \sin^2 \theta_{34}$ vs Δm^2_{41} space in green on the left compared with the previous analysis and with allowed regions and exclusion contours from other experiments on the right [91, 99, 100, 101, 102]. Regions to the right of the contours are excluded.

7.5 Summary

We present the observed results and relevant studies in this chapter. Beginning with the sideband studies for validation of the analysis, we then examine the sensitivities assuming the absence of sterile neutrinos. We thoroughly presented the Asimov sensitivities and the relevant source of improvement in θ_{24} and θ_{34} spaces. A fitting strategy involving the χ^2 calculation is also discussed in conjunction with the pseudo-experiment studies. In the end, we presented the data results observed from the analysis, which include the reconstructed energy spectra and the data contours. The data does not show any deficit or excess compared to the prediction and is well within our uncertainty band. NOvA presents world-leading limits in several regions of parameter space and excludes some of the regions allowed by the other experiments.

Chapter 8

Future Work

"Every answer raises new questions"

Richard P. Feynman

Introduction

In this thesis, we present the world leading limits in all the parameter spaces though we still have scope of the improvement and NOvA is still taking data that gives additional scope of improvement. The sensitivity in high Δm^2 region is primarily driven by the ND sample which is systematically dominated, so any additional data will not help in this region, so improvement will mainly come from the additional systematic constraints. In this chapter, we will discuss a novel technique developed for the additional constraint on the cross-section systematics. In Sec. 8.1, we will present the technique and Sec. 8.2 will show the effect of this approach on the sensitivity.

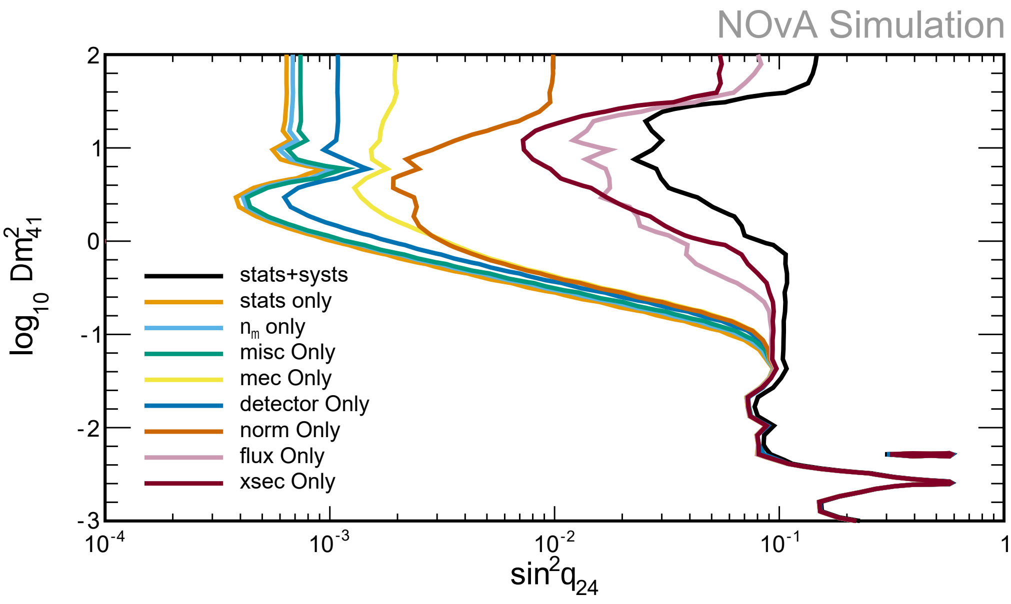

Figure 8.1: Asimov sensitivity contour (at 90% CL) showing the effect of different systematic groups on final results.

8.1 Improved Systematic Constraints

In the sterile neutrino analysis, we examine the deficit of neutrino events through the neutral current (NC) disappearance channel because NC events are independent of neutrino flavor. This allows us to measure active-sterile neutrino oscillations directly. However, uncertainties in cross-sections and fluxes significantly impact the analysis, as shown in Fig. 8.1. A major source of cross-section uncertainties is the challenge of distinguishing between the signal and cross-section effects. To reduce these uncertainties, it is crucial to better differentiate between the true signal and the cross-section effects.

8.1.1 Prong Based Splitting

We divide the neutral current samples into various subsamples based on interaction types to address this. This approach aims to disentangle the signal from cross-section uncertainties. The rationale is that if an event deficit is due to an oscillation signal, it should consistently affect all subsamples. Conversely, if the deficit is due to a cross-section effect, it will not uniformly affect all subsamples. By analyzing the behavior of different subsamples, we gain better control over cross-section systematics, thereby improving our ability to constrain these uncertainties. We analysed two approaches for splitting the near-detector (ND) neutral current (NC) samples.

It has been observed that the purity and efficiency of the samples defined based on final state topology Appendix A are not good enough because the approach depends on the particle ID, which is a trained variable and not a reconstructed information. Therefore, we look for an alternative approach to split the ND NC sample, which depends on a well-reconstructed quantity and can be easily derived from the real data. Therefore, we consider the number of prongs associated with an event that can be easily reconstructed. Fig. 8.2 shows the number of prongs with different interaction fractions. The distribution shows that the DIS interactions dominate the distribution beyond the five prongs and can easily be one of our samples. The numbers in the brackets in Tab. 8.1 correspond to the RHC sample.

Based on the Tab. 8.1 numbers, the defined sample categories will be:

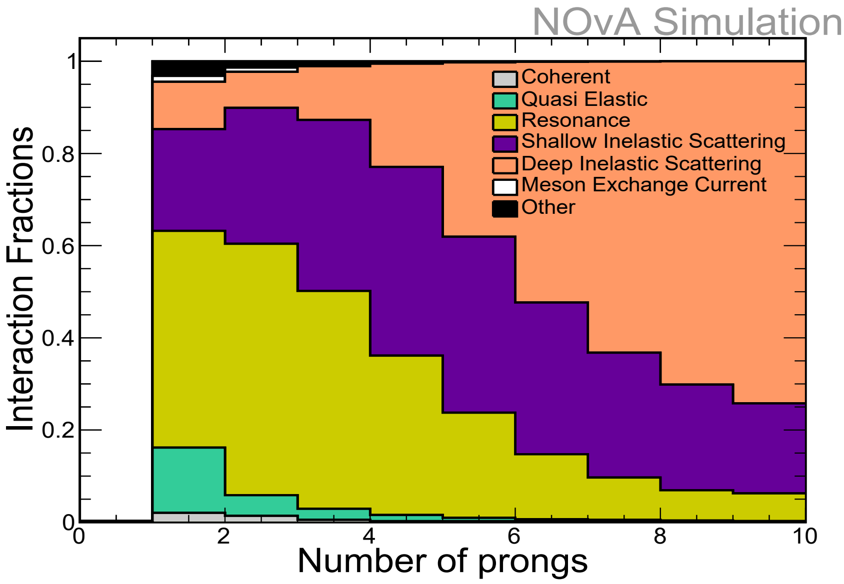

Figure 8.2: Distribution of the number of prongs associated with the events. This shows the fraction of each interaction type.

pngs	Coh	DIS	SIS	QE	Res
1	0.029(**0.071**)	0.055 (**0.046**)	0.236 (**0.254**)	0.147 (**0.091**)	0.531 (**0.535**)
2	0.016 (**0.038**)	0.051 (**0.051**)	0.315(**0.326**)	0.039 (**0.022**)	0.577 (**0.561**)
3	0.005(**0.011**)	0.103(**0.115**)	0.384(**0.393**)	0.022(**0.011**)	0.484(**0.467**)
4	0.001(**0.004**)	0.220(**0.247**)	0.414(**0.418**)	0.013(**0.006**)	0.350(**0.322**)
5	0 (**0.001**)	0.382 (**0.400**)	0.379 (**0.387**)	0.006 (**0.004**)	0.230 (**0.206**)
6	0 (**0.001**)	0.527 (**0.534**)	0.322 (**0.328**)	0.001 (**0.001**)	0.146 (**0.133**)
7	0 (0)	0.644 (**0.641**)	0.261 (**0.278**)	0 (**0.001**)	0.091 (**0.077**)
8	0	0.725 (**0.727**)	0.198 (**0.278**)	0 (0)	0.075 (**0.066**)
9	0	0.751 (**0.763**)	0.190 (**0.210**)	0	0.058 (**0.026**)

Table 8.1: Fraction of each interaction with # of prongs for **CVN>0.1**

- Single prong Sample: QE events are typically characterized by a single-prong sample.
- 2 and 3 Prong Sample: This sample is highly enriched in Res but has a contribution from SIS interaction as well.
- 4 Prong Sample: For 4 Prongs events, the DIS interaction starts

appearing, but SIS events dominate this region.

- >4 Prong Sample: The DIS interaction category highly dominates the events once we have more than four prongs.

8.2 Effect on sensitivity

The prong-based approach relies on a single, well-reconstructed variable and can be readily applied to real data. Nevertheless, Fig. 8.3 displays Asimov sensitivity contours at 90% CL for $\sin^2\theta_{24}$ vs Δm^2_{41} for three scenarios: FHC(ν), RHC($\bar{\nu}$), and joint FHC-RHC(ν-$\bar{\nu}$). This illustration reveals that despite slight differences between the two approaches, they yield comparable enhancements in sensitivity. Notably, given the ease of prong number reconstruction, we anticipate leveraging this technique in future analyses.

Moreover, significant impacts are observed upon incorporating

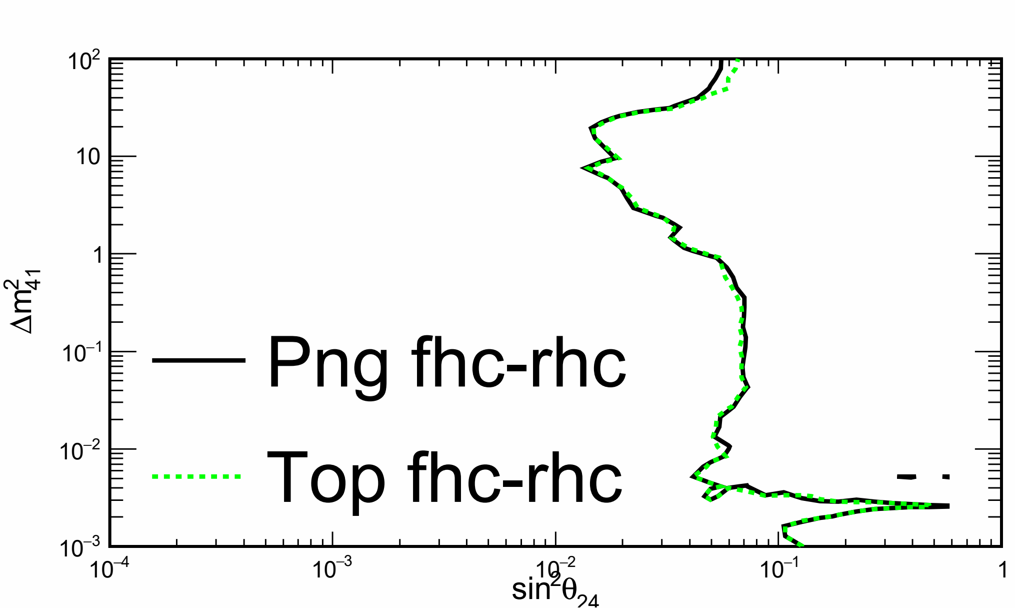

Figure 8.3: Asimov Sensitivity Contours at 90% CL for two different splitting approaches.

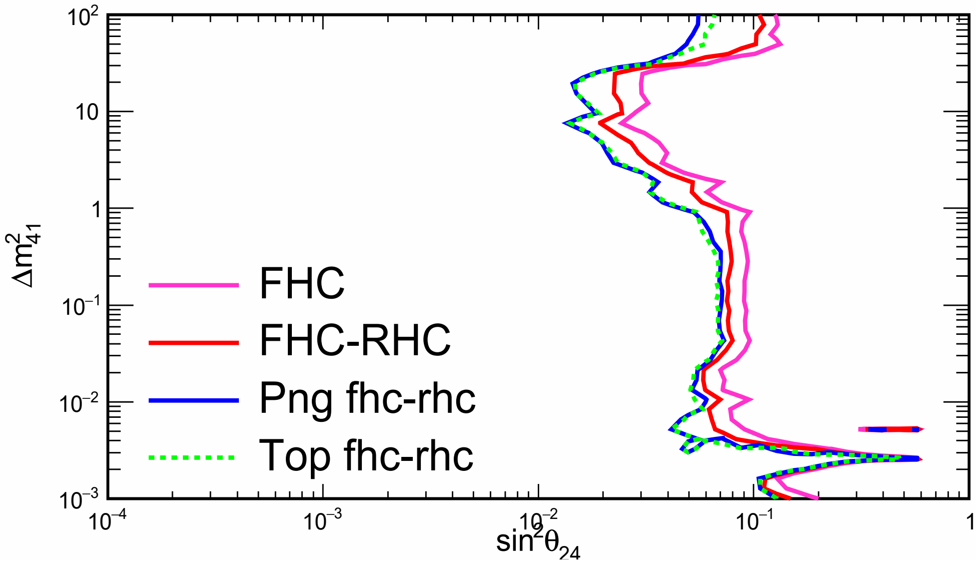

Figure 8.4: Asimov sensitivity contours at 90% CL for $\sin^2\theta_{24}$ vs Δm^2_{41} illustrating the impact of splitting on the current FHC outcome.

RHC and partitioning the ND NC sample. The rightmost contour in pink represents the most recent FHC results, while the leftmost blue dotted curve denotes a marked improvement post-splitting. Notably, the predominant effect is observed in the high Δm^2 range, primarily influenced by the ND component, prompting our decision to partition the ND sample.

Fig. 8.3 and Fig. 8.4 demonstrate that both approaches achieve similar outcomes. However, due to its ease of implementation, we will focus on the effect of prong-based splitting on the conditional uncertainty of the FD energy spectrum. Conditional uncertainty assesses the impact of introducing various constraints on the FD energy spectrum by adding different auxiliary samples. We load the systematic uncertainties in the covariance matrix for the joint two detector fit, where we look at the FD energy spectrum and add the constraints to it by adding more samples, which gets reflected as an effect on the FD spectrum.

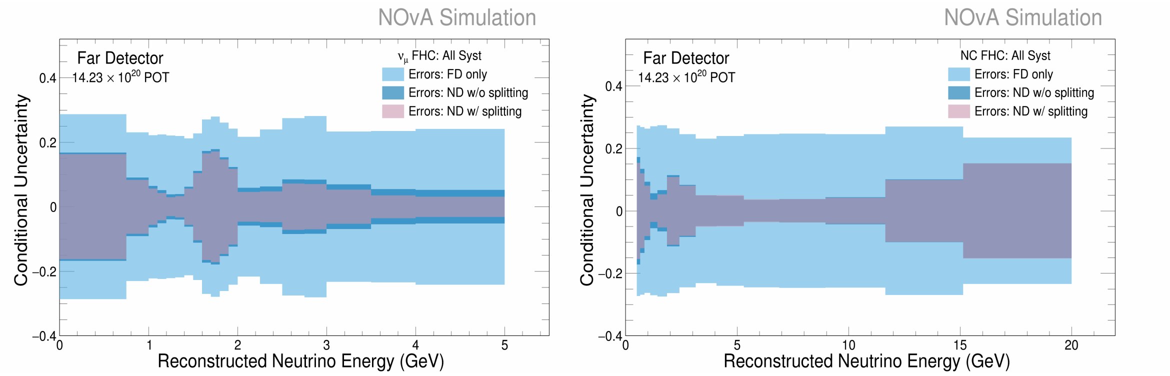

(a) ν_μ FD sample (b) NC FD sample

Figure 8.5: Both plots show the conditional uncertainty on FD reconstructed neutrino energy for all systematics. Left panel **(a)** shows results from ν_μ while the right panel **(b)** results from the neutral current for ν beam

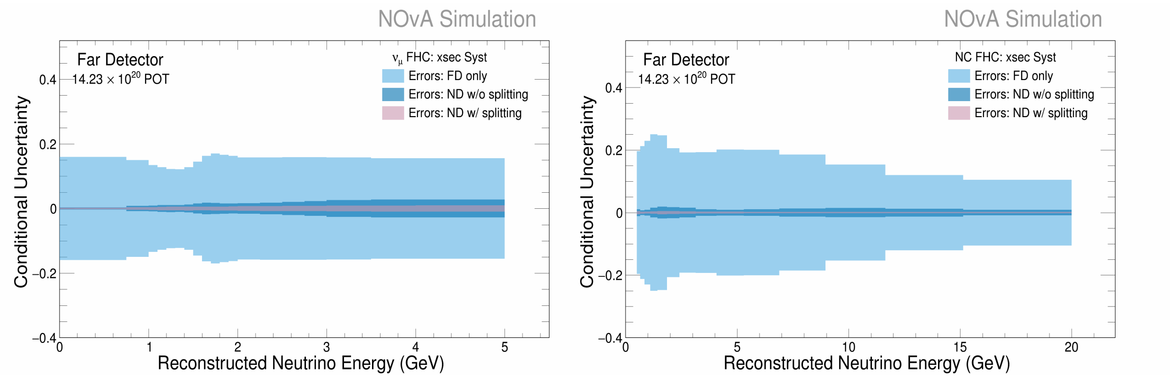

(a) ν_μ FD sample (b) NC FD sample

Figure 8.6: Both plots show the conditional uncertainty on FD reconstructed neutrino energy for cross-section systematics only. Left panel **(a)** shows results from ν_μ while the right panel **(b)** results from the neutral current for ν beam

Fig. 8.5 illustrates the impact of splitting the ND sample on the error bands, representing the conditional uncertainty for both the NC and ν_μ FD samples. It has been observed that splitting the NC sample does not significantly affect the FD NC error bands, indicating some complex underlying effects. This minimal impact on the FD NC error bands suggests that the $\sin^2\theta_{34}$ parameter

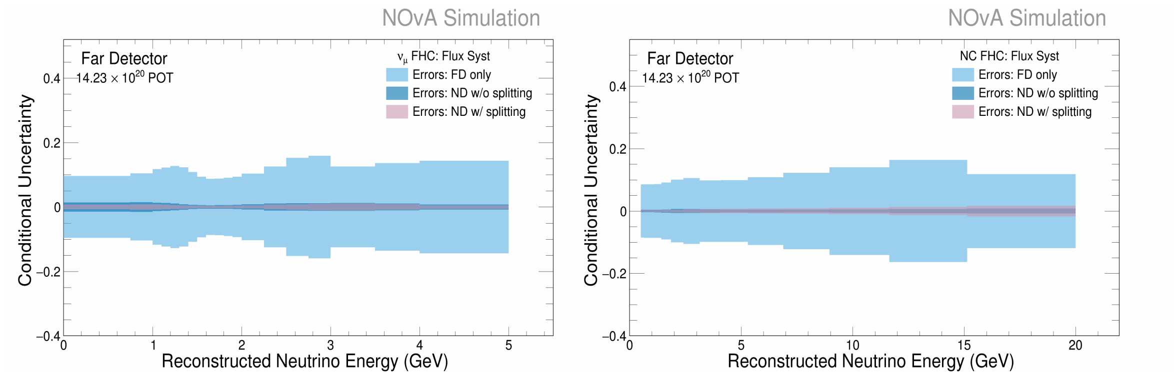

(a) ν_μ FD sample (b) NC FD sample

Figure 8.7: Both plots show the conditional uncertainty on FD reconstructed neutrino energy for flux systematics only. Left panel **(a)** shows results from ν_μ while the right panel **(b)** results from the neutral current for ν beam

space, which relies heavily on the FD NC sample for sensitivity, will also be influenced subtly.

We have separated the contributions from cross-section and flux systematic uncertainties to understand these effects better. Fig. 8.6 presents the error bands for cross-section systematics, showing a clear positive impact from the splitting, which is expected as it helps reduce these uncertainties. Conversely, Fig. 8.7 illustrates the systematic uncertainties that worsen due to the splitting. This degradation in flux uncertainties offsets the gains made in cross-section uncertainties, leading to a negligible effect on the FD NC systematic uncertainties.

8.3 Summary

In this chapter, we presented a novel technique for the future improvement in the sensitivity by constraining the cross-section systematics which is one of the major source of systematics for sterile neutrino analysis (Fig. 8.1). This approach shows around 25-30% improvement in the sensitivity could be achieved through this approach (Fig. 8.4). However, flux systematics being inversely related to this approach reduces the potential effect of this approach, therefore an in-situ constraint on the flux systematics could lead to more improvement in our sensitivities. There are several ongoing studies in NOvA that deals with the improvement in flux constraints.

Conclusion

Neutrino physics has made remarkable progress in the past few decades, from our understanding of active three-flavor neutrinos to the exploration of more complex models, such as the 3+1 framework. Despite the significant improvement in most of our models and experiments, there are still many unanswered questions, including the neutrino mass hierarchy, the octant of θ_{23}, and the possibility of more than three neutrinos. This thesis is an attempt to answer one such question by investigating the existence of sterile neutrinos. In particular, we presented the first sterile neutrino search using both neutrino and antineutrino data from the NOvA experiment. Although no significant evidence of sterile neutrino oscillation has been observed, this thesis contributes to resolving the long-lasting anomalies observed by various short-baseline experiments.

We presented a comprehensive overview of the theoretical framework necessary for this analysis, along with the motivation behind it and possible future improvements. A detailed overview of the NOvA experiment is provided in this thesis. The analysis focuses on the joint neutral current and ν_μ disappearance channels studies and therefore the primary part of the analysis begin with the selection of events and the energy reconstruction. Furthermore, the complex theory and experiments introduce systematic uncertainties, and with low statistics, we also have statistical uncertainties to contend with. Accordingly, a detailed overview of the systematic uncertainties and their sources is also presented in this thesis.

We found no significant deficit or excess of observed data events compared to the prediction, with the data remaining well within our estimated uncertainty bands. Sensitivity contours are derived from the fits of the data in three parameter space $\sin^2\theta_{24}$ vs Δm^2_{41}, $\sin^2\theta_{34}$ vs Δm^2_{41}, and $\sin^2 2\theta_{\mu\tau}$ vs Δm^2_{41}. This analysis demonstrates a significant improvement in sensitivity compared to the previous analysis, and in most regions of parameter space, the improvement exceeds 100%. We presented the competitive limits in high Δm^2_{41} range in $\sin^2\theta_{24}$ space even excluding the IceCube allowed region in 1.5 eV^2 $\leq$ Δm^2_{41} $\leq$10 eV^2 range. Furthermore, in $\sin^2\theta_{34}$ and $\sin^2 2\theta_{\mu\tau}$ space, this analysis sets the world-leading limits in the entire Δm^2_{41} range.

Finally, we introduced a novel technique to constrain the systematics, especially cross-section systematics, for future sterile neutrino analyses. With this new technique, we can expect an improvement of 25-30% in the sensitivity, highlighting its impact for the following sterile neutrino analyses at NOvA.

Appendix A

Topology Based Splitting

We have observed the positive effect of splitting of ND NC sample based on the prong multiplicity on the sensitivity. This appendix will discuss the alternate strategy to look for the final state topology of the events and tries to classify the events into different interaction categories: QE, DIS, Res, Coh, and others.

A.1 Single Proton Sample

When a neutrino interacts with a nucleus, it can scatter off the nucleus, transferring momentum to a nucleon elastically and emitting a proton from the nucleus. This phenomenon is commonly categorized as quasi-elastic scattering, typically occurring at lower energies. Detection of these interactions often relies on observing a single outgoing proton in the detector, which will be one of the obvious choices for the samples.

Fig. A.1 shows that the backgrounds highly dominate this sample and, hence, have a very low purity. However, at the same time, the amount of unselected signals is low, which enhances the efficiency

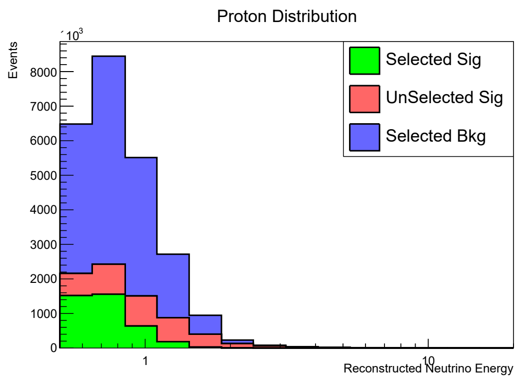

Figure A.1: Signal and Bkg Distribution for single proton sample

of this sample Tab. A.1.

A.2 Single π^0 Sample

At lower energies, neutrino interactions with nuclei occasionally produce π^0 particles, though these interactions are relatively less frequent. Following their creation, these π^0 particles promptly decay into photons, then detectable within the detector.

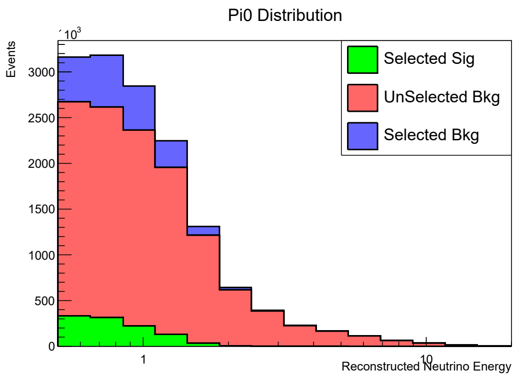

Figure A.2: Signal and Background Distribution for Single π^0 Sample

As depicted in Fig. A.2, the distribution of π^0 events exhibits a lower background level, enhancing the purity of this sample compared to samples featuring single protons. However, unlike the proton sample, this π^0 sample demonstrates lower efficiency due to unselected signals, as indicated in Tab. A.1.

A.3 Single Charged Pion Sample

Resonance excitation involves the neutrino interacting with a nucleon within the nucleus, creating a resonance state. This resonance state can subsequently decay into various particles, including pions. The charged pions ($\pi^{\pm}$) may be created through subsequent interactions of the produced particles.

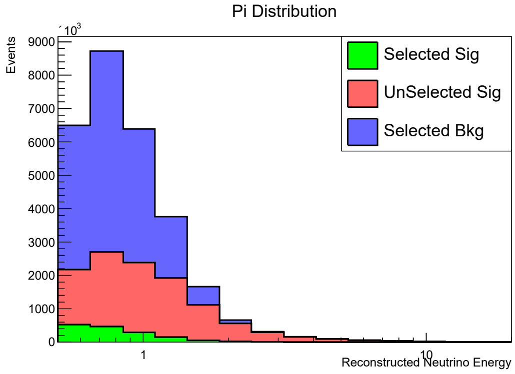

Figure A.3: Signal and Background Distribution for Single $\pi^{\pm}$ Sample

Fig. A.3 shows a similar distribution as we observed for the proton sample, where due to high background, the sample is not pure enough and due to low selected signal the efficiency is pretty low.

A.4 Proton + π^0 Sample

When incoming neutrinos possess sufficient energy to penetrate nucleons, they interact with the constituent quarks, giving rise to diverse hadronic states such as pions and protons. These interactions represent prime candidates for deep inelastic scattering (DIS).

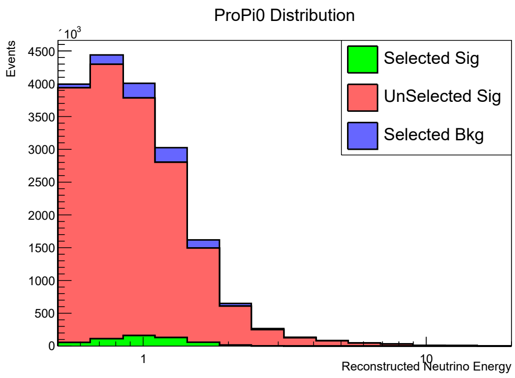

Figure A.4: Signal and Background Distribution for proton + π^0 Sample

Similar to what we have observed for a single π^0 sample (Fig. A.4), the amount of unselected signals is quite large compared to the selected one, which greatly reduces the efficiency of the sample (Tab. A.1).

A.5 Proton + $\pi^{\pm}$ Sample

Neutral current interactions can produce protons and charged pions through processes such as resonance excitation and deep inelastic scattering. In resonance excitation, the neutrino interacts with a nucleon within the nucleus, creating a resonance state that subsequently decays into particles such as protons and charged pions.

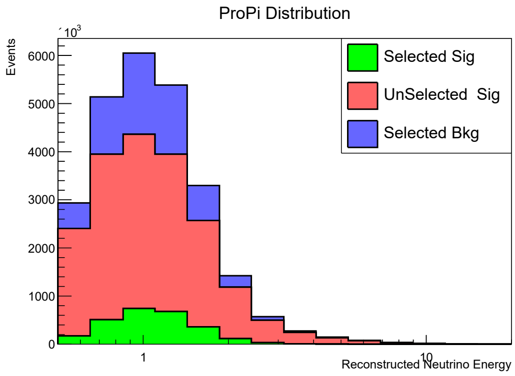

Figure A.5: Signal and Background Distribution for proton + $\pi^{\pm}$ Sample

Similar to what we have observed for a single $\pi^{\pm}$ sample (Fig. A.5), the amount of selected background is quite large compared to the selected signal, which reduces the purity of the sample (Tab. A.1).

- Selected: Sel, True: Signal
- Selected Signal: True and Selected, Selected Bkg: Selected and !True
- UnSelected Signal: True and UnSelected

Sample	Signal	Sel	Sel Signal	Sel Bkg	UnSel Sig	Purity	Efficiency
1p	7.6	20.7	3.92	16.8	3.7	18.89	51.48
1pi0	12.0	3.00	1.04	1.96	11.4	34.63	8.37
1pi	11.5	7.59	1.51	16.0	9.99	19.94	13.15
p+pi0	17.4	1.36	0.5	0.83	16.9	38.82	3.03
p+pi	19.4	8.56	2.6	5.94	16.8	30.56	13.47

Table A.1: Purity and efficiency for each sample. All values multiplied by 10^6 except purity and eff.

- Purity = $\frac{SelectedSignal}{Selected}$, eff = $\frac{SelectedSignal}{Signal}$

Appendix B

Full List of Systematics

1. NormNus5p1POT
2. NormNus5p1NDMass
3. NormNus5p1FDMass
4. NormNus5p1NDNumuOverlay
5. NormNus5p1NDNCOverlay
6. key_PPFXcomp1
7. key_PPFXcomp2
8. key_PPFXcomp3
9. key_PPFXcomp4
10. key_PPFXcomp5
11. key_PPFXcomp6
12. key_PPFXcomp7
13. key_PPFXcomp8

14. key_PPFXcomp9
15. key_PPFXcomp10
16. key_PPFXcomp11
17. key_PPFXcomp12
18. key_PPFXcomp13
19. key_PPFXcomp14
20. key_PPFXcomp15
21. key_PPFXcomp16
22. key_PPFXcomp17
23. key_PPFXcomp18
24. key_PPFXcomp19
25. key_PPFXcomp20
26. key_PPFXcomp21
27. key_PPFXcomp22
28. key_PPFXcomp23
29. key_PPFXcomp24
30. key_PPFXcomp25
31. key_PPFXcomp26
32. key_PPFXcomp27

33. key_PPFXcomp28
34. key_PPFXcomp29
35. key_PPFXcomp30
36. key_PPFXcomp31
37. key_PPFXcomp32
38. key_PPFXcomp33
39. key_PPFXcomp34
40. key_PPFXcomp35
41. key_PPFXcomp36
42. key_PPFXcomp37
43. key_PPFXcomp38
44. key_PPFXcomp39
45. key_PPFXcomp40
46. key_PPFXcomp41
47. key_PPFXcomp42
48. key_PPFXcomp43
49. key_PPFXcomp44
50. key_PPFXcomp45
51. key_PPFXcomp46

52. key_PPFXcomp47
53. key_PPFXcomp48
54. key_PPFXcomp49
55. key_PPFXcomp50
56. 2kAHornCurrent
57. 0p2mmBeamSpotSize
58. 1mmBeamShiftX
59. 1mmBeamShiftY
60. 3mmHorn1X
61. 3mmHorn1Y
62. 3mmHorn2X
63. 3mmHorn2Y
64. 7mmTargetZ
65. MagnFieldDecayPipe
66. NewTarget
67. NewTgt160to200kA
68. NewTgt180to200kA
69. 1mmHornWater
70. PiplusCex

71. PiplusDcex
72. PiplusQe
73. PiplusAbs
74. PiplusProd
75. PiminusCex
76. PiminusDcex
77. PiminusQe
78. PiminusAbs
79. PiminusProd
80. ProtonTot
81. RPAShapeenh2020
82. RPAShapesupp2020
83. ZExpAxialFFSyst2020_EV1
84. ZExpAxialFFSyst2020_EV2
85. ZExpAxialFFSyst2020_EV3
86. ZExpAxialFFSyst2020_EV4
87. LowQ2RESSupp2020
88. RESDeltaScaleSyst
89. RESOtherScaleSyst

90. RESvpvnRatioNuXSecSyst
91. RESvpvnRatioNubarXSecSyst
92. MECEnuShape2020Nu
93. MECEnuShape2020AntiNu
94. MECInitStateNPFrac2020Nu
95. MECInitStateNPFrac2020AntiNu
96. DISvpCC0pi_2020
97. DISvpCC1pi_2020
98. DISvpCC2pi_2020
99. DISvpCC3pi_2020
100. DISvpNC0pi_2020
101. DISvpNC1pi_2020
102. DISvpNC2pi_2020
103. DISvpNC3pi_2020
104. DISvnCC0pi_2020
105. DISvnCC1pi_2020
106. DISvnCC2pi_2020
107. DISvnCC3pi_2020
108. DISvnNC0pi_2020

109. DISvnNC1pi_2020
110. DISvnNC2pi_2020
111. DISvnNC3pi_2020
112. DISvbarpCC0pi_2020
113. DISvbarpCC1pi_2020
114. DISvbarpCC2pi_2020
115. DISvbarpCC3pi_2020
116. DISvbarpNC0pi_2020
117. DISvbarpNC1pi_2020
118. DISvbarpNC2pi_2020
119. DISvbarpNC3pi_2020
120. DISvbarnCC0pi_2020
121. DISvbarnCC1pi_2020
122. DISvbarnCC2pi_2020
123. DISvbarnCC3pi_2020
124. DISvbarnNC0pi_2020
125. DISvbarnNC1pi_2020
126. DISvbarnNC2pi_2020
127. DISvbarnNC3pi_2020

128. DISNuHadronQ1Syst
129. DISNuBarHadronQ0Syst
130. FormZone2024
131. hNFSI_FateFracEV1_2024
132. hNFSI_FateFracEV2_2024
133. hNFSI_FateFracEV3_2024
134. hNFSI_MFP_2024
135. radcorrnue
136. radcorrnuebar
137. 2ndclasscurr
138. MaNCEL
139. EtaNCEL
140. MaCCRES
141. MvCCRES
142. MaNCRES
143. MvNCRES
144. COHCCScale2018
145. COHNCScale2018
146. AhtBY

147. BhtBY
148. CV1uBY
149. CV2uBY
150. AGKYxF1pi
151. AGKYpT1pi
152. RDecBR1gamma
153. RDecBR1eta
154. Theta_Delta2Npi
155. ZNormCCQE
156. key_neardet_Calib
157. key_fardet_Calib
158. key_neardet_CalibShape
159. key_fardet_CalibShape
160. key_neardet_LightLevel
161. key_fardet_LightLevel
162. key_Cherenkov
163. key_neardet_Drift
164. key_fardet_Drift
165. key_Menate

166. key_MECcomp1
167. key_MECcomp2
168. Nus5p1MECNorm
169. Nus5p1KaonFlux10
170. Nus5p1KaonFluxRHC
171. Nus5p1RockNorm
172. Nus5p1NonRockNorm
173. Nus5p1TauNorm
174. CorrMuEScaleSyst2024
175. UnCorrMuCatMuESyst2024
176. UnCorrNDMuEScaleSyst2024
177. UnCorrFDMuEScaleSyst2024
178. PileupMuESyst2024

Bibliography

[1] C. T2K., "About neutrinos.," 2013.

[2] E. Fermi, "An attempt of a theory of beta radiation," *Zeitschrift für Physik*, vol. 88, pp. 161–177, 1934.

[3] H. BETHE and PEIERLS, "The "neutrino"," *Nature*, vol. 133, p. 532, 1934.

[4] B. Pontecorvo, "Inverse beta process," *Camb. Monogr. Part. Phys. Nucl. Phys. Cosmol.*, vol. 1, pp. 25–31, 1991.

[5] F. Reines and C. L. Cowan, "Detection of the free neutrino," *Physical Review*, vol. 92, pp. 830–831, 1953.

[6] J. A. Formaggio and G. P. Zeller, "From ev to eev: Neutrino cross sections across energy scales," *Reviews of Modern Physics*, vol. 84, pp. 1307–1341, Sept. 2012.

[7] J. N. Bahcall, *Neutrino Astrophysics*. Cambridge University Press, 1989.

[8] W. C. Haxton, A. Serenelli, and C. Peña-Garay, "Solar neutrinos: Status and prospects," *Annual Review of Astronomy and Astrophysics*, vol. 51, pp. 21–61, 2013.

[9] J. N. Bahcall and M. H. Pinsonneault, "What do we (not) know theoretically about solar neutrino fluxes?," *Phys. Rev. Lett.*, vol. 92, p. 121301, Mar 2004.

[10] T. K. Gaisser, *Cosmic Rays and Particle Physics*. Cambridge University Press, 1990.

[11] Y. e. a. Fukuda, "Evidence for oscillation of atmospheric neutrinos," *Physical Review Letters*, vol. 81, pp. 1562–1567, 1998.

[12] P. Vogel and J. Engel, "Neutrino electromagnetic form factors," *Physical Review D*, vol. 39, pp. 3378–3383, 1989.

[13] J. Kopp, "Accelerator neutrino beams," *Physics Reports*, vol. 439, pp. 101–159, 2013.

[14] R. Davis, "A review of the homestake solar neutrino experiment," *Progress in Particle and Nuclear Physics*, vol. 32, pp. 13–32, 1994.

[15] Y. Oyama, "Results from kamiokande-ii experiment," *Nuclear Physics B - Proceedings Supplements*, vol. 13, pp. 362–367, 1990.

[16] J. Boger, R. Hahn, *et al.*, "The sudbury neutrino observatory," *Nuclear Instruments and Methods in Physics Research Section A: Accelerators, Spectrometers, Detectors and Associated Equipment*, vol. 449, no. 1, pp. 172–207, 2000.

[17] J. N. Bahcall, "Solar models and solar neutrinos," *Physica Scripta*, vol. 2005, p. 46, jan 2005.

[18] M. Thomson, *Modern Particle Physics*. Cambridge University Press, 2013.

[19] F. Feruglio, "Lectures on neutrino physics,"

[20] K. Nakamura and P. D. Group), "Review of particle physics," *Journal of Physics G: Nuclear and Particle Physics*, vol. 37, p. 075021, jul 2010.

[21] T. Araki, K. Eguchi, *et al.*, "Measurement of neutrino oscillation with kamland: Evidence of spectral distortion," *Phys. Rev. Lett.*, vol. 94, p. 081801, Mar 2005.

[22] P. Adamson, C. Andreopoulos, *et al.*, "Measurement of neutrino oscillations with the minos detectors in the numi beam," *Phys. Rev. Lett.*, vol. 101, p. 131802, Sep 2008.

[23] R. Volkas, "Progress in particle and nuclear physics," *Phys. Rev. Lett.*, vol. 48, p. 161, 2002.

[24] K. S. Hirata, K. Inoue, and *et al*, "Observation of a small atmospheric ratio in kamiokande," *Phys. Lett. B*, vol. 280, pp. 146–152, 1992.

[25] Y. Fukuda, T. Hayakawa, , and *et al*, "Atmospheric ν_μ/ν_e ratio in the multi-gev energy range," *Physics Letters B*, vol. 335, no. 2, pp. 237–245, 1994.

[26] D. Casper, R. Becker-Szendy, and *et al*, "Measurement of atmospheric neutrino composition with the imb-3 detector," *Phys. Rev. Lett.*, vol. 66, pp. 2561–2564, May 1991.

[27] R. Becker-Szendy, C. B. Bratton, and *et al*, "Electron- and muon-neutrino content of the atmospheric flux," *Phys. Rev. D*, vol. 46, pp. 3720–3724, Nov 1992.

[28] E. Akhmedov, P. Lipari, and M. Lusignoli, "Matter effects in atmospheric neutrino oscillations," *Physics Letters B*, vol. 300, no. 1, pp. 128–136, 1993.

[29] Q. Liu and A. Smirnov, "Neutrino mass spectrum with $\nu_\mu \to \nu_s$ oscillations of atmospheric neutrinos," *Nuclear Physics B*, vol. 524, no. 3, pp. 505–523, 1998.

[30] D. O. Caldwell and R. N. Mohapatra, "Neutrino mass explanations of solar and atmospheric neutrino deficits and hot dark matter," *Phys. Rev. D*, vol. 48, pp. 3259–3263, Oct 1993.

[31] J. Peltoniemi and J. Valle, "Reconciling dark matter, solar and atmospheric neutrinos," *Nuclear Physics B*, vol. 406, no. 1, pp. 409–422, 1993.

[32] G. M. Fuller, J. R. Primack, and Y.-Z. Qian, "Do experiments and astrophysical considerations suggest an inverted neutrino mass hierarchy?," *Phys. Rev. D*, vol. 52, pp. 1288–1291, Jul 1995.

[33] J. J. Gomez-Cadenas and M. C. Gonzalez-Garcia, "Future ν_τ oscillation experiments and present data," *Zeitschrift für*

Physik C Particles and Fields, vol. 71, pp. 443–454, Jul 1996.

[34] L. Collaboration, "The liquid scintillator neutrino detector and lampf neutrino source," *Nuclear Instruments and Methods in Physics Research Section A: Accelerators, Spectrometers, Detectors and Associated Equipment*, vol. 388, no. 1, pp. 149–172, 1997.

[35] A. LSND Collaboration Aguilar *et al.*, "Evidence for neutrino oscillations from the observation of $\overline{\nu}_e$ appearance in a $\overline{\nu}_\mu$ beam," *Phys. Rev. D*, vol. 64, p. 112007, Nov 2001.

[36] A. A. Aguilar-Arevalo, C. E. Anderson, *et al.*, "Neutrino flux prediction at miniboone," *Phys. Rev. D*, vol. 79, p. 072002, Apr 2009.

[37] A. Aguilar-Arevalo, C. Anderson, *et al.*, "The miniboone detector," *Nuclear Instruments and Methods in Physics Research Section A: Accelerators, Spectrometers, Detectors and Associated Equipment*, vol. 599, no. 1, pp. 28–46, 2009.

[38] A. A. Aguilar-Arevalo, B. C. Brown, *et al.*, "Updated miniboone neutrino oscillation results with increased data and new background studies," *Phys. Rev. D*, vol. 103, p. 052002, Mar 2021.

[39] A. A. Aguilar-Arevalo, B. C. Brown, *et al.*, "Significant excess of electronlike events in the miniboone short-baseline neutrino experiment," *Phys. Rev. Lett.*, vol. 121, p. 221801, Nov 2018.

[40] F. REINES and C. L. COWANjun., "The neutrino," *Nature*, vol. 178, pp. 446–449, Sep 1956.

[41] C. L. Cowan, F. Reines, F. B. Harrison, H. W. Kruse, and A. D. McGuire, "Detection of the free neutrino: a confirmation," *Science*, vol. 124, no. 3212, pp. 103–104, 1956.

[42] T. A. Mueller, D. Lhuillier, *et al.*, "Improved predictions of reactor antineutrino spectra," *Phys. Rev. C*, vol. 83, p. 054615, May 2011.

[43] P. Huber, "Determination of antineutrino spectra from nuclear reactors," *Phys. Rev. C*, vol. 84, p. 024617, Aug 2011.

[44] N. Haag, A. Gütlein, M. Hofmann, L. Oberauer, W. Potzel, K. Schreckenbach, and F. M. Wagner, "Experimental determination of the antineutrino spectrum of the fission products of ^{238}U," *Phys. Rev. Lett.*, vol. 112, p. 122501, Mar 2014.

[45] C. Giunti, Y.-F. Li, and R. ping Zhang, "Revival of the reactor antineutrino anomaly," 2026.

[46] G. Mention, M. Fechner, T. Lasserre, T. A. Mueller, D. Lhuillier, M. Cribier, and A. Letourneau, "Reactor antineutrino anomaly," *Phys. Rev. D*, vol. 83, p. 073006, Apr 2011.

[47] W. Hampel, G. Heusser, J. Kiko, T. Kirsten, M. Laubenstein, E. Pernicka, W. Rau, U. Rönn, C. Schlosser, M. Wójcik, R. v. Ammon, K. Ebert, T. Fritsch, D. Heidt, E. Henrich, L. Stieglitz, F. Weirich, M. Balata, F. Hartmann, M. Sann,

E. Bellotti, C. Cattadori, O. Cremonesi, N. Ferrari, E. Fiorini, L. Zanotti, M. Altmann, F. v. Feilitzsch, R. Mößbauer, G. Berthomieu, E. Schatzman, I. Carmi, I. Dostrovsky, C. Bacci, P. Belli, R. Bernabei, S. d'Angelo, L. Paoluzi, A. Bevilacqua, M. Cribier, L. Gosset, J. Rich, M. Spiro, C. Tao, D. Vignaud, J. Boger, R. Hahn, J. Rowley, R. Stoenner, and J. Weneser, "Final results of the 51cr neutrino source experiments in gallex," *Physics Letters B*, vol. 420, no. 1, pp. 114–126, 1998.

[48] F. Kaether, W. Hampel, G. Heusser, J. Kiko, and T. Kirsten, "Reanalysis of the gallex solar neutrino flux and source experiments," *Physics Letters B*, vol. 685, no. 1, pp. 47–54, 2010.

[49] J. N. Abdurashitov, V. N. Gavrin, S. V. Girin, V. V. Gorbachev, P. P. Gurkina, T. V. Ibragimova, A. V. Kalikhov, N. G. Khairnasov, T. V. Knodel, V. A. Matveev, I. N. Mirmov, A. A. Shikhin, E. P. Veretenkin, V. M. Vermul, V. E. Yants, G. T. Zatsepin, T. J. Bowles, S. R. Elliott, W. A. Teasdale, B. T. Cleveland, W. C. Haxton, J. F. Wilkerson, J. S. Nico, A. Suzuki, K. Lande, Y. S. Khomyakov, V. M. Poplavsky, V. V. Popov, O. V. Mishin, A. N. Petrov, B. A. Vasiliev, S. A. Voronov, A. I. Karpenko, V. V. Maltsev, N. N. Oshkanov, A. M. Tuchkov, V. I. Barsanov, A. A. Janelidze, A. V. Korenkova, N. A. Kotelnikov, S. Y. Markov, V. V. Selin, Z. N. Shakirov, A. A. Zamyatina, and S. B. Zlokazov, "Mea-

surement of the response of a ga solar neutrino experiment to neutrinos from a ^{37}Ar source," *Phys. Rev. C*, vol. 73, p. 045805, Apr 2006.

[50] M. A. Acero, C. Giunti, and M. Laveder, "Limits on ν_e and $\overline{\nu}_e$ disappearance from gallium and reactor experiments," *Phys. Rev. D*, vol. 78, p. 073009, Oct 2008.

[51] C. Giunti and M. Laveder, "Statistical significance of the gallium anomaly," *Physical Review C*, vol. 83, no. 6, 2011.

[52] A. Aurisano, "Validating the approximation of sterile appearance," 2019.

[53] S. Yang, *Searching for Light Sterile Neutrinos with NOvA Through Neutral-Current Disappearance.* PhD thesis, Cincinnati U., 2019.

[54] J. J. Evans, "The minos experiment: Results and prospects," *Advances in High Energy Physics*, vol. 2013, no. 1, p. 182537, 2013.

[55] R. M. Zwaska, *Accelerator Systems and Instrumentation for the NuMI Neutrino Beam.* PhD thesis, Texas U., 2005.

[56] P. Adamson and K. A. et al., "The numi neutrino beam," *Nuclear Instruments and Methods in Physics Research Section A: Accelerators, Spectrometers, Detectors and Associated Equipment*, vol. 806, pp. 279–306, 2016.

[57] K. Anderson *et al.*, "The NuMI Facility Technical Design Report," 10 1998.

[58] P. Adamson and C. A. et al., “Study of muon neutrino disappearance using the fermilab main injector neutrino beam,” *Phys. Rev. D*, vol. 77, p. 072002, Apr 2008.

[59] J. G. Morfin, “The minerνa experiment at fermilab,” *Nuclear Physics B - Proceedings Supplements*, vol. 149, pp. 233–235, 2005. NuFact04.

[60] K. Yonehara, S. Ganguly, D. A. Wickremasinghe, P. Snopok, and Y. Yu, “Exploring the focusing mechanism of the numi horn magnets,” 2025.

[61] D. S. Ayres, G. R. Drake, *et al.*, “The nova technical design report,” tech. rep., Fermi National Accelerator Laboratory (FNAL), Batavia, IL, 10 2007.

[62] A. T.C. Sutton, *Neutrinos: A Desperate Remedy*, pp. 1–14. Cham: Springer Nature Switzerland, 2023.

[63] S. Mufson and B. B. et al., “Liquid scintillator production for the nova experiment,” *Nuclear Instruments and Methods in Physics Research Section A: Accelerators, Spectrometers, Detectors and Associated Equipment*, vol. 799, pp. 1–9, 2015.

[64] A. Norman, G. Davies, *et al.*, “Performance of the nova data acquisition and trigger systems for the full 14 kt far detector,” *Journal of Physics: Conference Series*, vol. 664, p. 082041, dec 2015.

[65] D. S. Pershey, *A Measurement of ν_e Appearance and ν_μ Disappearance Neutrino Oscillations with the NOvA Experiment*. PhD thesis, 06 2018.

[66] F. Psihas, "Event displays for nue selected events," *NOvA Internal Document 15647-v4*, 2016.

[67] v. Hewes, "Rock systematic for 2022 sterile analysis," 2022.

[68] Shivam, "Rock systematic study," 2024.

[69] A. Lister and H. R. Hausner, "Neutral Current Selection Technote," 2020.

[70] The NOvA Collaboration, "Precision measurement of neutrino oscillation parameters with 10 years of data from the nova experiment," 2025.

[71] P. J., "ReMId retraining 2019 technote." NOvA Internal Document 42277, 2019.

[72] M. R. C. MacMahon, "ana2024 numu event displays,"

[73] N. J. Raddatz, "ReMId Technical Note," 2014.

[74] J. Porter, "ReMId retraining 2019 technote," 2019.

[75] M. W, "NuMu Energy Estimator Technote for Prod5 MC," 2020.

[76] L. R. Prais, "Standard and non-standard neutrino oscillations at the nova experiment,"

[77] M. W, "NuMu Energy Spline Plots 2020," 2020.

[78] G. Cowan, K. Cranmer, E. Gross, and O. Vitells, "Statistical data analysis," 2020.

[79] v. Hewes, "PISCES technote." NOvA Internal Document 45977-v2, 2022.

[80] NOvA Collaboration, "Dual-baseline search for active-to-sterile neutrino oscillations in nova," *Phys. Rev. Lett.*, vol. 134, p. 081804, Feb 2025.

[81] N. Marumo, T. Okuno, and A. Takeda, "Majorization-minimization-based levenberg–marquardt method for constrained nonlinear least squares," *Phys. Rev. D*, vol. 84, pp. 833–874, April 2023.

[82] MINERνA Collaboration, "Neutrino flux predictions for the numi beam," *Phys. Rev. D*, vol. 94, p. 092005, Nov 2016.

[83] "https://ar5iv.labs.arxiv.org/html/1304.6014,"

[84] A. Norrick and v. Hewes, "Cross Section Uncertainties for Nux Analyses," 2020.

[85] Shivam and A. Norrick, "NC Selection Technote for Joint FHC-RHC Analysis." NOvA Internal Document 64862, 2024.

[86] Shivam, A. Lister, and A. Norrick, "NC Energy Estimator for the joint FHC-RHC Analysis." NOvA Internal Document 64475, 2024.

[87] A. Aurisano, "ND Blinding." NOvA Internal Document 43470, 2025.

[88] Shivam, "NuS5.1 ND Burner Sample Discussion." NOvA Internal Document 36776, 2025.

[89] Shivam, "NuMu Burner Sample." NOvA Internal Document 66730, 2025.

[90] P. Adamson, F. P. An, *et al.*, "Improved constraints on sterile neutrino mixing from disappearance searches in the minos, MINOS+, daya bay, and bugey-3 experiments," *Phys. Rev. Lett.*, vol. 125, p. 071801, Aug 2020.

[91] F. Dydak, G. Feldman, *et al.*, "A search for ν_μ oscillations in the δm^2 range 0.3–90 ev^2," *Physics Letters B*, vol. 134, no. 3, pp. 281–286, 1984.

[92] I. E. Stockdale, A. Bodek, *et al.*, "Limits on muon-neutrino oscillations in the mass range $30 < \Delta m^2 < 1000$ eV$^2/c^4$," *Phys. Rev. Lett.*, vol. 52, pp. 1384–1388, Apr 1984.

[93] K. Abe, R. Akutsu, *et al.*, "Search for light sterile neutrinos with the t2k far detector super-kamiokande at a baseline of 295 km," *Phys. Rev. D*, vol. 99, p. 071103, Apr 2019.

[94] K. B. M. Mahn, Y. Nakajima, *et al.*, "Dual baseline search for muon neutrino disappearance at $0.5 < \Delta m^2 < 40$ eV^2," *Phys. Rev. D*, vol. 85, p. 032007, Feb 2012.

[95] K. Abe, Y. Haga, *et al.*, "Limits on sterile neutrino mixing using atmospheric neutrinos in super-kamiokande," *Phys. Rev. D*, vol. 91, p. 052019, Mar 2015.

[96] P. Adamson, I. Anghel, *et al.*, “Search for sterile neutrinos mixing with muon neutrinos in minos,” *Phys. Rev. Lett.*, vol. 117, p. 151803, Oct 2016.

[97] M. G. Aartsen, M. Ackermann, *et al.*, “Search for sterile neutrino mixing using three years of icecube deepcore data,” *Phys. Rev. D*, vol. 95, p. 112002, Jun 2017.

[98] M. G. Aartsen, R. Abbasi, *et al.*, “ev-scale sterile neutrino search using eight years of atmospheric muon neutrino data from the icecube neutrino observatory,” *Phys. Rev. Lett.*, vol. 125, p. 141801, Sep 2020.

[99] E. Eskut, A. Kayis-Topaksu, *et al.*, “Final results on $\nu_\mu \to \nu_\tau$ oscillation from the chorus experiment,” *Nuclear Physics B*, vol. 793, no. 1, pp. 326–343, 2008.

[100] D. Naples, A. Romosan, *et al.*, “High statistics search for $v_e(v_e) \to v_\tau(v_\tau)$ oscillations,” *Phys. Rev. D*, vol. 59, p. 031101, Dec 1998.

[101] P. Astier, D. Autiero, *et al.*, “Final nomad results on $\nu_\mu \to \nu_\tau$ and $\nu_e \to \nu_\tau$ oscillations including a new search for ν_τ appearance using hadronic τ decays,” *Nuclear Physics B*, vol. 611, no. 1, pp. 3–39, 2001.

[102] N. Agafonova, A. Alexandrov, *et al.*, “Final results on neutrino oscillation parameters from the opera experiment in the cngs beam,” *Phys. Rev. D*, vol. 100, p. 051301, Sep 2019.